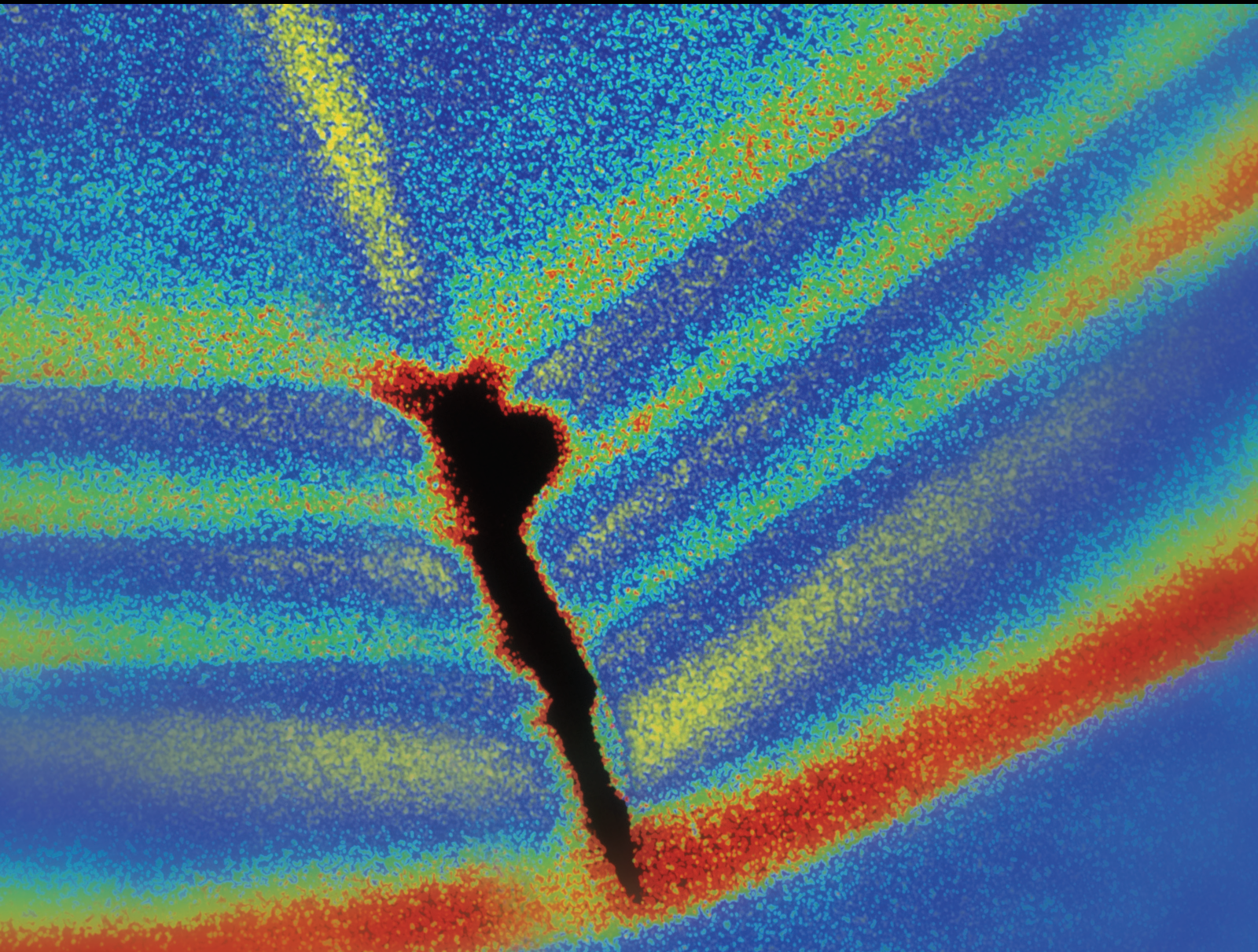# Performance Based Shock and Vibration Engineering of Infrastructures

Lead Guest Editor: S. Mahdi S. Kolbadi
Guest Editors: Ali Noorzad, Masoud Mirtaheri, Angelo Marcelo Tusset, Iolanda Nuzzo, and Wahyu Caesarendra

Performance Based Shock and Vibration Engineering of Infrastructures

Performance Based Shock and Vibration Engineering of Infrastructures

Lead Guest Editor: S. Mahdi S. Kolbadi
Guest Editors: Ali Noorzad, Masoud Mirtaheri,
Angelo Marcelo Tusset, Iolanda Nuzzo, and Wahyu
Caesarendra

Amal Hajjaj [iD], United Kingdom

Mohammad A. Hariri-Ardebili [iD], USA

Seyed M. Hashemi [iD], Canada

Xue-qiu He, China

Agustin Herrera-May [iD], Mexico

M.I. Herreros [iD], Spain

Duc-Duy Ho [iD], Vietnam

Hamid Hosano [iD], Japan

Jin Huang [iD], China

Ahmed Ibrahim [iD], USA

Bernard W. Ikua, Kenya

Xingxing Jiang [iD], China

Jiang Jin [iD], China

Xiaohang Jin, China

MOUSTAFA KASSEM [iD], Malaysia

Shao-Bo Kang [iD], China

Yuri S. Karinski [iD], Israel

Andrzej Katunin [iD], Poland

Manoj Khandelwal, Australia

Denise-Penelope Kontoni [iD], Greece

Mohammadreza Koopialipoor, Iran

Georges Kouroussis [iD], Belgium

Genadijus Kulvietis, Lithuania

Pradeep Kundu [iD], USA

Luca Landi [iD], Italy

Moon G. Lee [iD], Republic of Korea

Trupti Ranjan Lenka [iD], India

Arcanjo Lenzi, Brazil

Marco Lepidi [iD], Italy

Jinhua Li [iD], China

Shuang Li [iD], China

Zhixiong Li [iD], China

Xihui Liang [iD], Canada

Tzu-Kang Lin [iD], Taiwan

Jinxin Liu [iD], China

Ruonan Liu, China

Xiuquan Liu, China

Siliang Lu, China

Yixiang Lu [iD], China

R. Luo [iD], China

Tianshou Ma [iD], China

Nuno M. Maia [iD], Portugal

Abdollah Malekjafarian [iD], Ireland

Stefano Manzoni [iD], Italy

Stefano Marchesiello [iD], Italy

Francesco S. Marulo, Italy

Traian Mazilu [iD], Romania

Vittorio Memmolo [iD], Italy

Jean-Mathieu Mencik [iD], France

Laurent Mevel [iD], France

Letícia Fleck Fadel Miguel [iD], Brazil

FuRen Ming [iD], China

Fabio Minghini [iD], Italy

Marco Miniaci [iD], USA

Mahdi Mohammadpour [iD], United Kingdom

Rui Moreira [iD], Portugal

Emiliano Mucchi [iD], Italy

Peter Múčka [iD], Slovakia

Fehmi Najar, Tunisia

M. Z. Naser, USA

Amr A. Nassr, Egypt

Sundararajan Natarajan [iD], India

Toshiaki Natsuki, Japan

Miguel Neves [iD], Portugal

Sy Dzung Nguyen [iD], Republic of Korea

Trung Nguyen-Thoi [iD], Vietnam

Gianni Niccolini, Italy

Rodrigo Nicoletti [iD], Brazil

Bin Niu [iD], China

Leilei Niu, China

Yan Niu [iD], China

Lucio Olivares, Italy

Erkan Oterkus, United Kingdom

Roberto Palma [iD], Spain

Junhong Park [iD], Republic of Korea

Francesco Pellicano [iD], Italy

Paolo Pennacchi [iD], Italy

Giuseppe Petrone [iD], Italy

Evgeny Petrov, United Kingdom

Franck Poisson [iD], France

Luca Pugi [iD], Italy

Yi Qin [iD], China

Virginio Quaglini [iD], Italy

Mohammad Rafiee [iD], Canada

Carlo Rainieri [iD], Italy

Vasudevan Rajamohan [iD], India

Ricardo A. Ramirez-Mendoza [iD], Mexico

José J. Rangel-Magdaleno [iD], Mexico

Didier Rémond, France
Dario Richiedei, Italy
Fabio Rizzo, Italy
Carlo Rosso, Italy
Riccardo Rubini, Italy
Salvatore Russo, Italy
Giuseppe Ruta, Italy
Edoardo Sabbioni, Italy
Pouyan Roodgar Saffari, Iran
Filippo Santucci de Magistris, Italy
Fabrizio Scozzese, Italy
Abdullah Seçgin, Turkey
Roger Serra, France
S. Mahdi Seyed-Kolbadi, Iran
Yujie Shen, China
Bao-Jun Shi, China
Chengzhi Shi, USA
Gerardo Silva-Navarro, Mexico
Marcos Silveira, Brazil
Kumar V. Singh, USA
Jean-Jacques Sinou, France
Isabelle Sochet, France
Alba Sofi, Italy
Jussi Sopanen, Finland
Stefano Sorace, Italy
Andrea Spaggiari, Italy
Lei Su, China
Shuaishuai Sun, Australia
Fidelis Tawiah Suorineni, Kazakhstan
Cecilia Surace, Italy
Tomasz Szolc, Poland
Iacopo Tamellin, Italy
Zhuhua Tan, China
Gang Tang, China
Chao Tao, China
Tianyou Tao, China
Marco Tarabini, Italy
Hamid Toopchi-Nezhad, Iran
Carlo Trigona, Italy
Federica Tubino, Italy
Nerio Tullini, Italy
Nicolò Vaiana, Italy
Marcello Vanali, Italy
Christian Vanhille, Spain

Dr. Govind Vashishtha, Poland
F. Viadero, Spain
M. Ahmer Wadee, United Kingdom
C. M. Wang, Australia
Gaoxin Wang, China
Huiqi Wang, China
Pengfei Wang, China
Weiqiang Wang, Australia
Xian-Bo Wang, China
YuRen Wang, China
Wai-on Wong, Hong Kong
Yuanping XU, China
Biao Xiang, China
Qilong Xue, China
Xin Xue, China
Diansen Yang, China
Jie Yang, Australia
Chang-Ping Yi, Sweden
Nicolo Zampieri, Italy
Chao-Ping Zang, China
Enrico Zappino, Italy
Guo-Qing Zhang, China
Shaojian Zhang, China
Yongfang Zhang, China
Yaobing Zhao, China
Zhipeng Zhao, Japan
Changjie Zheng, China
Chuanbo Zhou, China
Hongwei Zhou, China
Hongyuan Zhou, China
Jiaxi Zhou, China
Yunlai Zhou, China
Radoslaw Zimroz, Poland

Contents

Research Article

A System Identification-Based Damage-Detection Method for Gravity Dams

Masoud Mirtaheri (ID),[1] **Mojtaba Salkhordeh** (ID),[1] **and Masoud Mohammadgholiha** (ID)[2]

[1]*Department of Civil and Environmental Engineering, K. N. Toosi University of Technology, Tehran, Iran*
[2]*Department of Electrical, Electronic, and Information Engineering, University of Bologna, Bologna 40136, Italy*

Correspondence should be addressed to Masoud Mirtaheri; mmirtaheri@kntu.ac.ir

Dams are essential infrastructures as they provide a range of economic, environmental, and social benefits to the local populations. Damage in the body of these structures may lead to an irreparable disaster. This paper presents a cost-effective vibration-based framework to identify the dynamic properties and damage of the dams. To this end, four commonly occurred damage scenarios, including (1) damage in the neck of the dam, (2) damage in the toe of the structure, (3) simultaneous damage in the neck and the toe of the dam, and (4) damage in the lifting joints of the dam, are considered. The proposed method is based on processing the acceleration response of a gravity dam under ambient excitations. First, the random decrement technique (RDT) is applied to determine the free-vibration of the structure using the structural response. Then, a combined method based on Hilbert–Huang Transform (HHT) and Wavelet Transform (WT) is presented to obtain the dynamic properties of the structure. Next, the cubic-spline technique is used to make the mode shapes differentiable. Finally, Continuous Wavelet Transform (CWT) is applied to the residual values of mode shape curvatures between intact and damaged structures to estimate the damage location. In order to evaluate the efficiency of the proposed method in field condition, 10% noise is added to the structural response. Results show promising accuracy in estimating the location of damage even when the structure is subjected to simultaneous damage in different locations.

1. Introduction

Civil engineering infrastructures provide the essential instruments for a community to have an immediate operation. These infrastructures include buildings, vehicular and pedestrian bridges, factories, transmission towers, and dams. Concrete dams provide economic benefits by supplying water for irrigation, energy for hydroelectricity generation, and obstacle for flood control. The performance of such infrastructures under ambient vibrations as well as the operational loads may reduce over their life-time. Failure of the dams leads to irreparable losses for beneficiary communities near these structures [1, 2]. The most important catastrophes that occurred in the recent years include the failure in 1864 of a 30 m embankment dam which claimed 254 people in Sheffield, UK [3], Canyon lake dam that claimed the lives of 236 people in Texas, USA [4], and Austin dam disaster that claimed the lives of 78 people [5]. Hence, a continuous Structural Health Monitoring (SHM) framework is needed to prevent such sudden failures in the dams.

The process of identifying and tracking the structural damage in a civil, mechanical, or electrical infrastructure is known as structural health monitoring [6]. The existence of damage in a structural system changes its dynamic properties such as damping, natural frequencies, and mode shapes. Therefore, the damage state of a structure can be determined by identifying and evaluating these dynamic parameters [7]. In the following section, a comprehensive literature review of damage detection in structural systems as well as recent advances in SHM of dams is presented.

1.1. Structural Damage Detection. Damage detection methods could be divided into two general categories, model-based and data-driven methods. In the former approach, a system identification algorithm should be employed for identifying the dynamic properties of the structure. Then, the structural health condition will be determined by capturing the variation of these dynamic properties. On the other hand, data-driven methods apply features extracted from the vibration response of the structure through a statistical learning algorithm to predict the damage [8]. Cui et al. [9] proposed a damage diagnosis procedure based on the natural excitation technique to identify the structural damage under ambient conditions. The authors combined the strain response with the Eigensystem realization algorithm to identify the strain modal parameters of a structure under ambient vibration. Montazer and Seyedpoor [10] presented a damage index based on flexibility index to detect the location of damage in truss systems. They implemented their proposed method on two numerical models, including a planar truss having 31 elements and a 47-bar planar power line tower. Lee and Eun [11] provided a static damage detection procedure by comparing the variation of stress distribution before and after damage. They showed the validity of their method utilizing two truss structures. Ding et al. [12] developed a method based on Modal Strain Energy (MSE) to identify the damage in the grid structures. They employed an updated mode shape expansion method to ensure that the modal shape obtained from the reference baseline model is reliable. Liu et al. [13] proposed a method based on Stationary Wavelet Transform (SWT) for the purpose of localization and severity detection of cracks in the cantilever beams. Montejo [14] evaluated different vibration-based damage diagnosis methods for the purpose of detecting the damage in the structures under ambient excitation. They concluded that the method based on Continuous Wavelet Transform (CWT) is much more efficient than uncovering the high-frequency spikes of the structural response obtained by Hilbert–Huang transform, high-pass filtering, or Discrete Wavelet Transform (DWT). Pu et al. [15] presented the use of Frequency Response Functions (FRFs) along with the model updating theory for identifying the damage occurred in concrete beams. They formulated an optimization algorithm to set the analytical FRFs from a benchmark finite element model with those obtained through the experimental response. Worden et al. [16] implemented a statistical approach based on Mahalanobis squared distances for healthy and damaged structures. This method was actually a novelty detection problem where a damaged structure should be diagnosed from the healthy cases. Ditommaso et al. [17] presented a method for damage detection of the framed-structures subjected to earthquake motions by evaluating the variation of modal curvature in the natural frequencies. They validated their method by using numerical models and implementing some experiments. Zhang et al. [18] proposed an innovative damage index according to the macrostrain modal shapes for the purpose of detecting the potential damage in steel bridges. Yazdanpanah et al. [19] presented a damage indicator based on modal information

for damage detection in beam-like structures. Their method was founded on three factors, namely, the mode shape, the slope of the mode shape, and the curvature of the mode shape. Figueiredo et al. [20] compared four different machine learning techniques by applying autoassociative neural network, factor analysis, Mahalanobis distance, and singular value decomposition to identify the structural damage. They have implemented their study on an experimental base-excited three-story frame structure. Ghiasi et al. [21] proposed a least square support vector machine based on the thin-plate spline Littlewood–Paley wavelet kernel function to identify the structural damage. Ghannadi and Kourehli [22] explored the efficiency of the moth flame optimization algorithm to identify the location and severity of structural damage. They used the Eigenvalues obtained from the equation of motion along with Modal Assurance Criteria (MAC) flexibility as damage indices. Nguyen et al. [23] presented a novel framework based on the transmissibility function fed to ANNs to identify the structural damage in bridges. They verified their method using data measured from an existing bridge in Taiwan.

1.2. Structural Health Monitoring of Dams. Wang and He [24] presented a methodology based on the reduction of natural frequencies to identify the crack location in arch dams. They proposed a statistical neural network to detect the crack by measuring the reductions of natural frequencies. Turker et al. [25] explored a method based on model updating to identify the global damage that occurred in the arch dams. They have validated their method on an experimental model under ambient excitation. Pirboudaghi et al. [26] proposed a multistage method based on the extended finite element method (XFEM) and continuous wavelet transform (CWT) to detect the seismic cracks of concrete dams. Sevim et al. [27] implemented an ambient vibration test to identify the dynamic properties of a real concrete arch dam, including modal frequencies, damping, and mode shapes. Bianchi and Bremen [28] proposed various procedures to capture the long-term performance of Ferden and Roggiasca dams in Switzerland. In this regard, they captured variations of the dam behavior before the snowfall and after the break period. Mata [29] conducted a comparative study on two statistical models named multiple linear regression (MLR) and neural network (NN) for monitoring of Alto Rabagão dam performance in the environmental condition. Seyed-Kolbadi et al. [30] evaluated the stability of the Boostan earth dam by processing its long-term performance and interpreting the measured data.

All the previous research assumed that the modal parameters of the dam are known. In fact, they directly used the modal parameter obtained from Finite Element (FE) analysis to identify the structural damage. It seems that there is a research gap in identifying the damage that occurred in dams especially when the modal parameters are calculated through the system identification process. In the light of previous research, in this paper, a combined method based on wavelet and Hilbert–Huang transform is proposed to identify the structural dynamics of the dam. In this regard,

four commonly occurred damage scenarios, including damage in the neck, damage in the toe, simultaneous damage in the neck and the toe, and damage in the lifting joints of the dam, are considered to verify the capability of the proposed method. An optimization technique based on minimizing the nondiagonal entries of the MAC matrix is implemented to optimize the location of sensors needed to install at the body of the dam. Next, by adding 10% noise to the structural response under the ambient excitation, the dynamic properties of the structure are obtained for predefined locations, and the cubic-spline technique is used to make the mode shapes differentiable. In the following, damage location is estimated through employing CWT on the difference between the curvature of the mode shapes of the intact and damaged structure.

2. Models and Materials

2.1. Model Description. In this study, a well-known reservoir dam named "Koyna" was numerically modeled in Ansys finite element software, and further investigations were implemented on the response obtained through the numerical analysis. The following sections introduce the structural behavior and modeling procedure of the understudy dam. Fluid–Structure Interaction (FSI) is an important issue in both linear and nonlinear analyses of hydraulic structures. There are three main solutions to resolve this problem, including added mass method, Eulerian method, and Lagrangian method. The added mass method is related to additional mass considered in the system because of the existence of an accelerating or decelerating body that must move some volume of surrounding fluid as it moves through it. The Lagrangian method is related to individual particles, which calculates the trajectory of each particle independently. The Eulerian method is based on the concentration of particles and computes the general convection of the particles [31]. The coupled fluid–structure equation of motion can be easily solved by applying some proper boundary conditions for the reservoir object. Readers are encouraged to study the paper presented by Park et al. [32] for more information about fluid–structure interaction modeling.

There are various types of foundation modeling procedures, such as rigid foundation and massless and massed foundation. The rigid foundation model disregards the interaction between the dam and its foundation. Actually, the stiffness and mass of the foundation are not considered in the global coupled equation of motion. Besides, the massless foundation model considers the flexibility of foundation in the FE model. In this problem, the foundation model must stretch to a large length so that its effects on stresses and strains of the dam approach to an enough small value [33]. Generally, in FE models, the meshing system includes solid elements to model the dam body and reservoir. In order to model the reservoir domain, pressure-based fluid elements were applied. The reservoir of the dam is modeled three-fifths of the dam's height. The water is defined as a linearly compressible and small-amplitude material. The Helmholtz equation is implemented as governing equation in the reservoir medium, as shown in Figure 1. In addition, the

boundary conditions considered for the modeling procedure are shown in this figure [34]. The coupled equation of the dam-foundation-reservoir system can be written as follows:

$$
\begin{bmatrix} M_s & 0 \\ \rho_w Q_{\mathrm{FSI}}^T & M_F \end{bmatrix} \{ \ddot{U}\,\ddot{P} \} + \begin{bmatrix} C_s & 0 \\ 0 & C_F \end{bmatrix} \{ \dot{U} \\ \dot{P} \} + \begin{bmatrix} K_s & -Q_{\mathrm{FSI}} \\ 0 & K_F \end{bmatrix} \{ U \\ P \} = \begin{bmatrix} F_{\mathrm{str}} \\ F_{\mathrm{acc}} \end{bmatrix},
$$
(1)

where K, C, and M are stiffness, damping, and mass matrices, F_{str} is the summation of external forces and ground excitation on the solid domain, Q_{FSI} is fluid–structure coupling matrix, F_{acc} is the summation of the forces that arise from ground motions on solid–fluid boundaries and the total acceleration acts on the other boundaries, P and U are the hydrodynamic pressures and displacements, and the subscripts "$_F$" and "$_S$" refer to fluid and structure, respectively.

2.2. Case Study. Koyna gravity dam is founded in India with a crest length equal to 807 m and a height of 103 m. Its thickness at the base and the crest is 70.2 and 12.1 m, respectively. The 1967 Koynanagar event imposed intensive damages to the dam, including horizontal cracks on the upstream and downstream faces, as a result of which the slope of the downstream face changes significantly [35]. Table 1 presents the mechanical properties of the concrete and the acoustic properties used to model the water dynamics.

According to the large dimensions in the cross-stream direction, the assumption of plane strain is applicable for gravity dams. Therefore, these structures are usually modeled and analyzed as 2D structures [36–38].

2.3. Modal Analysis. By discarding the damping term in the coupled equation of motion, one can derive the Eigenvalues of the undamped FE model as defined by Hariri-Ardebili and Saouma [33]. Since the mass matrix and stiffness matrix are unsymmetric, the Lanczos formulation is implemented to solve this equation. This technique uses a secondary variable and the undamped coupled equation is written as [39]

$$
\left(\begin{bmatrix} K_S & -Q_{\mathrm{FSI}} & 0 \\ -Q_{\mathrm{FSI}}^T & -M_F & K_F \\ 0 & K_F^T & 0 \end{bmatrix} - \begin{bmatrix} M_S & 0 & 0 \\ 0 & 0 & 0 \\ 0 & 0 & K_F \end{bmatrix} \right) \{ U \\ P \\ \Theta \} = \{ 0 \\ 0 \\ 0 \},
$$
(2)

where Θ is equal to $(1/\omega^2)\mathbf{P}$. Readers are encouraged to study the paper presented by Hariri-Ardebili and Saouma [33] for more information about FSI and modal analysis of the dam.

3. Methodology

3.1. Proposed Framework. This study presents a cost-effective method for the purpose of identifying dynamic properties and damage location of the dams. The optimum locations for sensor placements were determined through minimizing the nondiagonal entries of the MAC matrix. In

(a)

(b)

(c)
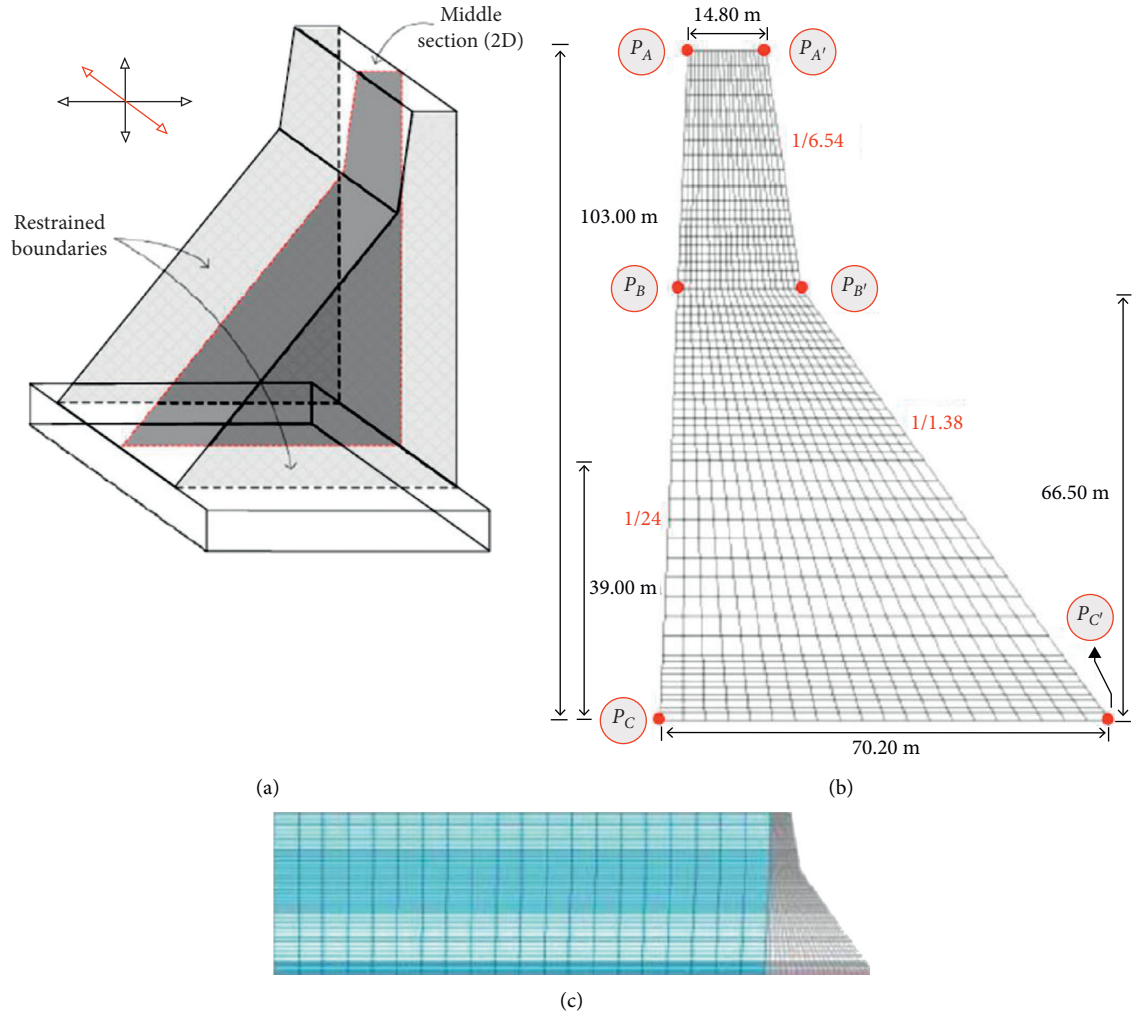
FIGURE 1: Numerical model of Koyna dam. (a) Schematic view of 3D model. (b) Mesh distribution at considered middle section. (c) Overall view of coupled dam–reservoir foundation system.

TABLE 1: Mechanical properties of the dam body and reservoir water.

Model part	Characteristic	Unit	Static	Dynamic
	Modulus of elasticity	GPa	31.0	35.7
Dam body	Poisson's ratio	—	0.02	0.14
	Density	Kg/m³	2643	2643
Reservoir water	Sonic velocity	m/s	—	—
	Density	Kg/m³	1000	1000

consequence, the dynamic properties of the dam were determined by processing the output signals captured from the structure under ambient vibration excitation. The dynamic properties of a structure will change by causing a damage to the body of the dam. The proposed method is based on the difference between curvature of the mode shapes in the healthy and defective structures. Eventually, by applying the continuous wavelet transform (CWT) on the residual of the curvature of the mode shapes, the location of the damage is estimated. Figure 2 shows the general view of the proposed framework.
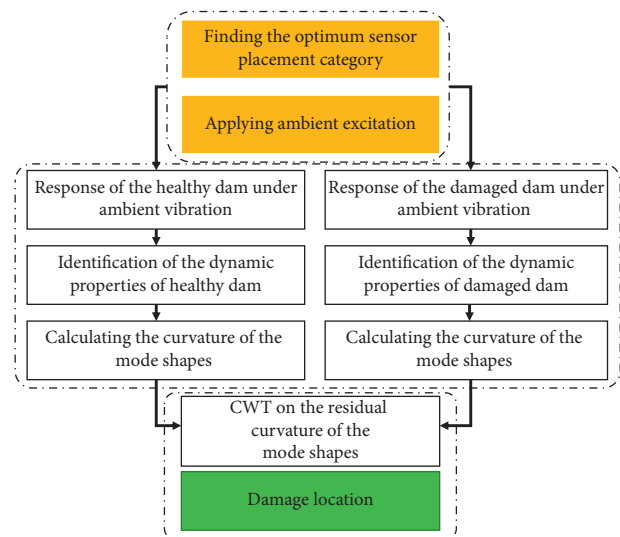
FIGURE 2: Main algorithm of the proposed method.

3.2. Theoretical Background of Continuous Wavelet Transform. Since the foundation of the proposed method is based on continuous wavelet transform, it is essential to present a brief theoretical background for the readers who are less familiar with the topic. A wavelet is a function $\psi(t) \in L^2(\mathfrak{R})$ with zero mean and defined as follows [40, 41]:

$$\psi_{a,b}(t) = |a|^{-0.5} \psi\left(\frac{t-b}{a}\right), \quad a > 0, \tag{3}$$

where $L^2(\mathfrak{R})$ is the set of integrable functions, a and b are scale and translation parameters, respectively, and $|a|^{-0.5}$ is used to ensure that $\|\psi_{a,b}\|$ is equal to unity. Also, ψ is the wavelet function (the mother wavelet), which must satisfy the admissibility condition

$$C_\psi = \int_{-\infty}^{+\infty} \frac{|\widehat{\psi}(\omega)|^2}{|\omega|} d\omega < \infty, \tag{4}$$

where ω is the frequency, and $\widehat{\psi}(\omega)$ is the Fourier transform of ψ. The continuous wavelet transform of $x(t)$ is the inner product of the family of wavelets $\psi_{a,b}(t)$ with the signal $x(t)$ as follows:

$$F_W(a,b) = \ <x(t), \psi_{a,b}(t)> \ = \int_{-\infty}^{+\infty} \frac{x(t)}{\sqrt{a}} \psi^*\left(\frac{t-b}{a}\right) dt, \tag{5}$$

where ψ^* is the complex conjugate of ψ. This condition guarantees the workability of the signal to be used as the mother wavelet in continuous wavelet transform. In this study, two different mother wavelets were used, i.e., Morlet and Daubechies. Complex Morlet wavelet has a close form to the following equation and applied to identify the modal properties of the dam:

$$\psi(t) = \frac{1}{\sqrt{\pi}} e^{-t^2} e^{i\omega_0 t}, \tag{6}$$

where t is the time, and ω_0 is the central frequency of the wavelet. By applying a as dilation and b as translation, a son wavelet is written as follows:

$$\psi_{a,b}(t) = \frac{1}{\sqrt{a\pi}} e^{-(t-b/a)^2} e^{i\omega_0 (t-b/a)}, \tag{7}$$

On the other hand, Daubechies wavelets are defined by computing the running average and difference of scalar products with wavelets and scaling signals. As the Daubechies wavelets apply overlapped windows, the high-frequency coefficient spectrum presents all high-frequency variations. It can be used as an appropriate wavelet to identify the high-frequency jumps resulting from damage in the response signal of the structures [42]. Therefore, the Daubechies mother wavelet was implemented to identify the structural damage that occurred in the dam.

3.3. Mathematics of Cubic Spline. The cubic-spline interpolation was presented to the best curve fitting between some discrete values. The cubic spline includes a set of

weights connected to a plane surface where the points are connected. A flexible strip is curved through each of these weights, which forms a straight and smooth curve. The foundation of this interpolation method is based on curve fitting of piecewise-defined function with the below form:

$$h(x) = \begin{cases} h_1(x), & \text{if } x_1 \le x < x_2, \\ h_2(x), & \text{if } x_2 \le x < x_3, \\ \dots \\ h_n(x), & \text{if } x_{n-1} \le x < x_n, \end{cases} \tag{8}$$

where h_i is a third polynomial function. The cubic spline must have the below conditions:

(1) The piecewise-defined function should interpolate all the points.

(2) $h(x), h'(x)$, and $h''(x)$ should be continuous in $[x_1, x_n]$; the cubic spline is widely applied to determine the slope (or cumulative variation) of a finite number of variables over an interval [43].

4. System Identification

4.1. Input Excitation. The input excitation considered to simulate the ambient vibration excitation to the dam was a Gaussian white noise signal. White noise is a random signal enjoying the same intensity at different frequencies, which provides a constant power spectral density. The $rand\,n$ function of MATLAB [44] was utilized to generate a white noise signal. The total time of the input signal was 1200 s, with the time step of 0.01 s. It should be noted that the input signal was applied to the whole structure of the dam for simulating the real condition. The dynamic characterization of the dam was performed by implementing ambient vibration analysis. It should be noted that the key reason for using such a long-duration signal was to reach a stationary condition, which was essential for proper ambient vibration analysis. Figure 3 illustrates the input excitation subjected to the dam.

4.2. Sensor Location Optimization. One of the main objectives of the present study was to optimize the location of sensors. Therefore, it was necessary to know how to place these instruments in such a way that the maximum agreement between the numerical modal shapes and those obtained through the finite number of sensors be obtained. In order to achieve an economical plan, as well as effective coverage of the whole dam body in terms of detecting the probable damage, the team decided to place only six sensors in this study. The following steps were implemented to determine the optimal locations:

(i) First, the height of the dam was divided into 60 locations, where it is possible to place the sensors.

(ii) Second, the mode shapes of the dam were determined for all the possible nodes by applying modal analysis. Figure 4 illustrates the first three mode shapes of the dam for 60 possible nodes.
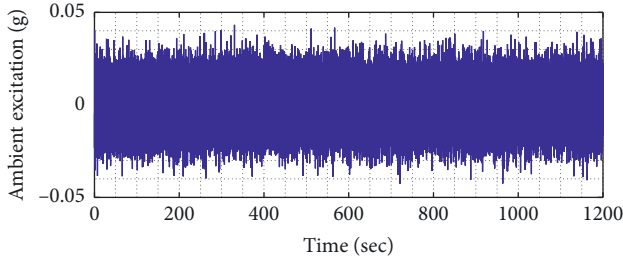
Figure 3: Input excitation signal.
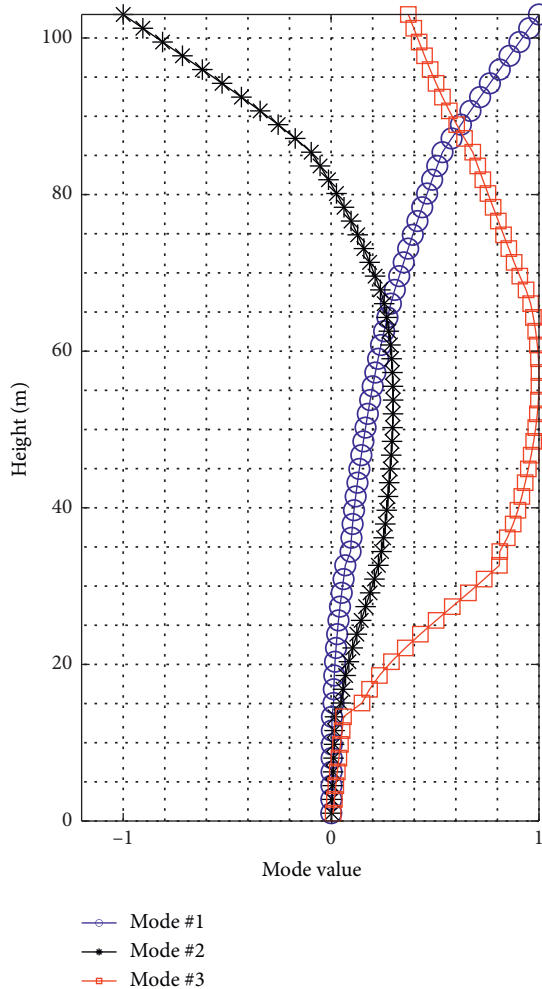
Figure 4: Mode shapes of the dam according to 60 possible nodes for sensor placement.

(iii) Third, six intended sensors should be placed at the possible nodes to achieve the maximum linear independency. In fact, the instrumentation should be conducted so that the nondiagonal entries of the MAC matrix converge to their minimum values [45]. To do so, the first sensor was placed at the summit of the dam. The next sensor was placed at one of the 59 remaining locations so that the nondiagonal entries of the MAC matrix became minimum.

(iv) This operation was repeated for other remained sensors until the best agreement was reached. Finally, the optimal location of the sensors was determined, as shown in Figure 5.

4.3. Free Vibration. In order to extract information about the dynamic properties of a structure from acceleration sensors, the vibration response of those structures must be measured. To this end, in this study, the random decrement technique (RDT) [46] was used. The concept behind the RDT is that by extracting a large number of time segments from the generated signal and averaging such signals, the random part of the response will continue to disappear from the system and only the response to the initial conditions will remain. For example, Figures 6(a) and 6(b) show the response of sensor no. 5 under ambient vibration excitation and corresponding free vibration obtained through RDT.

4.4. Mode Decomposition. The Continuous Wavelet Transform (CWT) of the free-vibration response gives time and scales coefficients of the wavelet coefficient contours. Considering this, a complex Morlet wavelet with a central frequency of 4.57 was used. As an example, Figure 7 depicts an instance of wavelet coefficients obtained for sensors no. 1 and no. 6. In the next step, the free vibration associated with each vibrating mode can be achieved by a plotting summation of the wavelet coefficient at a point where the wavelet coefficients were maximum (maximum of contours). In other words, one should find the local maximum of the wavelet contours presented in Figure 7. Then, by applying the complex Morlet wavelet to the signal obtained from these peak values and plotting the imaginary parts of the wavelet coefficient, free vibration of each mode will be obtained according to each peak value.

4.5. Modal Damping and Natural Frequencies. The Hilbert transform of the free vibration was then calculated to determine the natural frequency and modal damping ratio of each mode. Figure 8 displays an algorithm for computing the dynamic properties. The steps in this algorithm are as follows:

(1) Hilbert transform was applied to the free vibration of each mode

(2) The phase and amplitude of the signal obtained in the previous step was computed

(3) The rate of change of the amplitude and the phase signal are considered as $-\zeta_i\omega_i$ and ω_{Di}, respectively

(4) Finally, the fundamental concepts from dynamics of structures were used to find ω_i and ζ_i

For example, in an attempt to calculate the first and second natural frequencies, as well as modal damping ratios, it is required to employ the scaling of 60 in wavelet coefficient for the first mode and the scale of 145 in wavelet coefficient for the second mode as shown in Figure 7. According to Figure 8, the slope of L_{21} in the linear region is
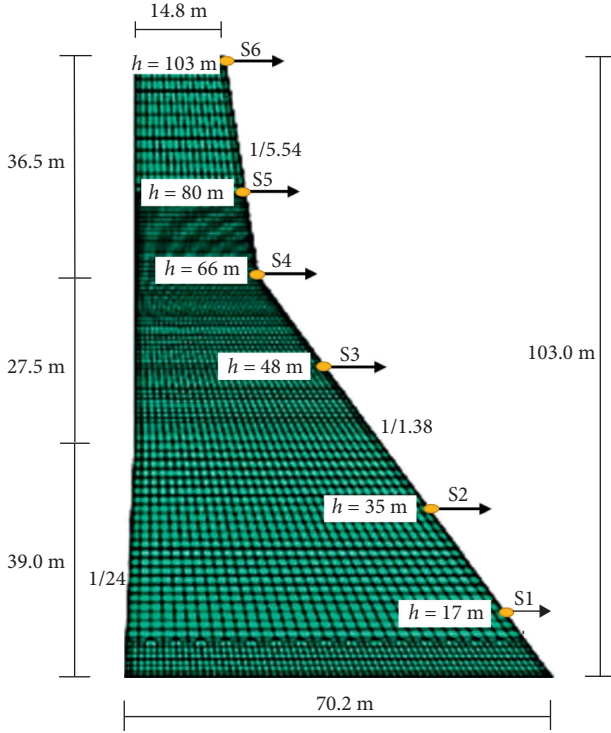
Figure 5: Optimal sensor location.

ω_{D1}, which is equal to $\omega_{D1} = 24.4$ rad (see Figure 9(a)). In addition, the slope of L_{11} in the linear region is $-\zeta_1\omega_1$, and as shown in Figure 9(b), the natural frequency and damping ratio of the first vibrating mode are obtained by implementing the following simple calculations:

$$\omega_{D1} = 244.0/10 = 24.4Hz \qquad \text{and}$$
$$-\zeta_1\omega_1 = -1.05 \longrightarrow \omega_1 =$$
$$24.4/\sqrt{1-(1.05/\omega_1)^2} \longrightarrow \omega_1 = 24.42\text{rad} \longrightarrow$$
$$f_1 = 3.88Hz \text{ and } \zeta_1 = 1.05/24.42 = 0.043$$

It is worth noting that using the same procedure, the second mode properties can be calculated. As illustrated in Figure 8, the slope of L_{22} in the linear region is ω_{D2}, which is obtained as $\omega_{D2} = 45.9$rad (see Figure 9(c)). Furthermore, the slope of L_{12} in the linear region is $-\zeta_2\omega_2$, and according to Figure 9(d), the natural frequency and damping ratio of the second mode can be computed by the following calculations:

$$\omega_{D2} = 459.0/10 = 45.9Hz \qquad \text{and}$$
$$-\zeta_2\omega_2 = -1.125 \longrightarrow \omega_2 =$$
$$45.9/\sqrt{1-(1.125/\omega_1)^2} \longrightarrow \omega_2 = 45.92\text{rad} \longrightarrow$$
$$f_2 = 7.31Hz \text{ and } \zeta_2 = 1.125/45.92 = 0.025$$

The first three natural frequencies and modal damping of the dam are calculated as shown in Table 2.

4.6. Noise Effect. In general, noise is an inevitable part of any measurement. Hence, there is a concept known as the Signal-to-Noise Ratio (SNR), which is defined as the ratio of signal power to the noise power, and commonly stated in

decibels (dB). A ratio higher than 1 denotes a higher amount of signal than noise [41]:

$$SNR = \frac{\sigma_{\text{signal}}^2}{\sigma_{\text{noise}}^2}, \qquad (9)$$

where σ_{signal}^2 is the variance of signal and σ_{noise}^2 represents the variance of the noise. For a more realistic simulation, an appropriate level of noise needs to be applied to the acceleration time history. In the present study, the structural response is polluted by 10% noise to evaluate the practical application of the proposed method. It is proved that this value is the upper bound value of noise used in the previous studies [47]. Table 2 also presents the effect of noise on the obtained modal parameter of the dam. The results show that the proposed method had a promising ability to identify the modal parameters of the dam in the presence of noise.

4.7. Mode Shape Identification. In an attempt to identify the structural mode shapes, a method presented by Yang et al. [43] is utilized. From the previous sections, it can be concluded that while the damping ratio and natural frequencies can be estimated by only one sensor, the acceleration time histories at all DOFs are required and should be measured to identify mode shapes. The absolute values of Eigenvectors (mode shapes) can be obtained using the below relation:

$$\frac{\left|\varphi_{pi}\right|}{\left|\varphi_{qi}\right|} = \exp\left[A'_{pi}(t_0) - A'_{qi}(t_0)\right], \qquad (10)$$

where φ_{pi} is the i_{th} mode shape at the p_{th} degree of freedom. Similar definition is valid for φ_{qi}. The parameters $A'_{pi}(t_0)$ and $A'_{qi}(t_0)$ are the values calculated from curve fitting of L_{2i} for p_{th} and q_{th} degrees of freedom at time t_0, respectively. It is notable that t_0 is the time at the median value of L_{2i}. McKinley and Levine [48] presented the below equation to calculate the sign of the mode shape at each degree of freedom:

$$\varphi_{pi,q} = \theta'_{pi}(t_0) - \theta'_{qi}(t_0), \qquad (11)$$

where $\varphi_{pi,q}$ denotes the difference between the phase value of two signals in p_{th} and q_{th} DOF and i_{th} mode. In addition, $\theta'_{pi}(t_0)$ and $\theta'_{qi}(t_0)$ are the values obtained through curve fitting to L_{1i} for p_{th} and q_{th} degree of freedom at time t_0, respectively. As the previous equation defines only the absolute value of mode shapes, in order to determine the sign of the mode shape entries, the following relations are presented:

$$\text{if } \varphi_{pi,q} = \mp 2m\pi \longrightarrow \frac{\varphi_{pi}}{\varphi_{qi}} > 0 \text{ and if } \varphi_{pi,q}$$
$$= \mp(2m+1)\pi \longrightarrow \frac{\varphi_{pi}}{\varphi_{qi}} < 0. \qquad (12)$$

By applying the abovementioned relations, the mode shape entries can be determined on the basis of free-vibration response of each mode with significant modal

(a)

(b)
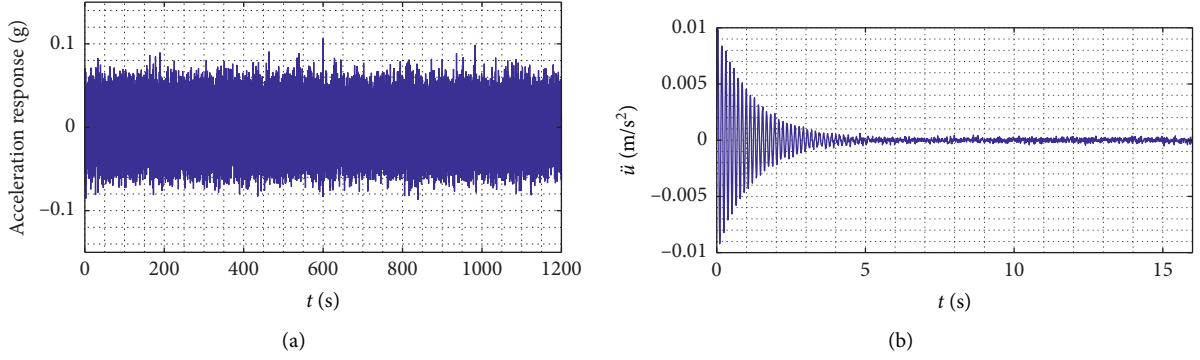
Figure 6: (a) Response recorded by sensor no. 5. (b) Free vibration obtained by RDT.

(a)

(b)
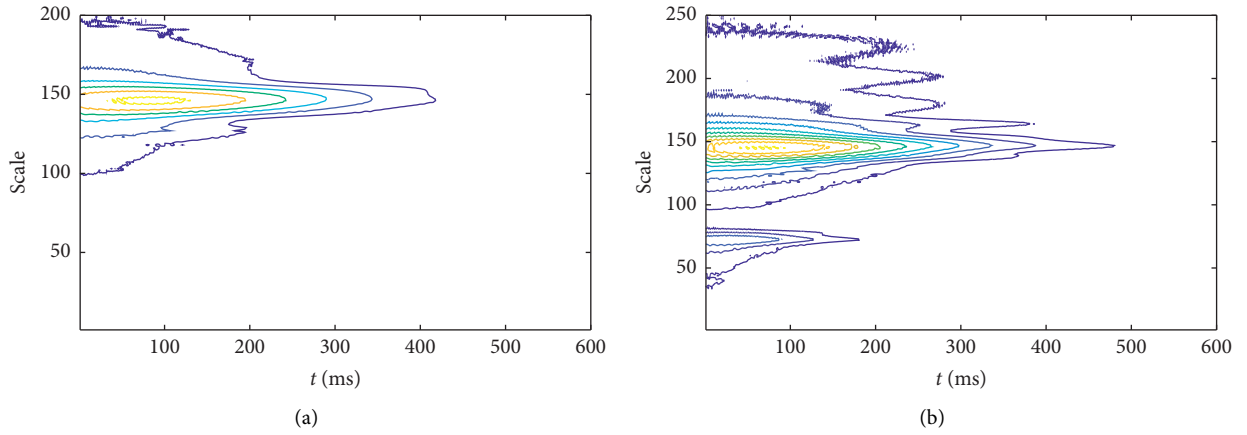
Figure 7: Wavelet coefficient contours. (a) Sensor no. 1; scale: 1,200. (b) Sensor no. 5; scale: 1,250.
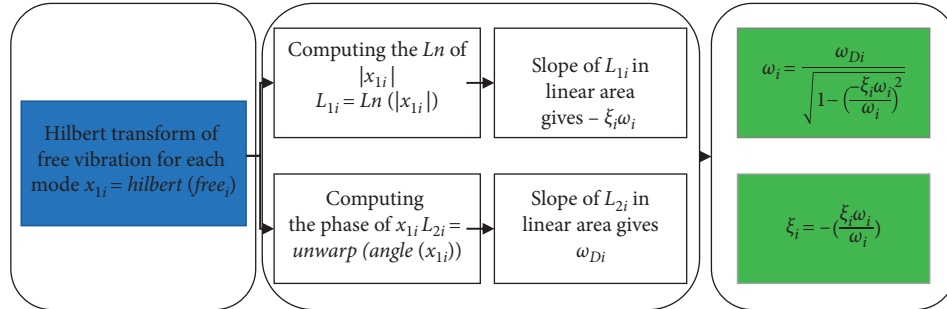
Figure 8: Algorithm for computing ζ_i and ω_i.

participating mass ratio. Comparison between finite element analysis mode shapes and corresponding signal processing (SP) values is shown in Figure 10. The results indicate that the mode shapes are identified with a similar trend. However, it is clear that the third mode shape was estimated with more errors as compared to the first two modes. In fact, variations in the mode values due to damage were less than the errors observed in identification process. This indeed makes this mode shape useless for identifying the structural damage.

In order to evaluate the efficiency of the cubic-spline technique, mode shapes obtained through the system identification (SI) process are compared with those modified by cubic spline (CS). Figure 11 illustrates the effectiveness of cubic spline in smoothing and interpolating the mode shapes.

5. Damage Detection

5.1. Proposed Method for Damage Detection. The presented method is based on applying CWT on the residual curvature of the mode shapes. Therefore, the curvature of the mode shapes was determined by using the following relation [49]:

$$\phi_i'' = \frac{\phi_{i+1} - 2\phi_i + \phi_{i-1}}{dh}, \tag{13}$$

(a)

(b)

(c)

(d)
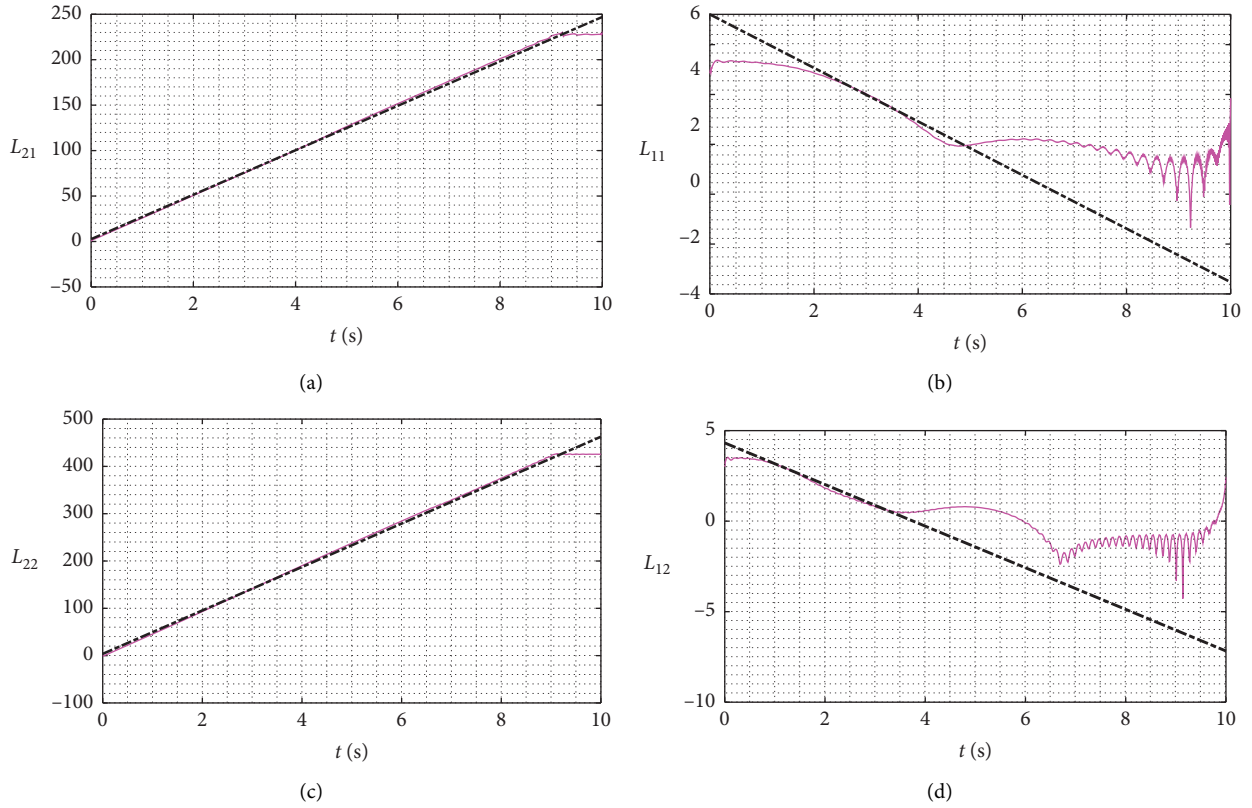
FIGURE 9: Curve fitting to extract the dynamic properties. First row for the first mode ($i = 1$) and second row for the second mode ($i = 2$).

TABLE 2: Estimated modal parameters.

Mode	Finite element model		Without noise		With 10% noise	
	Frequency (Hz)	Damping ratio (%)	Frequency (Hz)	Damping ratio (%)	Frequency (Hz)	Damping ratio (%)
1	3.67	4.0	3.88	4.3	3.92	4.2
2	7.95	4.0	7.31	2.5	7.45	3.1
3	11.80	4.0	11.91	4.1	11.82	4.2
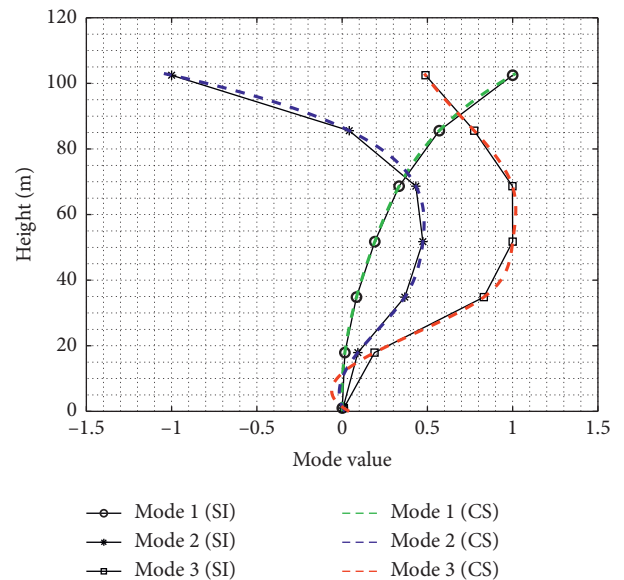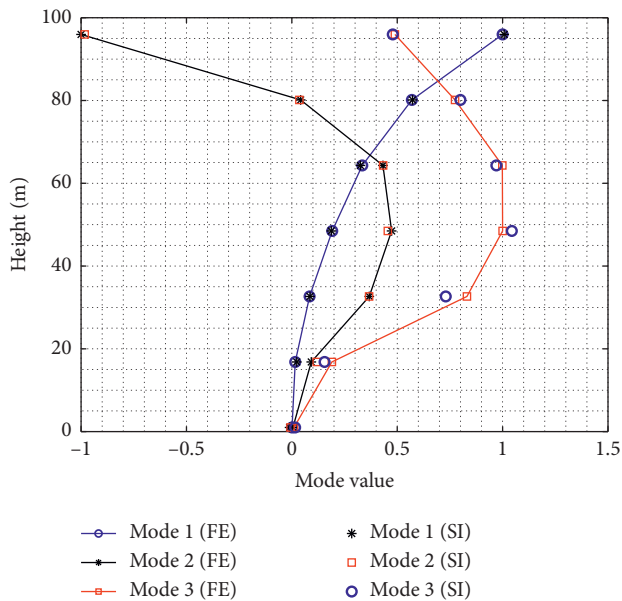
FIGURE 10: Difference between the mode shapes obtained by Finite Element (FE) analysis and System Identification (SI).

FIGURE 11: Comparison between identified model shapes and interpolated ones.

(a)

(b)

(c)

(d)
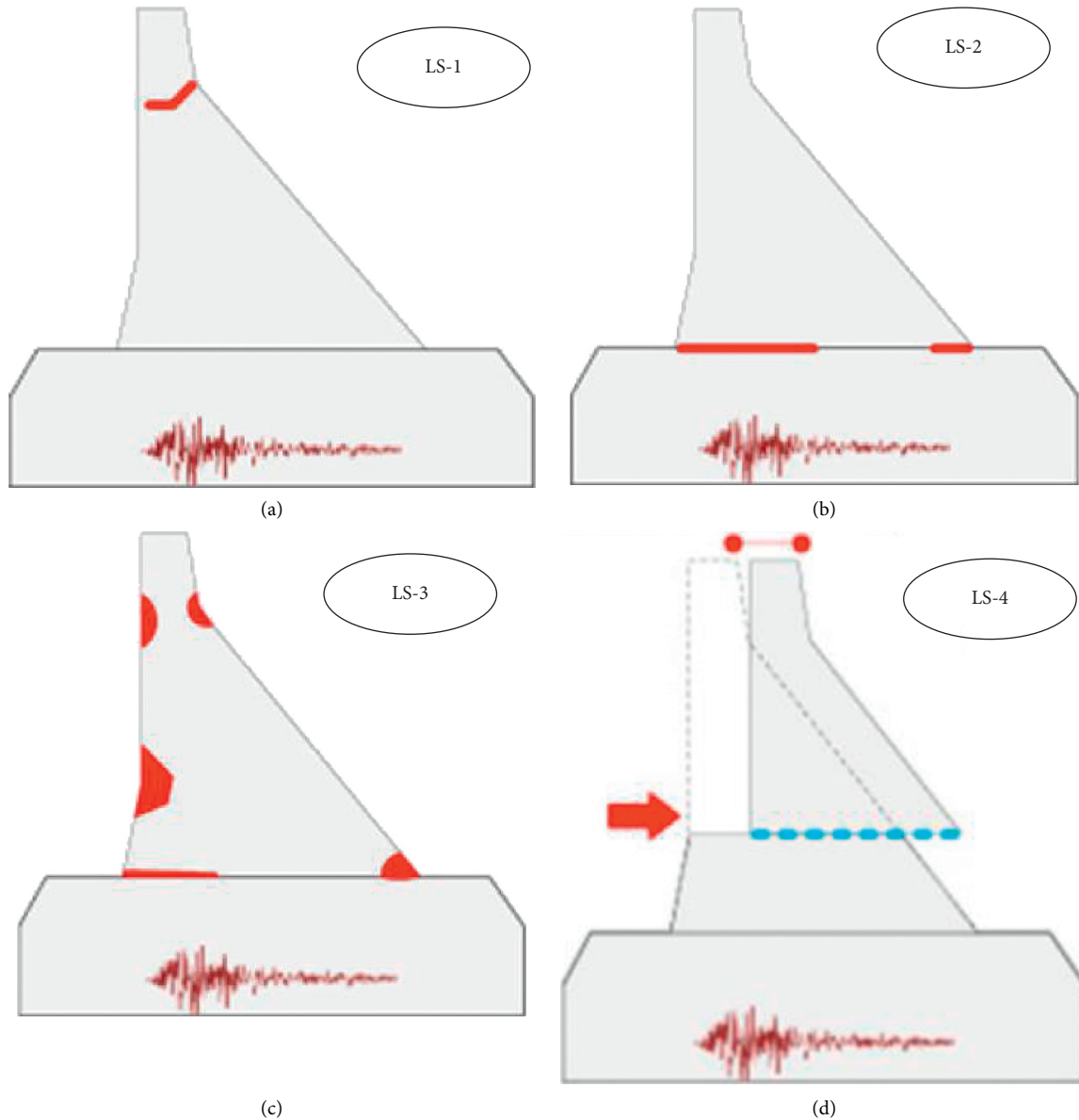
FIGURE 12: Damage scenarios. (a) Damage in the neck. (b) Damage in the toe. (c) Simultaneous damage. (d) Damage in lift joint elements.

where ϕ_i is the mode shape value at the ith height increment and dh is the corresponding height step. In general, a large enough number of data are needed to calculate the slope and the curvature of the mode shapes. Nevertheless, the present study aims to identify the structural properties as well as the damage by implementing only six sensors. This leads to only six data points for each mode shape, which makes it impossible to calculate the curvature of the signal. To address this issue, cubic spline technique was implemented in MATLAB [33] to create enough data for computing the rate of change as well as the curvature of the mode shapes. Next, the difference between the curvature of the interpolated mode shape in the healthy and damaged structures was obtained. Eventually, by applying CWTon the residual vector of the mode shape's curvature, the location of damage was determined. As mentioned before, Daubechies wavelets

were used to capture the changes occurring in the mode shape's curvature because of the structural damage.

5.2. Damage Scenarios. The general potential failure mechanisms in concrete gravity dams are overstressing, sliding along the weak surface. The intense earthquake may create tensile cracks at the base or near the downstream slope change discontinuity in concrete gravity dams. In certain earthquake motions, depending on whether the earthquake is near-field or far-field, simultaneous tensile cracks are observed in the neck and toe of the dam. In addition, rigid sliding at the lifting joints of dam was reported as a potential damage scenario for near-field motions [33]. To validate the presented method, four damage scenarios were considered as follows:
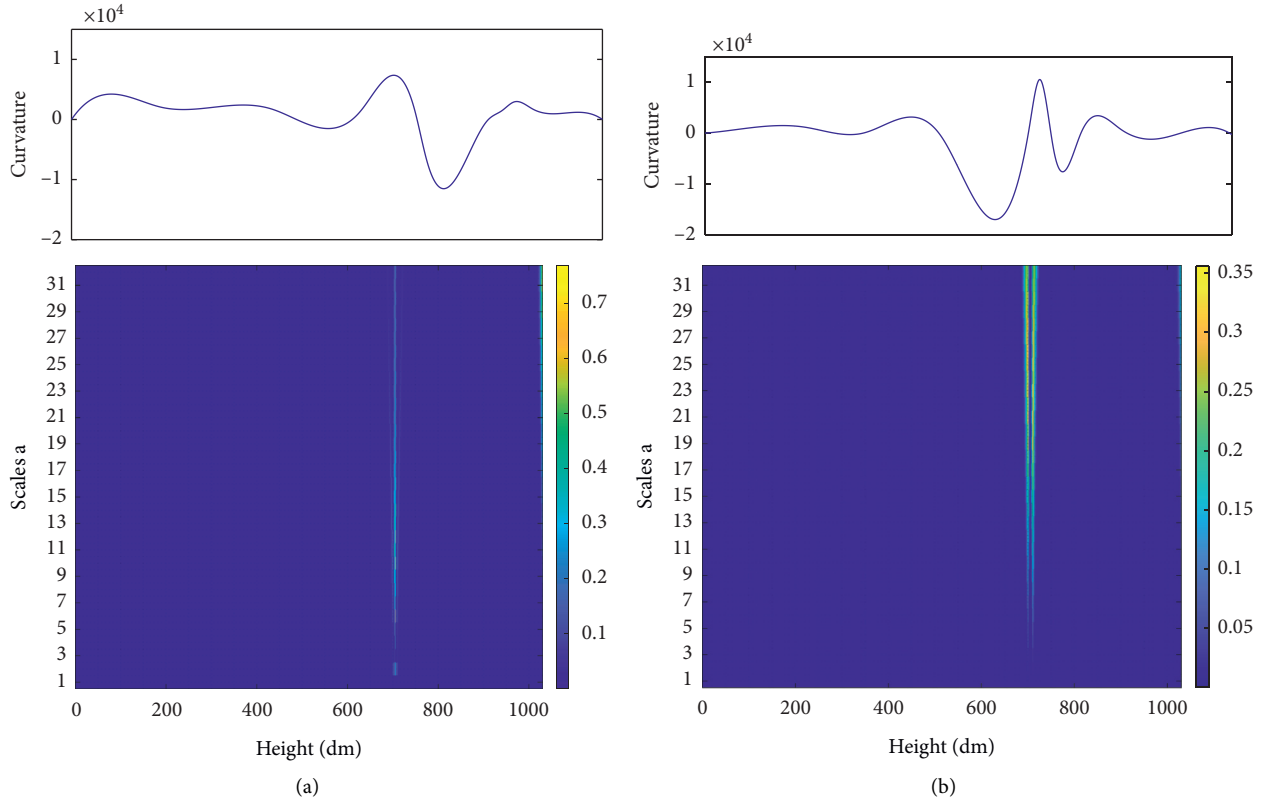
FIGURE 13: Residual value of mode-shape curvature and corresponding scalogram of CWT for the first scenario (damage in the neck). (a) First mode. (b) Second mode.

(i) *Scenario 1*. Neck: stiffness of a small region in the neck of the dam is reduced to 10% of its value in the healthy condition, as shown in Figure 12(a). To understand the extent of damage, the ratio of the defective elements to the total number of elements of the dam can be used. For example, in this scenario, 0.25% of the dam's elements have been injured (light damage on the neck). It is notable that the stiffness of elements is decreased by reducing the Young modulus of them.

(ii) *Scenario 2*. Toe: stiffness of a small region (0.35% damage) in the toe of the dam is decreased to 10% of its initial value in the intact condition, as shown in Figure 12(b) (light damage in the toe).

(iii) *Scenario 3*. Toe and neck together: stiffness of a small number of elements of the toe as well as the neck of the dam (0.6% damage) is reduced 90%, as illustrated in Figure 12(c) (light damage in the toe and neck).

(iv) *Scenario 4*. Lift joints: stiffness of a small number of elements in the lift joints (0.2% damage) are decreased to 10% of their initial value in the intact condition as shown in Figure 12(d).

5.3. Results. Figure 13 illustrates the residual mode shape curvature as well as wavelet coefficients corresponding to different scales vs. the dam height for the first scenario. As

mentioned before, since the third mode shape was obtained with a bias with respect to its real vector, this mode shape was not efficient in damage detection scheme. Therefore, results are shown only for the first and second mode shapes.

Results of CWT on the residual vector of curvature between the healthy and damaged dam for the first and second mode shape are shown in Figures 13(a) and 13(b), respectively. It is clear that at about 70% of the dam's total height, a mutation in the wavelet coefficients is revealed. In fact, this jump in the scalogram of wavelet coefficients occurs because of the existing damage in this location.

Figure 14 illustrates the result of damage detection for the second scenario. As it can be seen, the absolute value of wavelet coefficients is higher at the base of the dam as compared to other locations. Therefore, these spikes in the CWT at the base of the dam represent the location of the damage. Also, both mode shapes are applicable for identifying the location of the damage in this scenario.

Figure 15 presents the results of damage detection when the damage occurs in the toe and the neck of the dam simultaneously. Although the result of CWT on the first mode shape had not significant effect in detecting the damage in the toe of the dam, a jump in scalogram is observed in the height corresponds to the dam's neck. Moreover, for the second mode, by applying the CWT on the residual mode shape curvature of the healthy and defective structure, there are two jumps in the absolute values of CWT where the damage has occurred. It can be concluded that the second mode shape is much sensitive to
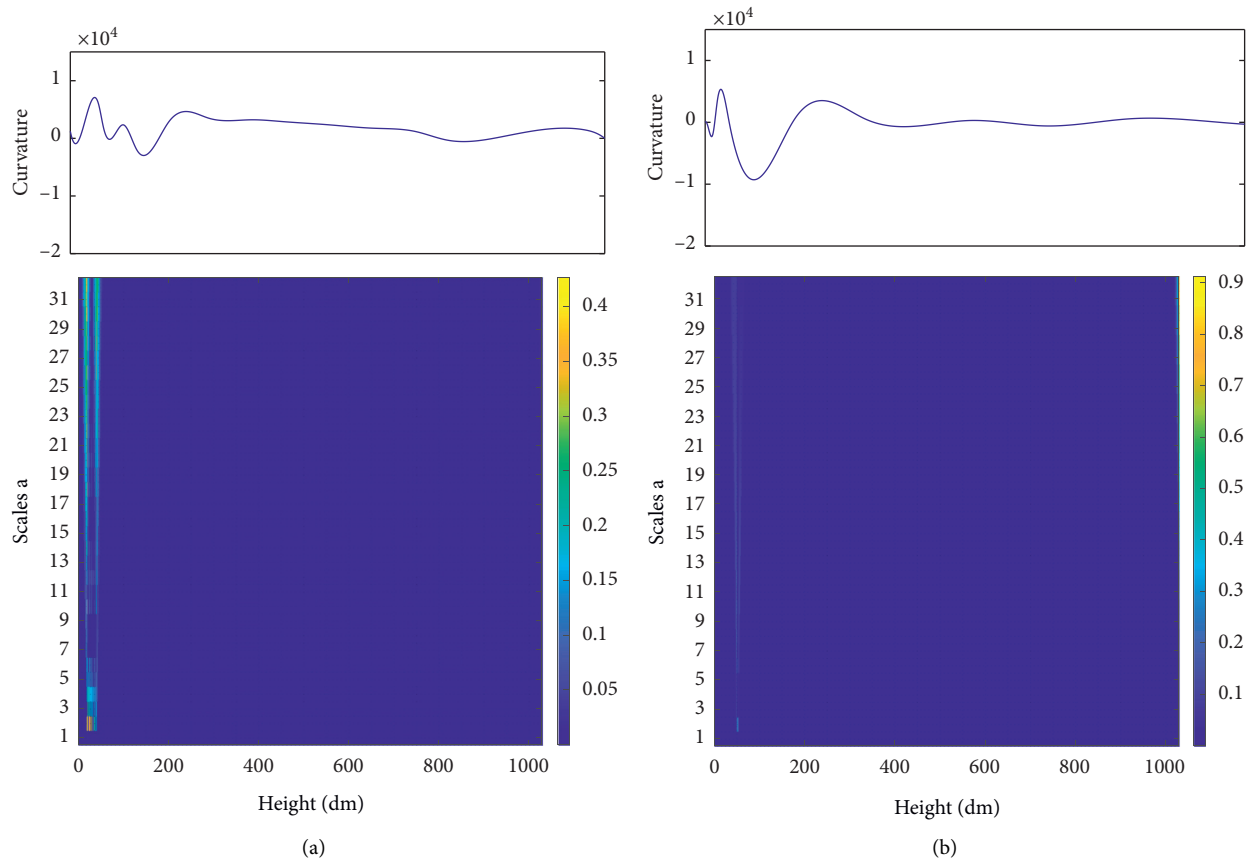
Figure 14: Residual value of mode-shape curvature and corresponding scalogram for the second scenario (damage in the toe). (a) First mode. (b) Second mode.
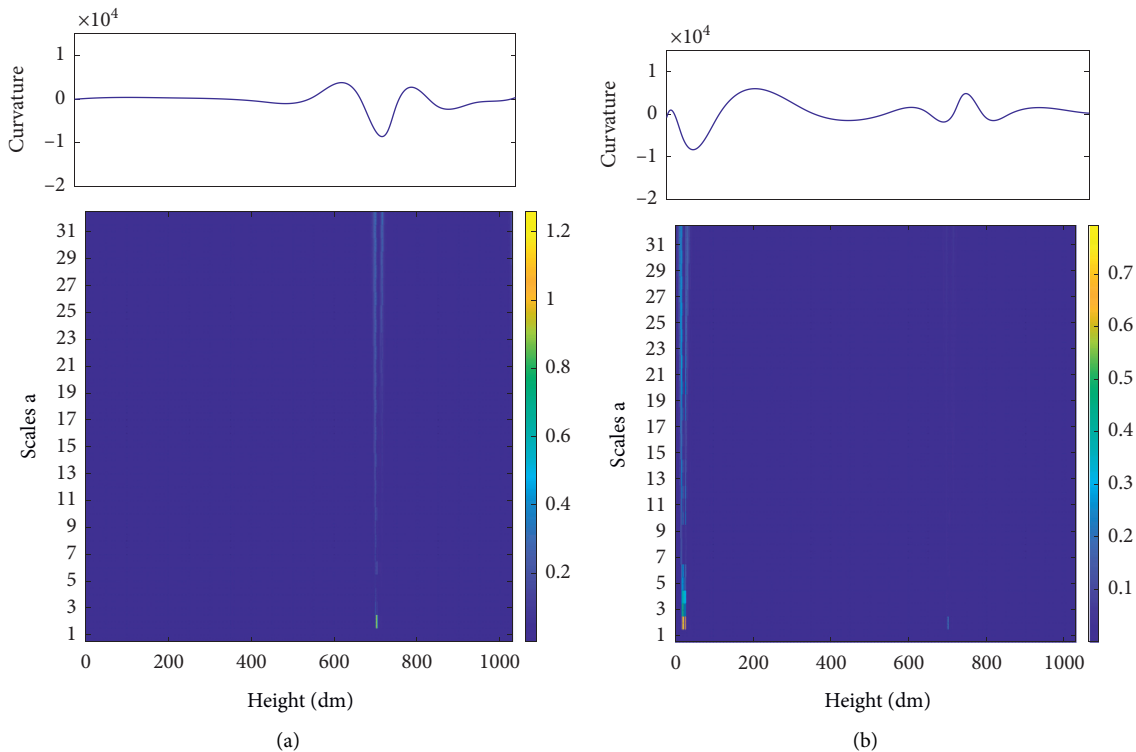
Figure 15: Residual value of mode-shape curvature and corresponding scalogram for the third scenario (damage in the toe and the neck). (a) First mode. (b) Second mode.
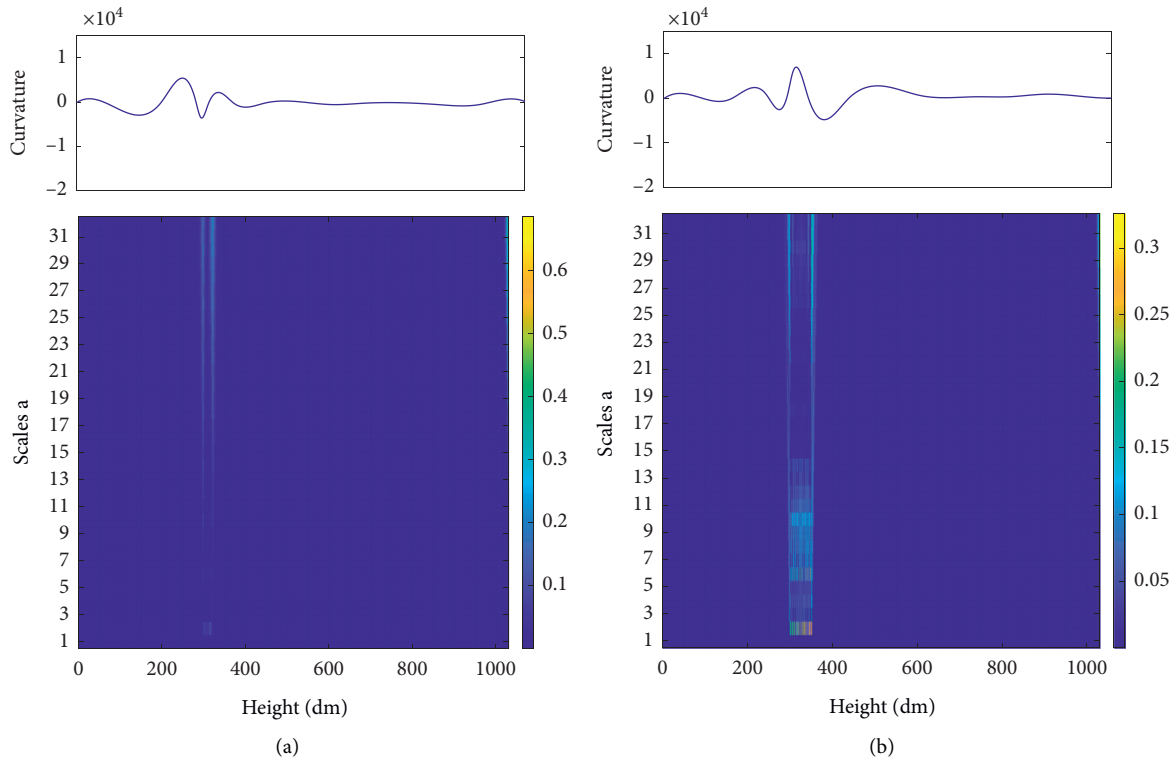
FIGURE 16: Residual value of mode-shape curvature and corresponding scalogram for the fourth scenario (damage in the lift nodes elements). (a) First mode. (b) Second mode.

the damage scenario where multiple instances of damage have occurred in the body of the dam.

Finally, Figure 16 shows the result of damage detection for the fourth damage scenario where slight damage was created in the elements located in the lift joints. As it can be seen, a sharp jump is revealed at the height where the damage has occurred. Moreover, it is evident that both mode shapes (first and second modes) were efficient for detecting the location of the damage.

6. Conclusions

This study presents a system identification-based damage detection procedure for the purpose of identifying the damage that occurred in the body of dam structures. An optimization algorithm based on minimizing the non-diagonal entries of the MAC matrix is applied to estimate the best location of sensors, which leads to the best possible precision of damage detection procedure. The proposed method requires to implement only six sensors along the height of dam. The conducted method present in this study is founded on identifying the modal properties of the structure under ambient excitation. To simulate the practical condition (effect of arbitrary noise), the structural response obtained through FE analysis was polluted with 10% noise. By applying the random decrement technique, the free vibration of the dam was identified at each sensor location. Then, the dynamic characteristics of the dam are detected using the Hilbert–Huang method. The mode shapes of the structure were calculated based on the method proposed by

Yang et al. [43]. Four potential damage scenarios were created, and mode shapes are obtained for both healthy and defective structures.

Eventually, by implementing CWT to the residual vector of the mode shape's curvature of the fully operational and damaged structures, the wavelet coefficients in terms of the scale parameter were calculated along the height of the dam. This research illustrated that the first, second, and fourth damage scenarios were easily detectable from the first two mode shapes. In addition, the damage scenario no. 3 was detected by only the second mode shape, and the first mode shape did not reveal the damage in the toe of the dam. Although the third mode shape of the structure was also identified, it did not contribute in detecting the location of the damage due to the high level of discrepancy compared to the ideal mode shape. The results show a promising and accurate framework in detecting the damage location even when the damage occurred in multiple locations. Also, regarding the high level of importance of such structures, it is recommended that the procedure presented in this study be accompanied by a visual inspection of experienced structural engineers. Finally, the authors propose additional research conducted by applying further experimental tests for dams with various size characteristics and element configurations.

Data Availability

All data are included within the article.

Conflicts of Interest

The authors declare that they have no conflicts of interest regarding the publication of this paper.

References

[1] P. Bukenya, P. Moyo, H. Beushausen, and C. Oosthuizen, "Health monitoring of concrete dams: a literature review," *Journal of Civil Structural Health Monitoring*, vol. 4, no. 4, pp. 235–244, 2014.

[2] R. Karami-Mohammadi, M. Mirtaheri, M. Salkhordeh, and M. A. Hariri-Ardebili, "Vibration anatomy and damage detection in power transmission towers with limited sensors," *Sensors*, vol. 20, no. 6, p. 1731, 2020.

[3] J. M. W. Brownjohn, "Structural health monitoring of civil infrastructure," *Philosophical Transactions of the Royal Society A: Mathematical, Physical and Engineering Sciences*, vol. 365, no. 1851, pp. 589–622, 2007.

[4] W. J. Graham, *A Procedure for Estimating Loss of Life Caused by Dam Failure*, US Department of the Interior, Bureau of Reclamation, Washington, DC, USA, 1999.

[5] T. P. Rich, "Lessons in social responsibility from the Austin dam failure," *International Journal of Engineering Education*, vol. 22, no. 6, p. 1287, 2006.

[6] P. C. Chang, A. Flatau, and S. C. Liu, "Review paper: health monitoring of civil infrastructure," *Structural Health Monitoring: An International Journal*, vol. 2, no. 3, pp. 257–267, 2003.

[7] R. Karami-Mohammadi, M. Mirtaheri, M. Salkhordeh, and M. A. Hariri-Ardebili, "A cost-effective neural network–based damage detection procedure for cylindrical equipment," *Advances in Mechanical Engineering*, vol. 11, no. 7, 2019.

[8] S. O. Sajedi and X. Liang, "A data-driven framework for near real-time and robust damage diagnosis of building structures," *Structural Control and Health Monitoring*, vol. 27, no. 3, p. e2488, 2020.

[9] H. Cui, X. Xu, W. Peng, Z. Zhou, and M. Hong, "A damage detection method based on strain modes for structures under ambient excitation," *Measurement*, vol. 125, pp. 438–446, 2018.

[10] M. Montazer and S. M. Seyedpoor, "A new flexibility based damage index for damage detection of truss structures," *Shock and Vibration*, vol. 2014, Article ID 460692, , 2014.

[11] E. T. Lee and H. C. Eun, "Disassembling-based structural damage detection using static measurement data," *Shock and Vibration*, vol. 2019, Article ID 6073828, , 2019.

[12] B. D. Ding, D. S. Feng, H. L. Lv, and X. Li, "Damage detection in grid structures using limited modal test data," *Mathematical Problems in Engineering*, vol. 2017, Article ID 1089645, , 2017.

[13] J. Liu, W. D. Zhu, P. G. Charalambides, Y. M. Shao, Y. F. Xu, and X. M. Fang, "A dynamic model of a cantilever beam with a closed, embedded horizontal crack including local flexibilities at crack tips," *Journal of Sound and Vibration*, vol. 382, pp. 274–290, 2016.

[14] L. A. Montejo, "Signal processing based damage detection in structures subjected to random excitations," *Structural Engineering and Mechanics*, vol. 40, no. 6, pp. 745–762, 2011.

[15] Q. Pu, Y. Hong, L. Chen, S. Yang, and X. Xu, "Model updating-based damage detection of a concrete beam utilizing experimental damped frequency response functions," *Advances in Structural Engineering*, vol. 22, no. 4, pp. 935–947, 2019.

[16] K. Worden, G. Manson, and N. R. J. Fieller, "Damage detection using outlier analysis," *Journal of Sound and Vibration*, vol. 229, no. 3, pp. 647–667, 2000.

[17] R. Ditommaso, F. C. Ponzo, and G. Auletta, "Damage detection on framed structures: modal curvature evaluation using stockwell transform under seismic excitation," *Earthquake Engineering and Engineering Vibration*, vol. 14, no. 2, pp. 265–274, 2015.

[18] J. Zhang, S. L. Guo, Z. S. Wu, and Q. Q. Zhang, "Structural identification and damage detection through long-gauge strain measurements," *Engineering Structures*, vol. 99, pp. 173–183, 2015.

[19] O. Yazdanpanah, S. M. Seyedpoor, and H. A. Bengar, "A new damage detection indicator for beams based on mode shape data," *Structural Engineering and Mechanics*, vol. 53, no. 4, pp. 725–744, 2015.

[20] E. Figueiredo, G. Park, C. R. Farrar, K. Worden, and J. Figueiras, "Machine learning algorithms for damage detection under operational and environmental variability," *Structural Health Monitoring*, vol. 10, no. 6, pp. 559–572, 2011.

[21] R. Ghiasi, P. Torkzadeh, and M. Noori, "A machine-learning approach for structural damage detection using least square support vector machine based on a new combinational kernel function," *Structural Health Monitoring: An International Journal*, vol. 15, no. 3, pp. 302–316, 2016.

[22] P. Ghannadi and S. S. Kourehli, "Structural damage detection based on MAC flexibility and frequency using moth-flame algorithm," *Structural Engineering and Mechanics*, vol. 70, no. 6, pp. 649–659, 2019.

[23] D. H. Nguyen, T. T. Bui, G. De Roeck, and M. A. Wahab, "Damage detection in Ca-Non Bridge using transmissibility and artificial neural networks," *Structural Engineering and Mechanics*, vol. 71, pp. 175–183, 2019.

[24] B. S. Wang and Z. C. He, "Crack detection of arch dam using statistical neural network based on the reductions of natural frequencies," *Journal of Sound and Vibration*, vol. 302, no. 4-5, pp. 1037–1047, 2007.

[25] T. Turker, A. Bayraktar, and B. Sevim, "Vibration based damage identification of concrete arch dams by finite element model updating," *Computers and Concrete*, vol. 13, no. 2, pp. 209–220, 2014.

[26] S. Pirboudaghi, R. Tarinejad, and M. T. Alami, "Damage detection based on system identification of concrete dams using an extended finite element-wavelet transform coupled procedure," *Journal of Vibration and Control*, vol. 24, no. 18, pp. 4226–4246, 2018.

[27] B. Sevim, A. C. Altunisik, and A. Bayraktar, "Structural identification of concrete arch dams by ambient vibration tests," *Advances in Concrete Construction*, vol. 1, no. 3, p. 227, 2013.

[28] E. M. Bianchi and E. R. Bremen, "July. Health monitoring of arch dams recent developments," in *Proceedings of the International Workshop on the Present and Future in Heath Monitoring*, Bauhaus University, Weimar, Germany, September 2000.

[29] J. Mata, "Interpretation of concrete dam behaviour with artificial neural network and multiple linear regression models," *Engineering Structures*, vol. 33, no. 3, pp. 903–910, 2011.

[30] S. M. Seyed-Kolbadi, M. A. Hariri-Ardebili, M. Mirtaheri, and F. Pourkamali-Anaraki, "Instrumented health monitoring of an earth dam," *Infrastructures*, vol. 5, no. 3, p. 26, 2020.

[31] M. S. Saidi, M. Rismanian, M. Monjezi, M. Zendehbad, and S. Fatehiboroujeni, "Comparison between Lagrangian and

Eulerian approaches in predicting motion of micron-sized particles in laminar flows," *Atmospheric Environment*, vol. 89, pp. 199–206, 2014.

[32] K. C. Park, C. A. Felippa, and J. A. DeRuntz, "Stabilization of staggered solution procedures for fluid-structure interaction analysis," *Computational Methods for Fluid-Structure Interaction Problems*, vol. 26, no. 94–124, p. 51, 1977.

[33] M. Hariri-Ardebili and V. Saouma, "Impact of near-fault vs. far-field ground motions on the seismic response of an arch dam with respect to foundation type," *Dam Engineering*, vol. 24, no. 1, pp. 19–52, 2014.

[34] M. A. Hariri-Ardebili, S. M. Seyed-Kolbadi, and H. Mirzabozorg, "A smeared crack model for seismic failure analysis of concrete gravity dams considering fracture energy effects," *Structural Engineering and Mechanics*, vol. 48, no. 1, pp. 17–39, 2013.

[35] A. K. Chopra, "Earthquake response analysis of concrete dams," in *Advanced Dam Engineering for Design, Construction, and Rehabilitation*, R. B. Jansen, Ed., Springer, Berlin, Germany, 1988.

[36] S. S. Bhattacharjee and P. Léger, "Application of NLFM models to predict cracking in concrete gravity dams," *Journal of Structural Engineering*, vol. 120, no. 4, pp. 1255–1271, 1994.

[37] M. A. Hariri-Ardebili and S. M. Seyed-Kolbadi, "Seismic cracking and instability of concrete dams: smeared crack approach," *Engineering Failure Analysis*, vol. 52, pp. 45–60, 2015.

[38] M. A. Hariri-Ardebili and V. E. Saouma, "Collapse fragility curves for concrete dams: comprehensive study," *Journal of Structural Engineering*, vol. 142, no. 10, Article ID 04016075, 2016.

[39] ABAQUS 2007, *Abaqus Theory Manual*, ABAQUS, Inc., Providence, RI, USA, 7th edition, 2007.

[40] J. Morlet, G. Arens, E. Fourgeau, and D. Glard, "Wave propagation and sampling theory-Part I: complex signal and scattering in multilayered media," *Geophysics*, vol. 47, no. 2, pp. 203–221, 1982.

[41] A. Grossmann, J. Morlet, and T. Paul, "Transforms associated to square integrable group representations. I. General results," *Journal of Mathematical Physics*, vol. 26, no. 10, pp. 2473–2479, 1985.

[42] D. Popov, A. Gapochkin, and A. Nekrasov, "An algorithm of daubechies wavelet transform in the final field when processing speech signals," *Electronics*, vol. 7, no. 7, p. 120, 2018.

[43] J. N. Yang, Y. Lei, S. Pan, and N. Huang, "System identification of linear structures based on Hilbert-Huang spectral analysis. part 1: normal modes," *Earthquake Engineering & Structural Dynamics*, vol. 32, no. 9, pp. 1443–1467, 2003.

[44] MATLAB, *MATLAB Version 9.1 (R2016b)*, The MathWorks Inc., Natick, MA, USA, 2016.

[45] M. Chang and S. N. Pakzad, "Optimal sensor placement for modal identification of bridge systems considering number of sensing nodes," *Journal of Bridge Engineering*, vol. 19, no. 6, Article ID 4014019, 2014.

[46] R. Morsy, H. Marzouk, X. Gu, and A. Elshafey, "Use of the random decrement technique for nondestructive detection of damage to beams," *Materials and Structures*, vol. 49, no. 11, pp. 4719–4727, 2016.

[47] Y.-Z. Lin, Z.-H. Nie, and H.-W. Ma, "Structural damage detection with automatic feature-extraction through deep learning," *Computer-Aided Civil and Infrastructure Engineering*, vol. 32, no. 12, pp. 1025–1046, 2017.

[48] S. McKinley and M. Levine, "Cubic spline interpolation," *College of the Redwoods*, vol. 45, pp. 1049–1060, 1998.

[49] R. Karami Mohammadi, M. Khalaj, and M. Mohammadgholiha, "Curvature method to detect location and depth of a plastic zone in frame members during an earthquake," *Numerical Methods in Civil Engineering*, vol. 3, no. 2, pp. 1–12, 2018.

Research Article

Investigation of Flexural Capacity of Concrete Containing Liquid Silicone Rubber

Alireza Khaloo ID [1] **and Yaser Parvin Darabad** ID [2]

[1]*Civil Engineering Department, Sharif University of Technology, Center of Excellence in Structures and Earthquake Engineering, Tehran, Iran*
[2]*Sharif University of Technology International Campus, Kish Island, Iran*

Correspondence should be addressed to Alireza Khaloo; khaloo@sharif.edu

Despite the great use of concrete, tensile strength and low flexibility and brittleness are its weaknesses. Many solutions have been provided to eliminate the mentioned defects. In order to increase the flexibility of concrete in previous studies, crushed rubber tire particles have been added to concrete. Recycling car tires helps the environment and makes concrete much more flexible than regular concrete. In this research, silicone rubber has been replaced by 0%, 2%, 4%, 8%, 12.5%, 25%, and 50% of mineral aggregates. This rubber was initially in liquid form, which, after mixing with ordinary concrete, dispersed into the concrete texture and formed a uniform mixture, and this liquid rubber became a flexible solid after 24 hours. Concrete containing silicone rubber is a new composite with new properties, and in this research, it is called Hybrid Silicone Rubber Concrete (HSRC). Also, to evaluate the effect of aggregate size in making experimental specimens, two coarse to fine aggregate ratios of $G/S = 0.7$, 1.1 were considered. Flexural strength tests were performed on hardened concrete beam specimens. The results showed that, with increasing the amount of silicone rubber in concrete, flexural strength decreased and this percentage of strength reduction was compared with the percentage of reduction in compression and splitting tensile strength. It was found that the reduction of flexural strength was less than compression and splitting tensile strength. Larger deformation was observed during all tests when the concentration of silicone rubber increased. It was observed that the higher the amount of silicone rubber in the specimens, the less noise and the less separation of aggregates with which the failure of the specimens was associated.

1. Introduction

Concrete is one of the most widely used materials in construction, but it is weak against tensile forces. Cement-based composite materials are cracked when subjected to tensile load, and the deformation corresponding to the cracking load is also very small relative to the ductile material. By increasing the corresponding displacement of cracking loads, the energy absorption capacity of the materials increases. To increase the ductility of concrete, fiber reinforced concrete has been developed since the 1960s [1]. Various types of fibers, such as steel, carbon, and glass fiber, were used to increase bending strength and concrete performance. Another way to increase the ductility of concrete is to add rubber particles to concrete. In previous studies, waste

tire rubber particles have been replaced with mineral aggregates [2]. The use of waste tire rubber has two benefits: one of them is the reduction of waste tire problem, and the other is the less consumption of natural resources for concrete production. In the first report on the use of waste tire rubber particles in concrete, chips and crumb rubber was used as a substitute for mineral aggregates in plain concrete. The results of the compressive tests showed that increasing the number of rubber particles in the concrete reduces the compressive strength of the concrete, but the flexibility is significantly increased. In a previous research, mechanical properties of concrete containing a high volume of the waste tire–rubber particles were investigated [3]. Recycling is considered as one of the measures of sustainable methods. The physical features of the asphalt mixture under the

influence of accelerated aging for asphalt concrete were determined [4]. Dynamic Parameter and Experimental Study of Tuned Slab Damper was conducted by Xu et al. Experimental result showed that the vibration of the absorbing plate was wasted by the damping property of the elastic element in order to reduce the peak value of the track vibration [5]. The study revealed that the addition of rubber particles to concrete has improved the brittle nature of the concrete and its low toughness, but the ultimate strength has significantly decreased. Flexural and compression tests were performed on concrete specimens including two types of rubber particles, such as fine crumb rubber and tire chips [6]. The waste tire in the form of fiber with various aspects of ratio was used in concrete. Increase in ductility and loss in compressive strength have been reported [7]. Recycled tire rubber particles replaced mineral aggregates in concrete and results showed that they reduced mechanical properties (compressive, flexural, and splitting tensile strength) but increased the impact resistance to 400% when 20% coarse aggregates and 20% fine aggregates are replaced by tire rubber particle, respectively [8]. Also, high volume recycled car tires were added to the concrete along with silica and the impact energy of the concrete was investigated. According to the results, energy absorption and impact energy capacity increased but compressive and tensile strengths decreased [9]. An experimental study on the use of latex in cement composites showed that tensile strength increased [10]. Replacement of mineral coarse aggregate with the tire rubber particles caused the reduction in compressive and flexural strength. As reported, the decrease in flexural strength was twice that in compressive strength [11]. According to the reported results, increasing the amount of rubber in rubberized concrete increases energy absorption and ductility [3]. The use of rubber particles in concrete affects the porosity and permeability of concrete. The permeability in porous materials has been studied [12]. In a study on the effect of the use of the silica fume in rubberized concrete (RC), it was concluded that silica fume improved mechanical properties of RC and reduced the amount of the reduction in compressive strength [13]. In most studies on RC, the impact of rubber concentration on concrete was studied. Generally, in these studies, a normal concrete mix has been selected, and different RC mixes are provided by introducing a different amount of tire rubber replaced with mineral aggregates in the original mix and then mechanical properties of the RCs are compared to the original concrete. Rubberized concrete exhibited lower compressive strength [6] and unit weight, compared to original normal concrete. RCs usually exhibit lower elastic modulus [11], tensile strength [12], and workability [13, 14], higher ductility [3], and higher energy absorption capacity [15]. The use of liquid silicone rubber coatings as a novel and successful alternative design has been introduced by applying the coating operation on the surface of the isolator of the distribution transformers [14]. Effect of Styrene-Butadiene Rubber (SBR), silica fume, and fly ash on compressive and flexure strengths of mortars was investigated by Hu Feng et al., and the result revealed that SBR reduced the mechanical strength of the mortars. SEM and EDS studies showed that SBR prevented the formation of albite, whereas silica content from silica fumes and fly ash changed $CaCO_3$ to Wollastonite (a white loose powder), which reduced the mechanical strength of mortars [16]. The purpose of this research is to investigate the flexural and compressive behavior of concrete containing room temperature vulcanization (RTV) liquid silicone rubber. For this purpose, the mineral has been replaced by aggregates liquid silicone rubber in various volumetric percentages. Experimental observations and explanations related to the behavior of HSRC under flexural and compressive tests are presented. Some weaknesses of concrete are low tensile strength and flexural strength against compressive strength. Concrete is also classified as a brittle material with low flexibility and energy absorption [17]. The use of silicone rubber in concrete increases the ductility of concrete and its energy absorption capacity, and increasing ductility improves the brittle nature of concrete and reduces the process of cracking and crack growth in concrete. Increasing the energy absorption capacity of concrete improves the seismic performance of structures and increasing the ductility also increases the deformation of flexural members and delays the occurrence of cracks [18].

2. Experimental Program

2.1. Materials and Methods

2.1.1. Liquid Silicone Rubber RTV. Liquid silicone rubber is a rubber-like material that is widely used in the industry [15]. Liquid silicone rubber RTV is generally stable, nonreactive, and compatible with the environment. For these properties and ease of working and shaping, silicone rubber can be found in a wide variety of products including electrical industry, instrument, medical device, wearing, and in many other fields of the industry [19]. Liquid silicone rubber RTV used in this study consists of two parts. One is a liquid silicone rubber polymer, and another is a hardener. 24 hours after mixing two components, liquid silicone rubber becomes solid flexible rubber. The characteristic of the silicone rubber is presented in Table 1.

2.1.2. Mixed Material. Portland cement in accordance with ASTM C150 standard with a specific gravity of $3.17 \, g/cm^3$ was used to make the specimens. Mineral aggregates including gravel with the maximum size of 19 mm and sand with the maximum size of 4.75 mm have been used as coarse and fine aggregates, respectively. The mineral aggregates from broken rock stone have been used. Grading curvature and the properties of aggregates are presented in Figure 1 and Table 2, respectively. To enhance the workability of the mixture, a polycarboxylate-based superplasticizer was used.

2.2. Concrete Mixtures. In order to study the HSRC mechanical properties, seven series of concrete mixtures were used. Liquid silicone rubber concentration was taken as the main variable in the experiment, which substituted the 0, 2, 4, 8, 12.5, 25, and 50 percent to the total mineral aggregate

Table 1: Silicone rubber specifications.

Property	Min value	Max value	SI unit
Density	1.1	2.3	Mg/m^3
Bulk modulus	1.5	2	GPa
Compressive strength	10	30	MPa
Elastic limit	2.4	5.5	MPa
Endurance limit	2.28	5.23	MPa
Fracture toughness	0.03	0.7	$MPa.m^{1/2}$
Modulus of rupture	2.4	5.5	MPa
Poisson's ratio	0.47	0.49	
Shear modulus	0.0003	0.02	GPa
Tensile strength	2.4	5.5	MPa
Young's modulus	0.001	0.05	GPa

Figure 1: Grading of mineral aggregates.

volume. In order to investigate the effect of the coarse aggregate to fine aggregate ratio (G/S) on concrete behavior, two ratios of 1.1 and 0.7 were considered. Water to cement ratio was 0.4 for all specimens. Water absorption of aggregates was considered for making the specimens. The amount of superplasticizer used in the mixture was 2% of the cement weight. Labeling of the specimens was performed using two factors, G/S and silicone rubber concentration. To identify the G/S, HF (high mineral fine aggregate with $G/S = 0.7$) and LF (low mineral fine aggregate with $G/S = 1.1$) were used. For example, LF-G2S2 mixture indicates liquid silicone rubber replaced by 2% of fine and coarse aggregate volume using low sand content ($G/S = 1.1$). The proportions of the concrete mixture and experimental program are given in Tables 3 and 4, respectively.

2.3. Manufacturing of Specimens and Testing. To make hybrid concrete specimens, at first, the cement is mixed with sand and gravel and then water containing superplasticizer is added to the mixture gradually. Liquid silicone rubber is prepared in such a way that liquid rubber is combined with its hardener. This mixture turns from liquid rubber to flexible solid rubber after 24 hours. The liquid silicone rubber mixture is added to the ordinary concrete, and the mixture is stirred to distribute the liquid silicone rubber uniformly throughout the concrete. For each mix design, cylindrical specimens 150×300 mm (diameter x height) and beams $100 \times 100 \times 350$ mm were prepared. All specimens were manufactured according to ASTM C 192/C–06 [20]. Specimens were remolded 24 hours after fabrication and then cured in a water tank at 25°C and 1 day before testing specimens were taken out of the water tank.

2.3.1. Test Method. For each mix design, slump and unit weight were measured in accordance to ASTM C143 [21] and ASTM C138 [22], respectively. Compression tests for hardened cylindrical specimens were performed according to standard ASTM C39, and splitting tensile tests were performed according to standard ASTM C496. To evaluate flexural strength, specimens were tested according to ASTM C78 [23]. The beam specimens installed as a hinge supported condition with 300 mm length between the two supports. Four-point flexural testing was conducted by a universal testing machine with 0.05 mm/sec rate of loading and test setup is shown in Figure 2. All tests were performed on specimens at 28 days of age.

3. Experimental Results and Discussion

3.1. Workability and Unit Weight. According to the results depicted in Figure 3, increasing the amount of liquid silicone rubber in concrete reduced the slump and weight in the mixture. In this study, by replacing the amount of liquid silicon rubber with 50% by volume of aggregates, the reported slump value is equal to 4. The reported greeting is appropriate in terms of executive work. The slump reported in this study is up to a maximum of 50% rubber, suitable for executive work. According to the results presented in Figure 3(b), with increasing the amount of silicone rubber in the mixture, the total weight decreases, which is due to the fact that the density of rubber is less than mineral aggregates.

3.2. Strength of Hardened Concrete. The experimental results of compressive, flexural, and splitting tensile strengths at the age of 28 days are presented in Table 5. The results demonstrate that, with increasing the amount of silicone rubber content in the mixture, all strengths such as flexural, compressive, and splitting tensile strength have decreased for both HF and LF specimens. This has been predictable based on previous studies on concretes in which crumb tire rubber has been added [3]. Figure 4 shows the percentage reduction in strength based on the percentage of silicone rubber in concrete. As shown in Figures 4(a) and 4(b), it is clear that as the amount of silicon rubber in the mixture increased, the compressive strength decreased more than the flexural and splitting tensile strength in the same silicone rubber content. Another point that can be drawn by referring to Figures 4(a) and 4(b) is that, as the amount of silicon rubber in the mixture increased, the flexural strength has decreased less than the compressive and tensile strength, which indicates that the sensitivity of the flexural strength to the increase of silicone rubber content in the mixture is less, compared to the compressive and tensile splitting strength. Also, the slope of the diagram in Figures 4(a) and 4(b) shows that when the amount of silicone rubber exceeded 12.5%, the

TABLE 2: Properties of mineral aggregates.

Aggregate type	Specific gravity	Water absorption (%)	Fineness modulus	Unit weight (kg/m^3)
Coarse aggregate	2.63	2.69	NA	1709.6
Fine aggregate	2.69	5.16	4.38	1729

TABLE 3: Experimental program.

Specimen designation	Liquid silicone rubber content (%) by total aggregates	Fine aggregate (%)	Coarse aggregate (%)	Superplasticizer to cement ratio (%)	Replicates of compressive test (at 28 days)
LF-G0S0	0	100	100	2	3
LF-G1S1	1	99	99	2	3
LF-G2S2	2	98	98	2	3
LF-G4S4	4	96	96	2	3
LF-G12.5S12.5	12.5	87.5	87.5	2	3
LF-G25S25	25	75	75	2	3
LF-G50S50	50	50	50	2	3
HF-G0S0	0	100	100	2	3
HF-G1S1	1	99	99	2	3
HF-G2S2	2	98	98	2	3
HF-G4S4	4	96	96	2	3
HF-G12.5S12.5	12.5	87.5	87.5	2	3
HF-G25S25	25	75	75	2	3
HF-G50S50	50	50	50	2	3

TABLE 4: Concrete mixture proportions.

Specimen	Water (Lit)	Cement (kg/m^3)	Gravel-sand G/S	Liquid silicone rubber (kg/m^3)	Coarse aggregate (kg/m^3)	Fine aggregate (kg/m^3)	Moisture of gravel (%)	Moisture of sand (%)
LF-G0S0	224	350		0.00	942.86	857.14	3	4
LF-G1S1	231	350		12.67	933.43	848.57	3	3.2
LF-G2S2	240	350		25.34	924.00	840.00	2	3
LF-G4S4	204	350	1.1	50.69	905.14	822.86	4	5
LF-G12.5S12.5	216	350		158.40	825.00	750.00	3	4
LF-G25S25	187	350		316.79	707.14	642.86	5	5
LF-G50S50	184	350		633.59	471.43	428.57	4	4.5
HF-G0S0	218	350		0.00	741.16	1058.80	4	4
HF-G1S1	238	350		12.66	733.75	1048.21	4	1.3
HF-G2S2	240	350		25.31	726.34	1037.62	3.2	2
HF-G4S4	236	350	0.7	50.62	711.51	1016.45	3.2	2.3
HF-G12.5S12.5	226	350		158.19	648.52	926.45	3	3.1
HF-G25S25	224	350		316.39	555.87	794.10	2.1	3
HF-G50S50	204	350		632.77	370.58	529.40	2	2.5

slope of the strength reduction decreased. Detailed examination of Figures 4(a) and 4(b) shows that, by increasing the silicone rubber content by up to 25%, it maintained a linear relationship between the increase in silicone rubber and the compressive strength and about 50% of the compressive strength was lost in 25% of the silicone rubber content. In the case where the amount of silicone rubber is more than 25%, the amount of strength reduction slope decreases. This trend is clear for the amount of silicone rubber between 25 and 50, and in the amount of 50% silicone rubber, the reduction of compressive strength is equal to 82.5%, and this amount of reduction in compressive strength limits the structural use of HSRC. Figure 5 shows the effect of silicone rubber content

on compressive strength, splitting tensile, and flexural strength on both LF and HF specimens. It can be seen that, in both HF and LF specimens, the slope of the bending strength reduction line is less than the tensile strength reduction and the slope of the tensile strength reduction line is less than the slope of the compressive strength reduction. In addition, the ratio of flexural strength to compressive strength (fb/fc) and splitting tensile strength to compressive strength (ft/fc) and the ration of flexural strength to splitting tensile strength, based on the experimental data, are presented in Table 6. The results in Table 6 indicate that as long as the percentage of silicone rubber was between 0 and 12.5%, the ratio of (ft/fc) was about 0.1, but with increasing the amount of silicone

FIGURE 2: Test setup.

(a)

(b)
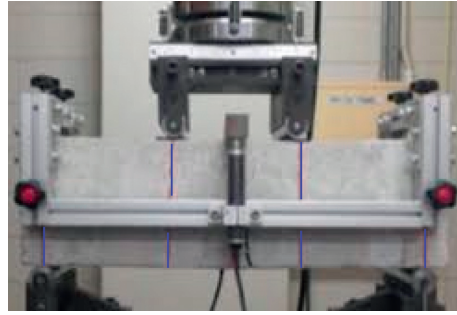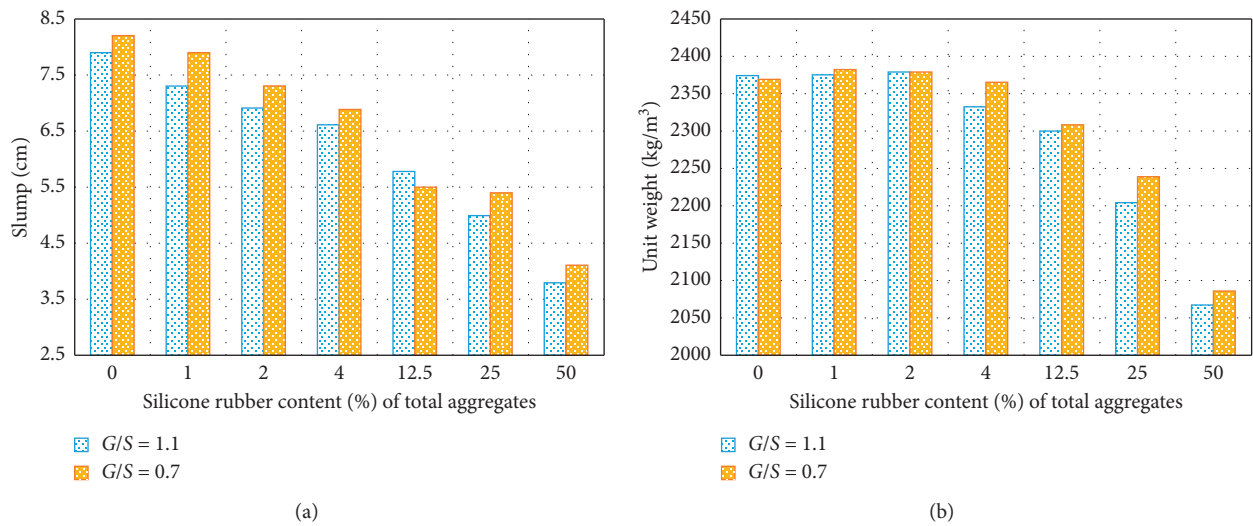
FIGURE 3: Properties of fresh HSRC. (a) Slump. (b) Unit weight of fresh HSRC.

TABLE 5: Changes in strengths with respect to control strength (LF specimens and HF specimens) and percentage of retained strength with respect to control specimen.

Concrete mixture	Total rubber content (%)	Splitting tensile strength ft (MPa)	ft maintained strength with respect to the control (%)	Bending strength fb (MPa)	fb maintained strength with respect to the control (%)	Compressive strength fc (MPa)	fc maintained strength with respect to the control (%)
LF-G0S0	0	2/90	100	4/06	0/00	29/33	100
LF-G1S1	1	2/79	96/41	3/94	2/78	28/15	95/98
LF-G2S2	2	2/59	89/24	3/83	5/59	26/96	91/93
LF-G4S4	4	2/52	87/04	3/63	10/61	24/83	84/66
LF-G12.5S12.5	12/5	1/84	63/48	2/93	27/69	17/59	59/98
LF-G25S25	25	1/39	48/01	2/27	43/93	10/71	36/51
LF-G50S50	50	0/84	29/00	1/74	56/99	5/17	17/63
HF-G0S0	0	3/64	100	4/31	0/00	31/93	100/00
HF-G1S1	1	3/40	93/48	4/18	3/03	30/56	93/48
HF-G2S2	2	3/13	85/95	4/07	5/47	29/47	85/95
HF-G4S4	4	2/98	81/93	3/85	10/52	27/19	81/93
HF-G12.5S12.5	12/5	2/29	62/90	3/08	28/56	19/08	62/90
HF-G25S25	25	1/78	48/85	2/37	45/04	11/66	48/85
HF-G50S50	50	1/09	29/86	1/78	58/59	5/57	29/86
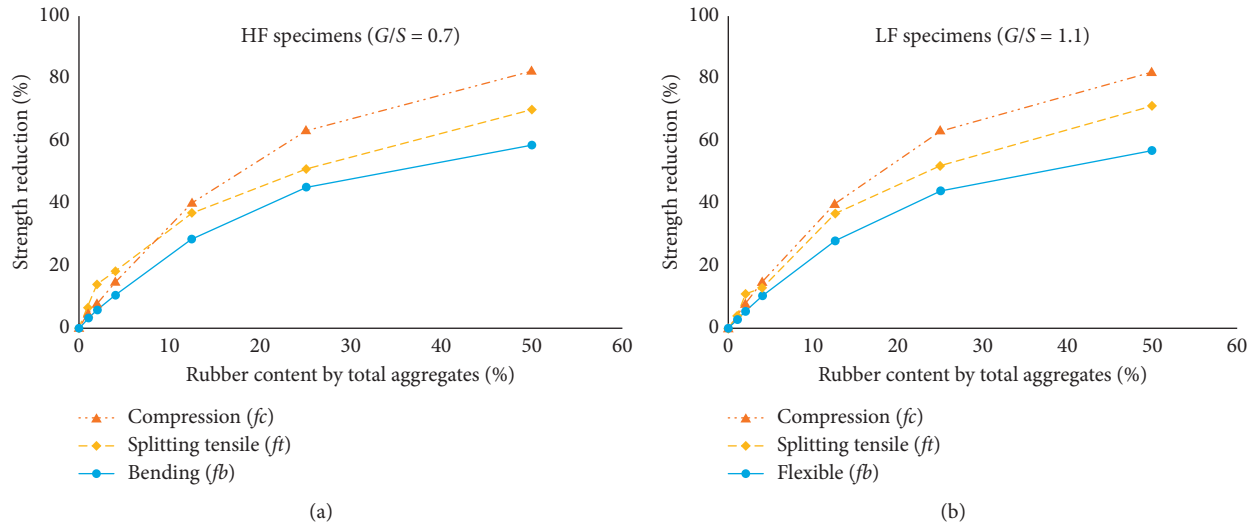
FIGURE 4: Comparison between strength reduction and silicone rubber content. (a) HF specimens. (b) LF specimens.
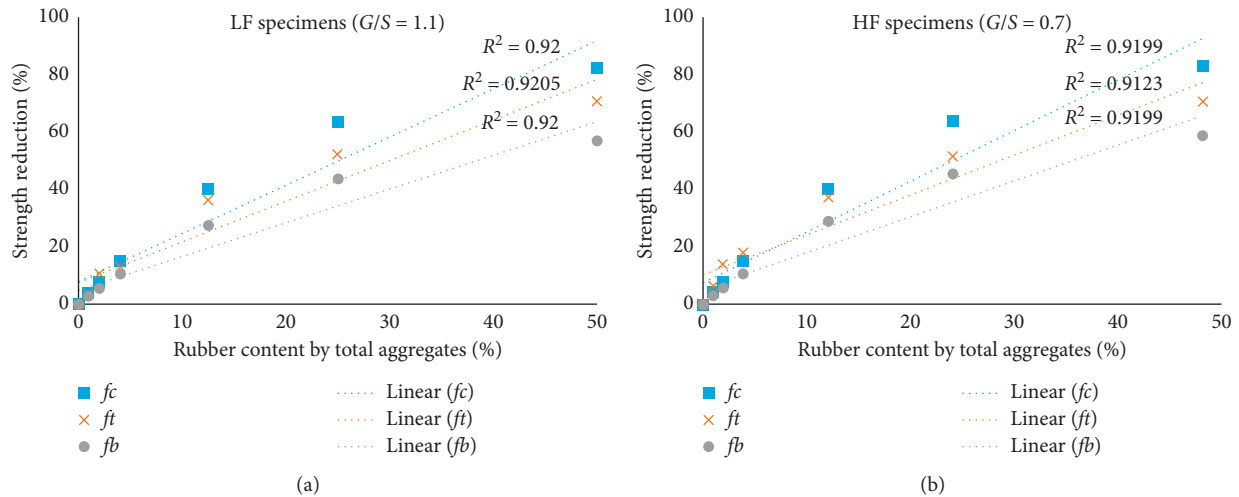
FIGURE 5: Effect of silicone rubber content on the compressive, tensile splitting, and bending strengths. (a) LF specimens. (b) HF specimens.

rubber from 12.5% to 50%, the ratio of (ft/fc) varies from 0.1 to 0.16% in the LF specimens, and also in the HF specimens when silicone rubber was between 0 and 12.5%, the ratio of (ft/fc) is about 0.11 and when increasing the amount of silicone rubber from 12.5% to 50%, the ratio of (ft/fc) varies from 0.11 to 0.195. In examining the changes in the (fb/fc) ratio according to the results of Table 6, it can be obtained that as long as the percentage of silicone rubber was between 0 and 4%, the ratio of (fb/fc) was about 0.14, but with increasing the amount of silicone rubber from 12.5% to 50%, the ratio of (fb/fc) varies from 0.17 to 0.34% in the LF specimens, and also in the HF specimens when silicone rubber was between 0 and 4%, the ratio of (fb/fc) is about 0.14 and when increasing the amount of silicone rubber from 12.5% to 50%, the ratio of (fb/fc) varies from 0.16 to 0.32, and in a similar review for ratios (ft/fb) as long as the percentage of silicone rubber was between 0 and 4%, the ratio of (ft/fb) was about 0.7, but with increasing the amount of silicone rubber from 12.5% to 50%, the ratio of (ft/fb) varies from 0/

63 to 0.43% in the LF specimens, and also in the HF specimens when silicone rubber was between 0 and 4%, the ratio of (ft/fb) is about 0.71 and when increasing the amount of silicone rubber from 12.5% to 50%, the ratio of (ft/fb) varies from 0.74 to 0.61. The effects of the various percentages of silicone rubber content on the retained compressive, splitting tensile, and bending strength compared to the control strength have been reported in Table 5 and depicted in Figure 6. The percentage changes in the retained strength to the amount of silicone rubber are given in Table 6. As shown in Table 6, when the amount of silicone rubber increased to 50%, the percentage of compressive strength maintained was 17.63% of the LF control specimen and 29.8% of the HF control specimen and also the percentage of splitting tensile strength maintained for both LF and HF control specimen was 29%. The percentage of flexural strength maintained for the LF control specimen was 57%, and for HF control specimen, it was 58.5%. It is significant that the rate of strength reduction with increasing

TABLE 6: Comparison of strength ratios based on the silicone rubber content.

Concrete mixture	Total rubber content (%)	ft/fc (Exp.)	fb/fc (Exp.)	ft/fb (Exp.)
LF-G0S0	0	0/099	0/138	0/714
LF-G1S1	1	0/100	0/140	0/710
LF-G2S2	2	0/096	0/142	0/676
LF-G4S4	4	0/101	0/146	0/695
LF-G12.5S12.5	13	0/105	0/167	0/630
LF-G25S25	25	0/130	0/212	0/611
LF-G50S50	50	0/163	0/338	0/483
HF-G0S0	0	0/114	0/135	0/844
HF-G1S1	1	0/111	0/136	0/814
HF-G2S2	2	0/106	0/138	0/768
HF-G4S4	4	0/110	0/142	0/774
HF-G12.5S12.5	13	0/120	0/161	0/744
HF-G25S25	25	0/153	0/203	0/753
HF-G50S50	50	0/194	0/319	0/609
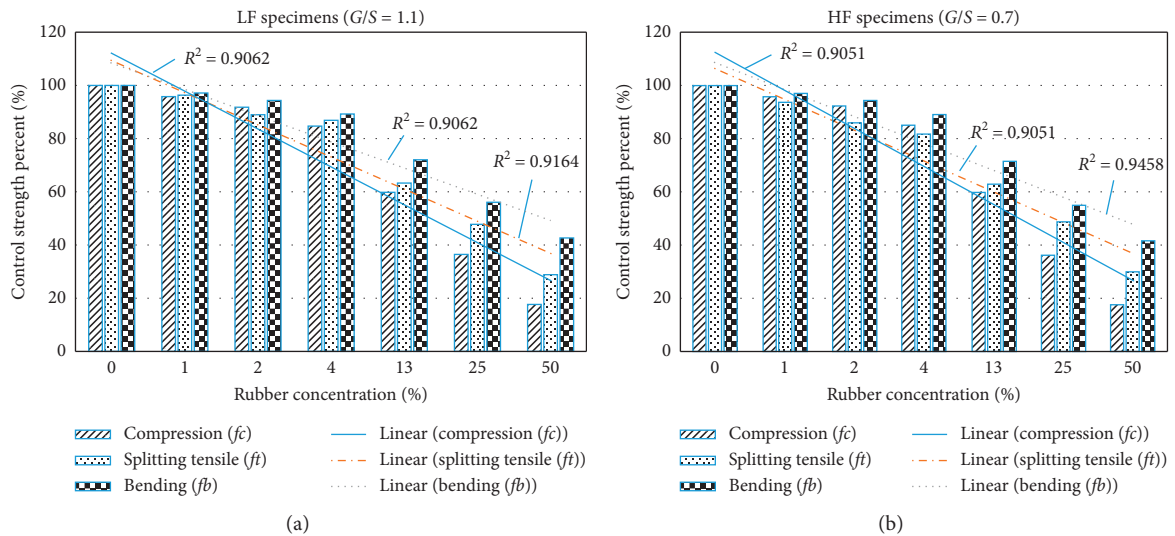
FIGURE 6: Variation of strengths with respect to control strength in different silicone rubber content. (a) LF specimens. (b) HF specimens.

silicone rubber content was not the same in compressive strength as it is in splitting tension strength. This is obvious in the bar chart of Figures 6(a) and 6(b), in which a trendline for the bars has been depicted, representing the three strengths of the bar chart. The results of this study were consistent with the results of a study conducted on rubberized concrete [24] that suggests that the rate of strength-loss in compression is higher than the rate of splitting tensile strength. Concrete strength, particularly in compression, depends on the paste quality, aggregate paste bond, and aggregate hardness. Generally substituting the harder dense natural aggregates with a softer, less dense silicone rubber will act as a stress concentrator, leading to microcracking of the concrete matrix, causing loss in strength [24]. This work concluded that the specimens with $G/S = 0.7$ presented higher strength in compression, splitting tensile, and flexural strength in comparison with $G/S = 1.1$, and failure mode has been changed from brittle to ductile failure with lower sound and separation of aggregate.

3.3. Proposed Model for Flexural Strength Reduction Factor of HSRC Specimens.

To measure the flexural strength reduction of the HSRC specimens in connection with silicone rubber content in the mixture, an effort was made to simulate the flexural strength reduction by a characteristic function and the parameters of this function specified by regression analysis. The amount of silicon rubber content plays a vital role in the mechanical property of HRSC specimens demonstrated by test results. Hence, the properties of HSRC can be expressed by a function using the percentage of the amount of silicone rubber in the mixture. The fb-RF is defined by the ratio of the flexural strength of the mixture containing silicone rubber content R to the strength of the control mixture. In the HSRC specimens, liquid silicone rubber has been replaced with the mineral aggregate of an equal volume. The content of liquid silicone rubber R is a volume ratio, which indicates the percentage of volume of silicone rubber replaced with the same volume of mineral aggregates. At 0% rubber, fb-RF must be equal to 1

TABLE 7: Parameter of reduction function for HSRC specimens at 28 days.

Model parameter	Concrete property	
	Flexural strength (fb) in HF specimens	Flexural strength (fb) in LF specimens
a	0/12	0/25
b	0/88	0/75
m	4/1	3/87
R-square	0/94	0/95
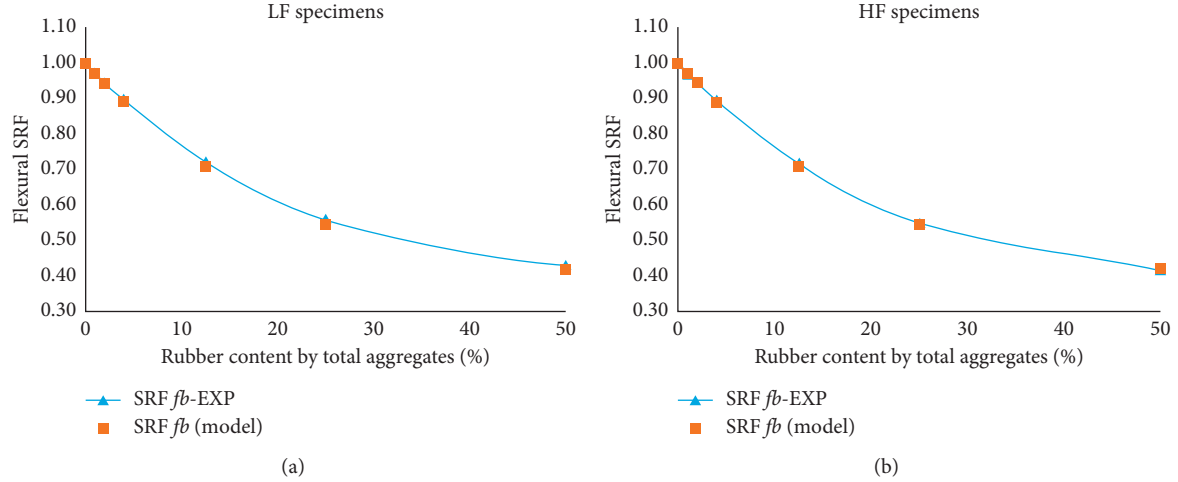
FIGURE 7: Comparison between experimental results and the proposed model. (a) LF specimens. (b) HF specimens.

(control mixture), and by increasing silicone rubber content in mixture, fb-RF will be decreased. According to similar studies carried out on rubber concrete by Khatib and Bayomy [24], the strength reduction function for flexural strength is used as follows:

$$fb - RF = a + b(1 - R)^m, \quad (1)$$

where fb-RF is flexural reduction factor, and the following condition must be satisfied in the above equation:

$$a + b = 1, \quad (2)$$

where a, b, and m are constant numeric parameters and R is specified as silicone rubber content in a volumetric ratio of total mineral aggregate volume. fb-RF defined as flexural strength reduction factor. A numerical analysis was conducted on the data obtained by experimental tests to specify the parameters (a, b, m). The error rate of the extracted functions was evaluated by the R-square test. The results are reported in Table 7.

Figure 7 compares the results of experimental flexural tests and the proposed numerical model. Examination of the diagrams in Figure 7 shows that there is a very good correlation between the proposed model fb-RF and the test results for both HF and LF specimens, and the answers are almost consistent. According to the studies conducted by Khatib and Bayomy [24] on concrete containing tire rubber particles, the value of m was considered to be 10. In comparison with this study, it is found that the sensitivity of the results obtained from this study is less than the changes in

comparison with research on tire rubber particles in concrete. Comparing the results of using liquid silicone rubber in concrete and crushed tire particles in concrete, it was concluded that the use of liquid silicone rubber instead of rubber particles caused mechanical properties such as compressive and flexural stresses to be reduced relatively less.

4. Conclusions and Recommendations

The results of this study showed that it is possible to use silicone rubber in the amounts of 1, 2, 4, 12.5, and 25% in executive works. The replacement of mineral aggregate with liquid silicone rubber in fresh concrete reduced compressive, splitting tensile, and flexural strength. Decrease in compressive strength was higher than the decrease in flexural strength and splitting tensile strength. The higher amount of silicone rubber results in the lower compressive and flexural and splitting tensile strength. Decrease in compressive strength was higher than the decrease in splitting tensile and flexural strength. The results show that, for a certain amount of silicone rubber and cement, HF specimens exhibited more flexural strength, about 7% than those of LF specimens. HSRC beam specimens exhibited more ductile behavior than plain concrete bending test. Failure was accompanied with lower sound than plain concrete. The failure of all the specimens was almost in one form. The main crack appeared in the middle of the span in the lower edge of the beam and continued upward. Physical exam of broken specimens indicated that there is a good engagement between silicone

rubber particles and concrete constituent, so that these particles are not easily detachable from the concrete. In this study, liquid silicone rubber was added to ordinary concrete, then the resulting mixture was well stirred so that the liquid silicone rubber was evenly distributed in the mixture. Based on observations of broken specimens at the time of testing, the silicone rubber is randomly formed into different shapes, and according to the observations, some of them were in the form of filaments and due to their geometric shape, they were well involved in the concrete texture. Based on previous experiences of making rubber concrete with crushed particles of waste car tires, it was seen that in this case the rubber particles could be easily separated from the broken specimens, but in this study it was observed that the silicone rubber particles in concrete were well involved with the concrete texture and they were not easily detachable. Load-deflection curves indicate that by the increasing silicone rubber content in concrete the deflection corresponding to cracking load was increased significantly, which is useful for structures located in severe environmental conditions. In elastic region before concrete cracking, the energy absorption capacity of HSRC is greater than control specimens. During the test, it was observed that, with the increase of silicone rubber in the specimens, they were broken with less noise and more flexibility was observed during the failure, which indicates that the use of silicone rubber in concrete improves the brittleness and inflexibility of the concrete.

Data Availability

All data will be available upon request.

Disclosure

This study is part of the second author's Ph.D. dissertation.

Conflicts of Interest

The authors declare that they have no conflicts of interest.

Acknowledgments

References

[1] J. P. Romualdi and G. B. Batson, "Mechanics of crack arrest in concrete," *Journal of the Engineering Mechanics Division*, vol. 89, no. 3, pp. 147–168, 1963.

[2] İ. B. Topçu, "Assessment of the brittleness index of rubberized concretes," *Cement and Concrete Research*, vol. 27, no. 2, 1997.

[3] A. R. Khaloo, M. Dehestani, and P. Rahmatabadi, "Mechanical properties of concrete containing a high volume of tire-rubber particles," *Waste Management*, vol. 28, no. 12, pp. 2472–2482, 2008.

[4] R. K. Hamdan and S. I. Sarsam, "Impact of rejuvenators type on physical properties of aged asphalt cement," *Civil Engineering Journal*, vol. 5, no. 9, pp. 2058–2069, 2019.

[5] G. H. Xu, "Dynamic parameter optimization and experimental study of tuned slab damper on metro systems," *Shock and Vibration*, vol. 2019, 2019.

[6] E. Ganjian and M. Khorami, "Scrap-tyre-rubber replacement for aggregate and filler in concrete," *Construction and Building Materials*, vol. 23, no. 5, pp. 1828–1836, 2009.

[7] A. A. Kadhim and H. M. K. Al-Mutairee, "An experimental study on behavior of sustainable rubberized concrete mixes," *Civil Engineering Journal*, vol. 6, no. 7, pp. 1273–1285, 2020.

[8] H. L. Li, Y. Xu, P. Y. Chen, J. J. Ge, and F. Wu, "Impact energy consumption of high-volume rubber concrete with silica fume," *Advances in Civil Engineering*, vol. 2019, 2019.

[9] V. R. Riley and I. Razl, "Polymer additives for cement composites: a review," *Composites*, vol. 5, no. 1, 1974.

[10] K. Malek, "Promoting the use of crumb rubber concrete in developing countries," *Waste Management*, vol. 28, no. 11, pp. 2171–2176, 2008.

[11] B. Fazelabdolabadi and M. H. Golestan, "Towards bayesian quantification of permeability in micro-scale porous structures-the database of micro networks," *HighTech and Innovation Journal*, vol. 1, no. 4, pp. 148–160, 2020.

[12] E. Güneyisi, M. Gesoğlu, and T. Öztu17an, "Properties of rubberized concretes containing silica fume," *Cement and Concrete Research*, vol. 34, no. 12, 2004.

[13] E. A. Cherney and R. S. Gorur, "RTV silicone rubber coatings for outdoor insulators," *IEEE Transactions on Dielectrics and Electrical Insulation*, vol. 6, no. 5, pp. 605–611, 1999.

[14] A. J. Shaukat, H. Feng, A. Khitab, and A. Jan, "Effect of admixtures on mechanical properties of cementitious mortar," *Civil Engineering Journal*, vol. 6, no. 11, pp. 2175–2187, 2020.

[15] E. Keith, "Polmanteer, silicone rubber, its development and technological progress," *Rubber Chemistry and Technology*, vol. 61, no. 3, pp. 470–502, 1988.

[16] L. Furgani, M. A. Hariri-Ardebili, M. Meghella, and S. M. Seyed-Kolbadi, "On the dynamic capacity of concrete dams," *Infrastructures*, vol. 4, no. 3, p. 57, 2019.

[17] S. M. S. Kolbadi, H. Davoodian, and S. M. S. Kolbadi, "Evaluation of nonlinear behavior of reinforced concrete frames by explosive dynamic loading using finite element method," *Civil Engineering Journal*, vol. 3, no. 12, p. 1198, 2018.

[18] S. C. Shit and P. Shah, "A review on silicone rubber," *Civil Engineering Journal*, vol. 36, pp. 355–365, 2013.

[19] ASTM C 192/06 Standard Practice for Making and Curing Concrete Test Specimens in the Laboratory.

[20] ASTM C 143 Standard Method of Test for Slump of Hydraulic Cement Concrete.

[21] ASTM C138/C138M-17a Standard Test Method for Density (Unit Weight), Yield, and Air Content (Gravimetric) of Concrete.

[22] ASTM C78, 2018, Standard Test Method for Flexural Strength of Concrete (Using Simple Beam with Third-Point Loading).

[23] C. G. Papakonstantinou and M. J. Tobolski, "Use of waste tire steel beads in Portland cement concrete," *Cement Concrete Research*, vol. 36, p. 1691, 2006.

[24] Z. K. Khatib and F. M. Bayomy, "Rubberized Portland cement concrete," *Cement Concrete Research*, vol. 11, no. 3, pp. 206–213, 1999.

Research Article

Performance Assessment of Shockwaves of Chute Spillways in Large Dams

S. M. Mousavimehr ⓘ**, Omid Aminoroayaie Yamini** ⓘ**, and M. R. Kavianpour** ⓘ

Department of Civil Engineering, K. N. Toosi University of Technology, Tehran, Iran

Correspondence should be addressed to Omid Aminoroayaie Yamini; o.aminoroaya@mail.kntu.ac.ir

Spillways are the most important structures of large dams that are responsible for releasing the excessive flood discharge from the reservoir. Although many studies have been performed to determine the flow characteristics over these structures, however, the available information on the shockwaves' characteristics for spillways' design is limited. The supercritical flow below the chute piers generates an aerated flow known as shockwaves. Due to the flow interaction with the chute piers, three kinds of standing waves just downstream of the pier, in the middle of the chute, and on the sidewalls are generated. This phenomenon affects the flow domain and its hydraulic characteristics along the chute spillway. The height of the waves increases downstream, where they hit the chute walls and reflect again into the flow to interact together again. The process repeated and intensified downstream in a lozenge shape. The height of these waves can be more than twice the depth flow and thus run over the sidewalls. This is important for the design of chute walls in chute spillways with control gates. In this study, the experimental formation of the shockwaves and their behavior along the chute and their reduction measures are presented. Experiments were conducted on a scaled physical model (1/50) of Kheirabad Dam, Water Research Institute, Iran. It was realized that apart from the geometry of piers and chute spillway, Froude number of flow and gate opening are the main effective parameters on the hydraulic performance of shockwaves' formation and their development on gated spillways.

1. Introduction

Spillways are one of the most significant structures of high or small dams that are responsible for discharging the excessive flood flow of the reservoir. Their flow hydraulic characteristics have drawn the attention of many researchers. These characteristics are high velocity, pressure loss, cavitation probability, and aeration. In this regard, several studies have investigated the above-mentioned issues [1–5]. In the spillways, gates are mounted on the crest of a free spillway that controls the head, discharge, reservoir volume and, reservoir level increase. The addition of these gates adds some new complex issues to the hydraulic subjects [6, 7]. Al-Mansori et al. [8] found that, with increasing hydraulic head, up to seven times that of the design head, the flow separation zone grows linearly. Discharge coefficients are studied for a wide range of head ratios. It is concluded that increasing

head ratio up to five leads to an increase in the discharge coefficient due to decreasing pressure on the ogee crest. Yang et al. [9] focused on the underlying influence of the air-water momentum exchange in the two-phase Two-Fluid Model. It is modified to better represent the drag force acting on a group of air bubbles and the wall lubrication force accounting for near-wall phase interactions. Samadi et al. [10] and Sylvain and Claire-Eleuthèriane [11] studied the multivariate adaptive regression splines (MARS) approach that has been adopted as a new soft computing tool for estimating the equilibrium scour depth below free overfall spillways. Khalifehei et al. [12, 13] studies investigated the stability of sediment particles using A-Jack concrete block armors. In this regard, the general forms of the incipient motion and incipient failure of A-Jack armor were extracted based on dimensional analysis and particle stability analysis. Karalar and Cavusli [14] studies aimed to examine the nonlinear

seismic behaviors of concrete gravity (CG) dams considering various epicenter distances. For this purpose, Boyabat CG dam that is one of the biggest concrete gravity dams in Turkey is selected as a numerical application. Karalar and Çavuşli [15] studies observed how the time-dependent displacement and stress behavior of a concrete-faced rockfill (CFR) dam change by the effect of the normal and shear interaction spring stiffness parameters. Ilısu Dam that is the longest concrete-faced rockfill dam in the world now and has been completed in the year 2017 is selected for the three-dimensional (3D) creep analyses.

Among gate discharge coefficient, gates location above the spillways, and separation of flow profile, the spillway transverse flows and waves are less known issues. These waves are called by different names such as shockwaves, lateral shockwaves, and rooster tail waves [16–18]. Their height is greater than the average. Additionally, they have a transverse velocity component. Thereupon, the shockwaves' flow moves from one side to the other, imposing a new hydraulic condition to which less attention is being given.

Despite many studies on the hydraulic characteristics of flow in chute spillway, there is insufficient knowledge of the formation of shockwaves. Investigations on the formation of the shockwaves flow in a horizontal rectangular channel by Reinaur and Hager [19] showed that, for the state of constant flow depth h0 and constant pier width bp, the height of waves 1 and 2 and their width increase with increasing of the Froude number. They also showed that wave 1 height was only a function of the ratio of the flow depth to the pier width H_o/b_p. The wave 1 height and wavelength increase by the Froude number increment. In 1997, Reinaur and Hager continued their previous studies on a chute spillway. They observed that if the depth measurements were taken perpendicularly to the chute spillway, the results would be consistent with the studies performed in the horizontal channel [20–22]. In 1998, they also investigated the effects of chute lateral wall convergence and chute floor slope on the rooster tail waves. They suggested a method for reducing transverse waves and designing lateral walls of a chute [23, 24]. In another study, investigations on this type of flow were presented as the standing wave analysis in a chute spillway [25, 26]. Further studies on the shockwaves flow in an aeration chute spillway have shown that the deployment of the aeration intensifies the shockwaves. The waves become larger with the increase of the Froude number [27, 28]. Wu et al. [29] conducted experiments to study shockwaves characteristics. The results revealed that the ratio of the lateral cavity length to the bottom cavity length had a dominant bearing on the intensities of the rooster tail. For the third type of shockwaves, Duan [30] developed a submerged sloping-tail pier for the deep hole gate of the chute of a hydroelectric project to eliminate the shockwaves. The principle and construction of a pier for eliminating the shockwaves were discussed. Reinauer and Hager [19, 22] found that shockwaves characteristics only depended on the ratio of approach flow depth to pier width in a series of experiments conducted in a horizontal channel and sloping chutes. Wu and Yan [31] and Smajdorová and Noskievičová [32] investigated the hydraulic characteristics of the

shockwaves induced by the pier of the discharge tunnel of the Sanbanxi hydropower station. It was observed that the primary reason for the shockwaves inception was the concavity of the water surface. Based on that, a new type of pier with a bottom underlay to control the shockwaves for the discharge tunnel was designed [31, 33].

The shockwaves are a parabolic roller flow that occurs in hydraulic structures under various conditions. The shockwaves flow occurs at the downstream piers of the chute gate, downstream arches of the tunnel spillways, the entrance of the bottom outlet tunnel, and the wall of the converging chute [34, 35]. The use of piers is inevitable due to the gates and bridges passage located on the crest of spillways. After passing the dam crest and piers, the supercritical flow of two sides of the pier collides and creates the standing wave at the downstream. These waves, known as pier waves, are referred to as wave 1 in this research. The wave in the form of the shockwaves of type 1 is formed based on the number of intermediate piers located on the spillways. Due to the interaction of these waves, they form regular geometric shapes of rhombic or other types over the spillway water surface (Figure 1). It should be noted that dotted lines are the place where shockwaves form.

Figure 1 shows the plan and schematic longitudinal cross section of the shockwaves flow at the downstream of the symmetric piers. The flow geometry and 3 waves formed on the spillways are shown while all the gates are open. Sections 1, 2, and 3 are the peak of the first, second, and third waves, respectively. In the middle of the spillway, the interference of wave 1 generated a larger one. In this study, this new wave is called wave 2 (Figure 1, section 2). Wave 2 also moves in the direction of the spillway width. In the following, the wave 2 impact on the wall of the chutes produced a new wave which is called wave 3 in this study (Figure 1, section 3). The chutes design and structures exposed to these flows should include the quantitative and qualitative identification of the above-mentioned waves and their detrimental effects on the performance of the spillway structure and in particular its walls [36]. Therefore, identifying their formation location, the characteristics of these waves, evaluating their pressure field and its variations, were considered as significant design hydraulic parameters. This information will considerably assist the designers of these structures.

Studying the shockwaves at the control point $x = 0$ (Figure 1), H_0, v_0, and $Fr = v_o/\sqrt{gH_o}$ are called flow depth, velocity depth, and the Froude number, respectively. The flow geometric parameters are the following: maximum flow depth H_m, flow width at the maximum flow depth location B_m, angle of pier waves formation α, pier width b_p, axial distance of piers b_a and the wave location relative to the control point x. A cavity is created behind the pier from section $X = 0$ to the initial point of wave 1 $X = X_{1i}$. Depending on the flow velocity, the cavity may be submerged or dry (Figure 2). At a distance of $X = 0$ to $X = X_{1i}$, the flow passing through the two sides of the pier collides like two jets and generates the first type of pier waves. This wave is a roller that reaches the maximum wave height (H_{1m}) at X_{1m} by excluding some of the water jets from the main core flow. At the endpoint of type 1 wave (X_{1e}), the core isolated from the
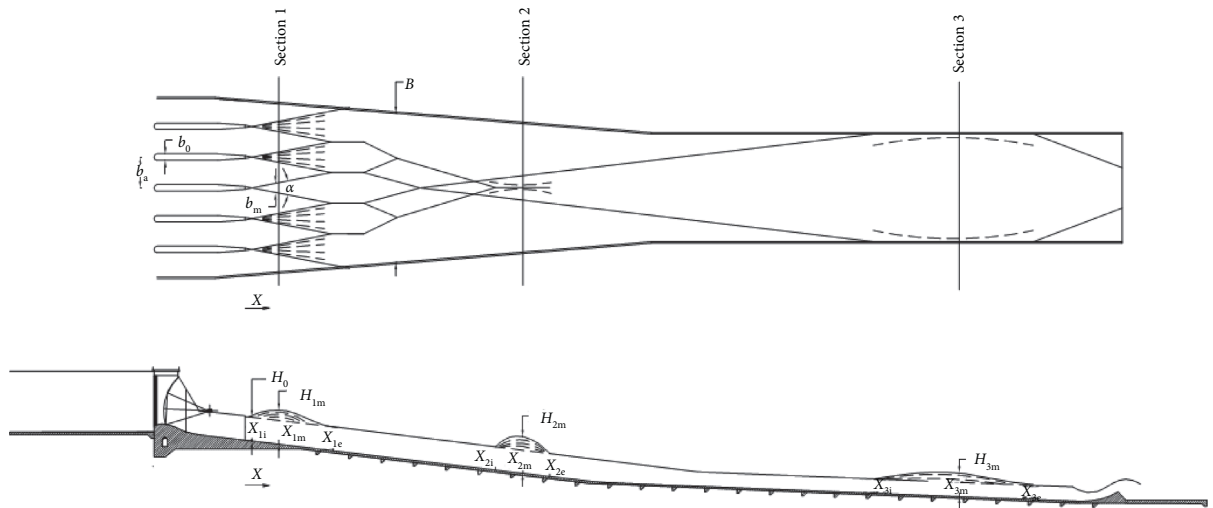
FIGURE 1: Waves at the downstream of pier chutes: (a) plan and (b) flow longitudinal section (the Kheirabad Dam is located in Khuzestan Province, Iran).
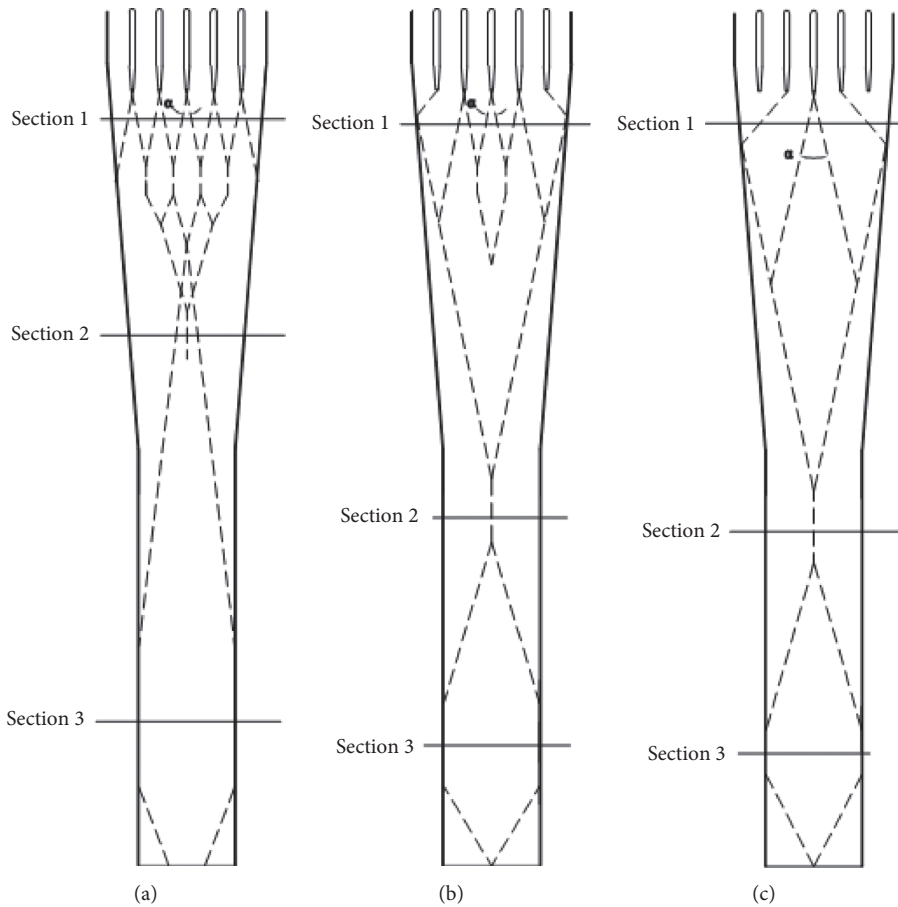
FIGURE 2: Flow geometric plan under the gates performances. (1) Six gates; (2) four middle gates; (3) two middle gates.

water jets falls to the side of the water padding. Because of wave collision and also due to the convergence of the lateral walls of the spillway, type 1 waves form a wave flow with regular shapes above the spillway. At the end of these shapes (location x_{2i}), wave type 2 is formed. This wave is observed at a maximum height of H_{2m}. Because of the interference of the waves over the spillway as well as the transverse movement of wave 2 at the farther downstream, a wave on the wall or a third wave also forms on the lateral wall of the spillway. Type 3 wave starts from the location $X = X_{3i}$ on the wall and

reaches the maximum height H_{3m} at $X = X_{3m}$ and then disappears into the mainstream at $X = X_{3e}$.

Investigations on hydraulic models of chute spillway at the Iranian Water Research Institute similarly confirm these issues [37]. Based on the observations, by crossing through each aeration, the waves intensify and their height increases. Therefore, these waves' intensity at the chute downstream with some surface aeration is significant. They require being accurately evaluated and mitigated if necessary. Kavianpour et al. [38] mentioned these results investigating the longitudinal and transverse profiles of shockwaves. They suggested a method to reduce these waves. They also showed that the shockwaves flow field over the spillway is a function of the Froude number, gate opening, head values over the spillway, spillway convergence, and pier geometry. Each of these factors can influence the flow field and cause adverse hydraulic conditions on the spillway. Figure 3 shows the flow geometry because of the 2, 4, and 6 middle gates opening. As can be seen, the flow geometry becomes more complex as the number of gate's performance increases. In this study, the shockwaves flow geometry over the spillway, the longitudinal and transverse profiles of the triple waves, and the static pressure of the shockwaves flow field are investigated. It should be noted that dotted lines are the place where shockwaves form.

In practical dam construction projects, ogee spillways with spindle-shaped, ellipse-shaped, or rectangle-shaped piers are most commonly used. Nevertheless, as mentioned before, there is a lack of knowledge on the shockwave for spillways, and most previous studies were conducted for specific dam construction projects, which limit their general applicability. It is, therefore, necessary to investigate the formation and characteristics of the shockwave. This article studies shockwaves formation in an ogee spillway along with a chute channel by physical experiments (scale 1 : 50). A formula for shockwaves height in a slope chute spillway with spindle-shaped or ellipse-shaped piers is also promoted. The causes of the shockwaves behind the pier of the chute spillway were analyzed at the same time. In addition, the conditions for the formation of shockwaves on the spillways have been analyzed at different gate openings.

2. Model Description and Methodology

The study was performed on the physical model of Kheirabad Dam spillway. The Kheirabad Dam is located in Khuzestan Province, Iran. According to the studies that were performed theoretically on different physical models, it was concluded that the Kheirabad Dam spillway is the best possible option in which the shockwaves flow conditions are clearly formed. The physical model was designed at a scale of 1/50 at the Iranian Water Research Institute. The linear geometric scaling of material, which follows Froude's scaling laws, may lead to very large viscous forces that in turn lead to very small Reynolds (Re) number. Since most flows at prototype are both turbulent and in the hydraulic rough regime, where losses are independent of (R), flows in hydraulic Froude models are often "shifted" to the hydraulic rough regime to better account for losses. When Re in the

core is higher than 2000, flow in the structure is turbulent, conforms to the prototype situation, and the viscous scale effects are negligible. In this model, the Reynolds number has been controlled, and Reynolds Number greater than 2000 (Re > 2000). The scale effect due to surface tension forces becomes important when water waves are very short or flow depth is less. Surface tension effects must be considered when wave periods are less than 0.35 s and water depth is less than 20 mm [39]. In the present study, it was found that both wave period and flow depth were considerably higher; thus, the scale effects by surface tension forces are negligible.

The experimental model includes ogee and chute spillways with 6 gates and 5 piers. Because of the flow collision to the base, there is a rooster tail or a shockwave flow. The laboratory trial and error obtains the pier section spindle-shaped to reduce the shockwaves' flow height in this section. The pier width is 2.4 cm and reaches 1 cm at the end of the spindle. The spillway pier length is 33.8 cm and the pier distance is 9 cm. The spillway chute consists of two parts, one with a 12% slope and the second with a 4% slope. The spillway width at the 12% slope is 132 cm at the beginning and 80 cm at the end. At the 4% slope, this width is fixed with a value of 80 cm. There is a flip bucket at the end of the chute. Due to the shockwaves flow development, the zigzag and waveforms flows are transversely visible on the flip bucket (see Figure 4).

The study found that the regular geometric wave height on the wall can be up to 2 times the water depth. This condition causes the erosion of the chute sidewalls. Figure 5 shows the spillway and the geometric shapes formed on it. In this spillway, the three maximum waves are significant that can cause hydraulically critical conditions. They can influence the chute wall design. Wave 1 is noticeable at the back of the pier. Wave 2 is prominent in the middle of the overflow length that is a consequence of the impact of the oblique and zigzag flows on the spillway. Wave 3 is noticeable on the chute wall. Figure 5 illustrates the collision of the waves with the pier and the created geometry at the downstream. Figure 6 also shows the 3 created maximum waves, locally.

This paper presents the longitudinal and transverse profile variations of the triple waves for three different discharges and also three different gate openings. In the first case, only the two middle gates are open. In the second condition, the four middle gates are open. Lastly, in the third case, all six gates operate.

In this study, the depth and velocity of the inflow to the spillway are changed by the partial opening of the gates. In this study, the partial opening of the gates changes the depth and velocity of the spillway inflow. This partial opening of the gates allows the ability of increasing the speed, decreasing the depth, and consequently the proper change for the Froude number. Also, the flow field piezometric pressure over the spillway is presented for the two operating modes of 6 and 4 middle gates. They are analyzed for 3 separate openings. A depth gauge measured the wave height and profile. Depth measurement error with the depth gauge is subject to the flow conditions. In the smooth flow without oscillation, the error is ±1 mm. In models of oscillatory flow such as the shockwaves, the error is up to ±5 mm [40, 41].

FIGURE 3: Interaction effect of jet flow with shockwaves in flip bucket area.
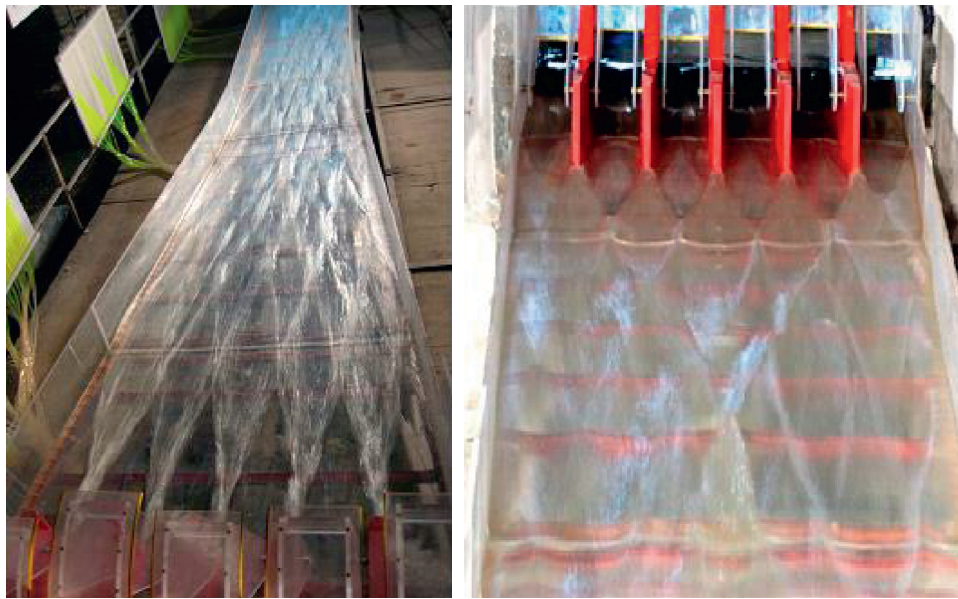
FIGURE 4: Geometric shapes formed from shockwaves over the chute.
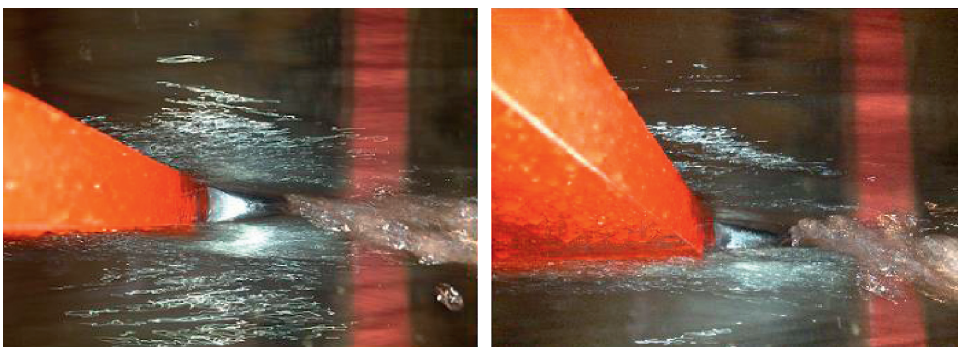
FIGURE 5: Cavity formation behind the pier.

In the present study, based on the flow conditions and the range of wave height variations, the maximum measurement error is 5%. A piezometer was also used to measure static pressure [42, 43]. The piezometer shows the fluid pressure as the liquid-equivalent height. The control or reference section was two piers between the gates with the "o" index. In this control point, the flow characteristics, the depth H_o, the velocity v_0, and the Froude number (Fr_o) (due to the gate function) were submitted in the table of each experiment. At the control section, the experimental Froude numbers change from 2 to 4. However, the variety of the Froude numbers is much larger at the downstream of the spillway, in the range of 8 to 10.

This research calculates the maximum wave height in terms of efficient parameters on the phenomenon as dimensionless graphs. In the chute spillway, the

(a)

(b)

(c)
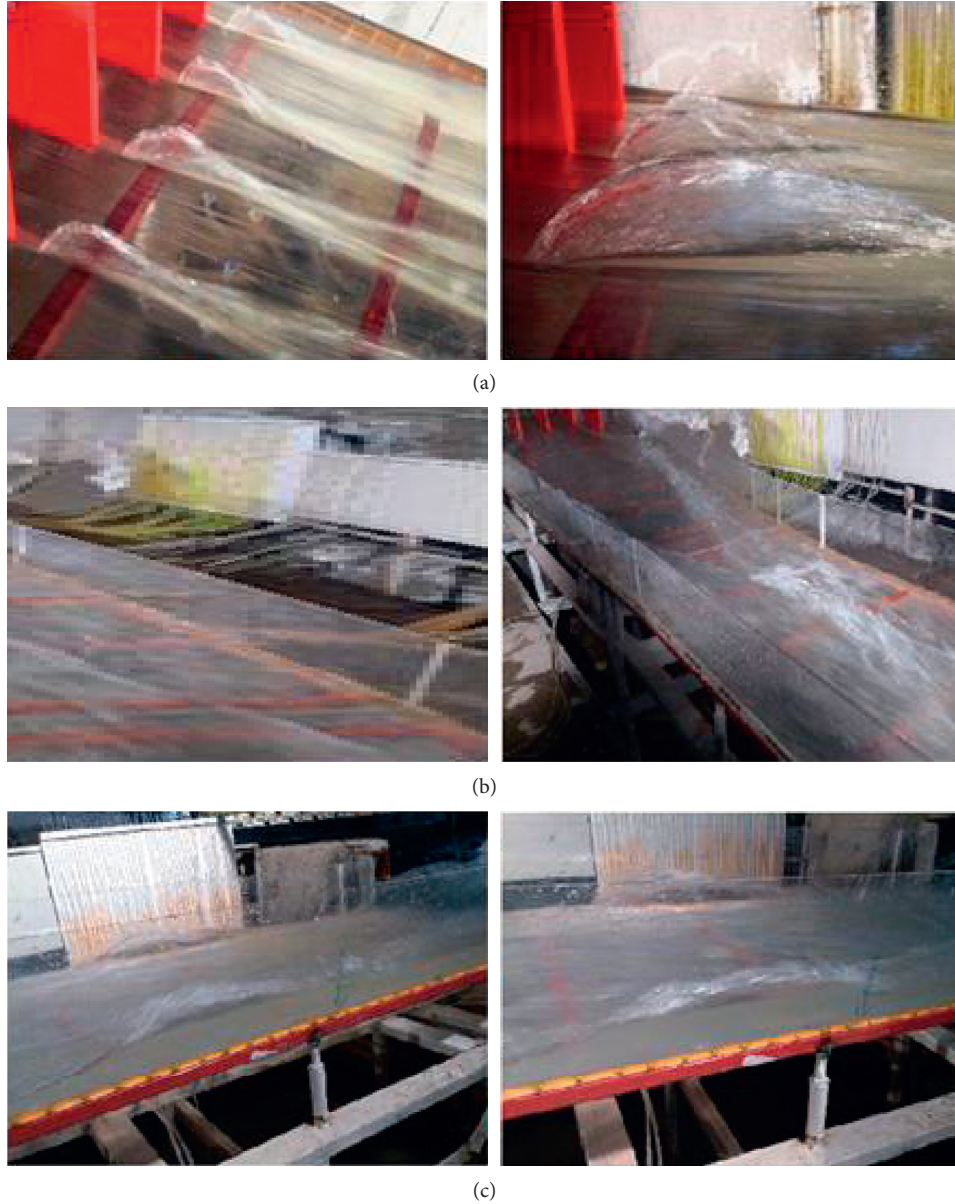
FIGURE 6: The shockwaves created over the chute. (a) Pier waves or wave 1. (b) Middle wave or wave 2. (c)Wave at the wall or wave 3.

important variables affecting the maximum wave height H_m include the fluid bulk density ρ, the fluid dynamic viscosity μ, the water surface tension coefficient σ, the gravity g, the flow depth at the control section H_o, the flow velocity at the control section v_0, the pier width b_p, the pier axial distance b_a, the spillway sidewall slope θ_w, and the spillway floor slope θ_b. A general function of effective variables on the height of shockwaves can be defined as

$$H_m = f\left(\rho, \mu, \sigma, H_\circ, v_\circ, b_p, b_a, \theta_b, \theta_w, g\right). \qquad (1)$$

In the physical model, it was not possible to change the geometrical parameters θ_w, θ_b, b_a, and b_p. As a result, the experiments were performed without any changes in the

physical model. Accordingly, these parameters could be extracted from this study's efficient variables. Employing Buckingham's theory, expressing the dimensionless wave maximum height in the form H_m/H_0 and ensuring the flow turbulence during the overflow, the Reynolds number effect is ignored. Additionally, as the water height above the spillway is always greater than 5 mm during the experiment, the Weber number effect is assumed to be negligible. So, H_m/H_0 is calculated as follows [44, 45]:

$$\frac{H_m}{H_\circ} = f\left(Fr_o\right). \qquad (2)$$

As can be seen, the dimensionless maximum height is function of the inflow depth H_o and the control section

Froude number Fr_0. In the following, the wave height variations are presented in dimensionless form.

3. Results and Discussion

3.1. Longitudinal and Transverse Wave Profiles. In this section, the longitudinal and transverse profiles of the waves for the operation of two middle gates, 4 mid gates, and 6 gates were investigated. The longitudinal sections are in the direction of the flow. The transverse sections are at the location of the maximum wave height. Figure 7 shows a view of this flow and the triple waves for the opening of the two middle gates. In this case, only one pier causes the formation of shockwaves flow.

Figure 8 illustrates the longitudinal and transverse profiles for the two middle gates' performances. The "a" curves represent 100% gate openings. The "b" curves represent 60% gate openings. The "c" curves represent 30% opening of the gate. It should be noted that all measurements were in the longitudinal direction from the end of the pier. The height of the waves was measured from the spillway floor. Parameter X is coordinated in the spillway direction. Parameter B is the coordinate at the spillway width. According to curve 1 of Figure 8, as the opening increases, the dimensionless height of wave 1 decreases, while its maximum location shifts toward upstream. A comparison of the wave transverse variations is also shown in curve 2 of Figure 8. For wave 2, the same trend is evident in curves of 3 and 4; however, as compared to wave 1, this wave affects only a small portion of the spillway width. Wave 2 dimensionless length increases with the decrease of opening. The trend of decreasing relative height and decreasing the relative distance of the wave peak upstream with the opening is repeated in wave 3 for wave 5. According to Figure 6, these waves only affect the wall region, which is a total of 25% of the spillway width on both sides.

Table 1 presents the flow characteristics for the two gates' operation mode studying waves 1, 2, and 3. According to Table 1, by the gate opening increment, the wave 1 height increases. Besides, its maximum location shifts toward upstream. Wave 2 height reduces by decreasing opening. With the increase in gate opening, the trend of height gain and the upward shift of the wave 3 peak is also noticeable.

Figure 9 shows the longitudinal and transverse profiles when the four middle gates operate. In this figure, the curves d, e, and f illustrate 100%, 60%, and 30% of gates opening, respectively. The flow characteristics of the four intermediate gates and waves 1, 2, and 3 are shown in Table 2.

Except for the number of pier waves, all trends and changes observed in the opening mode of two gates are also valid for the opening of 4 gates. There are three pier waves instead of one pier wave (according to curve 2 of Figure 9). Figure 10 also shows the longitudinal and transverse profiles of the six gates performances. The curves "g", "h," and "i" are 100%, 60%, and 30% openings, respectively. The flow characteristics of the six open gate operating modes and waves 1, 2, and 3 are also presented in Table 3. According to

curve 2 of Figure 10, all the trends and differences observed in the two preceding states are also true for the opening of 6 gates, other than the number of the pier waves. Five pier waves have occurred for the opening of 6 gates. However, the height of the pier waves also decreased with the increase of the pier.

As can be seen in Figures 8–10, the Froude number is an important parameter in the shockwaves' wave variation over the spillway. It results from the variation process that, for all three defined waves, the changes are made in the same way by the Froude number. So, the height and location of the wave peak, the end-of-wave cross section, and the pier wave formation angle change with the flow Froude number. As the Froude number increases, the waves get longer and thinner, and the peak and end sections of the wave are shifted toward farther downstream. In general, considering the range of Froude numbers in this study, it is observed that, in the six-gate operation mode, the height of waves 1, 2, and 3 (according to Table 3) is maximum 1.3, 1.5, and 1.3 times the average depth of flow at the same cross section. In the case of the four middle gates operation, these values are 1.4, 1.8, and 1.2, respectively. They are, respectively, 1.5, 2.3, and 2.5 for the two middle gates performance. Moreover, as the Froude number decreases, the wave height increases, the wavelength decreases, and the pier waves formation angle is increased. Separate experiments were performed to illustrate how the pier waves formation angle (α) changes with the Froude number. Figure 11 presents its physical outcomes. Figure 11 shows the results of two Froude numbers $Fr_0 = 2.07$ and 3.1 for a middle pier state. For $Fr_o = 2.07$, the pier wave formation angle (α) is noticeable; pier wave 1 with greater width is created. For $Fr_o = 3.1$, the pier wave formation angle (α) is smaller; the wave is narrower.

For the two increase options and by testing and observing the model flow conditions, to reduce the shape of the shockwaves flow and not affecting the flow behavior during the chute, the best option was selected for the downstream pier shape and stabilized in the model. Figure 12 shows the actual flow conditions for pier end different options at a discharge of 5000 cubic meters per second. By trial and error and observation for several different options, it was observed that, by increasing the pier length and decreasing its end thickness, the formation and skipping of the shockwaves' flow are stabilized in the model. These conditions also depend on structural and executive issues.

Research has recommended the use of pier-mounted blades to reduce the height of the waves so that the point of flow contact moves from the two sides of the pier to the blade tip [19]. This method is not executive and suitable. Changing the pier geometry as recommended in the present article, while applicable, significantly reduces the height of the created shockwaves' flow and decreases the wall wave height by decreasing wave 1 height.

Figure 13 shows the longitudinal sections of the triple waves along the spillway. In all three categories of waves, the process of change is the same in terms of the Froude number. The height of the waves, the location of the wave peak, the cross section of the wave, and the angle of wave

Figure 7: Flow and location of triple waves for two open middle gate modes.

(a)

(b)

(c)

(d)
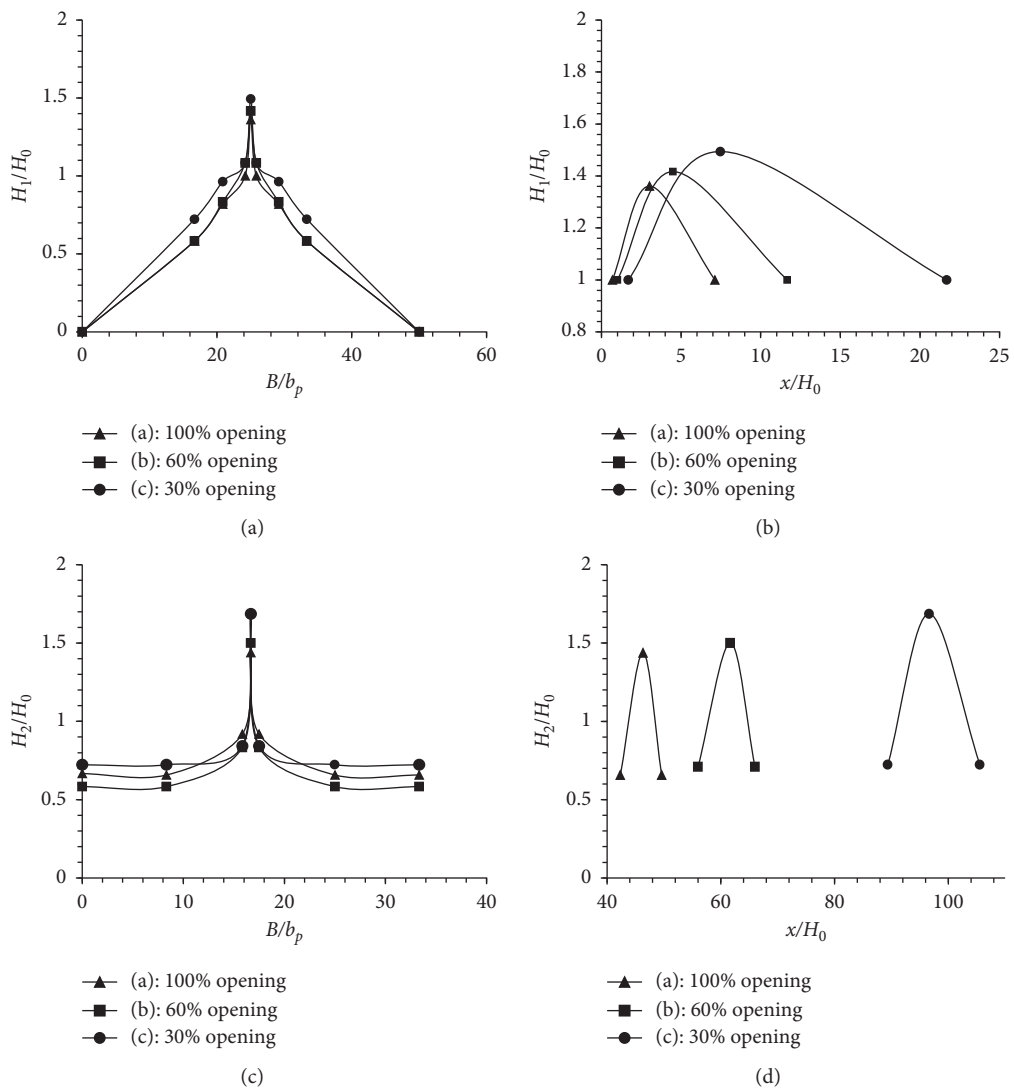
Figure 8: Continued.

(e)

(f)
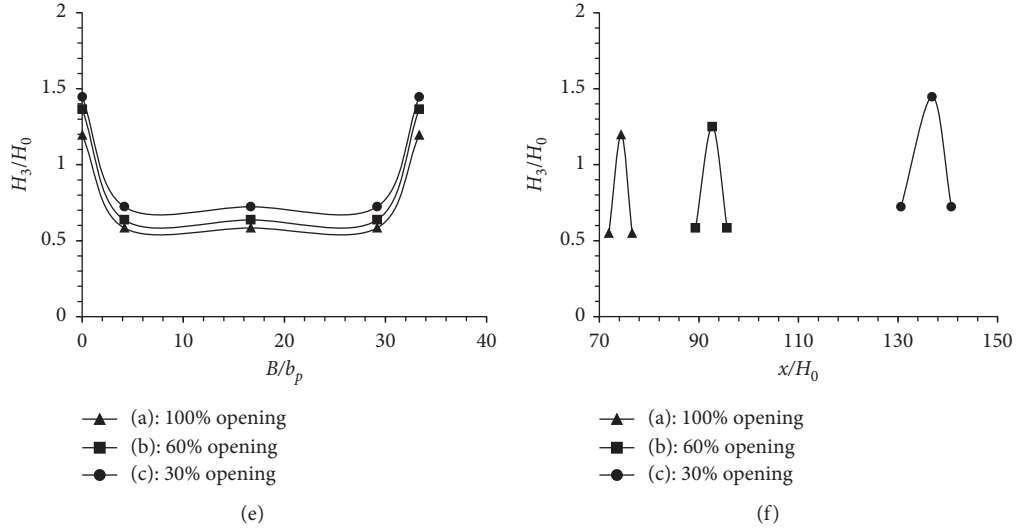
FIGURE 8: Longitudinal and transverse dimensionless profiles for the two middle gates' performances: (a) wave 1 longitudinal profile, (b) wave 1 transverse profile, (c) wave 2 longitudinal profile, (d) wave 2 transverse profile, (e) wave 3 longitudinal profile, and (f) wave 3 transverse profile.

TABLE 1: The shockwaves' flow characteristic for two middle gates' operations.

Type	Opening	Wave type	Fr_o	Q (lit/s)	H_m (cm)	X_i (cm)	X_m (cm)	L (cm)	α (degree)	B_m (cm)
		1			9.6	5	22	47	32.42	12.5
a	100%	2	2.05	91.2	10.5	309	338	53	—	—
		3			8.6	525	543	34	—	—
		1			8.5	6	27	64	28.37	11.68
b	60%	2	2.47	60.6	9	336	370	60	—	—
		3			7.5	536	556	38	—	—
		1			6	7	31	83	25.61	11.01
c	30%	2	3.07	44.4	7	370	400	67	—	—
		3			6	542	568	42	—	—

formation vary with the flow Froude number. As can be seen, as the Froude number increases, the length of the wave increases, while its height decreases. Also, the maximum end sections of the wave are moved downstream. The height of the waves depends on the flow depth and their length depends on the flow velocity. As a result, as the depth of flow increases; the height of the wave increases. Moreover, as the velocity of flow increases, the length of the waves increases. Also, with increasing the gates opening, the flow depth increases while the Froude number decreases. Consequently, the wave height increases while the wavelength decreases. The maximum end sections also move upstream. Also, by investigating the transverse sections of the waves, increasing the Froude number makes the waves narrower while the waves become wider by decreasing the Froude number. As can be seen in Figure 13, wave 2 (the spillways' middle wave) is much higher than the other two waves. Then, wave 3 and wave 1 are next in terms of height.

Figure 14 shows the location of the triple wave formation over the spillway plan. Wave 2 is formed over a broader range of spillway. The range of wave 3 formation is very critical because the wall wave is a shockwave that exerts

considerable dynamic pressure on the sidewall of the chute. On the contrary, the height of these waves can be larger than the height of the chute wall. Subsequently, wave 3 (wall wave) is essential from a design viewpoint.

Figure 15 shows the dimensionless curves of the maximum height of waves 1, 2, and 3 and their location of formation in terms of the Froude number for two, four, and six gate operations. For different operations of the gates, the height of all the waves and their longitudinal coordinates have a clear and relatively linear trend in terms of the Froude numbers. Figure 16 also shows the dimensionless curve of the wave 1 formation angle in terms of the Froude number. As the Froude number increases, the angle α decreases linearly, making the waves sharper and thinner.

3.2. Piezometric Pressure. The piezometric pressure distributions of the spillway floor were measured and given beneath the height maximum location and landing point of waves 1 and 2 as well as the place of wave 3 peaks on the walls. Considering two modes of six gates and four middle gates operating, Figures 17 and 18 show the piezometric pressure coefficient distribution of triple waves for the three
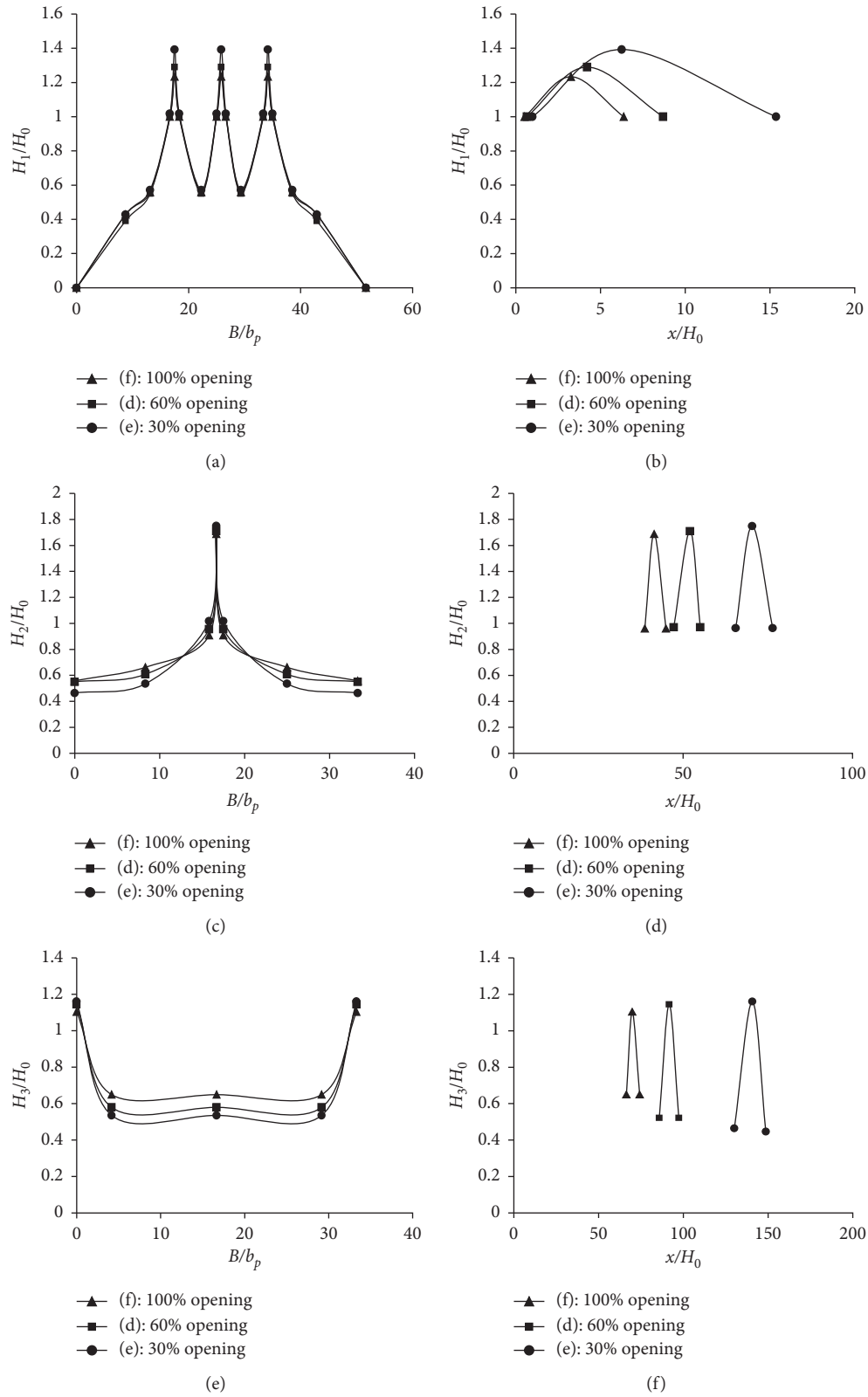
FIGURE 9: Longitudinal and transverse dimensionless profiles of waves for the four gates' performances.

openings 100%, 60%, and 30% with corresponding input Froude numbers. The vertical axis represents the pressure coefficient. In the control section, the pressure coefficient is dimensionless relative to the velocity head in the form of $c_p = (p/(V^2/2g))$. The horizontal axis also indicates the longitudinal distance of the points from the pier beginning.

TABLE 2: The shockwaves' flow characteristic for four middle gates' operations.

Type	Opening	Wave type	Fr_o	Q (lit/s)	H_m (cm)	X_i (cm)	X_m (cm)	L (cm)	α (degree)	B_m (cm)
d	100%	1	2.1	126	9.3	4	25	45	22.62	9.8
		2			14.1	298	349	48	—	—
		3			8.9	485	510	57	—	—
e	60%	1	2.75	90.6	8.5	4.5	29	55.5	19.87	8.22
		2			11.5	326	359	54	—	—
		3			7.7	515	550	69	—	—
f	30%	1	3.9	62.4	7.5	5.5	25	80.5	17.65	6.06
		2			8	367	394	61	—	—
		3			5.5	540	584	77	—	—

FIGURE 10: Continued.

(e)

(f)
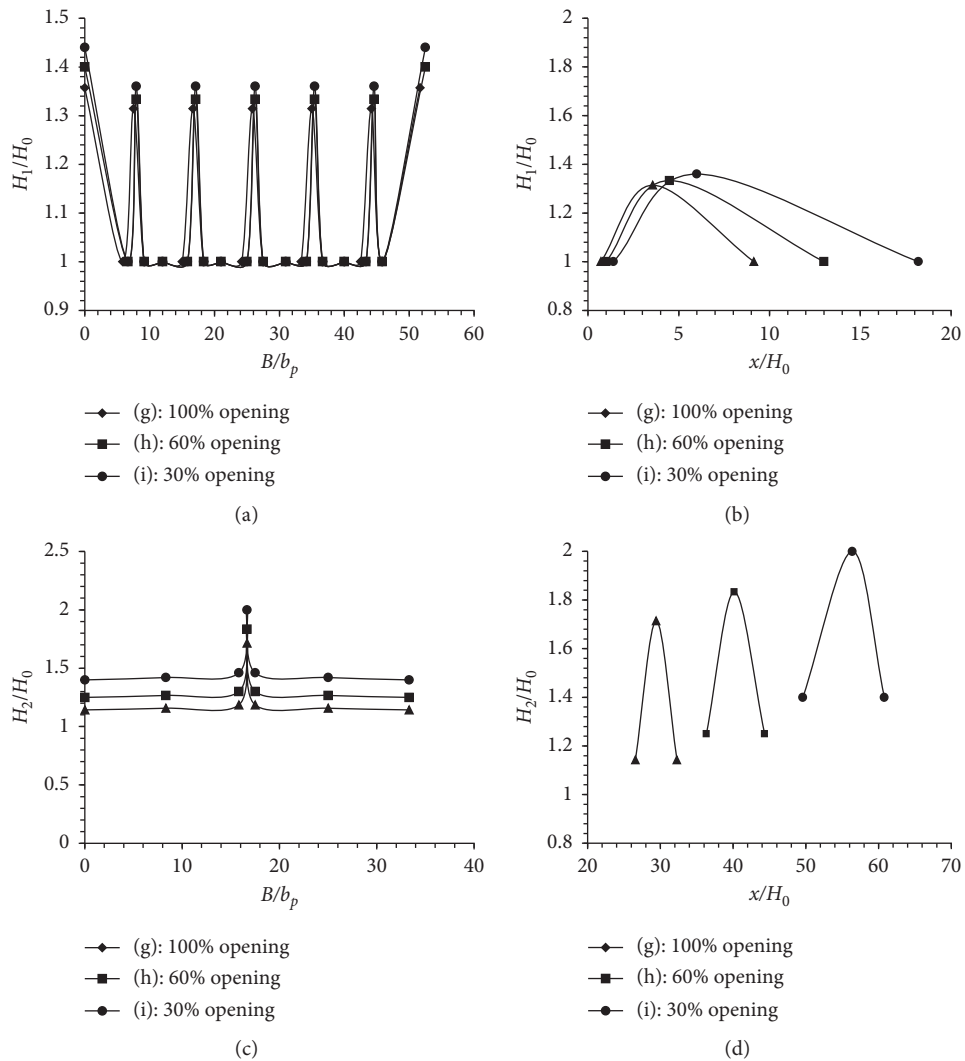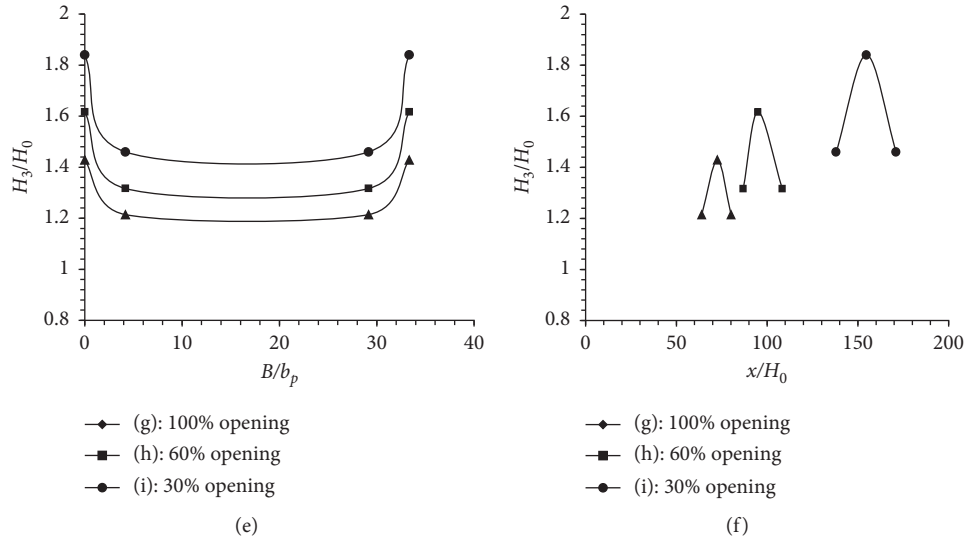
FIGURE 10: Longitudinal and transverse dimensionless profiles of waves for the six gates' performances; 1: longitudinal profile of wave 1.

TABLE 3: The shockwaves' flow characteristic for six middle gates' operations.

Type	Opening	Wave type	Fr_o	Q (lit/s)	H_m (cm)	X_i (cm)	X_m (cm)	L (cm)	α (degree)	B_m (cm)
g	100%	1	2.18	209.6	9.2	5	25	59	22.17	7.73
		2			12	186	206	40	—	—
		3			10	467	530	118	—	—
h	60%	1	3.1	125.8	8	6	27	72	16	5.88
		2			11	218	241	48	—	—
		3			9.7	521	570	99	—	—
i	30%	1	3.7	83.8	6.8	7	30	84	12.1	3.64
		2			10	248	282	56	—	—
		3			9.2	573	608	77	—	—

(a)   (b)
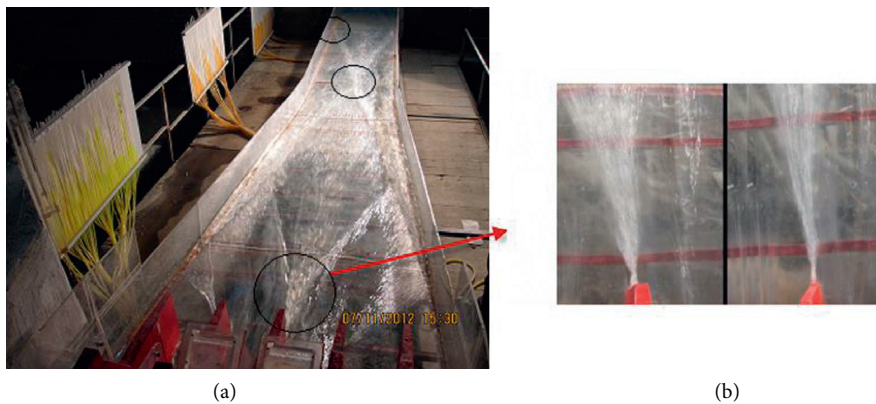
FIGURE 11: Wave 1 plan view: (a) $Fr_o = 3.1$ and (b) $Fr_o = 2.07$.

In these curves, the points from the left are, respectively, the location of the peak height and the landing point of wave 1 and 2 and the location of the peak wave 3 height formation on the spillway wall.

As shown, the piezometric pressure decreased as the water height decreased at the landing point of wave 1 relative to its maximum height point. In the following, as wave 2 height is higher than wave 1, the piezometric pressure increases. According to Figure 19, wave 2 is separated from the core of water over the spillway at the peak point. Likewise, as the water level rises at the landing point, the piezometric pressure is increased. The flow also hits the spillway sidewall

(a)   (b)   (c)
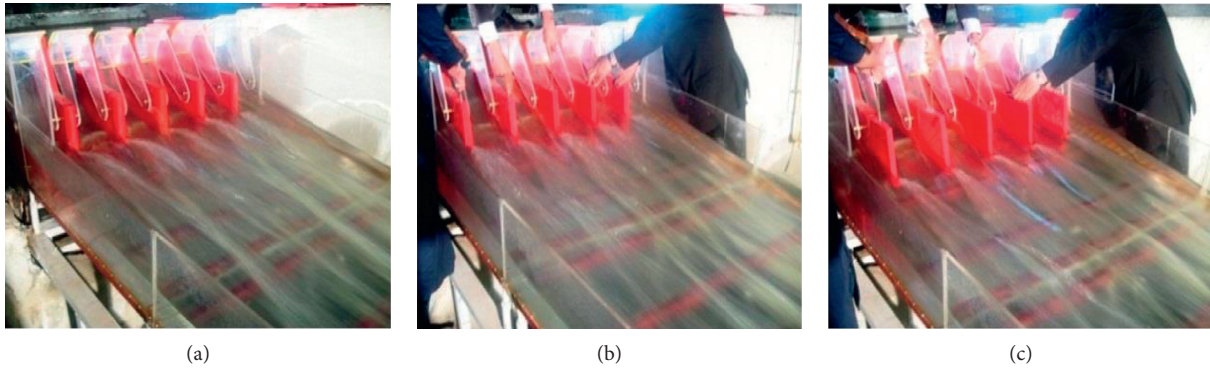
FIGURE 12: The shockwaves jump for different options at 5000 cubic meters per second: (a) initial plan, (b) first option, and (c) third option-final one.

—○— (g): 100% opening
—□— (h): 60% opening
—△— (i): 30% opening
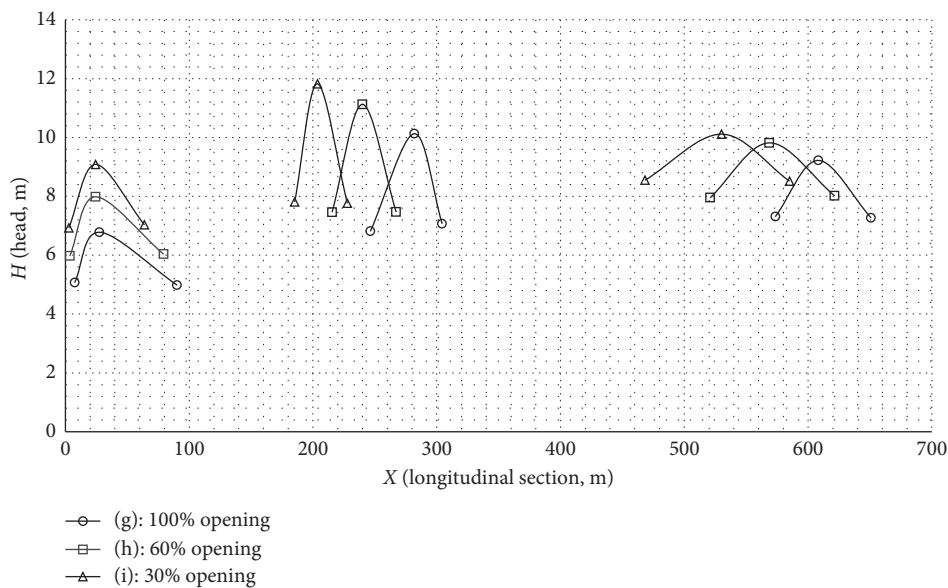
FIGURE 13: Waves 1, 2, and 3 variation along the spillway in terms of different openings and Froude number.
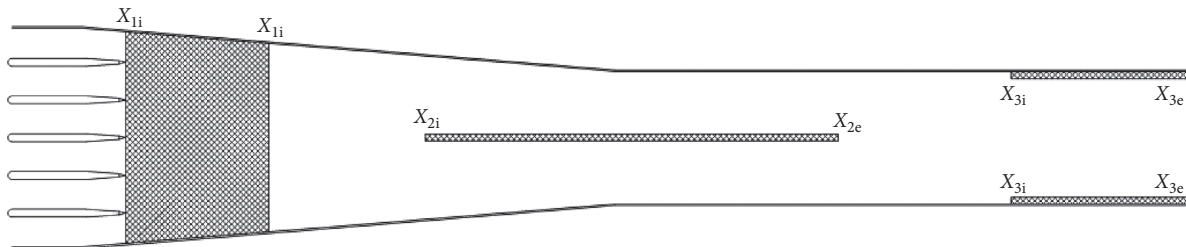
FIGURE 14: Location of the triple wave formation.

strongly at the location of wave 3 peak height; the piezometric pressure reaches its maximum value. As mentioned, by increasing the number of the Froude number and decreasing the percentage of gate openings, the height of the waves decreases while the waves become longer. Therefore, according to Figures 17 and 18, the piezometric pressure decreases with increasing input Froude number. Also, at the fixed opening for all gate performance modes, the pressure at the location of maximum wave 1 height is higher than that of wave landing, which is the opposite of wave 2. For wave 2, the pressure at the landing point is greater than its maximum height location.
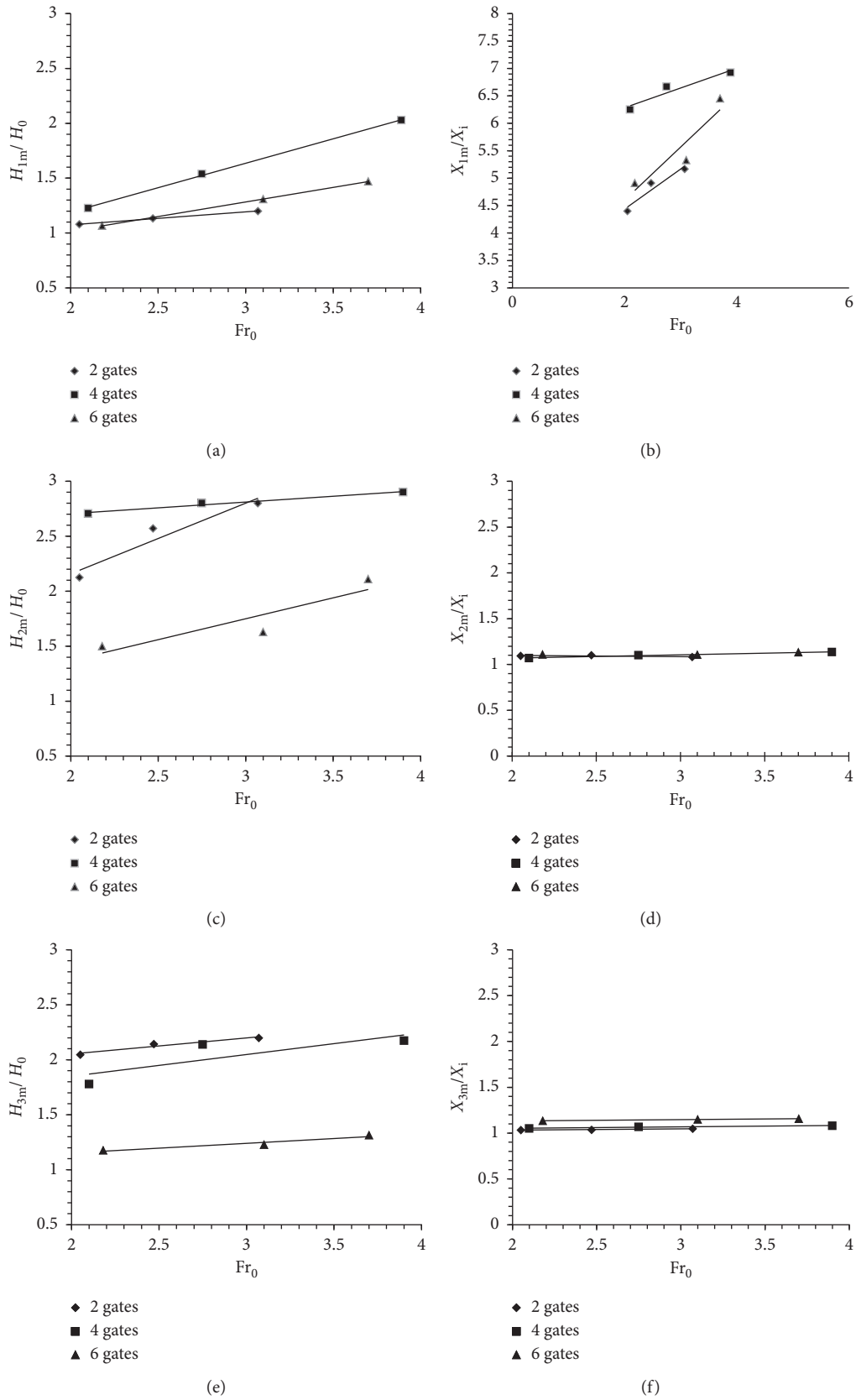
FIGURE 15: Dimensionless curves of maximum height variation and their formation location in terms of the Froude number for different gate performances.

$$\alpha/\alpha_{min} = -0.426\,Fr_0 + 2.53$$
$$R^2 = 0.536$$
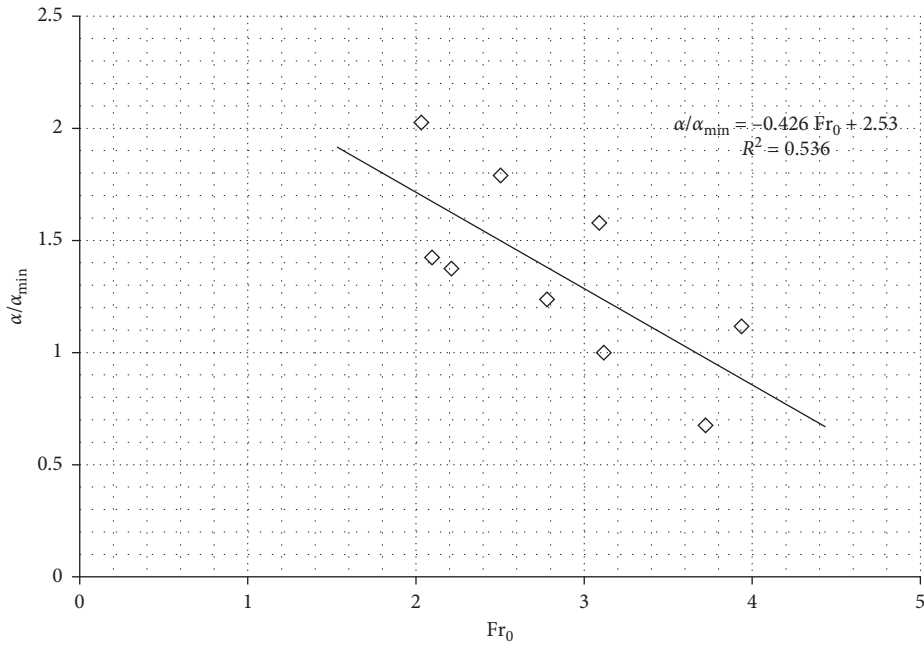
FIGURE 16: Dimensionless curves of the wave formation angle variation in terms of the Froude number.

100% ($Q = 230.36$, Fr = 2.19)
60% ($Q = 187.52$, Fr = 2.92)
30% ($Q = 146.38$, Fr = 3.62)
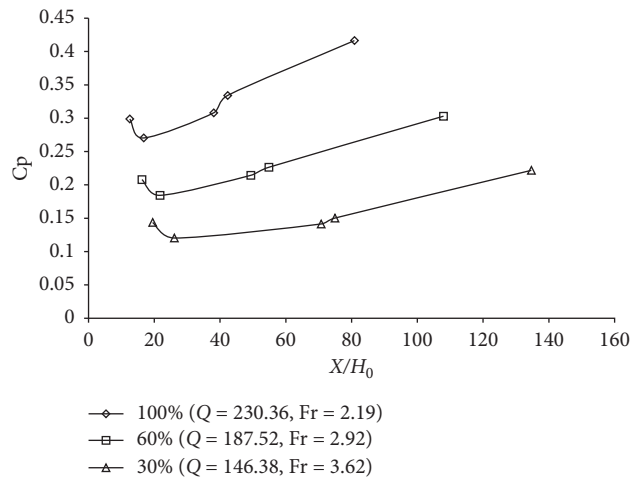
FIGURE 17: Piezometric pressure head distribution of triple waves for the performance of six middle gates' operation.

100% ($Q = 198.95$, Fr = 2.4)
60% ($Q = 162.28$, Fr = 2.96)
30% ($Q = 146.38$, Fr = 3.62)
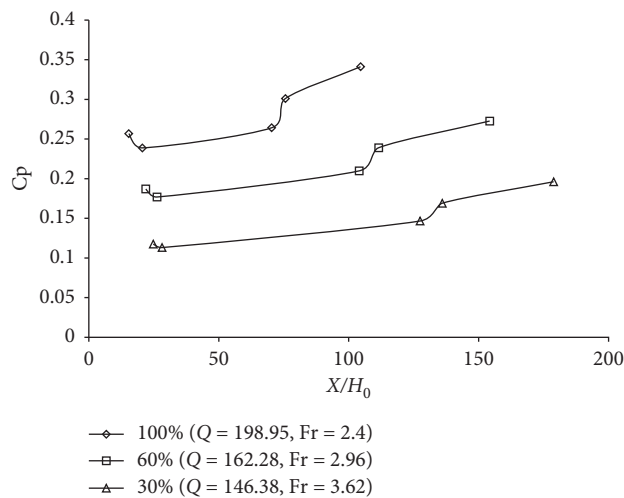
FIGURE 18: Piezometric pressure head distribution of triple waves for the performance of four middle gates' operation.

Figure 19: Separation of wave 2 from the main core of water flow.

4. Conclusion

At the downstream of the gates or bridge over the chute spillway, the supercritical flow generates standing waves, named shockwaves or rooster tail waves. The shockwaves' flow influences the flow field and hydraulic condition over the spillway as well as damages the walls of the spillway. Hydraulic flow conditions include the transverse and longitudinal distribution of velocity, pressure, and momentum, which can affect the hydraulic performance of the spillway structure, its structural design, and its dimensions and size. They were studied in three categories of waves 1, 2, and 3. Wave formation on the chute wall is also noteworthy because of its effect on the design process.

As the Froude number increases, the length of waves at the walls becomes longer, the wave height becomes shorter, and the waves are thinner. The maximum end sections of the wave are transmitted downstream. As the Froude number increases, the waves 1 and 2 become thinner while the waves get broader as the Froude number decreases. Wave 2 or spillway middle flow is higher than the other two waves. Next, wave 3 is higher than wave 1. Wave 2 is created over a broader range of the spillway. The wave at the spillway wall is a shockwave that exerts noticeable dynamic pressure on the chute sidewall. In this regard, the wave height can be bigger than the chute wall height. The height of all waves and their longitudinal coordinates represent a linear trend in terms of Froude numbers. Wave 1 has the highest while wave 2 has the least variation relative to the Froude number. By reducing the opening of the gates and consequently increasing the Froude number, the piezometric pressure decreases. At a fixed opening for each of the gate performance modes, the piezometric pressure of wave 3 is higher than the rest. The piezometric pressure of wave 2 is similarly higher than wave 1.

Data Availability

All the data used to support the findings of this study are included within the article.

Conflicts of Interest

The authors declare that they have no conflicts of interest.

References

[1] J. Lucas, W. H. Hager, and R. M. Boes, "Deflector effect on chute flow," *Journal of Hydraulic Engineering*, vol. 139, no. 4, pp. 444–449, 2013.

[2] K. W. Frizell, F. M. RennSa, and J. Matos, "Cavitation potential of flow on stepped spillways," *Journal of Hydraulic Engineering*, vol. 139, no. 6, pp. 630–636, 2013.

[3] M. Pfister, J. Lucas, and W. H. Hager, "Chute aerators: preaerated approach flow," *Journal of Hydraulic Engineering*, vol. 137, no. 11, pp. 1452–1461, 2011.

[4] P. Novak, A. I. B. Moffat, C. Nalluri, and R. Narayanan, *Hydraulic Structures*, Springer, Berlin, Germany, 4th edition, 2007.

[5] P. F. Borowski, "New technologies and innovative solutions in the development strategies of energy enterprises," *HighTech and Innovation Journal*, vol. 1, no. 2, pp. 39–58, 2020.

[6] K.-H. Lee, "Simulation of dam-breach outflow hydrographs using water level variations," *Water Resources Management*, vol. 33, no. 11, pp. 3781–3797, 2019.

[7] E. Eghlidi, G. A. Barani, and K. Qaderi, "Laboratory investigation of stilling basin slope effect on bed scour at downstream of stepped spillway: physical modeling of javeh RCC dam," *Water Resources Management*, vol. 34, pp. 1–14, 2019.

[8] N. J. H. Al-Mansori, N. J. Hussien, T. J. Mizhir Alfatlawi, T. J. M. Alfatlawi, and K. S. Hashim, "effects of different shaped baffle blocks on the energy dissipation," *Civil Engineering Journal*, vol. 6, no. 5, pp. 961–973, 2020.

[9] J. Al-Zubaidi, P. Teng, and H. Zhang, "Experiments and CFD modeling of high-velocity two-phase flows in a large chute aerator facility," *Engineering Applications of Computational Fluid Mechanics*, vol. 13, no. 1, pp. 48–66, 2019.

[10] M. Samadi, E. Jabbari, H. M. Azamathulla, and M. Mojallal, "Estimation of scour depth below free overfall spillways using multivariate adaptive regression splines and artificial neural networks," *Engineering Applications of Computational Fluid Mechanics*, vol. 9, no. 1, pp. 291–300, 2015.

[11] G. Sylvain and G. Claire-Eleuthèriane, "Overcoming the obstacle of time-dependent model output for statistical analysis by nonlinear methods," *HighTech and Innovation Journal*, vol. 2, no. 1, pp. 1–8, 2020.

[12] K. Khalifehei, G. Azizyan, M. Shafai-Bajestan, and K. W. Chau, "Experimental modeling and evaluation sediment scouring in riverbeds around downstream in flip buckets," *International Journal of Engineering*, vol. 33, no. 10, pp. 1904–1916, 2020.

[13] K. Khalifehei, G. Azizyan, M. Shafai-Bajestan, and K. W. Chau, "Stability of A-Jack concrete block armors protecting the riverbeds," *Ain Shams Engineering Journal*, In Press, 2020.

[14] M. Karalar and M. Cavusli, "Seismic effects of epicenter distance of earthquake on 3D damage performance of CG dams," *Earthquakes and Structures*, vol. 18, no. 2, pp. 201–213, 2020.

[15] M. Karalar and M. Çavuşli, "Effect of normal and shear interaction stiffnesses on three-dimensional viscoplastic creep behaviour of a CFR dam," *Advances in Civil Engineering*, vol. 2018, Article ID 2491652, 17 pages, 2018.

[16] H. Xue, M. Diao, Q. Ma, and H. Sun, "Hydraulic characteristics and reduction measure for rooster tails behind spillway piers," *Arabian Journal for Science and Engineering*, vol. 43, no. 10, pp. 5597–5604, 2018.

[17] V. H. Vayghan, M. Mohammadi, and A. Ranjbar, "Experimental study of the rooster tail jump and end sill in horseshoe

spillways," *Civil Engineering Journal*, vol. 5, no. 4, pp. 871–880, 2019.

[18] S. Jung, S. Peetz, and M. Koch, "Poeam - a method for the Part Orientation evaluation for additive manufacturing," *HighTech and Innovation Journal*, vol. 1, no. 1, pp. 21–27, 2020.

[19] R. Reinauer and W. H. Hager, "Supercritical flow behind chute piers," *Journal of Hydraulic Engineering*, vol. 120, no. 11, pp. 1292–1308, 1994.

[20] F. B. Becerro, "Phraseological variations in medical-pharmaceutical terminology and its applications for English and German into Spanish translations," *SciMedicine Journal*, vol. 2, no. 1, pp. 22–29, 2020.

[21] M. G. Mooselu, M. R. Nikoo, N. B. Rayani, and A. Izady, "Fuzzy multi-objective simulation-optimization of stepped spillways considering flood uncertainty," *Water Resources Management*, vol. 33, no. 7, pp. 2261–2275, 2019.

[22] R. Reinauer and W. H. Hager, "Pier waves in sloping chutes," *International Journal on Hydropower & Dams*, vol. 4, no. 3, pp. 100–103, 1997.

[23] R. Reinauer and W. H. Hager, "Supercritical flow in chute contraction," *Journal of Hydraulic Engineering*, vol. 124, no. 1, pp. 55–64, 1998.

[24] B. A. Parate, "Propellant actuated device for parachute deployment during seat ejection for an aircraft application," *HighTech and Innovation Journal*, vol. 1, no. 3, pp. 112–120, 2020.

[25] W. H. Hager and A. J. Schleiss, *Constructions Hydrauliques*, Presses Polytechniques Et Universitaires Romandes (PPUR), Lausanne, Switzerland, 2009.

[26] O. A. Yamini, M. R. Kavianpour, and A. Movahedi, "Pressure distribution on the bed of the compound flip buckets," *The Journal of Computational Multiphase Flows*, vol. 7, no. 3, pp. 181–194, 2015.

[27] S. Pagliara, S. M. Kurdistani, and T. Roshni, "Rooster tail wave hydraulics of chutes," *Journal of Hydraulic Engineering*, vol. 137, no. 9, pp. 1085–1088, 2011.

[28] K. Ha, "Innovative blade trailing edge flap design concept using flexible torsion bar and worm drive," *HighTech and Innovation Journal*, vol. 1, no. 3, pp. 101–106, 2020.

[29] J.-H. Wu, D. Li, F. Ma, and S.-T. Qian, "Fin characteristics of aerator devices with lateral deflectors," *Journal of Hydrodynamics*, vol. 25, no. 2, pp. 258–263, 2013.

[30] W. J. Duan, "The submerged sloping-tail pier—an effective measure to eliminate the crown of jumping flow," *Journal of Sichuan University: Engineering Science Edition's*, vol. 1, pp. 63–67, 1982, in Chinese.

[31] J.-H. Wu and Z.-M. Yan, "Hydraulic characteristics of bottom underlay-type pier for water-wing control," *Journal of Hydrodynamics*, vol. 20, no. 6, pp. 735–740, 2008.

[32] T. Smajdorová and D. Noskievičová, "Methodology for the application of nonparametric control charts into practice," *Emerging Science Journal*, vol. 4, no. 4, pp. 272–282, 2020.

[33] G. Mihajlović and M. Živković, "Sieving extremely wet earth mass by means of oscillatory transporting platform," *Emerging Science Journal*, vol. 4, no. 3, 2020.

[34] A. R. Sengupta, R. Gupta, and A. Biswas, "Computational fluid dynamics analysis of stove systems for cooking and drying of muga silk," *Emerging Science Journal*, vol. 3, no. 5, pp. 285–292, 2019.

[35] S. R. Alavi, E. N. Lay, and Z. A. Makhmali, "A CFD study of industrial double-cyclone in HDPE drying process," *Emerging Science Journal*, vol. 2, no. 1, pp. 31–38, 2018.

[36] S. Ghods, A. Kheyroddin, M. Nazeryan, and S. M. Mirtaheri, "Nonlinear behavior of connections in RCS frames with bracing and steel plate shear wall," *Steel and Composite Structures*, vol. 22, no. 4, pp. 915–935, 2016.

[37] R. Roshan, "Report of Kheirabad Dam Overflow Performance System," *Ministry of Water Research Institute*, WRI publisher, Iran, Tehran, 2019.

[38] M. R. Kavianpour, R. Roshan, and M. R. Najafi, "Controlling rooster tail development in gated tunnels," *International Journal on Hydropower & Dams*, vol. 20, no. 1, pp. 60–65, 2013.

[39] S. A. Hughes, "Physical models and laboratory techniques in coastal engineering," *World Scientific*, vol. 7, 1993.

[40] O. A. Yamini, S. H. Mousavi, and M. R. Kavianpour, "Experimental investigation of using geo-textile filter layer in articulated concrete block mattress revetment on coastal embankment," *Journal of Ocean Engineering and Marine Energy*, vol. 5, no. 2, pp. 119–133, 2019.

[41] O. A. Yamini, M. R. Kavianpour, and S. H. Mousavi, "Wave run-up and rundown on ACB Mats under granular and geotextile filters' condition," *Marine Georesources & Geotechnology*, vol. 36, no. 8, pp. 895–906, 2018.

[42] S.-R. Sabbagh-Yazdi and M. Bavandpour, "Numerical experiments on using incline collar rings for controlling mean and fluctuating forces on circular bridge piers," *Journal of Fluids and Structures*, vol. 91, Article ID 102696, 2019.

[43] M. Hambardzumyan and A. Hayrapetyan, "Differential diagnosis of malignant melanoma and benign cutaneous lesions by ultrasound analysis," *SciMedicine Journal*, vol. 2, no. 2, pp. 100–107, 2020.

[44] R. Reinauer and W. H. Hager, "Shockwave in air-water flows," *International Journal of Multiphase Flow*, vol. 22, no. 6, pp. 1255–1263, 1996.

[45] V. H. Vayghan, A. Saber, and S. Mortazavian, "Modification of classical horseshoe spillways: experimental study and design optimization," *Civil Engineering Journal*, vol. 5, no. 10, pp. 2093–2109, 2019.

Research Article

Investigation of Mechanical Properties of Concrete Containing Liquid Silicone Rubber Under Axial Loads

Alireza Khaloo [ID][1] **and Yaser Parvin darabad** [ID][2]

[1]*Civil Engineering Department, Sharif University of Technology, Center of Excellence in Structures and Earthquake Engineering, Tehran, Iran*
[2]*Sharif University of Technology, International Campus, Kish Island, Iran*

Correspondence should be addressed to Alireza Khaloo; khaloo@sharif.edu

As the experts who have taken for granted the merits of utilizing the concrete as the most common material in the structural industry, there is a need to take affirmative steps to enhance the concrete's weaknesses such as the low ductility and energy absorption capacity. One possible way to improve the mechanical properties of concrete is to add liquid silicone rubber to the concrete. Silicone rubber is an elastomer (rubber-like material) composed of liquid rubber polymer and its hardener which is widely used in voltage line insulators, automotive applications, and medical devices. In order to increase the ductility and energy absorption of concrete, the liquid silicone rubber replaced a portion of mineral aggregates in concrete. HSRC (hybrid silicone rubber concrete) is a mixture of liquid silicone rubber with fresh concrete that liquid silicone rubber after 24 hours becomes a flexible solid rubber with low strength. In this paper, liquid silicone rubber was used to replace 0%, 2%, 4%, 8%, 12.5%, 25%, and 50% of the total mineral aggregate's volume in concrete. Standard specimens were fabricated and tested. The fresh HSRC exhibited acceptable workability and lower unit weight compared to ordinary plain concrete. The uniaxial compressive strain-control test was conducted on the hardened HSRC specimens to obtain the complete stress-strain curve. The results showed that, with the increase of liquid silicone rubber in concrete, the amount of compressive strength, splitting tensile stress, and elastic modulus decreased. It was also observed that the percentage of reduction in compressive strength was greater than the percentage of reduction in tensile strength. Increasing silicone rubber concentration in HSRC changes the brittle mode of failure to ductile that demonstrated using nonlinearity indices. Unlike plain concrete, the failure state in HSRC occurs gently and uniformly and does not cause so much separation in the specimens. Larger deformation and higher toughness indices were obtained, when the silicone rubber concentration was increased.

1. Introduction

Silicone rubber is a widely used polymer and it is more specifically categorized as an elastomer or a rubber-like material. It is highly valued in various industries due to its chemical and mechanical resistance and stability in extreme environments. Silicone-based elastomers were first used in the 1940s in Corning Glass and General Electric because of their heat-resistant properties [1]. The simplicity of making and shaping of this material comes from the use of liquid silicone rubber, a two-part thermoset elastomer [2]. By separating the material into two parts, the uncured material takes on gel-like properties. This gel can be molded into the desired shape before it is catalyzed or cured, after which it turns into its final solid form. There are many applications for silicone rubber, including the automotive, health, medical, electrical, and other industries. Room temperature vulcanizing (RTV) silicone rubber coatings were used as electrical insulators to ameliorate their pursuant insulation strength, especially under wet conditions [3]. The use of new materials in the construction industry and maintaining the appropriate structural and architectural performance is of great functional importance [4]. Many advances have been made in creative technology in the construction industry

and the role of ethics for sustainable development is undeniable [5]. In previous research, the effect of replacing mineral aggregates with tire-rubber particles on the properties of concrete was experimentally investigated [6]. The study revealed that the brittle nature of concrete and its low toughness was improved; however, the ultimate strength was decreased significantly. In the present study, liquid silicone rubber was used to replace mineral aggregate. Previous investigations showed the use of waste tires could improve the properties of concrete. The idea of using waste rubber as an engineering material to improve concrete properties was introduced by (Eldin and Senouci) [7]. They used tire chips and crumb rubber as aggregate in plain concrete. Investigation showed that using particle rubber instead of part of mineral aggregate causes plastic failure, more ductility, and lower compressive strength in concrete compare to control portland cement concrete. Khatib and Bayomy studied rubberized concrete using two types of tire rubber, fine crumb rubber, and coarse tire chips. Specimens were tested under compressive and flexural loads. Also, a characteristic function that quantifies the reduction in strength was developed and sensitivity analysis was performed [8]. Guoqiang Li et al. used waste tires in the form of fibers with various aspect ratios, in which waste tire was treated by Na(OH) before being used in concrete [9]. The recycled tire is also used in the construction of asphalt procedures and has a positive effect on its performance [10]. In other research, natural materials have been used as additives to concrete, and the structural character of deep beams made of reinforced palm kernel concrete (PKSC) was investigated by Mark Adom-Asamoah et al. [11]. The result showed that calibrated shear strength models revealed the compressive strength and the ratio of the shear span-to-total depth as significant influential parameters for correcting the inherent bias in the original deterministic shear strength models. An experimental study on the behavior of rubberized concrete mixes was conducted by Kadhim and Al-Mutairee in this research; waste tire-rubber particles were used to replace part of aggregate [12]. The static and dynamic behavior of recycled tire-rubber particle and polypropylene fibers filled concrete were investigated by Hernandez-Olivares et al. [13]. Siddiquel and Naik studied an overview of the use of scraptires in portland cement concrete [14]. Dessouki et al. studied the composites, based on Portland cement and natural rubber latex. They investigated the effective factors in the production of composite specimens such as the concentration of each component, additives incorporation, and the effect of retarding agents like sodium metasilicate. Adding retarding agent to the rubber latex increased time for molding, with no effect on the cement. The experimental result revealed that the rise in rubber latex concentration decreases compressive strength and increases tensile strength. It is concluded that cement-natural rubber molds can be used as a filling material for joints, cracks, and soil injection [15]. Toutanji studied the effect of replacement of mineral coarse aggregate with tire-rubber particle. The result showed that adding tire-rubber chips in concrete caused a reduction in compressive and flexural strengths. The compressive strength reduction was approximate twice the

reduction of flexural strength. Test results revealed that specimens containing tire-rubber chips presented higher toughness and ductile failure compared to control specimens [16]. Topcu, I.B., studied the mechanical properties of rubberized concrete in terms of both size and amount of the rubber chips changes. Concrete specimens with C20 compressive strength were produced and rubbers with volume ratios of 15, 30, and 45% were added to the concrete. Tests were conducted at 28 days, and σ-ε diagrams were obtained. It was shown that plastic energy capacity began to increase when rubber chips were added to the concrete. Rubberized concrete due to its high plastic energy capacity presented higher strains compared to plain concrete [17]. Segre and Joekes investigated the mechanical properties of rubberized concretes with and without silica fume. The research concluded that a large reduction in strength and elastic modulus values resulted when rubber content is increased. Adding the silica fume into the concrete mixture improved the mechanical properties of the rubberized concretes and decreased the strength loss. Previous findings show that the properties of concrete containing tire-rubber particles are affected by type, size, content, shape, and the procedure of mixing the rubber into the concrete [18]. The comparative study on the flexural behavior of rubberized reinforced concrete beams conducted by Alasmari et al. revealed an ameliorated performance with the use of the hybrid beams [19]. The effect of using waste tire rubber and nanomaterial in the construction of concrete curbs has been studied by Komaki et al. The results showed a positive effect on durability and abrasion resistance [20]. In this research study, hybrid silicone rubber concrete (HSRC) properties using mechanical tests on the different percent of liquid silicone rubber to the total mineral aggregate's volume in concrete at different ages are investigated. The experimental observations and subsequent explanations of HSRC behavior under compressive loading are presented. HSRC is expected to have high flexibility. Flexible materials are widely used in industry [21]. Flexibility has a great impact on the behavior of structures and improves their seismic performance in both steel and RC structures [22].

2. Experimental Program

In order to study the mechanical properties of HSRC, specimens of a cylindrical shape (15×30 cm) were fabricated and tested. These specimens were different in the content of liquid silicone rubber as a portion of total aggregates in concrete.

2.1. Materials. Constituent materials for concrete mixes included type II Portland cement corresponding to ASTM C150 [23] requirements, gravel with a maximum size of 19 mm as coarse aggregate, sand with 4.75 mm maximum size as fine aggregate, and liquid silicone rubber RTV. The word RTV is abbreviated from the three words "room temperature vulcanizing." Generally, silicone rubber is used for molding and sculpting. The liquid silicone rubber RTV contains two parts, One part is liquid silicone rubber, and

the other is hardener. After combining these two parts together, the resulting mixture turns into solid silicone rubber after 18 to 24 hours. The hardener should be used according to the manufacturer's instructions. In this study, liquid silicone rubber produced by JINGYI Company was used. Silicone rubber specifications are summarized in Table 1. These specifications are based on the factory test. The properties of fine and coarse aggregates were determined according to ASTM C127, 128, 129 standard test methods. Gradation curves of sand and gravel aggregates are presented in Figure 1. The properties of aggregates are presented in Table 2. The specific gravity of the Portland cement type II was 3.17 g.cm^3.

2.2. Concrete Specimens Mixtures and Manufacturing.

The experimental setup and specimen mix design content are summarized in Tables 3 and 4, respectively. In order to evaluate the effect of the amount of liquid silicone rubber on the properties of concrete in low and high volume values, the range of mineral aggregates replacement was considered between 0 and 50% by the total volume of aggregates. Also to study the process of increasing the amount of silicone rubber and its effect on the mechanical properties of concrete, the percentages of liquid silicone rubber volume to the total mineral aggregate volume include 0, 2, 4, 8, 12.5, 25, and 50 percent. The weight of fine and coarse aggregates was adjusted by the percentage of silicone rubber replacements. A normal Portland cement concrete, with a 35 MPa targeted compressive strength, was designed as the control mix following ACI standard 211.1–81 [24]. The water to cement ratio is considered to be 0.4 and two values for gravel to sand ratio of 1.1 and 0.7 are utilized. Polycarboxylate based superplasticizer was used to increase workability. Specimens were remolded 24 hours after casting and then cured in water until 24 hours before testing. Increasing the amount of sand in concrete improves the mechanical properties of fiber-reinforced concrete [25]. To determine the influence of G/S (gravel to sand ratio) changes on the mechanical properties of HSRC, two ratios of G/S = 0.7 and 1.1 were considered. Water absorption of aggregates before making specimens was considered in the concrete mix design. Seven mix designs were used and the proportions are presented in Table 4. For the labeling of concrete specimens, in terms of the ratio of the coarse to fine aggregate, two concrete grades, LF (low mineral fine aggregate with G/S = 1.1) and HF (high mineral fine aggregate with G/S = 0.7), were used. Citing an example, the HF-G4S4 mixture indicates that liquid silicone rubber was replaced by 4% of coarse aggregate and 4% of fine aggregate of the volume using high sand content.

2.3. Test Methods.

To evaluate the characteristics of fresh HSRC, slump and unit weight were measured in accordance to ASTM C143 [26] and ASTM C138 [27], respectively. A compressive strain-control test was performed on hardened specimens to obtain the complete stress-strain curves. The test was conducted by a universal testing machine with 0.05 mm/sec rate of loading. Compressive tests were performed at 28 days and the test setup is shown in Figure 2. For all specimens, the tangential modulus of elasticity at 40% of the ultimate stress on the elastic region of the stress-strain diagrams was determined. Also, the splitting tensile strength of the HSRC specimens was determined on the cylindrical specimens (15×30 cm) according to ASTM C469.

3. Experimental Results and Discussion

3.1. Properties of Fresh Concrete.

The slump and unit weight of the fresh concrete with respect to silicone rubber content are presented in Figure 3. The workability of fresh concrete is affected by the interactions of liquid silicone rubber and mineral aggregates. As shown in Figure 3(a), the slump of the specimens decreased when liquid silicone rubber content is increased. LF specimens exhibited a lower slump compared to those of HF specimens with the same silicone rubber concentration. The test result revealed that the fresh HSRC with liquid silicone rubber content up to 50% exhibits acceptable workability in terms of fabricating, placement, and finishing. As shown in Figure 3(b), the unit weight of the HSRC reduced from 2390 to 2070 kg·m^3, depending on the silicone rubber content.

3.2. Hardened Concrete Properties

3.2.1. Visual Observation of HSRC Specimen Behavior.

Duration to concrete failure is defined as failure duration [1]. In plain concrete, failure is abrupt and explosive; however, in HSRC specimen, failure duration is gradual and longer, and also failure is not explosive because HSRC becomes flexible by the addition of silicone rubber content. As shown in Figure 4, white color particles are silicone rubber, which are relatively well distributed in concrete. Figures 5 and 6 show that the stress-strain curves of HSRC specimens withstand loads beyond the peak load like flexible materials that are referred to as postpeak strength. The failure state in control specimens (without silicone rubber) was abrupt with loud sound and the failure state is accompanied by separation of pieces from the specimens. HSRC specimen failure state was accompanied by less separation of pieces from the specimen compared to control concrete specimen; as shown in Figure 7, the failure state was not explosive. HSRC specimens exhibited large deformations compared to control specimens and cracks propagated relatively uniformly and gradually in HSRC specimens. Well propagated cracks and dispersed failures for HSRC specimens were observed in comparison with plain concrete. As shown in Figure 3, the particle of silicone rubber particles distributed in concrete is clearly visible.

The lateral deformations of HSRC specimens are larger than those of plain concrete specimens because of the porosity due to the substitution of silicone rubber with mineral aggregate and also due to higher Poisson's ratio of HSRC than that for plain concrete. It should be noted that the behavior of HSRC is not perfectly elastic, since Poisson's ratio is not constant for the concrete composite during ascending loading process. Poisson's ratio increases as the silicone rubber content is increased and the behavior of HSRC tends to behave as a plastic material. As shown in

TABLE 1: Silicone rubber specifications.

Property	Minimum value	Maximum value	SI unit
Atomic volume (average)	0.0035	0.0055	$m^3 \cdot kmol$
Density	1.1	2.3	$Mg \cdot m^3$
Bulk modulus	1.5	2	GPa
Compressive strength	10	30	MPa
Elastic limit	2.4	5.5	MPa
Endurance limit	2.28	5.23	MPa
Fracture toughness	0.03	0.7	$MPa \cdot m^{1.2}$
Modulus of rupture	2.4	5.5	MPa
Poisson's ratio	0.47	0.49	
Shear modulus	0.0003	0.02	GPa
Tensile strength	2.4	5.5	MPa
Young's modulus	0.001	0.05	GPa
Glass temperature	150	200	K
Maximum service temperature	500	560	K
Minimum service temperature	200	225	K
Specific heat	1050	1300	$J \cdot kg \cdot K$
Thermal conductivity	0.2	2.55	$W \cdot m \cdot K$
Thermal expansion	250	300	$10^{-6} \cdot K$
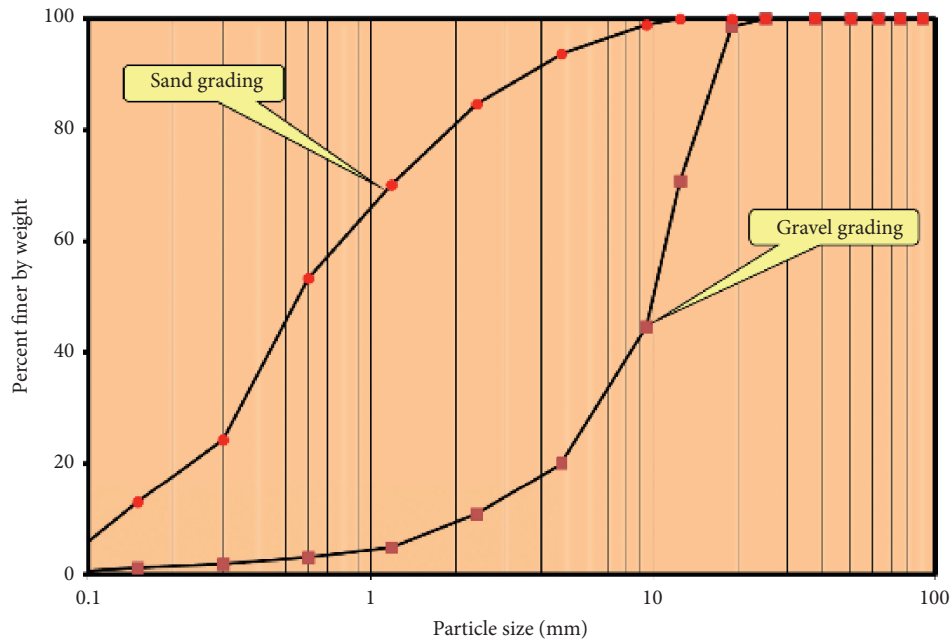
FIGURE 1: Gradation of mineral aggregates.

TABLE 2: Properties of aggregates.

Aggregate type	Specific gravity	Water absorption (%)	Fineness modulus	Unit weight ($kg \cdot m^3$)
Coarse aggregate	2.63	2.69	NA	1709.6
Fine aggregate	2.69	5.16	4.38	1729

Figure 5, considerable lateral deformations were observed in HSRC specimens at the end of the loading process.

3.2.2. Stress-Strain Response. The stress-strain curves of HSRC specimens with different mixtures and various concentrations of silicone rubber are shown in Figures 6–8.

The curves indicate that the HSRC specimens are more ductile compared to those for plain concrete specimens. The behavior of LF-G25S25, HF-G25S25, LF-G50S50, and HF-G50S50 specimens is like the nonlinear material and post-peak strength is clearly visible. To compare the nonlinearity between HSRC specimens and control specimens, the nonlinearity index was expressed as the ratio of the slope of

TABLE 3: Experimental program.

Specimen designation	Liquid silicone rubber content (%) by total aggregates	Fine aggregate (%)	Coarse aggregate (%)	Superplasticizer to cement ratio (%)	Replicates of compressive test (at 28 days)
LF-G0S0	0	100	100	2	3
LF-G1S1	1	99	99	2	3
LF-G2S2	2	98	98	2	3
LF-G4S4	4	96	96	2	3
LF-G12.5S12.5	12.5	87.5	87.5	2	3
LF-G25S25	25	75	75	2	3
LF-G50S50	50	50	50	2	3
HF-G0S0	0	100	100	2	3
HF-G1S1	1	99	99	2	3
HF-G2S2	2	98	98	2	3
HF-G4S4	4	96	96	2	3
HF-G12.5S12.5	12.5	87.5	87.5	2	3
HF-G25S25	25	75	75	2	3
HF-G50S50	50	50	50	2	3

TABLE 4: Concrete mixture proportions.

Specimen	Water (lit)	Cement (kg/m^3)	Gravel. Sand G/S	Liquid silicone rubber (kg/m^3)	Coarse aggregate (kg/m^3)	Fine aggregate (kg/m^3)	Moisture of gravel (%)	Moisture of sand (%)
LF-G0S0	224	350		0.00	942.86	857.14	3	4
LF-G1S1	231	350		12.67	933.43	848.57	3	3.2
LF-G2S2	240	350		25.34	924.00	840.00	2	3
LF-G4S4	204	350	1.1	50.69	905.14	822.86	4	5
LF-G12.5S12.5	216	350		158.40	825.00	750.00	3	4
LF-G25S25	187	350		316.79	707.14	642.86	5	5
LF-G50S50	184	350		633.59	471.43	428.57	4	4.5
HF-G0S0	218	350		0.00	741.16	1058.80	4	4
HF-G1S1	238	350		12.66	733.75	1048.21	4	1.3
HF-G2S2	240	350		25.31	726.34	1037.62	3.2	2
HF-G4S4	236	350	0.7	50.62	711.51	1016.45	3.2	2.3
HF-G12.5S12.5	226	350		158.19	648.52	926.45	3	3.1
HF-G25S25	224	350		316.39	555.87	794.10	2.1	3
HF-G50S50	204	350		632.77	370.58	529.40	2	2.5

FIGURE 2: Test setup.

the line connecting the origin to the point at 40% of ultimate stress on the stress-strain curve, to the slope of the line from the origin to the ultimate stress as shown in Figure 9(a). Based on the results presented in Figure 9(b), for both LF and HF specimens, it can be seen that, with increasing the amount of silicone rubber from 0 to 25%, nonlinearity index has an increasing trend, but with the increase in the amount of silicone rubber, the nonlinearity index has decreased by 25%. A comparison between the investigated mixtures indicates that the HF specimen's behavior is a little more
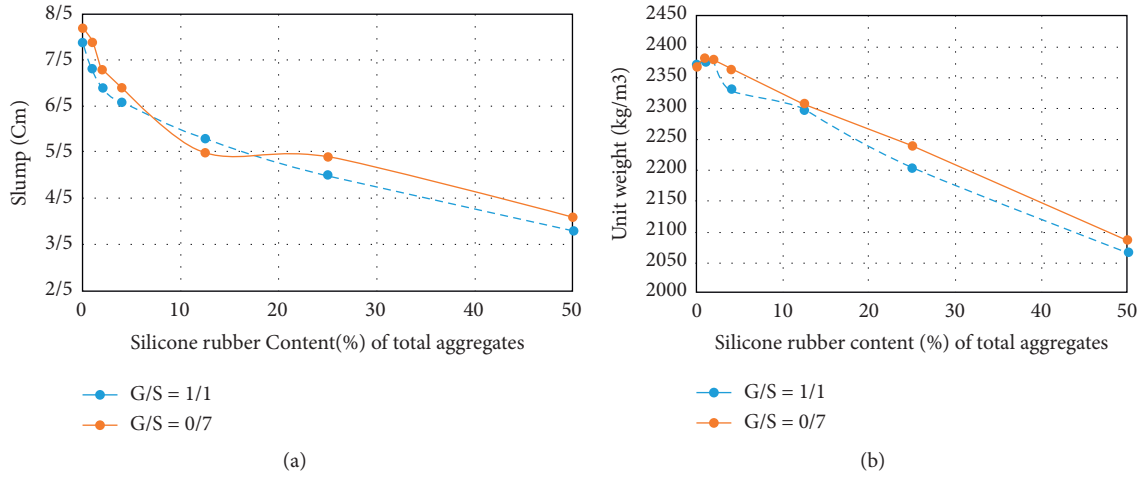
Figure 3: Properties of fresh HSRC. (a) Slump. (b) Unit weight of fresh HSRC.
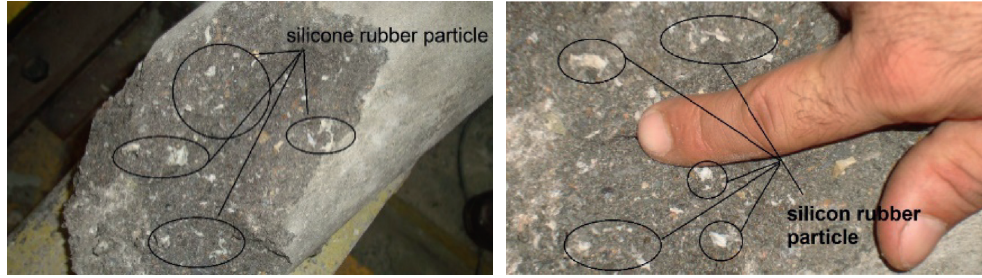
Figure 4: Silicone rubber particles distributed in HSRC specimens.

nonlinear compared to those for LF specimens with the same silicone rubber concentration. The substitution of silicone rubber for mineral aggregates caused more uniform crack development and crack propagation, compared to control specimens. The stress-strain curves indicated that HSRC specimens exhibit larger deformation compared to control specimens. In the stress-strain curve, the slope of the tangent line at the point that stress is 40% of the ultimate stress is expressed as E_t and obtained from the following equation:

$$E_t = \frac{d\sigma}{d\varepsilon} \text{ at 40\% of ultimate stress,} \tag{1}$$

where $d\sigma$ in and $d\varepsilon$ are stress and strain changes at the point that stress is 40% of the ultimate stress. E_t is a suitable factor to indicate the stiffness attributed to elastic deformation in HSRC specimens. E_t for different mixtures and silicone rubber concentrations are given in Table 5. A decrease in E_t for HSRC specimens implies larger deformations. A comparison of the results in Table 5 indicates that HF specimens result in higher E_t than LF specimens for the same silicone rubber concentration.

3.2.3. Compressive and Tensile Strengths.

As shown in Table 5, an increase in silicone rubber concentration of HSRC specimens decreased the ultimate compressive strength and tensile splitting strength. The maximum strength reduction for 50% silicone rubber replacement is 82% percent in average according to Table 5. As shown in Figure 10(a), the ultimate compressive and splitting tensile strength of HF specimens are more than those of LF specimens for the same silicone rubber concentration. While reducing ultimate strength, SHRC provides ductile behavior and failure in HSRC specimens.

3.2.4. Toughness of HSRC.

Toughness is the ability of the material to absorb energy by plastic deformation before rupturing. The toughness of HSRC was determined by calculating the area under the stress-strain curve up to a point corresponding to 80% of maximum stress in the postpeak region. The toughness index T_i, is expressed as the ratio of the area under the stress-strain curve up to 80% of the maximum stress in the postpeak region $T_{80\%}$, to the area

FIGURE 5: Stress-strain curve of HF specimens at 28 days. (a) Stress-strain diagrams of all HF specimens at 28 days. (b) Stress-strain diagrams of HF specimens with low content of silicone rubber at 28 days. (c) Stress-strain diagrams of HF specimens with a high content of silicone rubber at 28 days.

under the stress-strain curve up to the maximum stress $T_{100\%}$, as shown in Figure 11(a). Choosing 80% of maximum stress is due to the fact that strength reduced to this amount is an acceptable level of service load. The toughness index T_i is defined as follows:

$$T_i = \frac{\text{Area}\,(T_{80\%})}{\text{Area}\,(T_{100\%})}, \qquad (2)$$

where T_i for HSRC specimens with various concentrations of silicone rubber are presented in Figure 11(b). As shown in Figure 11(b), T_i showed an upward trend with an increase in silicone rubber concentration in concrete up to 25% and an amount of 50% silicone rubber concentration T_i showed a downward trend. Maximum T_i was obtained for LF-C25F25

and HF–C25F25 mixtures. Maximum T_i was obtained for specimen HF with 25% of silicone rubber concentration.

4. Reduction Factor (RF) for Hardened HSRC Specimens

The test results of HSRC specimens showed that the amount of silicone rubber content plays a decisive role in the mechanical property of this type of concrete. Therefore, by using the amount of rubber, a function can be extracted that expresses the properties of HSRC based on the percentage of silicone rubber content in the mixture. The RF function is defined as the ratio of the compressive or tensile strength and modulus of elasticity of silicone rubber-containing

(a)   (b)
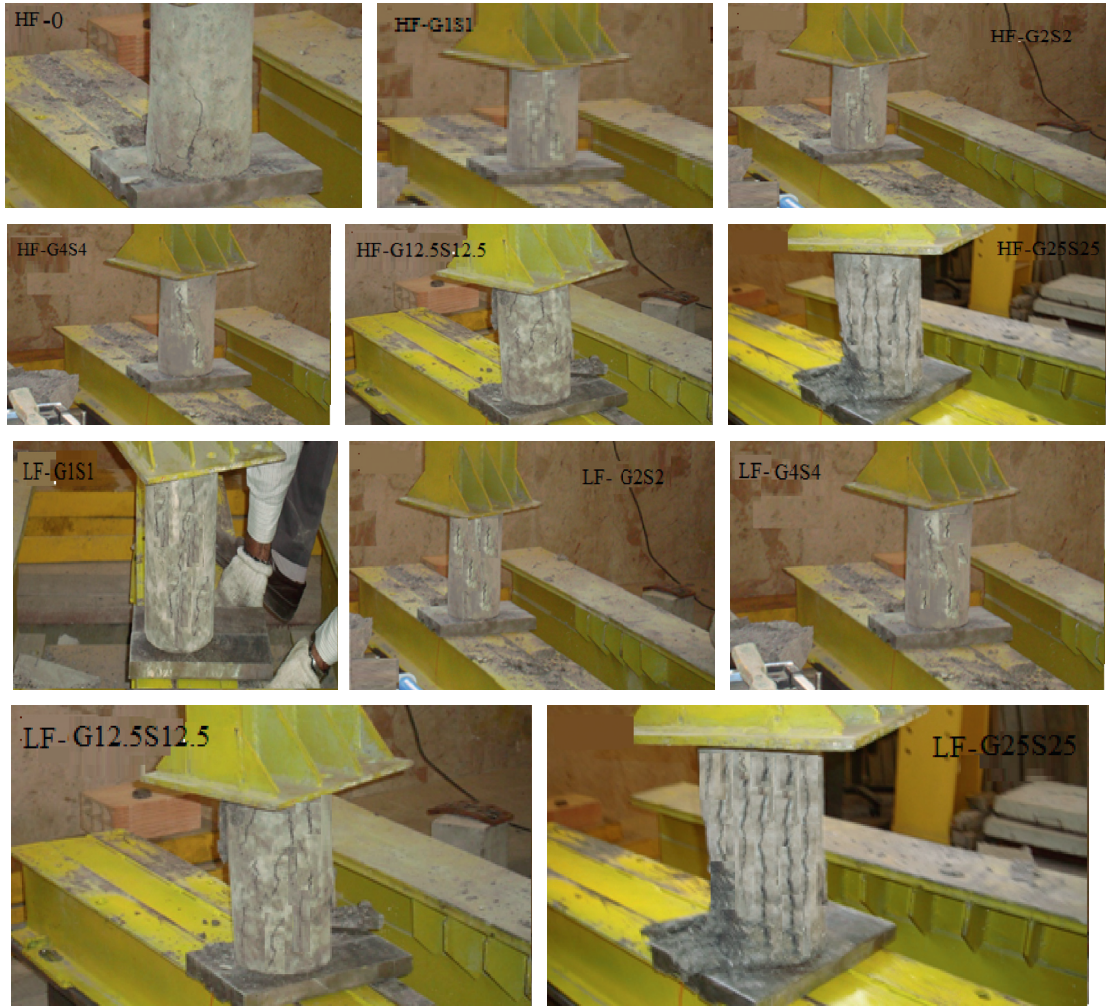

(c)

Figure 6: Stress-strain curve of LF specimens at 28 days. (a) Stress-strain diagrams of all LF specimens at 28 days. (b) Stress-strain diagrams of LF specimens with low content of silicone rubber at 28 days. (c) Stress-strain diagrams of LF specimens with a high content of silicone rubber at 28 days.

specimens to a silicone rubber-free control. When the goal is to determine the compressive or tensile strength of the specimen, the function is called the Fc-RF or Ft-RC, respectively, and if the goal is to determine the modulus of elasticity, it is called the Et-RF. The RF value will be 1 when the percentage of silicone rubber is zero (control specimen) and the value of RF decreases with increasing silicone rubber content. Based on similar studies performed on rubber concrete by Khatib and Bayomi (1999) [3], the following general formula is used to calculate the percentage of the reduction value:

$$\text{RF} = a + b\,(1 - R)^{m}. \tag{3}$$

RF is the reduction factor and RF will be equal to 1 when R is 0%. The following condition should be considered in the above equation:

$$a + b = 1. \tag{4}$$

The value of the RF varies between 1 and 0, and R is defined as rubber content in a volumetric ratio of total aggregate volume; also, a, b, m are numeric parameters. The Fc-RF function is introduced as the compressive strength reduction factor, and the Et-RF function is introduced as the elastic modules reduction factor. Numerical analysis was performed on the experimental data to obtain the parameters a, b, m and also the R-square test was used to check the

(a)

(b)

(c)
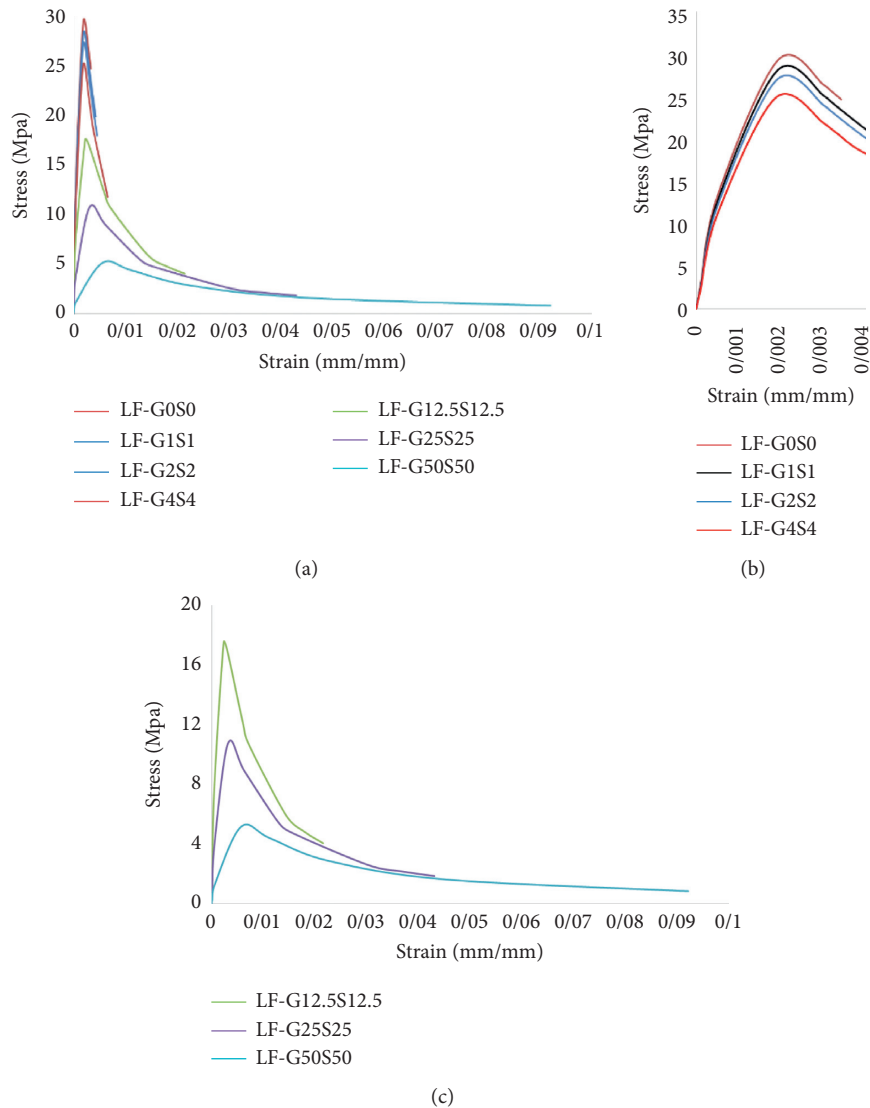
FIGURE 7: Failure types of HSRC specimens under compression test.

error rate of the extracted functions. The results are shown in Table 6. Comparison of the extracted RF-functions results and HSRC specimens test results is presented in Figure 12.

5. Conclusions and Recommendations

Increasing silicone rubber content in fresh HSRC specimens resulted in lower unit weights compared to control plain concrete. The workability of HSRC specimens was reduced by increasing liquid silicone rubber concentration. For maximum silicone rubber replacement of 50% by total volume of aggregates, HSRC provided acceptable workability. With increasing the amount of silicone rubber in concrete, a decrease in concrete strength was observed. There is an 83% reduction in compressive strength and 70% reduction in splitting tensile strength when the amount of silicone rubber is equal to 50% (LF-G50S50 and HF-G50S50). The nonlinearity indices and compressive toughness increased when silicone rubber concentration increased for all specimens up to 25% and nonlinearity indices and compressive toughness decreased for values greater than 25% silicone rubber. HSRC specimens exhibited more ductile behavior than plain concrete specimens under the compression load, the failure state in HSRC specimens is not brittle, and the failure does not occur suddenly like plain concrete. As the amount of silicone rubber in the specimens increased, the crushing of the specimens became slower and accompanied by less sound and the behavior became more ductile. To compare the effect of the fine to coarse aggregate ratio, it is worth mentioning that HF specimens (G/S = 0.7) exhibited greater compressive strength than LF (G/S = 1.1) specimens with the same total silicone rubber concentration. This suggests that compressive strength increases with increasing fine aggregates. These findings show that although the mechanical properties of HSRC are mainly dependent on the total rubber content, the ratio of coarse to fine particles can be used for behavior adjustment.
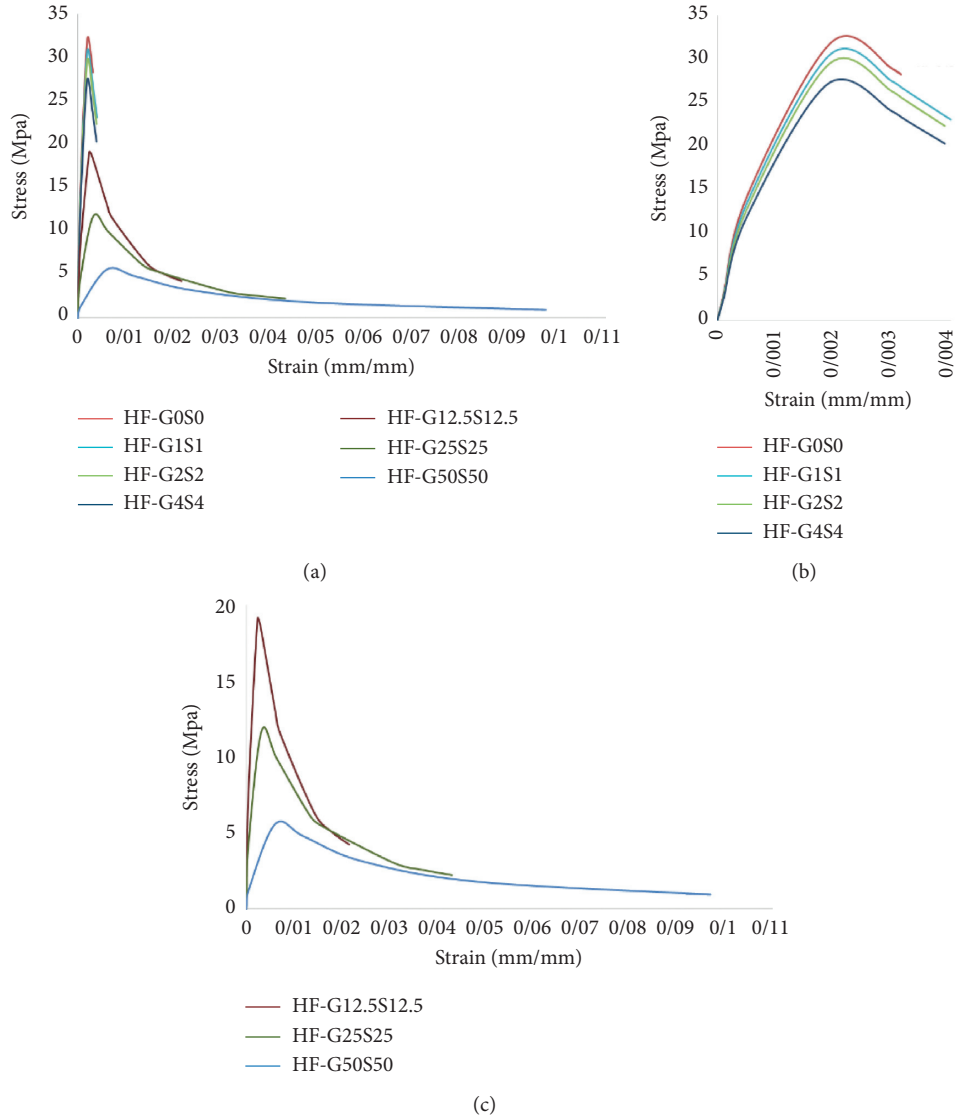
(a)

(b)

(c)
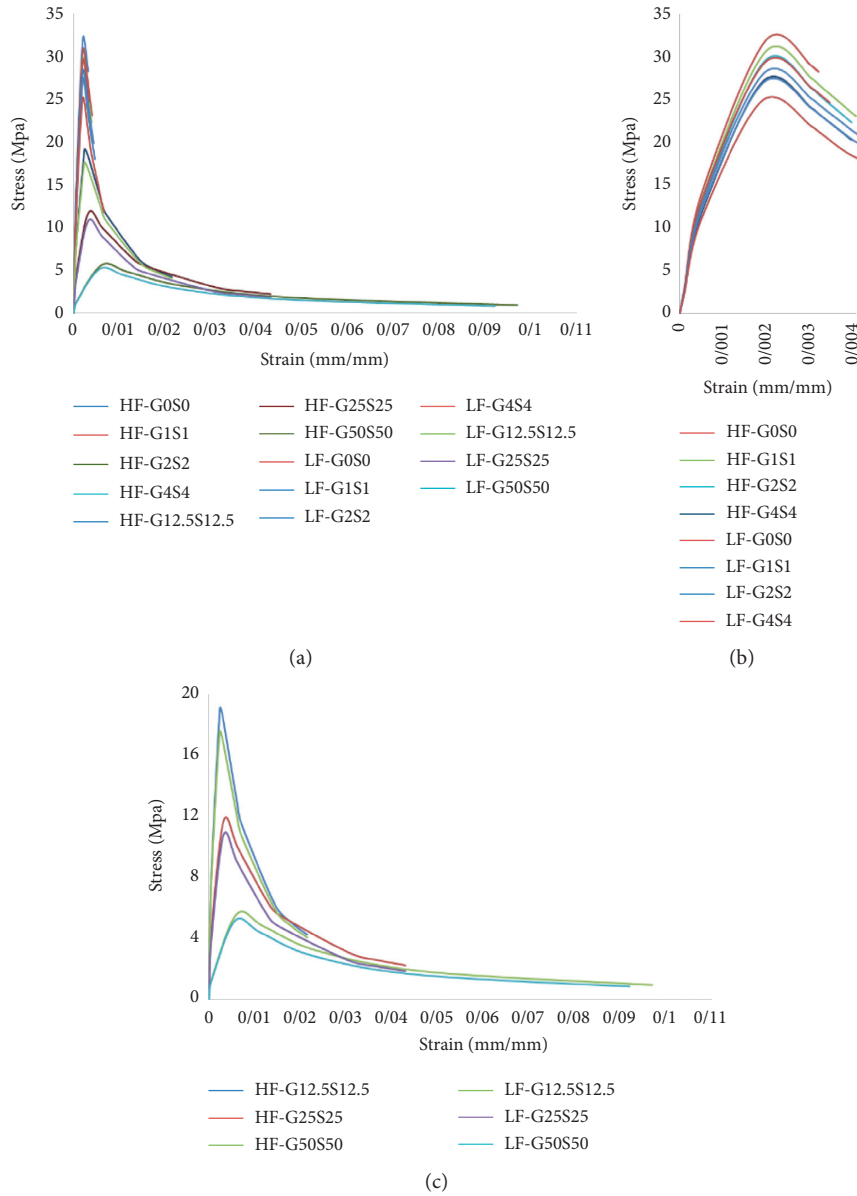
FIGURE 8: Stress-strain curve of HF&LF specimens at 28 days. (a) Stress-strain diagrams of all HF&LF specimens at 28 days. (b) Stress-strain diagrams of HF&LF specimens contain a low content of silicone rubber at 28 days. (c) Stress-strain diagrams of HF&LF specimens contain a high content of silicone rubber at 28 days.

(a)

(b)
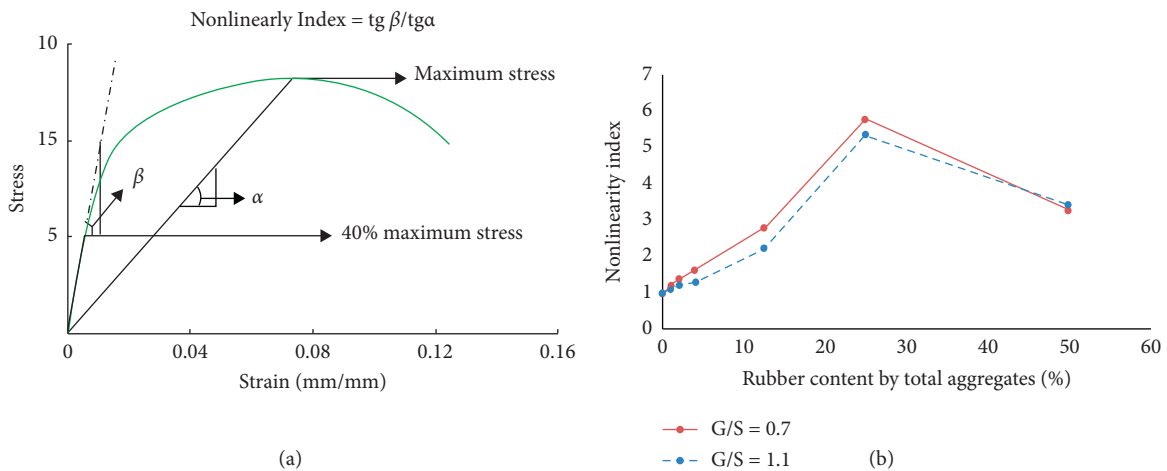
FIGURE 9: (a) Evaluation of nonlinearity index. (b) Nonlinearity index for HSRC specimens at 28 days.

TABLE 5: Maximum stress and tangential moduli of elasticity and tensile splitting stress for HSRC at 28 days.

Concrete mixture	Total rubber content (%)	Fc-max (MPa)	Et (GPa)	Ft-splitting (MPa)
LF-G0S0	0	29.35	2.67	2.90
LF-G1S1	1	28.14	2.52	2.79
LF-G2S2	2	27.02	2.39	2.59
LF-G4S4	4	24.86	2.18	2.52
LF-G12.5S12.5	12.5	17.52	1.69	1.84
LF-G25S25	25	10.70	0.84	1.39
LF-G50S50	50	5.19	0.25	0.84
HF-G0S0	0	32.00	2.80	3.64
HF-G1S1	1	30.58	2.63	3.40
HF-G2S2	2	29.53	2.44	3.13
HF-G4S4	4	27.22	2.27	2.98
HF-G12.5S12.5	12.5	19.16	1.67	2.29
HF-G25S25	25	11.70	0.99	1.78
HF-G50S50	50	5.64	0.27	1.09
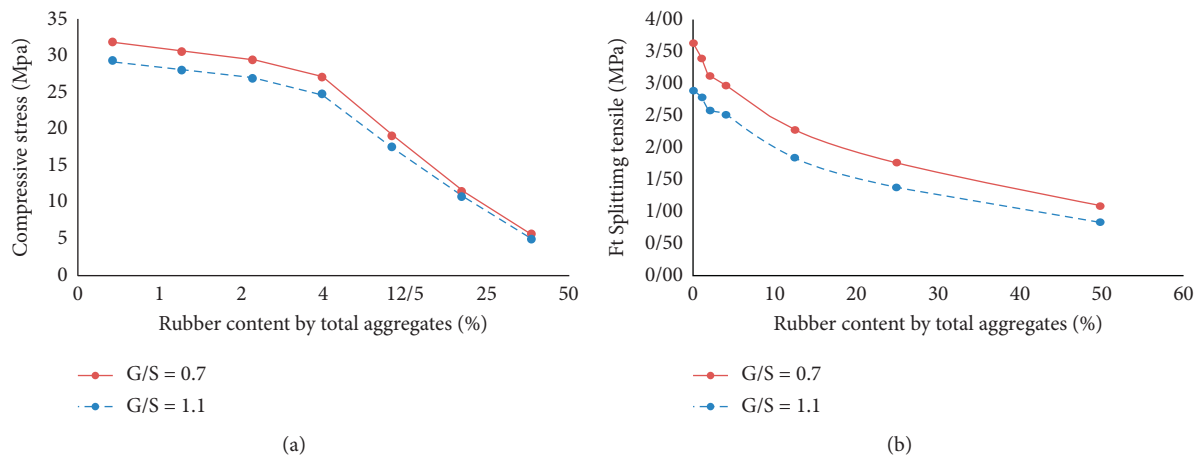
FIGURE 10: (a) Maximum compressive stress of HSRC specimens at 28 days. (b) Maximum tensile splitting stress of HSRC specimens at 28 days.
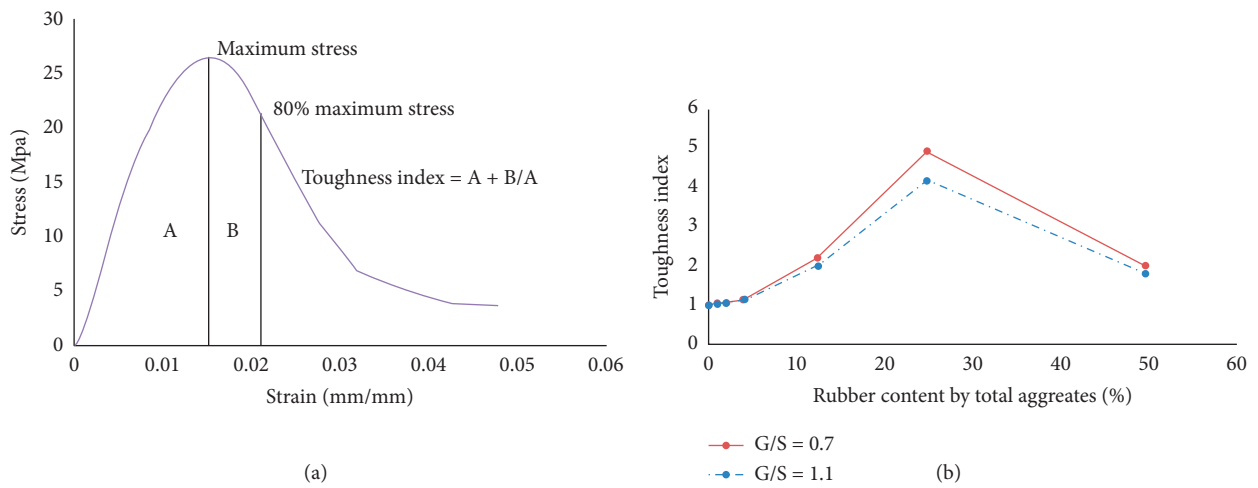
FIGURE 11: (a) Evaluation of toughness index. (b) The toughness index value for HSRC specimens at 28 days.

TABLE 6: Parameter of reduction function for HSRC specimens at 28 days.

Model parameter	Concrete property		
	Compressive strength (Fc)	Splitting tensile strength (Ft)	Modulus of elasticity (Et)
A	0.12	0.25	0.22
B	0.88	0.75	0.78
M	4.1	3.87	6.86
R-square	0.94	0.95	0.85

(a)

(b)

(c)
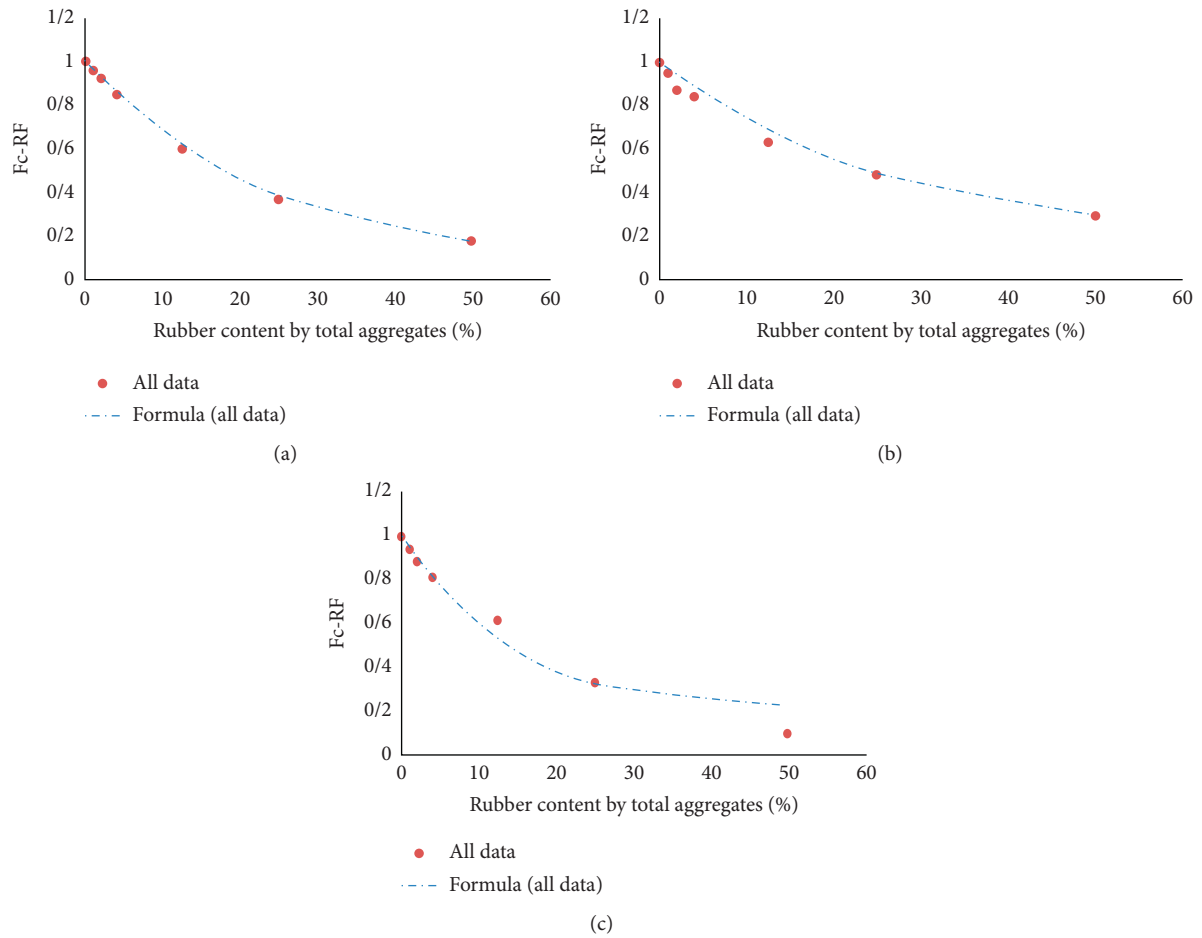
FIGURE 12: (a) Compressive strength reduction factor, (b) splitting tensile strength reduction factor, and (c) elastic modulus reduction factor of all types of rubberized concrete containing different silicone rubber content.

Data Availability

The results are obtained from the laboratory, and any data will be made available if needed.

Disclosure

This work forms a part of the Ph.D. dissertation of the second author.

Conflicts of Interest

The authors declare that there are no conflicts of interest regarding the publication of this manuscript.

Acknowledgments

References

[1] S. Hamdani, C. Longuet, D. Perrin, J.-M. Lopez-Cuesta, and F. Ganachaud, "Flame retardancy of silicone-based materials,"

Polymer Degradation and Stability, vol. 94, no. 4, pp. 465–495, 2009.

[2] L. Meunier, G. Chagnon, D. Favier, L. Orgéas, and P. Vacher, "Mechanical experimental characterisation and numerical modelling of an unfilled silicone rubber," *Polymer Testing*, vol. 27, no. 6, pp. 765–777, 2008.

[3] S.-H. Kim, E. A. Cherney, and R. Hackam, "Hydrophobic behavior of insulators coated with RTV silicone rubber," *IEEE Transactions on Electrical Insulation*, vol. 27, no. 3, pp. 610–622, 1992.

[4] A. P. Pinheiro, "Architectural rehabilitation and sustainability of green buildings in historic preservation," *HighTech and Innovation Journal*, vol. 1, no. 4, pp. 172–178, 2020.

[5] C. Vargas-Elizondo, "On the role of ethics in shaping technology development," *HighTech and Innovation Journal*, vol. 1, no. 2, pp. 86–100, 2020.

[6] A. R. Khaloo, M. Dehestani, and P. Rahmatabadi, "Mechanical properties of concrete containing a high volume of tire-rubber particles," *Waste Management*, vol. 28, no. 12, pp. 2472–2482, 2008.

[7] N. N. Eldin and A. B. Senouci, "Rubber-tire particles as concrete aggregate," *Journal of Materials in Civil Engineering*, vol. 5, no. 4, pp. 478–496, 1993.

[8] Z. K. Khatib and F. M. Bayomy, "Rubberized Portland cement concrete," *Journal of Materials in Civil Engineering*, vol. 11, no. 3, pp. 206–213, 1999.

[9] G. Li, G. Garrick, J. Eggers, C. Abadie, M. A. Stubblefield, and S. Pang, "Waste tire fiber modified concrete," *Composites Part B: Engineering*, vol. 35, no. 4, pp. 305–312, 2004.

[10] J. Khan, A. Hussain, F. Haq, K. Ahmad, and K. Mushtaq, "Performance evaluation of modified bitumen with replaced percentage of waste cooking oil & tire rubber with bagasse ash as modifier," *Civil Engineering Journal*, vol. 5, no. 3, pp. 587–596, 2019.

[11] M. Adom-Asamoah, J. B. Osei, and K. Adinkra-Appiah, "Structural characteristics of reinforced palm kernel shell concrete deep beams," *Civil Engineering Journal*, vol. 4, no. 7, p. 1477, 2018.

[12] A. A. Kadhim and H. M. K. Al-Mutairee, "An experimental study on behavior of sustainable rubberized concrete mixes," *Civil Engineering Journal*, vol. 6, no. 7, pp. 1273–1285, 2020.

[13] F. Hernández-Olivares, G. Barluenga, M. Bollati, and B. Witoszek, "Static and dynamic behaviour of recycled tyre rubber-filled concrete," *Cement and Concrete Research*, vol. 32, no. 10, pp. 1587–1596, 2002.

[14] R. Siddique and T. R. Naik, "Properties of concrete containing scrap-tire rubber - an overview," *Waste Management*, vol. 24, no. 6, pp. 563–569, 2004.

[15] A. M. Dessouki, N. H. Taher, and H. H. El-Nahas, "Preparation of composites of natural rubber latex-Portland cement for moulds," *Polymer International*, vol. 45, no. 4, pp. 339–346, 1998.

[16] H. A. Toutanji, "The use of rubber tire particles in concrete to replace mineral aggregates," *Cement and Concrete Composites*, vol. 18, no. 2, pp. 135–139, 1996.

[17] I. B. Topçu, "The properties of rubberized concretes," *Cement and Concrete Research*, vol. 25, no. 2, pp. 304–310, 1995.

[18] N. Segre and I. Joekes, "Use of tire rubber particles as addition to cement paste," *Cement and Concrete Research*, vol. 30, no. 9, pp. 1421–1425, 2000.

[19] H. A. Alasmari, B. H. Abu Bakar, and A. T. Noaman, "A comparative study on the flexural behaviour of rubberized and hybrid rubberized reinforced concrete beams," *Civil Engineering Journal*, vol. 5, no. 5, pp. 1052–1067, 2019.

[20] M. E. Komaki, A. Ghodrati Dolatshamloo, M. Eslami, and S. Heydari, "Ameliorating precast concrete curbs using rubber and nano material," *Civil Engineering Journal*, vol. 3, no. 2, pp. 105–110, 2017.

[21] K. Ha, "Innovative blade trailing edge flap design concept using flexible torsion bar and worm drive," *HighTech and Innovation Journal*, vol. 1, no. 3, pp. 101–106, 2020.

[22] S. Ghods, A. Kheyroddin, M. Nazeryan, S. M. Mirtaheri, and M. Gholhaki, "Nonlinear behavior of connections in RCS frames with bracing and steel plate shear wall," *Steel and Composite Structures*, vol. 22, no. 4, pp. 915–935, 2016.

[23] ASTM C 150-07, *Standard Specification for Portland Cement*, ASTM, West Conshohocken, PA, USA, 2020.

[24] American Concrete Institute, *Standard Practice for Selecting Proportions for Normal, Heavyweight and Mass Concrete*, pp. 1–91, American Concrete Institute, Farmington Hills, MI, USA, 2002.

[25] A. Khaloo, E. M. Raisi, P. Hosseini, and H. Tahsiri, "Mechanical performance of self-compacting concrete reinforced with steel fibers," *Construction and Building Materials*, vol. 51, pp. 179–186, 2014.

[26] ASTM C 143, *Standard Method of Test for Slump of Hydraulic Cement Concrete*, ASTM, West Conshohocken, PA, USA, 2020.

[27] ASTM C138/C138M—17a, *Standard Test Method for Density (Unit Weight), Yield, and Air Content (Gravimetric) of Concrete*, ASTM, West Conshohocken, PA, USA, 2020.

Research Article

Seismic Performance Evaluation of Buried Sewage Collection Pipelines

Abolfazl Rahimi[1] and Mohammad Rezaii [2]

[1]Department of Civil Engineering, Islamic Azad University, Gorgan, Iran
[2]Department of Civil Engineering, NIT, Babol, Iran

Correspondence should be addressed to Mohammad Rezaii; rezaii@abfagolestan.ir

One of the systems which is damaged because of earthquake is an urban wastewater network. In this paper, it is tried to study the damages occurred on urban wastewater networks in a selected network. The most important definitions by the network about some branches of the wastewater network and relevant reformations are studied. Then, the function of pipeline networks buried by the previous earthquake is studied and also it is proceeded about the research studies done regarding the relationships dominant on susceptibility in which some of the mentioned relationships are studied. The statistical society of some methods used in this research is studied, and the software applied in this part is introduced. Finally, the data of the output results are analysed in which the results obtained by this research are including the output drawings of the software GIS that demonstrate the occurred damages in applied and clear way. Some suggestions for using the aforesaid results by the researchers and authorities, especially disaster headquarter, have been presented. The results of this study showed that the assumptions and also the modelling process have handled the simulation well and this process is an effective method in decision making.

1. Introduction

Lifeline refers to a set of structures, facilities, and installation which play a pivotal role in storing, supplying, transferring, and distributing basic necessities, such as water, electricity, and gas, or collecting, storing, purifying, and recycling wastewater and other trash, or even making communication, such as landline, cell phone, Internet, and data [1]. As their names suggest, broadness and continuous performance are defining characteristics of such structures as mentioned in Figure 1 [2].

These structures share common features. Obviously, lifeline function a significant performance in the city and supply basic necessities. As an illustration of this, the wastewater system is a most important lifeline. Raw sewage always has a great deal of matters having detrimental effects on beings which would result in even unknown infectious diseases, for example, pestilence and cholera. In addition, combination of sewer gases, such as methane, ethane, and

benzene, with air increases the likelihood of explosion [3]. In general speaking, there are two analytical and statistic approaches to studying susceptibility of underground pipelines when it comes to earthquake. As such, the analytical view aims to present relations in order to find strain in pipes through physical laws. Considering this view, recent literature is setting out to find how such seismic parameters such as MMI, PG, and PGV bring about destruction. A sewage system is made up of linear and stationary structures (Figure 2).

The sewage system pipelines are classified into seven groups. By moving from top to down, the importance and diameter of pipes are decreased. Table 1 illustrates the classification. It is worth mentioning that material of pipes has dramatically affected last earthquake data. As fittings of the sewage system have not been made to endure pressure, they are weak. Rigid fittings refer to those that avoid two adjacent parts from displacement at the end, while flexible fittings allow two adjacent parts to locally rotate or transfer.
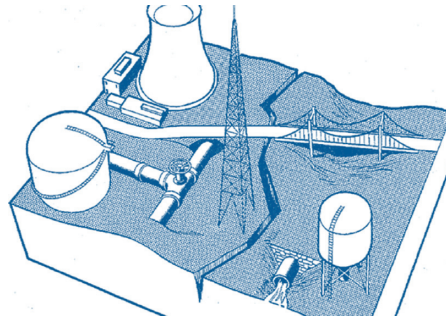
Figure 1: Scheme of lifelines.
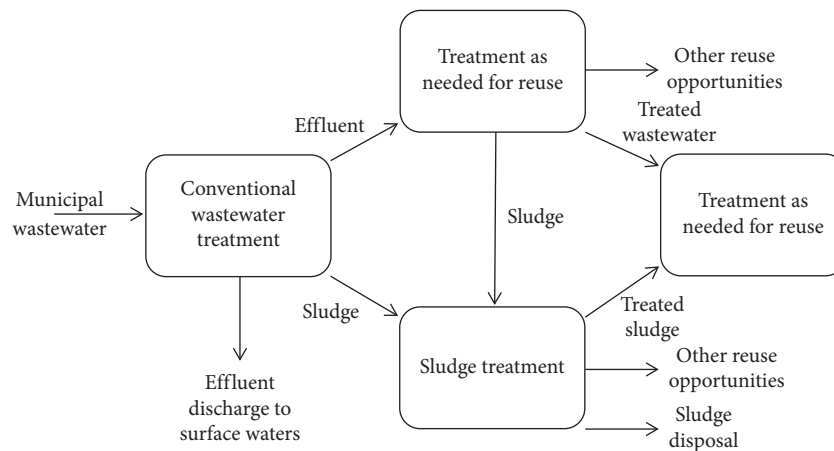
Figure 2: The scheme of a sewage system.

Table 1: Classification of the sewage system parts into linear and stationary.

Type of the sewage system component	Title of component
Stationary	Installation of sewage storage including surface and ground basins
Stationary	Installation for pumping
Linear	Pipelines and ground main transfer tunnel
Stationary	Sewage-treatment plant
Linear	Pipelines for collecting sewage
Stationary	Manhole
Stationary	Administrative, public, and supporting buildings
Stationary	Water and wastewater subscribers

Sewage pipes and fittings are commonly made up of ceramic, concrete, cement asbestos, plastic, poly ethylene, UPVC, GRP, cast iron, and steel.

Iran is located on the Alp belt extending from the Alps Mountains to the Mediterranean Sea. Iran's plate consisted of Iran, Arabian, and Eurasian plates. Arabian plate pulls that of Iran. Zagros pressure region as well as mountains shows a common boundary between the two plates which has resulted in reverse faults. On the other hand, Iran's plate is surrounded by the Eurasian, Indian, and Anatolian plates from the north, east, and west, respectively. As such, pressure arising from the Arabian plate prevents Iranian plate from any transfer.

According to the Lifeline Earthquake Engineering Council, founded by the US Civil Engineering Council in 1974, it has been estimated that almost half of pipelines in Iran are at the risk of bursting in case of happening an earthquakes. On the other hand, although behaviour of ground pipelines has been studied during 10 last years, there is much room for argument. The direct relationship between the sewage system and public health, on the one hand, and having difficulty in finding location of leakage and breakage in pipes due to force of gravity in the sewage system after an earthquake taken place on the other hand, attaches importance to study susceptibility of the system. In addition, considering depth of the sewage system replacing and fixing damaged pipes would be extremely costly. So far, a lot of research has been done on the different functions of buried pipes. These studies have been conducted to better identify the behaviours of these sensitive infrastructures. In this study, the behaviour of these structures in the face of earthquake force for a relatively large area has been evaluated.

2. Literature Review

According to this analytical method, the results offered by Chu and Shah [4], as well as Goodling and Iqbal [5], suggest that inlet and outlet branches of the bended pipes seemed to be flexible but the sag assumed rigid; that is to say, they considered no relative rotation resulting from bending

between inlet and outlet tangents. Moreover, relocation arising from slipping (Δ) measured by subtracting the relocation of a piece of pipe ($p\Delta$) from relocation of soil ($s\Delta$). Although the previous method assumed bending rigid, there tends to be some transformations in sags creating tendency to decrease in flexural moment.

Goodling [5] put forward equations based on analysing bending in thin-walled curved pipes. In a research study, [6] suggested a method for predicting relocation of the sag in which the Riley wave was assumed as a transmittal sine wave with limited wave length. In the same token, relocation of the pipe was assumed equal to that of ground where displacement of ground was zero, and they developed a simple equation for pipe strain in the point of sags based on correspondent structural analyses. They assumed effective length (L') one-fourth of the wave length, so anchors could be measured by virtue of displacement compatibility equations in the curve.

Takada and Tanabe [7] put forward knee and T-joints are more susceptible to damage than other parts of a pipeline and maximum tensile pressure can affect them. In 2003, O'Rourke and McLaughlin developed a two-dimensional finite-element model as their PhD dissertation. They entered a quasistatic sine Riley wave into the numerical model and compared results obtained from a steel pipe having a diameter and thickness of 24 and 5 inch in a sand soil with a reduction factor (0.6) with that of obtained by Shah and Chu [4] as well as [6] for a flat surface steel.

Moreover, O'Rourke and Jeon [1] utilized a finite-element model developed in Nastran software to stimulate the problem and comparing analytical results. They assumed the pipe as a column element for modelling, and each bending had a length of 125 meters equal to one-fourth of a wave length having 500 meters. To verify this model, data collected from the analytical method were compared with that of the finite-element model. So, it was found that results obtained from the analytical method were almost better in all cases. As can be seen from prior works, most of numerical analyses concerning were quasistatic; however, studies on dynamic behaviour of pipe under earthquake loading are still lacking.

In 2008, F. R. Rofooei and R. Qorbani did a research on continuous pipes assuming vertical wave propagation and then compared obtained strain results with that of observed in a pipe having a knee-joint. Results showed that the existent sag led to an increase in strain and pressure in the knee-joint than a continuous pipe. Moreover, Takada et al. [8] did a numerical research on a set of pipes combining T and knee-joint and showed that the seismic behaviour of a pipe network was more than a continuous one. In addition, adjacent pipes showed inconsiderable increased behaviour than patchy ones.

Dai et al. [9] studied about analysis and comparison of long-distance pipeline failures, and they found that according to the statistical results, PNGPC is not very far compared with foreign countries. There are still some aspects both in technology and in management that should be improved, such as quality of manufacture and construction of pipeline and third-party monitoring. Also, Yang et al. [10] did research about numerical simulation of pipeline-pavement damage

caused by explosion of leakage gas in buried pipelines and showed that the results can provide theoretical basis for municipal pipeline construction design and urban safety planning and provide references for the risk assessment of gas explosion in buried pipelines.

2.1. New Zealand Earthquake. Christchurch is New Zealand's second biggest city. Its sewage system covers almost 150,000 families. Although, the system is made up of concrete, ceramic, UPVC, and asbestos pipes, it has a high percentage of concrete one. An earthquake measuring 7.1 on the Richter scale hit the city on 4th September 2010 (Figure 3). The sewage system was badly destroyed. Demolition rate of pipes made up of concrete and reinforced concrete (0.9) increases the likelihood of corrosion [11].

2.2. Japan Earthquakes. An earthquake measuring 6.8 on the Richter scale, called Nigata-Ken Chuetsu, hit the city in October 2004. Destruction of the sewage-treatment plant led to flow of raw sewage into the city, to such an extent that 151 kilometer sewage pipeline was destroyed and 2056 manholes were also damaged. The greatest damage recorded for tucking water behind manholes and pipes which not only generated heavy traffic but also caused failure to pump houses' sewage. Another earthquake measuring 7.5 on the Richter scale hit Nigata, Japan, on 16th January 1964. Over 470 km pipeline, namely, 68% of pipes, is damaged. The most destruction was recorded for cast iron pipes and joints. According to data, other pipes, especially those with small diameter, showed more damage due to bending. Many pipes and installation became visible on the ground because of soil liquefaction. In addition, slope of the soil is also considered as an important factor in damages [12].

2.3. Manjil Earthquake, Iran (1990). An earthquake hit Rodbar and Manjil, Iran, on 21st July 1990. It caused severe damage to several buildings, roads, installation, and even the Sefidrood concrete dam [13]. There are still insufficient data for the extent of damage to the water supply system. Although buildings' water pipes had been badly damaged, main pipelines of the city water supply system were in a satisfactory condition thanks to putting new pipes in depth (Figure 4).

2.4. Bam Earthquake (2003). An earthquake measuring 6.8 on the Richter scale struck Bam, Iran, on 26 December 2003. The city had a total population of 12000. According to reports, asbestos fittings of pipes had been damaged but the main water supply system was slightly damaged [14]. Although water gushed from broken domestic pipes, water tanks were not badly damaged, mainly because they were underground (Figure 5).

3. Material and Methods

3.1. Effective Factors Causing Damage to Pipelines after Occurrence of an Earthquake. Multiple parameters have impact

Damage rate
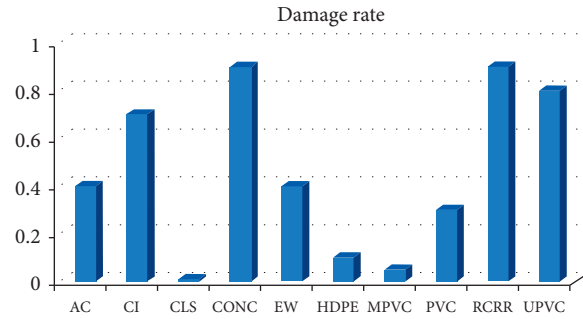
FIGURE 3: Demolition rate of pipelines considering their type in the New Zealand earthquake.

FIGURE 4: Damage occurred from Manjil earthquake.
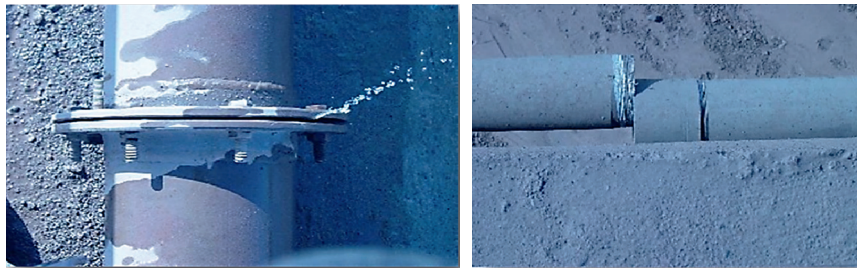
FIGURE 5: Damage occurred from Bam earthquake.

on damage to underground pipelines after occurring an earthquake. In general, characteristics of a pipeline, soil, and magnitude of an earthquake affect the seismic behaviour of the pipeline. As such, there are considerable factors having effect on the seismic behaviour of buried pipelines. In a research, Eguchi et al. studied factors affecting susceptibility of buried pipelines when an earthquake happens through analysing damage to the buildings destroyed in the San Francisco earthquake [15]. Evidence suggested that the devastating effect of faulting was much more than distortion due to earthquake movements. As a result, the closer a building is to the fault, the worse it would be destroyed. A pipeline would be inevitably face to more dangers, due to its extent, than other installations which cover a small area, simply because long pipelines are spread over regions having active faults or soil liquefaction. The term faulting is meant fracture of faults which is happened on the ground. There are three main types of faulting, including horizontal, vertical, or a combination of them. Installations located on the fault line are much more susceptible to the earthquake (Figure 6).
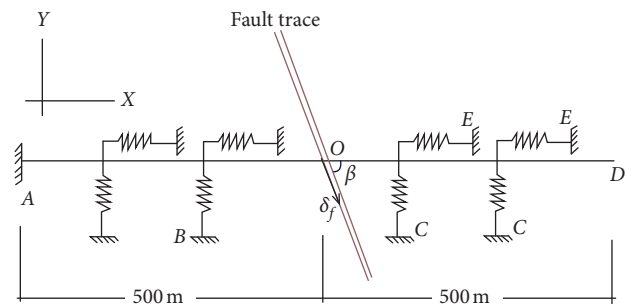
FIGURE 6: Ideal structural model during faulting.

Figure 6 shows an ideal structural model on a fault line, and the probability and extent of soil liquefaction will increase by increase in the continuance in earthquake. Soil liquefaction as well as lateral movements is viewed as devastating parameters which may lead to bury surface structures under soil or help underground structures to become visible. Shaking cause to compress soil, and subsidence is occurred. However, the extent of persistent

relocation due to subsidence is less than that of due to soil liquefaction. Notwithstanding, subsidence is of importance because of making heterogeneous dislocations in soil.

3.2. Features of the Pipeline Affecting Susceptibility of the Buried Pipelines due to an Earthquake.

Most of parameters affecting susceptibility of buried pipelines due to an earthquake have much to do with characteristics of the pipeline. Prior studies showed that type of the pipe plays a pivotal role. To put it simply, its flexibility helps the piping system because it leads to easily movement of soil along with the pipe, which prevent the pipe from bursting during an earthquake. Increase in the internal diameter of pipelines decreases both bending and axial tensions due to affecting soil-pipe interaction. Final conditions have marginal effect on tensions created in cross sections when it comes to length of pipe. With regard to data collected from the analysis, it is highly likely that the pipe will rupture at its junction with other installations, such as manholes and storages, than other sections of the pipeline (Figure 7–9).

The pipeline bears lateral loads during an earthquake which it oscillates pipes and cuts their connections with the saddle. However, bracing spaces helps the system not to be devastated. Figure 10 illustrates demolition of pipes' support due to soil liquefaction in the Northbridge earthquake (1994).

However, seismic and flexible joints have been found to suggest great function during an earthquake which it leads to decrease in demolition of the water supply system. On the other hand, accruing to data collected from prior research, continuous pipes, such as the ones made up of steel with welded joints, have shown greater function than sectional pipes with lots of joints. In addition, the extent of demolition observed for asbestos pipes in Loma Prieta (1989) and Northridge (1994) earthquakes was less than that recorded for Mexico City earthquake (1985).

Researchers also argue that connection behaviour would prove to be linear when pipes' relative rotation is 0.05 radian. Moreover, bending experiments on fittings used in flexible cast iron pipes having rubber-made washers and different diameters showed that rotation of joints is done around the pipe. Improper hardness distribution is the leading cause of most of the destructions of the water supply system. As a result, relocations arising from such shakes are different and cause to break joints between pipes (Figures 11 and 12).

3.3. Methods of Studying the Seismic Behaviour of a Pipeline.

With regard to the destructions left after earthquakes, researchers set the stage to conduct a comprehensive study in order to develop some methods to find how seismic behaviour affects the pipelines. The methods are generally divided into three groups, including approximate analysis [16], accurate analysis, and building code methods. Shakes arising from an earthquake go through many changes due to several reasons before happening which will affect structures in different ways. Initial works in the field of buried pipelines focused preliminary on the main factor, that is to say, the path through which waves move. In addition, as can be seen
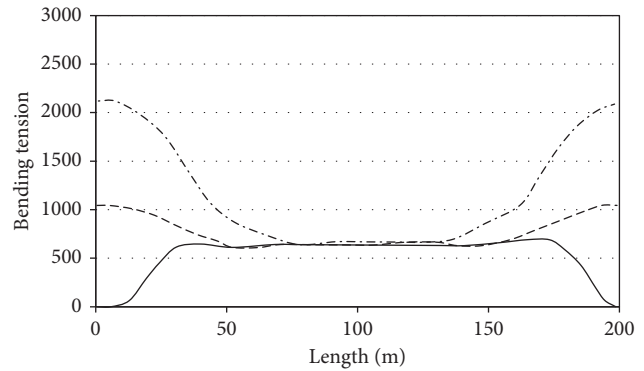
FIGURE 7: Variation in the extent of maximum bending tensions along the pipeline with different final conditions.
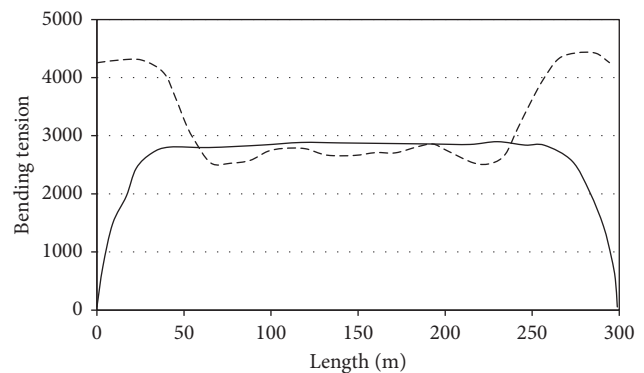
FIGURE 8: Variation in the extent of maximum axial tensions along the pipeline with different final conditions.
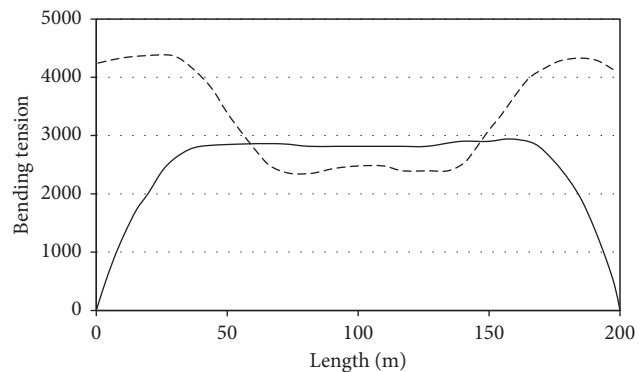
FIGURE 9: Variation in the extent of maximum axial tensions along the pipeline with different final conditions.

from numerical calculations, its effect has been considered in the form of a semistatic factor.

Regarding dynamic analyses done on buried pipelines, especially on their bending points, the impact of this factor has omitted, and pipes were only analysed by taking vertical distribution and synchronous shakes throughout all points into account. Wave propagation velocity functions as a leading parameter to calculate strain. Shear wave velocity was used to calculate the extent of axial strain in areas having

FIGURE 10: Demolition of pipes' support due to soil liquefaction in the Northbridge earthquake (1994).
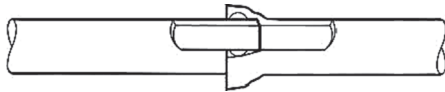
FIGURE 11: Cracks observed in the joint between a restrained weak pipe and an unrestrained one [11].
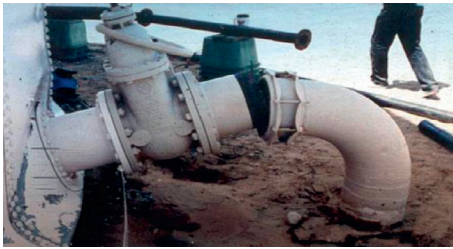
FIGURE 12: Cracks in the pipe connected to the storage (ALA 2002).

FIGURE 13: Comparing R and S waves in designing pipes.

focal length less than five times of the distance from focal depth to the epicentre of an earthquake, while Riley wave velocity was utilized to calculate distances more than given amount. In a research study, O'Rourke et al. studied horizontal apparent speed for body waves. They developed an analytical method to assess the shear wave angle of incident. So, apparent speed for shear waves is calculated as

$$\text{Cs - apparent} = \frac{\text{cs}}{\sin \theta}, \tag{1}$$

where θ is the incident angle of the shear wave to the horizontal and Cs is the velocity of shear waves in surface soil. Phase velocity of the wave is the same apparent velocity. Unlike body waves, phase velocity depends upon frequency. With regard to the Riley wave, there is relation among wave length (λ), frequency, and phase velocity. Figure 13–15 illustrate a scheme of Riley wave propagation with an apparent velocity.

Wave propagation has been found to put strain on the ground. Measuring strain of ground is done by studying simple transitional movement of a wave having fixed shape. It was assumed that velocity and movement of two points throughout a propagation path simply differ in a time lag in which, in turn, it is a function of the distance between two points and the seismic wave velocity. In the same token, maximum tensile or compressive strain of the earth (gϵ) in the direction of wave propagation is measured as

FIGURE 14: Apparent propagation of a shear wave.

$$\varepsilon g = \frac{\text{Vm}}{C}, \tag{2}$$

where Vm is the maximum horizontal velocity of the earth in the direction of wave propagation and C is the apparent propagation velocity of the seismic wave. To propagate a Riley wave, strain parallel with the ground could be measured using the equation above, where C is replaced by the value of phase velocity according to the wave length equivalent to four times of the separation distance (the length of the pipe located between two bridles which is about to analyse). The equation needs to be changed when the given direction is parallel to the line of wave propagation. Generally, as can be seen from the figure below, the wave has angle in both vertical and horizontal plates. So, the equation
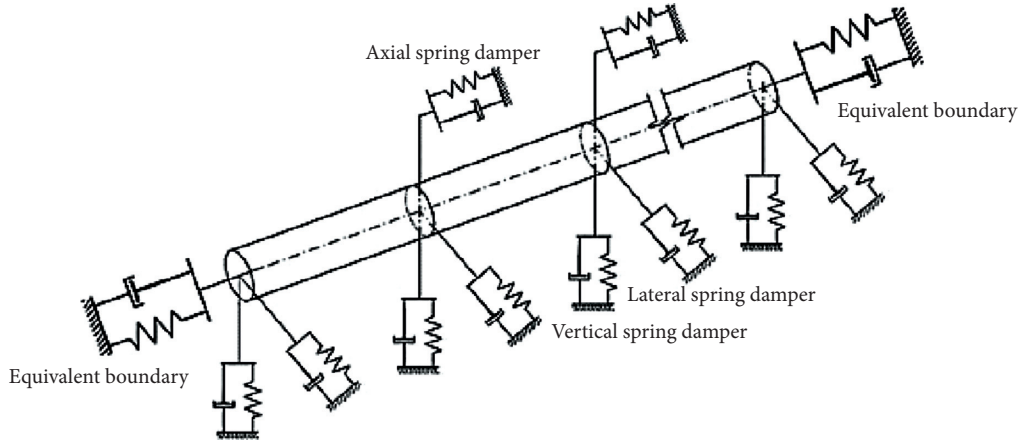
FIGURE 15: Apparent propagation of an R wave, strain of the ground, and curvature results.

below is used to measure apparent wave velocity in the direction of pipe's axis:

$$Cs\text{-}apparent = \frac{cs}{\sin\theta \cdot \cos\gamma}. \qquad (3)$$

Yeh [17] illustrated that maximum strain of the earth is measured by $45 = \theta = \gamma$ in given plates.

3.4. Studying Seismic Behaviour of a Soil-Pipe System concerning Continuous Buried Pipelines.

A structure bears bending or axial transformations after an earthquake. Providing satisfying plasticity in order to absorb transformations due to earthquake without decrease in static loading capacity acts as an important design criterion. Generally, developed axial strain throughout a continuous direct pipe depends upon such factors as shape of the earth, transmittal wave length, and soil-pipe interaction forces. Although strain of pipe and soil are assumed equal for small- to medium-sized movements, the same is not true for great strains because of existent slipping between soil and pipe. It has been found to decrease pipe strain compared to that of soil. Newmark [16] put forward a simple method to determine how the pipeline acts when earthquake waves are propagated. Then, other researchers, such as Yeh, revised it.

Seismic movement of the earth, which is defined as the history of velocity-time and velocity-displacement, functions as a transmittal wave with fixed shape. It suggests that two points along the propagation path simply shake by a time lag. Inertia involved in small movement equations is too small to be measured. Later, the assumption was studied by many researchers and their works showed that it acts as a reasonable engineering approximation. It is assumed that no relative movement happens in the soil-pipe interaction, and pipe's strain equals to that of soil. In addition, O'Rourke and El Hamadi developed an analytical method to estimate maximum pipe strain.

The method assumes that first, axial strain in soil equals pipe strain arising from length friction between soil and pipe and second, waves are propagated parallel to the axis of pipe. In a research study, O'Rourke and Jeon [1] compared data collected from three mentioned analytical methods when it came to the continuous pipeline under the Riley wave's propagation. Besides, the model put forward by Takada [18] suggested that pipe is modelled in the form of a shell having a length of 60 D adjacent to the fault, but it could be in the form of an beam element where the distance from the pipe to the fault is almost 300 meters and the extent of soil and pipe slipping and strains are insignificant (Figure 16). All things being equal, soil surrounded the pipe is modelled using soil springs according to the seismic designing regulation of buried oil and gas pipes [19].

In 2004, Takada et al. reported on a new model according to changes in boundary conditions. They suggest that the pipe should be modelled in the junction with the fault in the form of a shell element due to local strain and big transformations just the same as before. Moreover, each point of the shell element is connected to three soil springs in axial, lateral, and vertical directions. Finally, the relation between the axial force (f) and increased length ΔL, which is regarded to boundary conditions for nonelastic springs, is measured as

$$F(\Delta L) = \sqrt{\frac{3EAfs}{2}} \ \frac{U01}{6}\Delta L\frac{2}{3}, \quad 0 < \Delta L < U0, \qquad (4)$$

$$\sqrt{3EAfs\left(\frac{\Delta L - 1}{4U0}\right)} \ \frac{\sigma y2\,A}{2Efs} + \frac{U0}{4}, \qquad (5)$$

where $Y\sigma$ acts as pipe's yield stress and elasticity modulus. It has been suggested that tensile rupture, local buckling, and thimble buckling are among the most significant damage to continuous pipes while tensile and compression ruptures of pipe joints as well as local bending were the most common damage observed in apart pipeline [20]. Concerning modelling of continuous pipes, Halabian and Hokmabadi [21] stimulated faulting and wave propagation in the laboratory of Isfahan Technological University, Iran, and adopted equivalent boundary conditions put forward by Takada when it came to boundary conditions related to the end of the pipe, so they conducted a parametric study on the behaviour of buried pipelines.
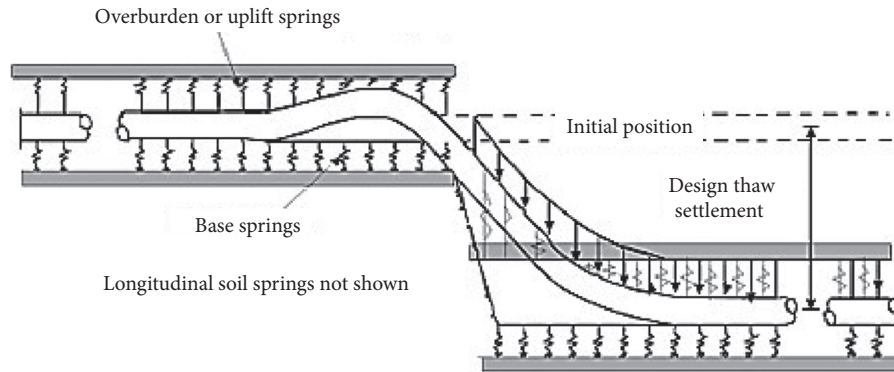
FIGURE 16: Finite-element model of a shell element in collision with the fault.

Rofooei and Qorbani [19] assumed a vertical wave propagation in order to conduct a parametric study on continuous pipes under earthquake loading. They stimulated the pipe and surrounding soil through springs according to the ALA regulation using ANSIS software. Considering data collected from effects of pipe and soil geometric changes on their relative displacement, they observed increase in relocation in the soil-pipe boundary due to decrease in soil aggregation.

3.5. The Seismic Susceptibility Model concerning Buried Pipelines.
Hazus.sr2i is a guideline on estimating damage to structures due to the earthquake which was developed by FEMA and the national institute of the US Architecture. It is comprised of ways to estimate the extent of earthquake damage to various structures, including lifelines. Accordingly, the guideline suggests that leakage tends to happen because of earthquake waves in which 80% depends upon maximum earth velocity and 20% is a function of earth's permanent transformations, while it has been found that pipe breakage proves to be due to earth's big transformations in which 20% and 80% depend upon PGA and PGD, respectively.

Furthermore, the method divides pipes into two groups, including frangible and flexible. As a result, susceptibility of flexible pipes decreases by 70%. The likelihood of soil liquefaction has been directly entered to the Hazus model which is assumed as the most significant factor on pipe displacement. The algorithm concerning susceptibility of buried pipes under earthquake waves was found by analysing experimental data collected from four earthquakes in the US and two in Mexico. Then, data were adjusted to the Hazus method.

The guideline divides pipes into small and big groups in order to estimate time required for reconstructing pipelines damaged in earthquakes. Accordingly, the small group includes pipes having a diameter of 20 inch or less while others are put in the big group. The method also estimates days required for reconstruction of the water supply system. The following assumptions suggest how to measure days for repair the pipeline. It takes an equipped four-man team for four and eight hours to repair a leaky and a broken pipe, respectively. It takes an equipped four-man team for six and

twelve hours to repair a leaky and a broken pipe, respectively. There is a linear link between repair program and time. As a result, the extent of repairs done on a pipeline which needs (a) days within (b) days with a fixed number of workers is measured b/a (Table 2).

3.6. The Susceptibility Index VI.
In this method, the weighted coefficient is assumed as a factor covering pipe diameter cd, conditions of the ground cg, magnitude of the earthquake based on the Mercalli intensity scale ci, pipe passage through the fault cf, soil liquefaction c1, and potential land slide occurrence potential. Tables 3–10 give information about weighted coefficients. Susceptibility of each part in the wastewater system is achieved by giving weight to above-mentioned factors in different conditions and then multiplying the value by the weighted coefficient of each factor. Considering data from Table 10 and based on values obtained from forgoing equation (6), susceptibility of the wastewater system is divided into three groups, including high, medium, and low. It is worth mentioning that weighted coefficients concerning each factor have been selected based on maximum recorded damage to the buried pipeline in past earthquakes. Table 5 gives information about weighted coefficient regarding conditions of the ground based on different types of soil. In addition, Table 6 illustrates magnitude of an earthquake as well as correspondent improved intensity scale (MMI) in PGA:

$$VI = cd \cdot cp \cdot cf \cdot cg \cdot ci \cdot cl \cdot cs. \qquad (6)$$

4. Numerical Simulation

A complete set is comprised of software, hardware, data, models, algorithms, and human resources for collecting, preparing, organizing, storing, updating, processing, and analysing different types of local data. Such a system aims to manage and handle information collected from the reference place in order to make sensible decisions. The data model indicates transformation of the real world, by observing related geometrical relations and descriptive information, to a reasonable and digital one. The model represents all objects in the form of points, lines, or polygon. However, topological data aim to extract relations between phenomena. Existing

TABLE 2: Hazus equations concerning the ratio of damage to a buried pipeline.

Type of pipe	The ratio of damage to a PGV pipe per kilometer	The ratio of damage to a PGD pipe per kilometer
Fragile	RR = 0.0001 * PGV2.25	RR = prob * PGD0.56
Flexible	RR = 0.3 * 0.0001 * PGV2.25	RR = 0.3 * prob * PGD0.56

PR is defined as the extent of damage to the pipe per kilometer
PGV (cm.s^{-1})
PGD (inch)

TABLE 3: Weighted coefficient for diameter of a pipe.

Coefficient cd	Pipe diameter (d)
$D < 75$ mm	1.6
75 mm $< d <$ 150 mm	1.0
150 mm $< d <$ 250 mm	0.9
250 mm $< d <$ 450 mm	0.7
450 mm $< d <$ 1000 mm	0.5
$d >$ 1000 mm	0.4

TABLE 4: Weighted coefficient for type of pipe.

Type of the pipeline	Coefficient (cp)
Soft cast iron	0.3
Cast iron	1.0
Ceramic	3
Asbestos	2.5
Poly ethylene	0.1
Concrete	2

TABLE 5: Weighted coefficient for conditions of the ground.

Type of soil	Coefficient
Type I	0.5
Type II	1
Type III	2
Type IV	2.9

TABLE 6: Weighted coefficient for magnitude of the earthquake.

Magnitude of the earthquake	Coefficient
MMI < 8 PGA < 0.25 G	1.0
8 < MMI < 9 0.25 G < PGA < 0.45 G	2.1
9 < MMI < 10 0.45 G < PGA < 0.6 G	2.4
10 < MMI < 11 0.6 G < PGA < 0.9 G	3.0
11 < MMI PGA > 0.9 G	3.5

TABLE 7: Weighted coefficient for passage of the pipeline through the fault.

Passage of the pipeline through a fault	Coefficient
No passage	1
One passage	2
Multiple passages	2.4

TABLE 8: Weighted coefficient for soil liquefaction.

Liquefaction	Coefficient
0 < PL1 < 5	1
5 < PL < 15	2
PL > 15	2.4

TABLE 9: Weighted coefficient for the land slide potential CS.

Potential of the land slide	Coefficient
No danger	1
Medium danger	2
High danger	2.4

TABLE 10: Classification of the extent of seismic susceptibility of the wastewater system.

Color	Susceptibility level	VI index
Green	Low	0 < VI < 5
Orange	Medium	5 < VI < 12
Red	High	VI > 12

ability to interpret and analyse data in such systems and software enables us to review multiple parameters and factors affecting different analyses and achieve reliable results. Research has proved the applicability of GIS to analyse data and extract results in the field of water and wastewater engineering. In the current research, the most well-known software package appertain to geographical information, ArcGIS Desktop 10.1, has been used to analyse data. For the purpose of analysis, first, software's default data and geographical tiers, called GIS READY, were prepared. The process was comprised of improving designing mistakes and then doing a georeferencing operation.

Since most of data were in the form of paper maps, they were first scanned and then by taking the scale of data into account, data were turned into a numerical one. Finally, with regard to available data as well as type of analysis, all data were changed into a roster model based on their effective parameters (Figure 17).

relations between phenomena in local data function as part and particle of some GIS analysing systems. In the raster model, the whole map is divided into a set of small and regular cells called pixel. The raster format is actually composed of an $n*m$ array of pixels.

The geographical information system (GIS) has recently attracted the attention of different engineering fields. The

Figure 17: The algorithm determining the extent of damage observed under an earthquake wave in GIS.

Figure 18: Geographical location of Gorgan.
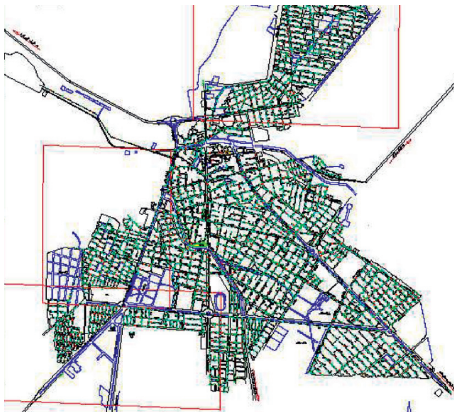
Figure 19: The organization map of the urban wastewater system.

Figure 20: The map of Borujen wastewater system (diameter of pipes).

4.1. Statistical Population.

4.1. Statistical Population. Gorgan, a city in Golestan, Iran, was selected in the current case study research. It has been the first city in the province equipped with the wastewater system. As the city experiences dozens of small earthquakes every day, it is worth studying susceptibility of the wastewater system to earthquake. The wastewater system is 124 meters in length (Figure 18).
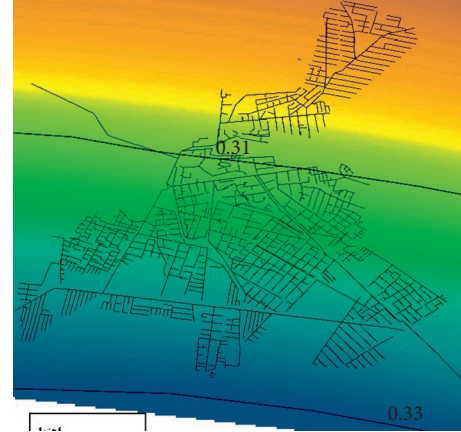
Figure 21: The PGA10 map and Borujen's wastewater system.

First, maps developed in AutoCAD software pertinent to the Gorgan wastewater system were collected in order to assess the extent of damage to the system due to earthquakes. Next, maps were turned into GIS data. Both 2 and 10 percent danger analysis maps were adjusted to aerial photos, and then corrected ones were entered into GIS software to measure the seismic susceptibility ratio under maximum land movement.

4.2. Sampling Method and Sample Size. In the current research, two types of data, including maps of seismic analysis and wastewater pipelines' code were used. The former includes curves aligned with velocity of potential approaches of the vertical element which are pertinent to a return period of 75 years for 2% PGA and a return period of 475 years for 10% PGA for an estimated 50 year service life.

4.3. The Map of Selected Wastewater System. The Gorgan water and wastewater organization has provided the researcher with given maps as well as a file containing pipelines' codes (Figures 19 and 20). Then, the file entered into the GIS software and improved.

4.4. Data Analysis. Research variables include characteristics of pipes as well as velocity of the earthquake which have been drawn by adjusting rough maps of earthquake velocity and the city's wastewater system (Figures 21 and 22).

5. Results and Discussion

Raw data were put into GIS software as input, and two output data were obtained. Figures 23 and 24 illustrate the
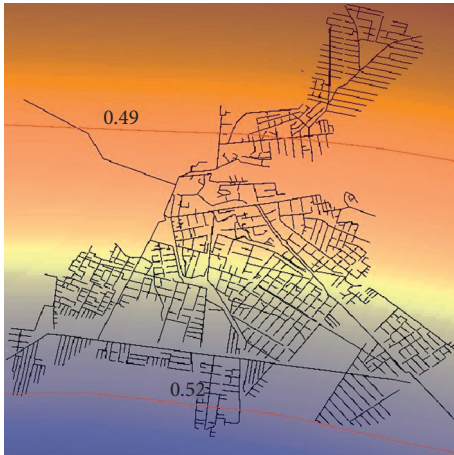
FIGURE 22: The PGA2 map and wastewater system.

FIGURE 25: The total number of damage under PGA2% according to the VI method.

Number of repair10

- 0.867840466–3.7318188
- 3.73181886–6.59579725
- 6.595797252–9.4597756
- 9.459775645–12.323754
- 12.32375405–15.187732
- 15.18773244–18.051710
- 18.05171083–20.915689
- 20.91568922–23.779667
- 23.77966762–26.643646
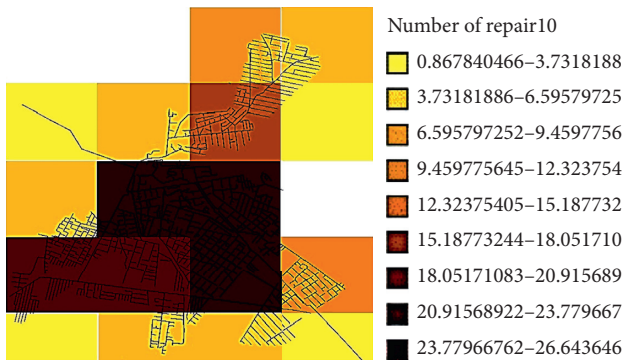
FIGURE 23: The total number of Hazus SR2 damage under PGA10%.

Number of repair2 value

- 494
- 688
- 1,080
- 1,714
- 3,028
- 3,107
- 3,363
- 3,443
- 3,718
- 5,316
- 7,709
- 11,684
- 13,469
- 14,669
- 15,752
- 16,365
- 17,644

FIGURE 24: The total number of Hazus SR2 damage under PGA2%.

FIGURE 26: The total number of damage under PGA10% according to the VI method.

6. Conclusion

Comparing HAUS and VI methods suggests that the former gives more accurate and detailed data, so it enables authorities to make better decisions for boosting and planning structures and finding their susceptible points. Moreover, as the method helps to find out the extent of damage structures would suffer after occurrence of an earthquake, reconstruction process would be done quickly and precisely.

Considering the point that the region has always been earthquake-prone, reviewing data obtained from maps show a high level of damage. Maps are indicating the first prediction of the current research, that is to say, susceptibility of the wastewater system to occurrence of any earthquake, so it focuses on the necessity for replacing existent pipelines with more resistant ones.

Data Availability

The data used to support the findings of this study are available from the corresponding author upon request.

extent of damage to pipes using Hazus based on two different earthquake velocities, namely, PGA 2% and PGA 10%.

Figures 25 and 26 give information about the extent of damage under two different earthquakes according to the VI method.

Conflicts of Interest

The authors declare that there are no conflicts of interest regarding the publication of this paper.

References

[1] T. D. O'Rourke and S. S. Jeon, "Factors affecting the earthquake damage of water distribution systems, in optimizing post-earthquake lifeline system in optimizing post-life line system reliability," in *Proceedings of the Fifth U.S. Conference on Lifeline Earthquake Engineering ASCE*, Seattle, WC, USA, 1999.

[2] U. Albayrak, A. Loai, and M. Morshid, "Evaluation of seismic performance of steel lattice transmission towers," *Civil Engineering Journal*, vol. 6, no. 10, pp. 1–21, 2020.

[3] B. Cai and M. H. Golestan, "Towards bayesian quantification of permeability in micro-scale porous structures," *The Database of Micro Networks*, vol. 1, no. 4, pp. 1–13, 2020.

[4] H. Shah and S. Chu, "Seismic analysis of underground structural elements," *Journal of the Power Division*, vol. 100, no. 1, pp. 53–62, 1974.

[5] E. C. Goodling, "Buried piping–an analysis procedure update," in *Proceedings of the International Symposium on Lifeline Earthquake Engineering*, vol. 77, pp. 225–237, ASME, Portland, Oregon, May 1983.

[6] M. Shinozuka and T. Koike, "Estimation of structural strain in underground lifeline pipes," *Lifeline Earthquake Engineering-Buried Pipeline, Seismic Risk, and Instrumentation*, vol. 34, pp. 31–48, 1979.

[7] S. Takada and K. Tanabe, "Three-dimensional seismic response analysis of buried continuous or jointed pipelines," *Journal of Pressure Vessel Technology*, vol. 109, no. 1, pp. 80–87, 1987.

[8] S. Takada, A. Carlo, S. Bo, and X. Wuhu, *Current State of the Arts on Pipeline Earthquake Engineering in Japan*, The Construction Engineering Research Foundation, Pune, Maharashtra, India, vol. 1, 1992.

[9] L. Dai, D. Wang, T. Wang, Q. Feng, and X. Yang, "Analysis and comparison of long-distance pipeline failures," *Journal of Petroleum Engineering*, vol. 2017, no. 1, 7 pages, Article ID 3174636, 2017.

[10] Y. Yang, S. Yang, Z. Li et al., "Analysis of hazard area of dispersion caused by leakage from underground gas-storage caverns in salt rock," *Advances in Civil Engineering*, vol. 2020, no. 1, 11 pages.

[11] M. Cubrinovski, *Geotechnical Reconnaissance of the 2010 Darfield (New Zealand) Earthquake*, University of Canterbury, Christchurch, New Zealand, 2010.

[12] Y. Maruyama and F. Yamazaki, "Construction of fragility curve for water distribution pipes based on damage datasets from recent earthquakes in Japan," in *Proceedings of the 9th US National and 10th Canadian Conference on Earthquake Engineering*, Toronto, ON, Canada, July 2010.

[13] J. F. Bird and J. J. Bommer, "Earthquake losses due to ground failure," *Engineering Geology*, vol. 75, no. 2, pp. 147–179, 2004.

[14] M. Zare and S. Wilkinson, "Earthquake damage in wastewater system and post earthquake repair methodslimitation and practce," in *Proceedings of the Australian Earthquake Engineering Society Conference Novotel Bavossa Valley Rwsort*, Barossa Valley, South Australia, November 2011.

[15] R. T. Eguchi, "Seismic vulnerability models for underground pipes," in *Proceedings of the International Symposium on EarthquakeBehavior and Safety of Oil and Gas Storage Facilities, Buried Pipelines and Equipment*, American Society of Mechanical Engineers (ASME), New York, NY, USA, January 1983.

[16] N. M. Newmark, "Seismic design criteria for structures and facilities, Trans-Alaska pipeline system," in *Proceedings of the US National Conference on Earthquake Engineering*, Earthquake Engineering Institute, San Francisco, CA, USA, June 1975.

[17] G. Yeh, "Seismic analysis of slender buried beams," *The Bulletin of the. Seismological Society of America*, vol. 64o, no. 5, pp. 1551–1562, 1974.

[18] S. Takada, N. Hassani, and K. Fukuda, "A new proposal for simplified design of buried steel pipes crossing active faults," *Earthquake Engineering & Structural Dynamics*, vol. 30, no. 8, pp. 1243–1257, 2001.

[19] F. R. Rofooei and R. Qorbani, "A parametric study on seismic behavior of continuous buried pipeline due to wave propagation," in *Proceedings of the 14th World Conference on Earthquake Engineering*, Beijing, China, October 2008.

[20] M. Hosseini and S. Jallili, "Assessment of the nonlinear behavior of connection in water distribution networks for their seimic evaluation," *Procedia Engineering*, vol. 14, pp. 2878–2883, 2011.

[21] A. M. Halabian and T. Hokmabadi, "A new hybrid model for rigorous analysis of buried pipelines under general faulting accounting for material and geometrical non-linearities with focusing on corrugated HDPE pipelines," *Soil Dynamics and Earthquake Engineering*, vol. 115, pp. 1–17, 2018.

Research Article

Introduction and Application of a Simple Probabilistic Liquefaction Hazard Analysis Program: HAZ45PL Module

Jui-Ching Chou [1], Pao-Shan Hsieh,[2] Po-Shen Lin,[2] Yin-Tung Yen,[2] and Yu-Hsi Lin[3]

^{1}*Department of Civil Engineering, National Chung-Hsing University, Taichung 40227, Taiwan*
^{2}*Sinotech Engineering Consultants, Inc., Taipei 11494, Taiwan*
^{3}*Liming Engineering Consultants Co., LTS., Taichung 40848, Taiwan*

Correspondence should be addressed to Jui-Ching Chou; jccchou@nchu.edu.tw

The 2016 Meinong Earthquake hit southern Taiwan and many shallow foundation structures were damaged due to soil liquefaction. In response, the government initiated an investigation project to construct liquefaction potential maps for metropolitans in Taiwan. These maps were used for the preliminary safety assessment of infrastructures or buildings. However, the constructed liquefaction potential map used the pseudo-probabilistic approach, which has inconsistent return period. To solve the inconsistency, the probabilistic liquefaction hazard analysis (PLHA) was introduced. However, due to its complicated calculation procedure, PLHA is not easy and convenient for engineers to use without a specialized program, such as in Taiwan. Therefore, PLHA is not a popular liquefaction evaluation procedure in practice. This study presents a simple PLHA program, HAZ45PL Module, customized for Taiwan. Sites in Tainan City and Yuanlin City are evaluated using the HAZ45PL Module to obtain the hazard curve and to construct the liquefaction probability map. The liquefaction probability map provides probabilities of different liquefaction potential levels for engineers or owners to assess the performance of an infrastructure or to design a mitigation plan.

1. Introduction

The 2016 Meinong Earthquake ($M_w = 6.5$) struck south Taiwan on February 6, 2016. The strong ground motion caused huge loss of lives (117 people dead and 504 people injured) [1]. Many shallow foundation structure in Tainan area were damaged due to soil liquefaction which thus gained considerable public attention. In response, the government initiated a project to evaluate and construct the liquefaction potential map for the urban areas of Taiwan. This map was constructed based on the liquefaction potential index (LPI) [2] which is calculated using the factor of safety against liquefaction (FS_L) determined from a simplified liquefaction evaluation procedure. Engineers and owners use the liquefaction potential map to perform a preliminary safety evaluation on infrastructures or buildings and to determine the need of a mitigation plan.

The procedures for the LPI calculation in Taiwan are (1) select the design level (e.g., 475-year return period) peak ground acceleration (PGA); (2) pair PGA with a single earthquake magnitude (M_w) obtained from the deaggregation process of the probabilistic seismic hazard analysis (PSHA) at the same return period; (3) decide a representative water table level; (4) calculate FS_L using a simplified liquefaction evaluation procedure with the selected PGA, M_w, and water table level; and (5) estimate LPI according to the depth and FS_L. The estimated LPI or other related hazards are assumed to correspond to the same return period of PGA. This approach is named the "pseudo-probabilistic" approach [3–5].

In the pseudo-probabilistic approach, LPI at a site is estimated from a selected pair of PGA and M_w, and M_w is assumed to have the same return period with the selected PGA. However, from the PSHA concept, a site could be subjected to numerous pairs of PGA and M_w. Each pair has its own rate of occurrence. Therefore, LPI estimated from the pseudo-probabilistic approach and the selected PGA will not

have a consistent return period as expected [2, 6–8]. As a solution to this inconsistency issue, a probabilistic approach, the performance-based earthquake engineering (PBEE) or the probabilistic liquefaction hazard analysis (PLHA), was introduced to incorporate the occurrence of the ground motion (PGA and M_w pairs) obtained from PSHA into the calculation of LPI or other liquefaction hazards [9–11].

In PLHA, engineers no longer need to select one representative pair of PGA and M_w as analysis inputs. All scenarios (PGA and M_w pairs) and their occurrence frequencies are considered in PSHA by accounting for the uncertainties of earthquake occurrence, ground-motion attenuation, and site effects. The calculation of PSHA is complicated, and thus PLHA is not easy and convenient for engineers to use without a specialized program. Recently, several simplified performance-based methods [8, 9, 12–14] were established for engineers to perform PLHA in an approximated way. Available seismic hazard curves and deaggregation results provided by the United States Geological Survey (USGS) are used to obtain the occurrence frequency of PGA and M_w pairs in these simplified methods.

In Taiwan, without tools for PLHA, the current liquefaction analysis approach is still based on the pseudo-probabilistic approach. In addition, the simplified performance-based method mentioned above cannot be utilized because the seismic hazard curve and the deaggregation result are not yet available. This study presents a simple PLHA program, HAZ45PL Module, customized for engineers in Taiwan to obtain the LPI hazard curve. Moreover, a new application of PLHA results, the probability of exceedance map of LPI, is demonstrated. The probability information can help engineers, owners, or government agencies to carry out a performance assessment on infrastructures or prioritize a mitigation plan. In addition, because of the importance of the water table level on LPI, the HAZ45PL Module includes the uncertainty of the seasonal water table level in the LPI calculation.

2. Methodology of HAZ45PL Module

The HAZ45PL Module consists of HAZ45PL and R language code [15]. HAZ45PL is an executable file calculating LPI of each soil layer based on a PGA and M_w pair obtained from earthquake scenarios in PSHA. HAZ45PL is modified from HAZ45, an open source FORTRAN code developed by Dr. Norm Abrahamson for PSHA [16]. The steps of HAZ45PL Module to construct the LPI hazard curve are explained as follows: (1) generate an earthquake scenario following procedures in HAZ45; (2) provide M_w and the occurrence frequency of the earthquake scenario; (3) calculate PGA using reasonable ground-motion prediction equations (GMPE) for the earthquake scenario; (4) calculate FS_L of each soil layer using PGA and M_w from Steps (2) and (3); (5) estimate LPI according to FS_L from Step (4); (6) export LPI and the occurrence frequency of each soil layer; (7) repeat Steps (1)–(6) for earthquake scenarios from all seismic sources; (8) use R

language code as a post-process platform to process LPI and the occurrence frequency of the corresponding PGA and M_w pairs and generate the LPI hazard curve.

The input data files of the HAZ45PL Module include the seismic source and the soil property data files. Input data of seismic sources are obtained from Central Geological Survey [17], Cheng et al. [18], and Cheng et al. [19]. In Taiwan, seismogenic sources can be categorized as follows: (1) shallow regional source, (2) deep regional source, (3) crustal active fault source, (4) subduction interface source, and (5) subduction intraslab source. Because the contribution of the deep regional source is much less comparing to other seismic sources [20], in order to shorten the analysis time, the deep regional source is not included in the current HAZ45PL Module. The needed input data of soil properties are unit weight, SPT N, fines content, plastic index, and clay content.

GMPEs used in the current version of the HAZ45PL Module are built in equations for regional, crustal, and subduction seismic sources. Two crustal GMPEs, Lin11 [21] and CY14 [22], are selected for regional and crustal sources. Lin11 was built using a GMPE model for the tectonic setting of Taiwan and the mostly used GMPE in Taiwan. Lin11 includes the site response effect and the hanging wall and footwall effect on GMPE. CY14 is a GMPE from NGA-West2 selected for considering the ground-motion prediction model uncertainty (epistemic uncertainty) in the HAZ45PL Module. CY14 was built using a GMPE model for the tectonic setting similar to Taiwan and also includes the site condition effect and the hanging wall and footwall effect on GMPE. LL08 [23] and BCH16 [24] are two GMPEs selected for subduction sources. LL08 was built using data of subduction earthquakes in Taiwan and is also the mostly used GMPE in Taiwan. BCH16 is for worldwide subduction earthquakes and selected for considering the ground-motion prediction model uncertainty (epistemic uncertainty) in the HAZ45PL Module. In the current version of HAZ45PL Module, in order to simplify the analysis process, the variation of GMPE on PGA is estimated using the three-point approximation method [25].

Five frequently used simplified liquefaction evaluation procedures for FS_L calculation in Taiwan are included in the HAZ45PL Module as follows: National Center for Earthquake Engineering Research (NCEER) procedure [26], Hyperbolic Function (HBF) procedure [27], Japan Road Association (JRA) procedure [28], Tokimatsu and Yoshimi (T-Y) procedure [29], and Architecture Institute of Japan (AIJ) procedure [30]. FS_L estimated from the above procedures are used to obtain LPI following equations from Iwasaki et al. [2]:

$$LPI = \sum_{i=1}^{n} F_i \times W_i \times H_i, \qquad (1)$$

where i is the layer number (total number of soil layers is n), $F_i = 1 - FS_{L_i}$ ($F_i = 0$ for $FS_{L_i} \geq 1$), $W_i = 10 - 0.5 \, Z_i$ is the weighting factor for i^{th} layer and Z_i is the depth (in meters) of

i^{th} layer, and H_i is thickness (in meters) of ith layer. The liquefaction potential is categorized in four levels: (1) LPI = 0, the liquefaction potential is very low; (2) $0 < \text{LPI} \leq 5$, the liquefaction potential is low; (3) $5 < \text{LPI} \leq 15$, the liquefaction potential is high; and (4) $15 < \text{LPI}$, the liquefaction potential is very high. The uncertainty of the evaluation procedure of FS_L on LPI is considered via the logic tree approach.

Apart from ground motion and soil properties, the variation of water table level is another important factor affecting the liquefaction potential. In the HAZ45PL Module, the variation of the water table level is included via the logic tree approach. The logic tree used in the HAZ45PL Module is shown in Figure 1. Weights and variations of GMPE are fixed while those of the water table level and the liquefaction potential calculation procedure can be adjusted by users.

3. Applications of HAZ45PL Module

Applications on a single location using PLHA results are demonstrated in Tainan City, and applications of PLHA results on liquefaction potential maps are demonstrated in Changhua County.

3.1. Tainan City. First, the HAZ45PL Module is applied to two sites (Annan and Xinshi Sites) in Tainan City, where a detailed investigation with 18 boreholes was performed after the 2016 Meinong Earthquake. In this study, six boreholes (BH-A1 to BH-A3 of Annan Site and BH-S1 to BH-S3 of Xinshi Site) are used for analyses. Figure 2 and Table 1 show the site locations and their information, respectively. Soil layers of Annan and Xinshi Sites are mostly Silty Sand (SM) layers or Silt (ML) layers with few Clay (CL) layers, as shown in Figure 3. Shallow SM or ML layers (<10 m) have relatively low SPT N values (<10) and water table levels are high (between 0.6 and 0.9 m below the ground surface). These make Annan and Xinshi Sites susceptible to liquefaction during earthquakes. Detailed investigation information refers to NCEER [31].

Hazard curves of LPI for boreholes in Annan and Xinshi Sites are shown in Figure 4 and the 475-year return period LPIs are listed in Table 2. Results of the pseudo-probabilistic approach using PGA and M_w pairs in Table 1 are also marked for comparisons. The water table used here is the water table during the site investigation, as listed in Figure 3. Effects of water table on LPI are discussed later. All listed liquefaction potential calculation procedures in Figure 1 are used and equal weights are assigned to each procedure in this analysis for simplicity. LPI hazard curves at the same site from different boreholes (BH-A1 to BH-A3 of Annan Site or BH-S1 to BH-S3 Xinshi Site) show different levels of variations because of the spatial variation and randomness of

soil properties. Table 2 shows that LPIs at 475-year return period (475 yr RP) differ from those of the pseudo-probabilistic approach with 475 yr RP PGA. In addition, return periods of LPIs of the pseudo-probabilistic approach are quite different between boreholes. The inconsistencies of LPIs and return periods are caused by the incapability of the pseudo-probabilistic approach to include the occurrence frequency of the PGA and M_w pairs. PGA and M_w pairs and their rate contributions to PGA at 475 yr RP at two sites are deaggregated and shown in Figure 5. Clearly, each PGA and M_w pair contributes differently to the total hazard and cannot be represented by only one PGA and M_w pair, such as used in the pseudo-probabilistic approach. The only way to obtain the correct LPI at 475 yr RP is to include the occurrence frequency of all PGA and M_w pairs in the LPI estimation.

Next, BH-S1 is used to demonstrate the effects of the water table on LPI. As a continuous random variable, the variation of the water table also can be approximated using the three-point approximation method [25]. Weights are assigned to different water table levels (shown in Figure 1) as follows: (1) High Water Table: average water table (sets at the ground surface) of the high water table period with a weighting of 0.185. (2) Yearly Average: long term water table (sets at the water table in Figure 3) with a weighting of 0.630. (3) Low Water Table: average water table (sets at 2.0 m below the ground surface) of the low water table period with a weighting of 0.185. Figure 6 and Table 3 show LPI hazard curves and the pseudo-probabilistic approach results of BH-S1 at different water table levels. It is obvious that the water table level has a significant impact on LPI and the return period. In the current practice, LPI is estimated using the pseudo-probabilistic approach with the high water table because engineers presume that the LPI at this water table level is relatively conservative. However, the conservativeness cannot be reasonably quantified using the pseudo-probabilistic approach. In PLHA, the water table fluctuation can be considered via a probabilistic approach and the LPI hazard curve can reasonably reflect effects of the water table fluctuation.

Other than the inconsistency in return period, another disadvantage of the pseudo-probabilistic approach is the provision of one LPI value (Tables 2 or 3) for engineers or owners to evaluate the need and the priority of mitigation schemes for infrastructures. For example, BH-S1 and BH-A1 have LPI = 20.6 and 36.4 from the pseudo-probabilistic approach. When LPI > 15, the liquefaction potential is very high and the mitigation plan on soil liquefaction is needed [2]. Therefore, the mitigation is necessary for infrastructures in both sites. On the contrary, PLHA can provide not only LPI but also the return period which can be converted to the probability of exceedance for ≥LPI in certain exposure period (e.g., lifetime of infrastructure) using the Poisson process. Table 4 lists the probabilities of LPI > 15 for BH-S1

Seismic source inputs	GMPE	Variation of GMPE	Water table level	Liquefaction potential calculation
Cheng et al. (2007)	Crustal source	95th percentile [0.185]	High water table	NCEER + P_L
Cheng et al. (2007)	Lin11 [0.5]*			HBF + P_L
CGS (2012)	CY14 [0.5]	Mean [0.63]	Yearly average	JRA + P_L
	Subduction source	5th percentile [0.185]	Low water table	T-Y + P_L
*[Weights]	LL08 [0.5] BCH [0.5]			AIJ + P_L
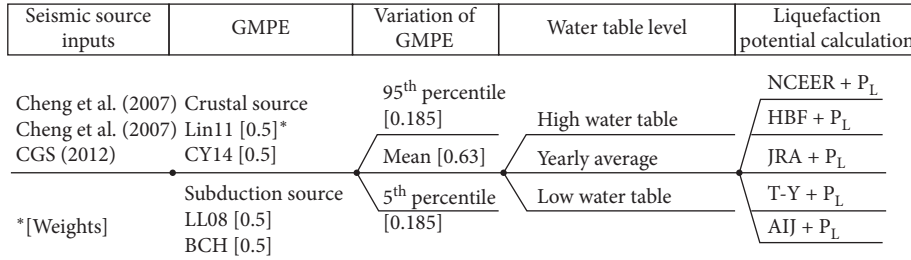
FIGURE 1: Logic tree used in the HAZ45PL module.

FIGURE 2: Location of Annan and Xinshi sites in Tainan city (from Google Earth).

TABLE 1: Information of Annan and Xinshi sites in Tainan city.

Information	Annan site	Xinshi site
Location (latitude, longitude)	(23.0253, 120.2074)	(23.0810, 120.3025)
V_{s30} (m/s)	~200 m/s	~200 m/s
PGA and M_w at 475-year return period from HAZ45PL Module	PGA = 0.47 g M_w = 6.25	PGA = 0.50 g M_w = 6.5

BH-A1 WTD[1] = 0.94 m				BH-A2 WTD[1] = 0.80 m				BH-A3 WTD[1] = 0.84 m				BH-S1 WTD[1] = 0.70 m				BH-S2 WTD[1] = 0.60 m				BH-S3 WTD[1] = 0.86 m			
Depth (m)	Soil	N	FC (%)	Depth (m)	Soil	N	FC (%)	Depth (m)	Soil	N	FC (%)	Depth (m)	Soil	N	FC (%)	Depth (m)	Soil	N	FC (%)	Depth (m)	Soil	N	FC (%)
1.50		1	75	1.50		0.66	26	1.50		22	25	1.50		11	22	1.50		22.0	93	1.50		5.0	97
3.25		2.5	56	3.25		1.33	79	3.25		1.5	24	3.25		1	94	3.25		10.0	36	3.25		2.0	52
5.00		8	97	5.00		6	78	5.00		2.5	94	5.00		7	88	5.00		4.5	90	5.00		6.0	90
6.75		1.5	33	6.75		3	65	6.75		10	63	6.75		6	96	6.75		5.0	92	6.75		8.0	95
8.50		2.5	97	8.50		4.5	86	8.50		2	91	8.50		4	97	8.50		4.0	84	8.50		3.0	97
10.25		11	51	10.25		3.5	98	10.25		8	47	10.25		10	67	10.25		11.0	75	10.25		7.0	52
12.00		10	20	12.00		18	20	12.00		19	29	11.90		9	83	12.00		9.0	79	12.00		8.0	88
13.75		28	27	13.55		19	48	13.75		12	32	13.75		10	98	13.75		14.0	96	13.75		12.0	94
15.50		15	25	15.30		18	44	15.50		3	57	15.50		8	84	15.50		6.0	89	15.50		10.0	94
16.45		24	36	17.05		17	38	18.00		37	16	17.25		7	86	17.25		13.0	82	17.25		15.0	85
18.00		31	28	18.80		42	16	20.00		25	26	19.00		13	99	19.00		15.0	97	19.00		13.0	79
				19.50		28	17					20.00		11	100	20.00		12.0	97	20.00		19.0	70
[1]WTD = water table depth				Soil type legend :		SM			CL			ML											

FIGURE 3: Investigation results of boreholes.
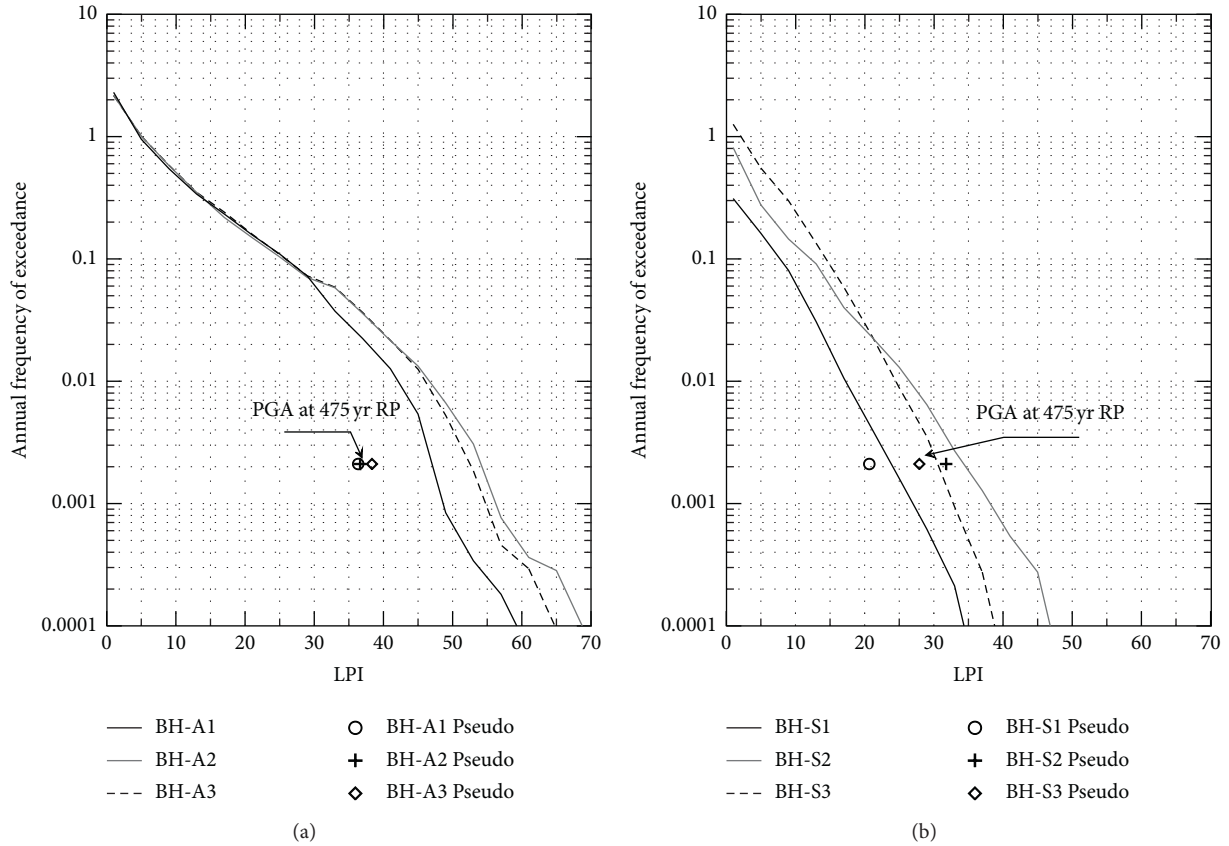
FIGURE 4: Hazard curves of LPI from the HAZ45PL Module. (a) Annan site and (b) Xinshi site.

TABLE 2: LPI results of Annan and Xinshi sites in Tainan city.

Liquefaction analysis approach		Annan site			Xinshi site		
		BH-A1	BH-A2	BH-A3	BH-S1	BH-S2	BH-S3
Pseudo-probabilistic approach with PGA at 475-year RP1	LPI	36.4	36.6	38.3	20.6	31.8	27.9
	RP year	45	28	33	222	333	238
PLHA at 475-year RP	LPI	46.5	54.5	52.5	24.0	33.5	30.5

RP = return period.
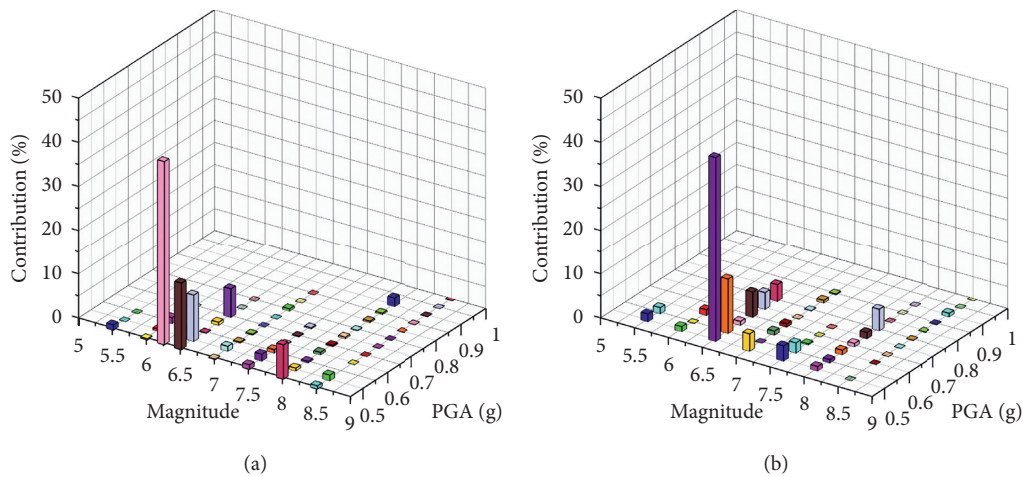
FIGURE 5: Deaggregation results of PGA at 475-year return period. (a) Annan site and (b) Xinshi site.
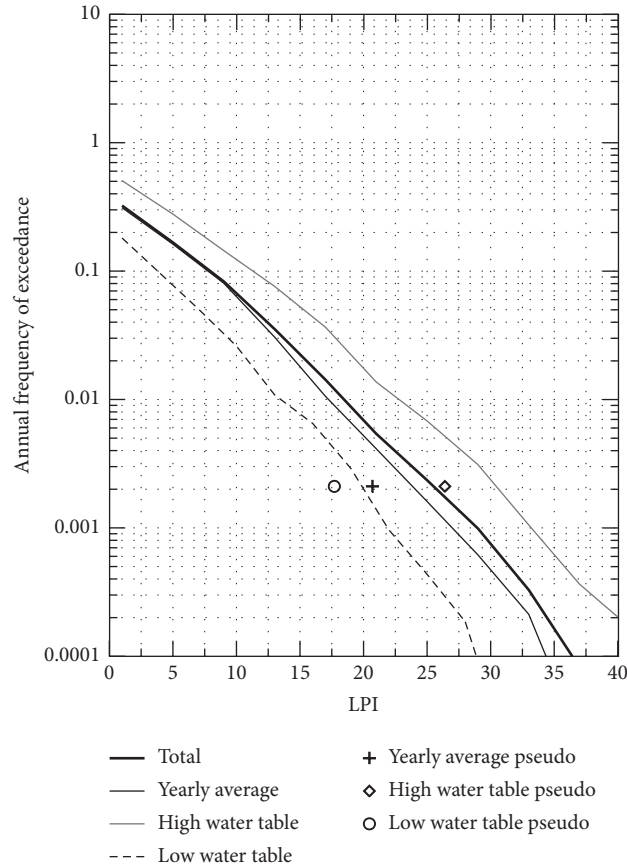
FIGURE 6: Total and unweighted LPI hazard curves from different water table levels of BH-S1.

TABLE 3: Results of BH-S1 at different water table levels.

		High water level	Average water level	Low water level
Pseudo-probabilistic approach with PGA at 475-year RP	LPI	26.4	20.7	17.7
	RP	630	170	90
PLHA at 475-yr RP	LPI		25.5	

TABLE 4: Probability of LPI > 15 during different exposure time periods.

	Return period at LPI > 15	Exposure time 100 years (%)	Exposure time 50 years (%)
BH-A1	5-year	99.9	99.9
BH-S1	52-year	85.6	62.1

and BH-A1 during different exposure periods as a reference. Engineers or owners can easily and rationally make the final design decision according to the probability information.

3.2. Changhua County. The HAZ45PL Module is applied to Yuanlin City, Changhua County (Figure 7), to demonstrate the construction of the liquefaction potential contour maps (Figures 8 and 9) using the Kriging method. In Figure 8, liquefaction potential levels follow the guidelines in Iwasaki et al. [2]. Comparing Figures 8(a) and 8(b), the pseudo-probabilistic approach obviously underestimates the liquefaction potential. In Figure 8(b), the east side of Yuanlin City is at a very high liquefaction potential. For future infrastructure or mitigation projects in this area, engineers and owners must
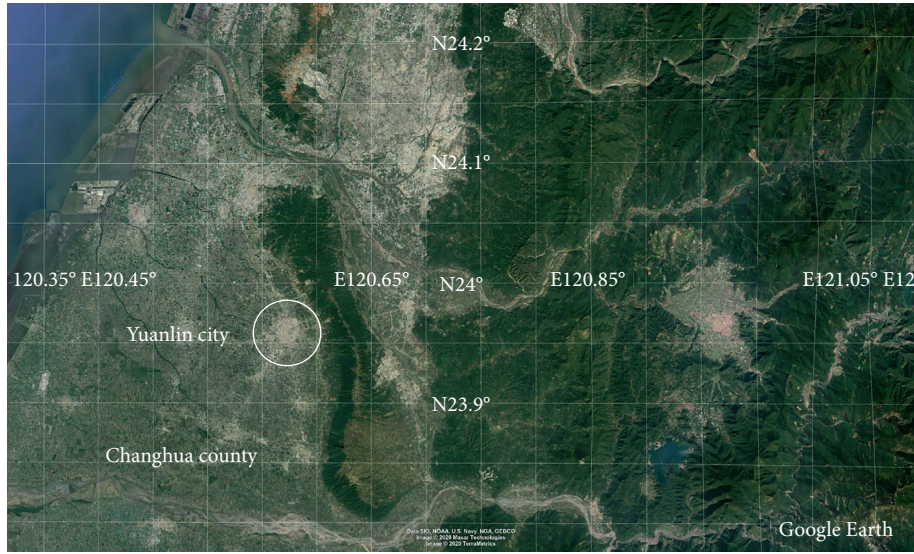
FIGURE 7: Location of Yuanlin City, Changhua County (from Google Earth).
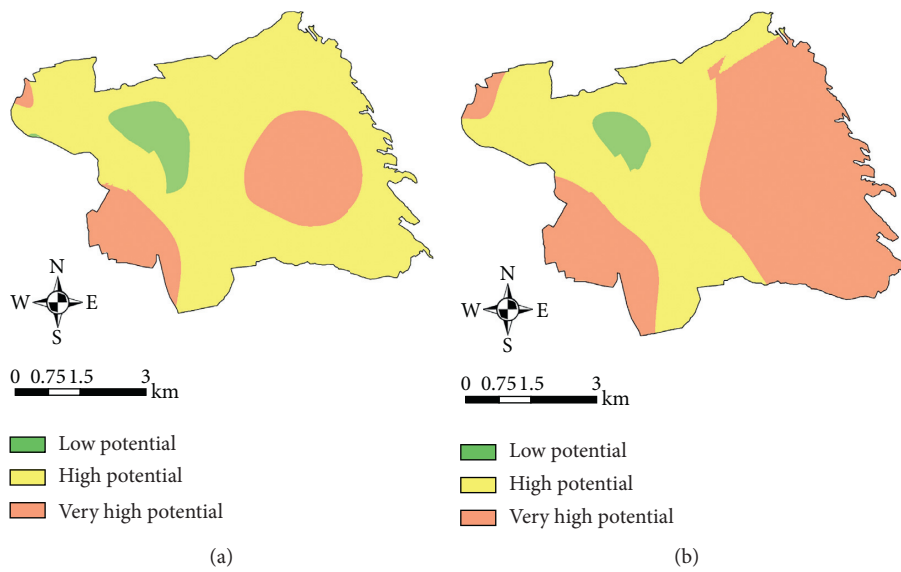
FIGURE 8: Liquefaction potential level at 475-year return period. (a) Pseudo-probabilistic approach and (b) PLHA.

optimize the mitigation plan and prioritize the site. As mentioned earlier, PLHA can provide the probability of exceedance in different exposure periods. Figure 9 shows probabilities of exceedance having LPI ≥5 (high liquefaction potential) and LPI ≥ 15 (very high liquefaction potential) in 50 years. Inside the very high liquefaction potential level area (the east side of Yuanlin City), probabilities in Figure 9(b) are divided into three groups

20%–40%, 40%–60%, and 60%–80%. Comparing to use only Figure 8(b) as a reference, engineers or owners can make reasonable choices on the construction site or the mitigation plan for infrastructures or other buildings based on the probability information shown in Figure 9(b). The probability information also provides a valuable reference for the government to make an appropriate emergency response and evacuation plan.
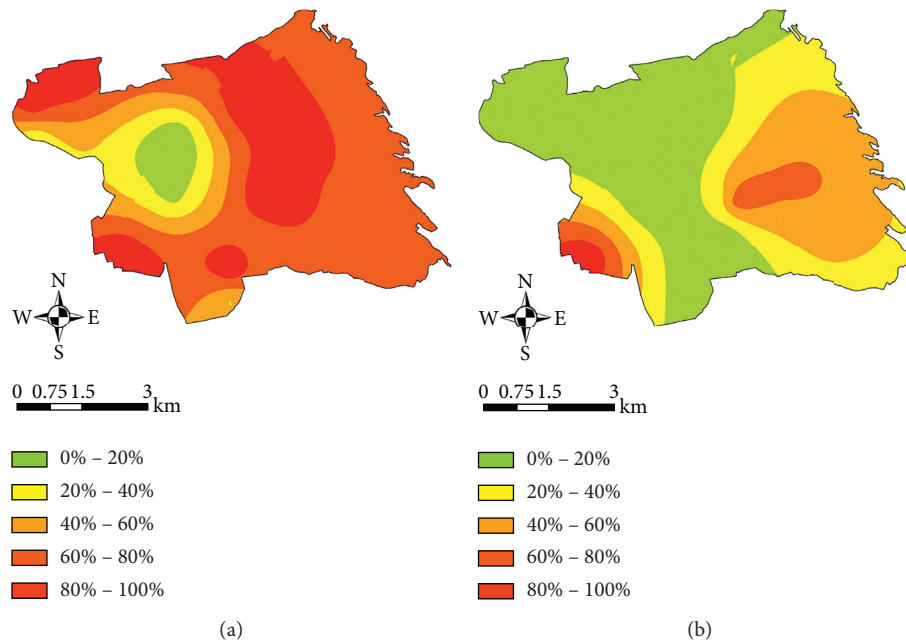
FIGURE 9: Liquefaction probability map. (a) Prob. of exceedance having LPI $\geq$ 5 in 50 years and (b) prob. of exceedance having LPI $\geq$ 15 in 50 years.

4. Conclusions

After the 2016 Meinong Earthquake, in response of the public concern on the soil liquefaction hazard, the central government initiated a project to evaluate and construct the liquefaction potential map. The common procedure used for constructing these maps is called the pseudo-probabilistic approach, which uses a pair of PGA and M_w at the selected return period with a "representative" water table level to estimate LPI for the map. The use of the pseudo-probabilistic approach has two weakness points: (1) the inconsistent return period of the estimated LPI and (2) the difficulty to select a representative water table level. PLHA was introduced to incorporate the occurrence of the ground motion (PGA and M_w pairs) into LPI calculation to solve the inconsistency issue. In addition, the difficulty of water table level selection can also be solved in PLHA via the logic tree or the probability density function. However, given the lack of an appropriate tool, PLHA is not popular in Taiwan. In this study, a simple PLHA program, HAZ45PL Module, is developed for engineers in Taiwan to obtain the LPI in a probabilistic way.

The HAZ45PL Module is applied to two selected sites to demonstrate the use of PLHA results, the hazard curve of LPI and the liquefaction probability map. With the LPI hazard curve and the Poisson process, PLHA can provide the probability of exceedance information to construct liquefaction probability maps, which enable engineers or owners to easily assess the performance of an infrastructure or to design a mitigation plan. The government can make an emergency response and evacuation plan according to the liquefaction probability map too. The liquefaction probability map was not introduced or used in previous PLHA studies.

In the current HAZ45PL Module, to keep the calculation simple and easy, the variability of the liquefaction resistance of soil is not included and the variations of PGA from GMPE are estimated using the three-point approximation. The ongoing modification of the HAZ45PL Module addresses these issues. Moreover, using the liquefaction potential only can indirectly assess the infrastructure or facility safety. In the next version of the HAZ45PL Module, the probability of liquefaction-related hazards (e.g., settlement of structure and uplift of underground structure) can be incorporated to provide a direct assessment.

Data Availability

The data used to support the findings of this study are available from the corresponding author upon request.

Conflicts of Interest

The authors declare that they have no conflicts of interest.

Acknowledgments

References

[1] Central Weather Bureau, 2020, https://scweb.cwb.gov.tw/zh-tw/page/disaster/6.

[2] T. Iwasaki, K. Tokida, and F. Tatsuoka, "Soil liquefaction potential evaluation with use of the simplified procedure," in

Proceedings of the International Conference on Recent Advances in Geotechnical Earthquake Engineering and Soil Dynamics, St. Louis, MO, USA, 1981.

[3] T. J. Katona, E. Győri, and L. Tóth, "Applicability of pseudoprobabilistic method of liquefaction hazard assessment for nuclear power plants at diffuse seismicity sites," *Science and Technology of Nuclear Installations*, vol. 2019, 2019.

[4] K. W. Franke, B. N. Lingwall, T. L. Youd, J. Blonquist, and J. H. Liang, "Overestimation of liquefaction hazard in areas of low to moderate seismicity due to improper characterization of probabilistic seismic loading," *Soil Dynamics and Earthquake Engineering*, vol. 116, pp. 681–691, 2019.

[5] E. M. Rathje and G. Saygili, "Probabilistic seismic hazard analysis for the sliding displacement of slopes: scalar and vector approaches," *Journal of Geotechnical and Geoenvironmental Engineering*, vol. 134, no. 6, pp. 804–814, 2008.

[6] K. W. Franke and S. L. Kramer, "Procedure for the empirical evaluation of lateral spread displacement hazard curves," *Journal of Geotechnical and Geoenvironmental Engineering*, vol. 140, no. 1, pp. 110–120, 2014.

[7] C. H. Juang, D. K. Li, S. Y. Fang, Z. Liu, and E. H. Khor, "Simplified procedure for developing joint distribution of a max and M_w for probabilistic liquefaction hazard analysis," *Journal of Geotechnical and Geoenvironmental Engineering*, vol. 134, no. 8, pp. 1050–1058, 2008.

[8] R. T. Mayfield, S. L. Kramer, and Y. M. Huang, "Simplified approximation procedure for performance-based evaluation of liquefaction potential," *Journal of Geotechnical and Geoenvironmental Engineering*, vol. 136, no. 1, pp. 140–150, 2010.

[9] C. H. Cramer, G. J. Rix, and K. Tucker, "Probabilistic liquefaction hazard maps for Memphis, Tennessee," *Seismological Research Letters*, vol. 79, no. 3, pp. 416–423, 2008.

[10] J. H. Hwang, C. H. Chen, and C. H. Juang, "Liquefaction hazard analysis: a fully probabilistic method," in *Proceedings of the Sessions of the Geo-Frontiers 2005 Congress, Earthquake Engineering and Soil Dynamics (GSP 133)*, R. W. Boulanger, M. Dewoolker, and N. Gucunski, Eds., ASCE, Austin, TX, USA, January 2005.

[11] S. L. Kramer and R. T. Mayfield, "Return period of soil liquefaction," *Journal of Geotechnical and Geoenvironmental Engineering*, vol. 133, no. 7, pp. 802–813, 2007.

[12] M. S. Dhar and C. H. Cramer, "Probabilistic seismic and liquefaction hazard analysis of the Mississippi embayment incorporating nonlinear effects," *Seismological Research Letters*, vol. 89, no. 1, pp. 253–267, 2018.

[13] K. W. Franke, K. J. Ulmer, L. T. Ekstrom, and J. F. Meneses, "Clarifying the differences between traditional liquefaction hazard maps and probabilistic liquefaction reference parameter maps," *Soil Dynamics and Earthquake Engineering*, vol. 90, pp. 240–249, 2016.

[14] C. H. Juang, C. Y. Ou, C. C. Lu, and Z. Luo, "Probabilistic framework for assessing liquefaction hazard at a given site in a specified exposure time using standard penetration testing," *Canadian Geotechnical Journal*, vol. 47, no. 6, pp. 674–687, 2010.

[15] R Core Team, *A Language and Environment for Statistical Computing*, R Foundation for Statistical Computing, Vienna, Austria, 2018, https://www.R-project.org/.

[16] Pacific Gas & Electric Company, Verification of PSHA code Haz43, GEO.DCPP.10.03 Rev 0, 2010.

[17] Central Geological Survey, 2020, http://fault.moeacgs.gov.tw/TaiwanFaults_2009/Page Content. aspx?type=C&id=5.

[18] C. T. Cheng, P. S. Hsieh, P. S. Lin, Y. T. Yen, and C. H. Chan, "Probability seismic hazard mapping of Taiwan," in *Encyclopedia of Earthquake Engineering*, p. 25, Springer, Berlin Heidelberg, 2015.

[19] C. T. Cheng, S. J. Chiou, C. T. Lee, and Y. B. Tsai, "Study on probabilistic seismic hazard maps of Taiwan after Chi-Chi earthquake," *Journal of GeoEngineering*, vol. 2, no. 1, pp. 19–28, 2007.

[20] C. T. Cheng, *Uncertainty Analysis and Deaggregation of Seismic Hazard in Taiwan*, Ph.D. Thesis, National Central University, Chung-Li, Taiwan, 2002.

[21] P. S. Lin, C. T. Lee, C. T. Cheng, and C. H. Sung, "Response spectral attenuation relations for shallow crustal earthquakes in Taiwan," *Engineering Geology*, vol. 121, no. 3-4, pp. 150–164, 2011.

[22] B. S.-J. Chiou and R. R. Youngs, "Update of the Chiou and Youngs NGA model for the average horizontal component of peak ground motion and response spectra," *Earthquake Spectra*, vol. 30, pp. 1117–1153, 2014.

[23] P. S. Lin and C. T. Lee, "Ground-motion attenuation relationships for subduction-zone earthquakes in northeastern Taiwan," *Bulletin of the Seismological Society of America*, vol. 98, no. 1, pp. 220–240, 2008.

[24] N. Abrahamson, N. Gregor, and K. B. C. Addo, "Hydro ground motion prediction equations for subduction earthquakes," *Earthquake Spectra*, vol. 32, no. 1, pp. 23–44, 2016.

[25] D. L. Keefer and S. E. Bodily, "Three-point approximations for continuous random variables," *Management Science*, vol. 29, no. 5, pp. 595–609, 1983.

[26] T. L. Youd, I. M. Idriss, R. D. Andrus et al., "Liquefaction resistance of soils: summary report from the 1996 NCEER and 1998 NCEER/NSF workshops on evaluation of liquefaction resistance of soils," *Journal of Geotechnical and Geoenvironmental Engineering, ASCE*, vol. 127, no. 10, pp. 817–833, 2001.

[27] J. H. Hwang, C. H. Chen, and C. H. Juang, "Calibrating the model uncertainty of the HBF simplified method for assessing liquefaction potential of soils," *Sino-geotechnics*, vol. 133, pp. 77–86, 2012, (in Chinese).

[28] Japan Road Association (JRA), *Specification for Highway Bridges, Part V: Seismic Design*, Japan Road Association, Japan, 1996.

[29] K. Tokimatsu and Y. Yoshimi, "Empirical correlation of soil liquefaction based on SPT N-value and fines content," *Soils and Foundations*, vol. 23, no. 4, pp. 56–74, 1983.

[30] Architecture Institute of Japan (AIJ), *Recommendations for Design of Building Foundations*, Architectural Institute of Japan, Japan, 2001, in Japanese.

[31] National Center for Research on Earthquake Engineering (NCREE), *Research Report*, National Center for Research on Earthquake Engineering, Taiwan, 2016, in Chinese.

Research Article

Interactional Effect of the Influential Parameters on Seismic Behaviour of the Concrete Surface Tanks

Alirezar Hassanpour Yasaghi,[1] Mazhar Fatahi [iD],[2] and Seyed Mehdi Seyed Alizadeh[3]

[1]*Department of Civil Engineering, Islamic Azad University, Mashhad, Iran*
[2]*Department of Civil Engineering, Loghman Hakim Golestan Non-Profit Institute, Agh-Ghala, Iran*
[3]*Petroleum Engineering Department, Australian College of Kuwait, West Mishref, Kuwait, Kuwait*

Correspondence should be addressed to Mazhar Fatahi; mazharfatahi@gmail.com

Given to the importance of the tanks and their various applications in different industries, studying the seismic behaviour of these facilities is essential. In such structures, obtaining exact theoretical solution for the seismic behaviour of the tanks is very difficult due to the existence of the soil-structure interaction. In this study, seismic behaviour studying has been taken into account and in addition to considering three-dimensional model of finite element model of a surface rectangular tank and its beneath soil given to SSI and FSI effect, we have done required analysis and Drucker–Prager nonlinear model has been used to investigating more exactly to describe soil behaviour. Euler–Lagrange view with optional mesh displacement has been used for modelling tank-water interaction. According to the obtained results from this modelling, soil beneath the tank and soil-structure interaction affect highly on seismic behaviour of the surface tanks. Meanwhile, the response of the structure to the density changes and soil modulus of elasticity is more sensitive and changes in the coefficient of friction coefficient between the foundation surface and the soil and the internal friction angle do not have tangible effect on the response. The results reveal that the liquid containers response is more sensitive to the changes of the density and the soil modulus of elasticity more than friction coefficient between the surfaces and foundation and internal angle friction.

1. Introduction

Due to the expansion of cities and the development of industries, the need for storage tanks for fluids such as water, oil, chemicals, and fuel has increased. One of the main pressures on this kind of structures is the pressure of the earthquake and considering that the country is very seismic then maintenance and continuous exploitation of such facilities when earthquake is occurred and after that is essential. For example, water tanks hitting due to earthquake will lead to significant problems such as inability to extinguish fire results from earthquake and lack of access to potable water. Selected model, concrete surface tank to supply potable water, is obtained according to the actual tank which was established in 1395 in Kermanshah (Figure 1).

Given to the importance of the tanks and their various applications in different industries studying the seismic behaviour of these facilities is essential. In such structures, obtaining exact theoretical solution for the seismic behaviour of the tanks is very difficult due to the existence of the soil-structure interaction. In this study, seismic behaviour studying has been taken into account and in addition to considering three-dimensional model of the finite element model of a surface rectangular tank and its beneath soil given to SSI and FSI effect, we have done required analysis and Drucker–Prager nonlinear model has been used to investigating more exactly to describe soil behaviour. Euler–Lagrange view with optional mesh displacement has been used for modelling tank-water interaction.

Up to date, various studies have been conducted regarding seismic behaviour of the tanks. Jacobsený was

FIGURE 1: Concrete surface tank with 5000 m^3 volume in Kermanshah.

among the first researchers who had done many studies on dynamic behaviour of the water tanks. He In 1954, modeled a cubic and cylindrical fluid storage tank [1]. He also calculated the hydrodynamic pressure distributed by the fluid and the height of the surface waves caused by the horizontal vibrations using a mass-spring dynamic system [2]. Haron and Housner developed a single ring model using finite element model and integral boarder assumption for the fluid model and the crust around it as a reliable method for dynamic analysis of the flexible tanks [3]. Haron (1992) further studied an experimental model for the tanks established on the soil given to the soil-tank interaction effect. Then, numerical methods, especially finite element was used broadly to model carefully fluid behaviour in addition to the tank behaviour. Bernal [4] studied seismic response of the cylindrical tanks on the earth under the earthquake record using three-dimensional finite element models [5].

Heavy damages have been reported due to the frequent and strong earthquakes such as Niigata (1934), Alaska (1964), Parkfield (1966), Imperial City (1979), Coalinga (1983), Northridge (1994), Cocalo (1999), and Beijing (2001) that some of them have been reported by Adlparvar et al. [6], Mohammadi et al. [7], and Ibarra and Krawinkler [8]. Concrete tanks are damaging greatly too. For instance, so many concrete tanks are broken when they are rising in height or are damaged strongly in Chili earthquake in 1960 and Beijing earthquake in 2001. In addition, big and intense damages were imposed to rectangular tanks under the earth which has been reported by Kim and Kim [9] in Kobe earthquake.

After that, Husner has formulated ideas in 1957 [10] and 1963 [11] which are usually used in the civil engineering course to meet seismic response of the liquid in rigid and flexible rectangular and cylindrical tanks. This liquid is considered as incompressible and inviscid. In this method, hydrodynamic pressure resulted from seismic excitation has been divided to the thermal and impact components using approximate value for lump mass. Impact pressure is generated by a part of the liquid or tank acceleration while thermal pressure is generated by a part of the liquid

oscillation in the tank. Accordingly, Husner has decreased these pressures by expanding simplified statements or lump mass model. Lump mass from impact pressure point of view is connected intensively to the tank's wall but lump mass from thermal pressure point of view is connected to the wall's tank using the sources. This model with some changes is approved in many current codes and standards [12].

2. Methods and Materials

2.1. Fluid-Structure Interaction (FSI). Fluid-structure interaction (FSI) is the interaction of some movable or deformable structures with an internal or surrounding fluid flow. In this article, contact element is used to introduce interaction. In this element, all forces are transferred in two tangential and vertical directions from a surface to another one. Tangential behaviour (tangential components) includes relative motion (slide) of the surfaces and if shear stresses are existed as the effect of the friction. To determine whether transferable shear forces between the surfaces are in contact with each other, analysis needs calculation of the friction forces which is resisted against relative slide between the surfaces. One of the common models in defining tangential components of the interaction between the contact surfaces is Coulomb friction model. It determines the friction behaviour between the contact surfaces using a friction coefficient μ. Default friction coefficient is zero. Tangential displacement will be zero to the extent which surface tension does not exceed a critical value for shear stress. Shear stress is determined as the following equation [13]:

$$\tau_{\text{crit}} = \mu\rho, \tag{1}$$

in which μ is the friction coefficient and ρ is the contact pressure between two surfaces. This equitation gained limit value for shear stress for the participated surfaces in the contact. Contact surfaces will not have any slide on each other up to the time when shear stress between them becomes equal to the limited friction shear stress; for the most surfaces, μ is usually less than 1. To define water-structure interaction from Euler–Lagrange view with optional mesh

displacement has been used in which intense transformations of the mesh are limited and generation of the new meshes is allowed at every moment in the transformed points. Indeed in this approach, it is assumed that the displacement of the mesh nodes is independent of the modelled materials and indeed can flux inside the mesh. One of the main advantages of this method is that it provides the possibility of local amendment of the mesh without changing the whole mesh. On the other hand, it can be said that investigated materials are fixed but its mesh is changing every moment and the solution is transferred from the first to the second unit. Euler relation (relation (2)) is written as below just by taking hydrodynamic pressure into account from the following equation [14]:

$$\rho \frac{D\overrightarrow{V}}{Dt} = -\overrightarrow{\nabla} p. \tag{2}$$

Therefore, prominent assumptions on Euler equation (in the third type interaction) are small displacements, non-rotating motion, and ignoring viscosity (adhesion effect). Given to the abovementioned three assumptions, prominent equation on the tank's water is the same as Euler equation. By taking into account the hydrodynamic pressure, equation (3) can be extracted [15]:

$$\rho \frac{D\overrightarrow{V}}{Dt} = -\overrightarrow{\nabla} p \longrightarrow \rho \frac{\partial \overrightarrow{V}}{\partial t} + \rho (\overrightarrow{\nabla} . \overrightarrow{V}) \overrightarrow{V} = -\overrightarrow{\nabla} p. \tag{3}$$

Given that displacement range and speed in the third type interaction is very limited, then the second statement in the left hand of the equation can be ignored. Therefore, the final form of the prominent Euler's equation of motion is obtained as the following equation [16]:

$$\rho \frac{\partial \overrightarrow{V}}{\partial t} = -\overrightarrow{\nabla} p. \tag{4}$$

2.2. Soil-Structure Interaction (SSI).

The concept of structure-soil-structure dynamic interaction was introduced, and the research methods were discussed [17]. Based on several documents, a systematic summary of the history and status of the structure-soil-structure dynamic interaction research that considers adjacent structures was proposed as a reference for researchers [18]. The most common way to solve soil-structure interaction problem is analysis according to substructure method. In this approach, linear problem of soil-structure interaction is divided into a series of subproblems and then the results are combined using superposition principle. In the approach of the separation and dividing of the substructures [19], the whole system of soil-structure is represented in Figure 1 which is divided into three substructures. I substructure includes the free field of the site, II substructure includes excavated soil volume, and III substructure includes surface structure and its foundation. In the method of separation of the substructures, it is assumed that the soil-structure interaction is occurred only in the common boarders of the substructures, contact surface, or soil. Substructures' equation of motion

represented in Figure 1 can be written in a matrix form of the following equation [20]:

$$[M]\{\ddot{\widehat{u}}\} + [K]\{\widehat{u}\} = \{\widehat{Q}\}. \tag{5}$$

For imposed harmonic excitation, with ω frequency, load vector and displacement can be written as the following equations [21]:

$$\{\widehat{Q}\} = \{Q\}\exp(i\omega t), \tag{6}$$

$$\{\widehat{u}\} = \{u\}\exp(i\omega t). \tag{7}$$

When $\{Q\}$ and $\{u\}$ are integrated force vector and displacement in ω frequency. Therefore, for each frequency, the equation of motion will be as the following equations [22]:

$$[C]\{Q\} = \{Q\}, \tag{8}$$

$$\{\widehat{u}\} = \{u\}\exp(i\omega t). \tag{9}$$

The equation of motion for the soil-structure interaction system is separated as the following equation [23]:

$$\begin{bmatrix} C_{ii}^{III} - C_{ii}^{II} + X_{ii} & -C_{iw}^{II} & C_{is}^{III} \\ -C_{wi}^{II} & -C_{ww}^{II} & 0 \\ -C_{si}^{III} & 0 & C_{ss}^{II} \end{bmatrix} \begin{Bmatrix} u_i \\ u_w \\ u_s \end{Bmatrix} = \begin{Bmatrix} X_{ii}u \\ 0 \\ 0 \end{Bmatrix}, \tag{10}$$

where indices I, II, and III are related to three substructures and i, w, and s indices are related to degrees of freedom corresponding to the available nodes in the border between the soil and structure, excavated soil volume, and surface structure, respectively (Figure 2) [25].

At the left hand side of the equation, the combined dynamic stiffness matrix related to the frequency indicated simply that according to the above category, the stiffness matrix of the excavated soil is subtracted from the dynamic stiffness of the structure and the free field. Matrix related to frequency $\lfloor X_{ff} \rfloor$ is called impedance matrix which is obtained from I substructure transformer. $\{u_i'\}$ or $\{u_f'\}$ vector is obtained from motion of the site's free field at the interaction points indicated in I substructure. The DOF interactions is considered between the site model and the horizontal layers during the impedance and external load vector calculations [4]. Also, the assumption of the linear transformation changes inside the layer can be divided into the Rayleigh and love wave as the algebraic eigenvalue. Using the separated soil model, eigenvalue equation for the motion of the Rayleigh wave can be written as the following equation [26]:

$$\left([A]K^2 + i[B]K + [G] - \omega^2 [M]\right)\{V\} = 0. \tag{11}$$

In this model at each border between two layers, two degrees of freedom are existed then every n layer system will have $2n$ degree of freedom. At the previous equation, ω and k are angular frequency of the mode vibration and eigenvalue, respectively, and $\{V\}$ is the component-wise $2n$ eigenvector. Dimensions of the $[A]$, $[B]$, $[G]$, and $[M]$ matrices are
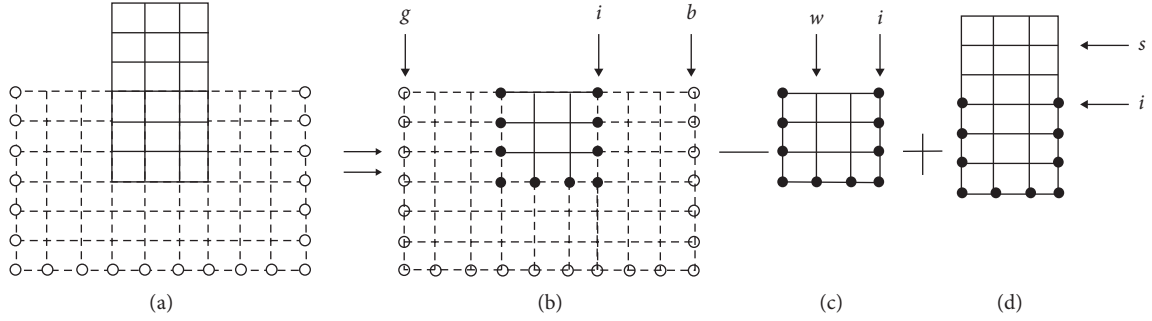
Figure 2: Separation of the substructures to simplify calculations [24]. (a) Total system. (b) Substructure 1: free field. (c) Substructure 2: excavated soil. (d) Substructure 3: build structure.

$2n \times 2n$ and these matrices are gained by summing related matrices of the sublayers. Considering the h_j as the depth, Ro_j as the density, G_j as the shear modulus and land a_j as the constant of the jth layer, then the matrix can be expressed as follows [27]:

$$[A_j] = \frac{h_j}{6} \begin{bmatrix} 2(\lambda_j + 2G_j) & 0 & (\lambda_j + 2G_j) & 0 \\ 0 & 2G_j & 0 & G_j \\ (\lambda_j + 2G_j) & 0 & 2(\lambda_j + 2G_j) & 0 \\ 0 & G_j & 0 & 2G_j \end{bmatrix}, \quad (12)$$

$$[B_j] = \frac{1}{6} \begin{bmatrix} 0 & -(\lambda_j - G_j) & 0 & (\lambda_j + G_j) \\ (\lambda_j - G_j) & 0 & (\lambda_j + G_j) & 0 \\ 0 & -(\lambda_j + G_j) & 0 & (\lambda_j - G_j) \\ -(\lambda_j + G_j) & 0 & -(\lambda_j - G_j) & 0 \end{bmatrix}, \quad (13)$$

$$[G_j] = \frac{1}{h_j} \begin{bmatrix} G_j & 0 & G_j & 0 \\ 0 & (\lambda_j + 2G_j) & 0 & -(\lambda_j - 2G_j) \\ -G_j & 0 & G_j & 0 \\ 0 & -(\lambda_j - 2G_j) & 0 & (\lambda_j + 2G_j) \end{bmatrix}, \quad (14)$$

$$[M_j]^{[l]} = \frac{\rho_j h_j}{6} \begin{bmatrix} 0 & 0 & 0 & 0 \\ 0 & 1 & 0 & 0 \\ 0 & 0 & 1 & 0 \\ 0 & 0 & 0 & 1 \end{bmatrix} [M_j]^{[c]} = \frac{\rho_j h_j}{6} \begin{bmatrix} 2 & 0 & 1 & 0 \\ 0 & 2 & 0 & 1 \\ 1 & 0 & 2 & 0 \\ 0 & 1 & 0 & 2 \end{bmatrix}, \quad (15)$$

where $[M_j]^{[c]}$ and $[M_j]^{[l]}$ are the continuous mass and lumped mass matrices. Using numerical techniques proposed by Vas, eigenvalue equation of equation (14) can be solved. At the separation of the substructure method, SSI system motion equations, including $[X_{ff}]$ impedance matrix, are the same as shown in equation (15). In this method, impedance matrix is calculated just for border nodes (i nodes in Figure 2). In each frequency, the

impedance matrix analysis is calculated by dynamic softness matrix. In the three-dimensional problems, the problem of estimating dynamic softness matrix is decreased to the problem of finding the response of horizontal layer system to the loading at the border of the layers. After the calculation of the elements of the mass and stiffness matrices, the motion equation will be as the following equation [28]:

$$\begin{bmatrix} C_{CC} & C_{CP} \\ C_{PC} & C_{PP} + R \end{bmatrix} \begin{Bmatrix} u_c \\ u_p \end{Bmatrix} = \begin{Bmatrix} Q_c \\ 0 \end{Bmatrix}, \quad (16)$$

in which C is the dynamic stiffness matrix ($C = K - \omega^2 M$) and R is the impedance matrix of the energy absorbing borders. p and c indices are related to the degrees of freedom on the border line and circumference of the modulus u_c and u_p is the amount of the correspondent displacements. Displacement of the external nodes of the model ($r > r_0$) is obtained by the following equation [29]:

$$\{u(r)\}_m = [w(r)]_m \{\Delta\}_m. \quad (17)$$

The m index is related to the Fourier harmonic degree and the vector below modal participation coefficient, related to $3n$, is the transformational mode of the n layer soil system:

$$\{\Delta\}_m^T = \langle \alpha_1, \alpha_2, \ldots, \alpha_{3n} \rangle, \quad (18)$$

and $[W(r)]_m$ matrix is a $3n \times 3n$ matrix which is a function of radial distance from the model axis, eigenvalue, eigenvector, and Hankel function of the second kind of the mth degree [30]. Having modular participation vector, equation (11) is applied to calculate displacement, at each point with radial distance r from the axis of the model. Dynamic softness matrix at each analysis frequency is a $3i \times 3i$ matrix for a system with i interactional node at the environment of the soil-free field.

3. Numerical Modelling

In this study, using limited components software, a conducted tank in reality is studied dynamically and three-dimensional. Then, one of the surface tanks of the

Kermanshah is selected and the solid element is used for modelling [31].

3.1. Mechanical Characteristics of the Material.

To state the behaviour of the steel, nonlinear behaviour with kinematic hardening is used. Plastic behaviour of the model is based on von Mises yield criterion and is selected based on stress-strain graph ST37. Given to Figure 3, Young's modulus and Poisson's ratio are considered as $2 \times 10^6 \text{ kg/cm}^2$ and 0.3, respectively [32].

Behaviour al model which has been taken into account for soil in this article is the Drucker–Prager model in which identical theory of elasticity is used for the elastic behaviour and hardening Drucker–Prager plasticity model is used for plasticity behaviour. This model is known as the nonlinear model of the soil behaviour using modified Drucker–Prager plasticity model (cap) in which yield surface, flow rule, and hardening rule should be taken into account too [33]. Drucker–Prager surface of rapture is obtained from the below relation [34]:

$$F_s = t - p \tan \beta - d = 0, \qquad (19)$$

$$F_s = t - p \tan \beta - d = 0, \qquad (20)$$

in which $\beta(\theta, f_i)$ and $d(\theta, f_i)$ represented friction angle of the material and its adhesion, respectively, and can be affected by temperature, θ, and other defined factors. t and P are the amount of deviator stress and equivalent compressive stress, respectively [33].

To study the effect of the soil type in soil-structure interaction, three kinds of soil, soft, moderate, and hard, are used and obtained results are compared with each other. Characteristics of the soil used in the models are indicated in Table 1 [35].

In Table 1, φC and ψ are soil's internal friction angle, adhesion, and soil dilation angle, respectively. This model is stated using nonlinear behaviour in the compressive area and linear behaviour in the tensile area [33]. Meanwhile, Table 2 is used to introduce concrete through linear behaviour and Figure 4 through nonlinear behaviour [36].

To introduce the fluid inside the tank water with density 1000 kg/m^3, dynamic viscosity 0.0013 N·sec/m^2 and shear wave velocity in water 1400 m/s have been taken into account. The selected tank is located in Jungle Street in Kermanshah. Total dimensions of this tank are $50 * 40$ with nearly 4 m height. The twin tank is established to supply potable water of Kermanshah in 1395.

3.2. Geometrical Specifications of the Model.

This tank includes 36 columns with 3 m height and $40 * 40$ cm dimensions and $60 * 60$ cm crown. The tank includes foundation, surrounding walls and middle wall, columns, and ceiling (Figure 5).

To mesh the geometric model of the tank, its columns and walls, hexagonal 8-node elements have been used; the final model is shown in Figure 6.

3.3. Loading.

For doing dynamic analysis, seismic excitation is imposed through low borders as a time history of the displacement on the model used. These excitations are transient and in the direction of the X axis (Figure 7). Meanwhile, since just the effect of the influential parameters on the response of the structure has been investigated, then seismic load is imposed only in the horizontal direction on the soil mass [37].

4. Results Analysis

So many factors are affecting on seismic response of the surface tanks including soil type, soil's modulus of elasticity, angle of friction between the structure (foundation) and soil, height of the fluid inside the tank, and flexibility of the tank's wall. In this study, it is tried to study how the first few factors are influential [38].

4.1. The Effect of the Soil Type.

Time history of the horizontal displacement in the direction of the load imposed above the tank for different kinds of the soil is shown in Figures 8 and 9. Given to this diagram, it can be seen that the horizontal displacement on the tank is more in the soft soil than moderate and hard soils. Indeed, the lower the shear waves velocity in the soil, the greater the effect of soil-structure interaction on the analysis and the softer the structure and the more displacement on the tank will occur. Increasing the effect of the soil-structure interaction raises damping of the structure, decreases input displacement, and decreases frequency of the structure (increased period of the structure and therefore its softening). The effect of the soil type in the shear stress generated at the foot of the tank (at the connection site of the tank with foundation) is represented in Figures 8 and 9. As it can be seen, stress on the tank foot in the soft soil is less than moderate and hard soil. As it is said before, by reducing the shear wave velocity in the soil, the effect of soil-structure interaction increases and, as a result, the stress decreases (stress decreases as the effect of seismic input decreased and damping increased).

4.2. The Effect of the Soil Density.

With decreasing the soil density, maximum displacement increases above the tank. With decreasing density by 15%, the soil becomes softer and the soil-structure interactional effect increases and therefore the structure becomes softer and maximum displacement increases by nearly 17%. Maximum shear stress at the foot tank can be seen in Figures 10 and 11. By decreasing soil density by 15%, soil becomes softer and interactional effect and maximum tension decrease.

4.3. The Effect of the Soil Modulus of Elasticity.

As it can be seen in Figures 12 and 13 with 30% decrease in the soil modulus of elasticity, maximum displacement increases 50% above the tank. With decreasing modulus of elasticity by 30%, the soil becomes softer and soil-structure interactional effect increases and therefore the structure becomes softer and maximum displacement increases by 16%.
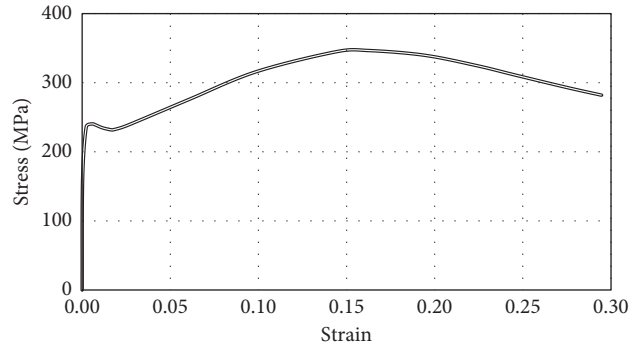
FIGURE 3: Steels' behaviour al nonlinear model.

TABLE 1: Characteristics of the soil used in the model.

Soil type	ρ (kg/m^3)	E (MPa)	ν	φ	C (N/m^2)	ψ
Hard soil	2000	10	0.4	35	0.8	4.81
Moderate soil	1700	7	0.4	35	0.8	4.81
Soft soil	1500	5	0.4	35	0.8	4.81

TABLE 2: Characteristics of the concrete used in the tank and foundation.

ρ (kg/m^3)	ν	E (GPa)
2450	0.2	19.7
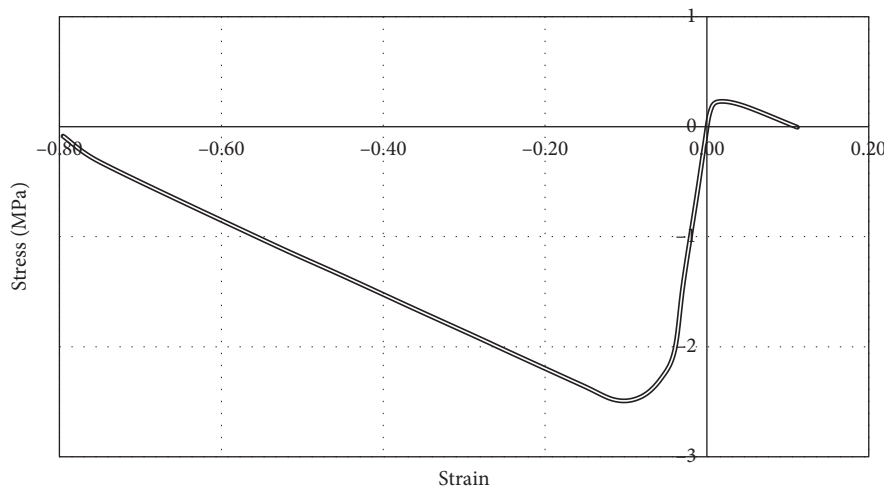
FIGURE 4: Compressive and tensile behaviour of the concrete [33].

4.4. The Effect of the Friction Coefficient between the Soil and Foundation of the Tank. To study the interactional effect on the seismic response of the surface tank, friction coefficients between the foundation and soil surfaces are considered as 0.1, 0.2, 0.4, and 0.7. It is seen that with increasing friction coefficient between the soil and foundation surfaces, maximum displacement above the tank increases. Indeed, with increasing the friction coefficient between the soil and foundation surfaces, slip between the surfaces decreases and input displacement to the tank increases and therefore maximum displacement increases above the tank. On the other hand, with increasing the soil stiffness by nearly 15%, maximum amounts of the displacement decreases by 15% too (Figure 14).

4.5. The Effect of the Soil's Angle of the Internal Friction Amount. With increasing internal angle friction of the soil, maximum displacement decreases too. With the effect of the internal angle of the friction of the soil by 6 times, involvement between the soil granules increases and interactional effect decreases and therefore maximum

Foundation   Ceiling   Walls

Column   Column armature networking   Foundation armature networking

Total geometrical figure of the tank
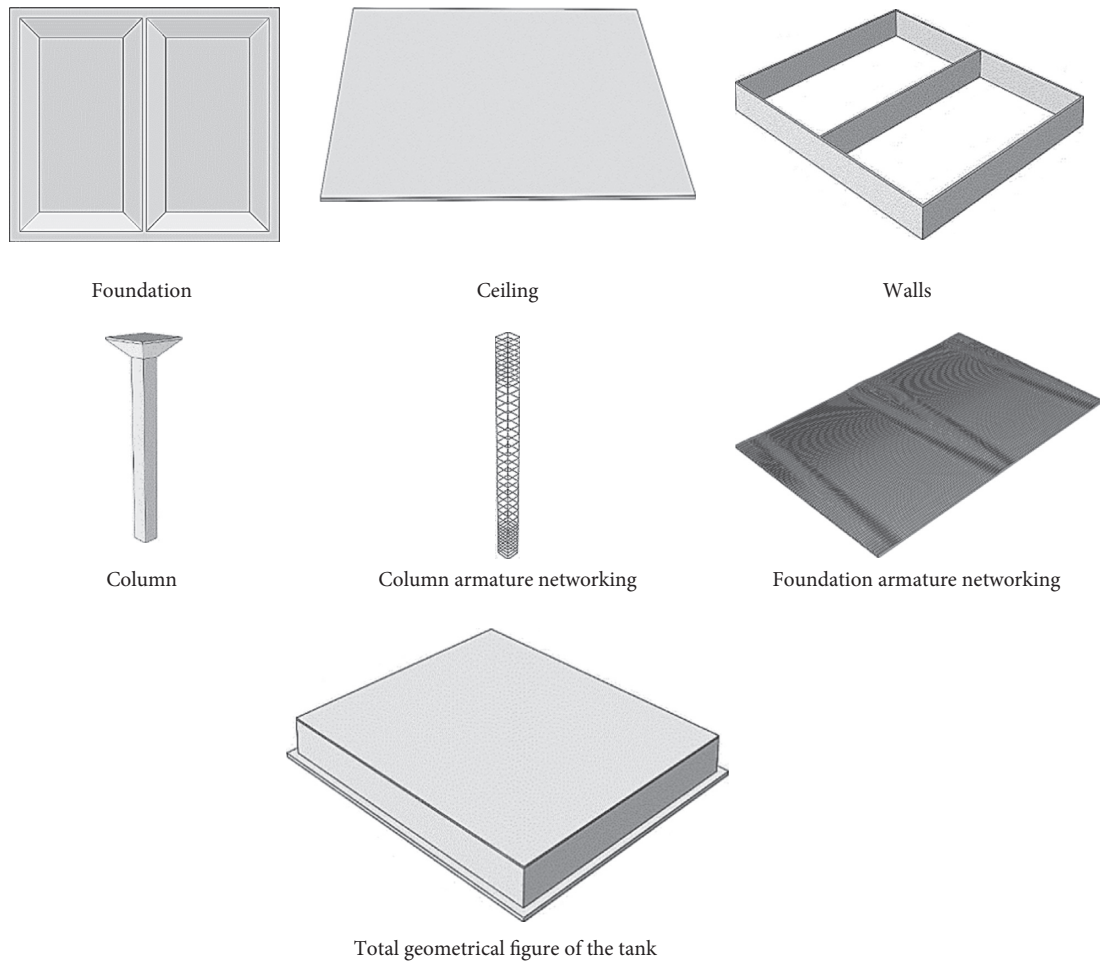
FIGURE 5: Geometrical scheme of the finite components model of the surface tank.
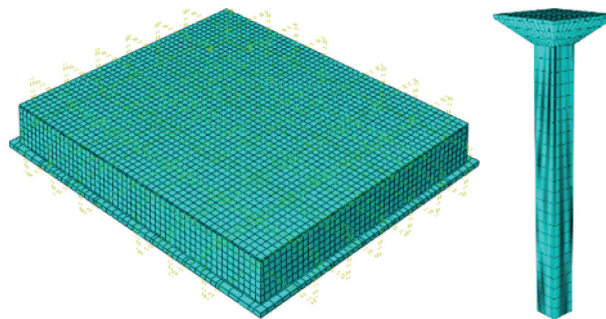
FIGURE 6: Numerical meshing model.

displacement above the tank decreases intangibly less than 1% (Figure 15).

4.6. The Effect of the Fluid (Water) Height inside the Tank and Turbulence. To study the effect of the height inside the tank on its seismic response, the heights of the water inside the tank are considered as 2, 5, and 7 and displacement above the tank and stress at the foot of the tank have been calculated in the moderate soil. Figure 16 indicated the time history of the shear stress on the foot of the tank in three states of the water

height inside the tank and in moderate soil. With increasing the water height inside the tank by 2 m, hydrodynamic pressure of the water imposed to the wall of the tank increases and, on the other hand, led to increase in mass of the tank and therefore greater seismic force is imposed to the tank and then stress on the foot of the tank decreases by nearly 20%.

To study turbulence effect, two samples in turbulence and without turbulence states are modelling whose results are compared in Figure 17. Shear stress at the foot of the tank by taking turbulence of the water into account will be nearly
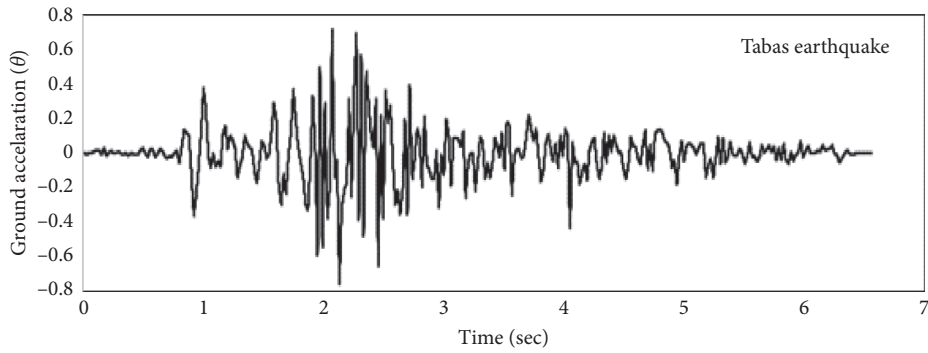
FIGURE 7: Accelerograph of the Tabas earthquake.
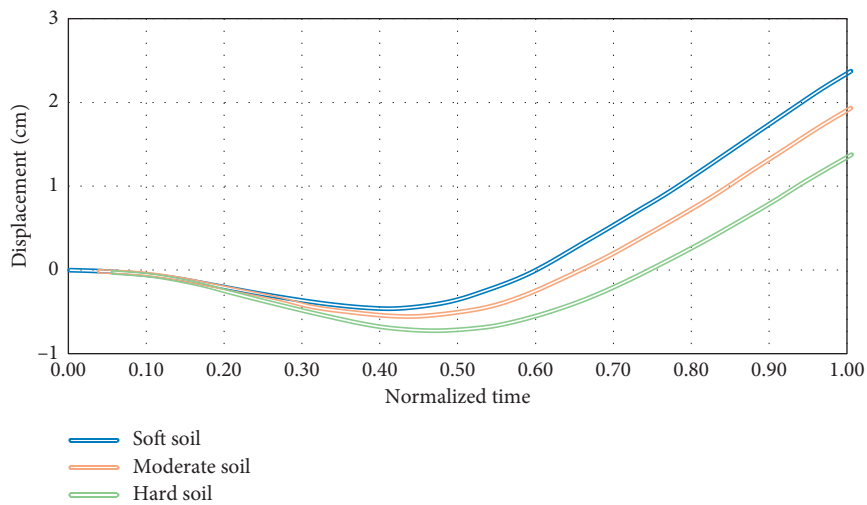
FIGURE 8: Time history of the horizontal displacement above the tank.
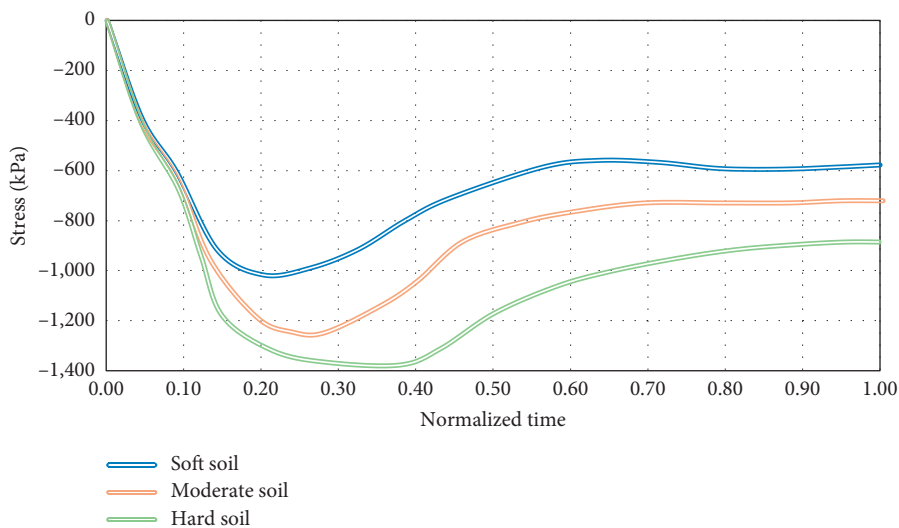
FIGURE 9: Time history of the shear stress in the connection site of the tank with foundation.

30% higher than base stress from the size point of view. The response variation rates must be considered to estimate the parameters effects on reservoir tanks behavior. Then, a parameter as λ is defined which is obtained through the following relation: λ = absolute (quotient of the changes percent of the responses to the changes of the given parameter).

Figure 18 indicated that the structure response is more sensitive to the changes of the density and soil's modulus of elasticity and changes of the friction angle between the soil
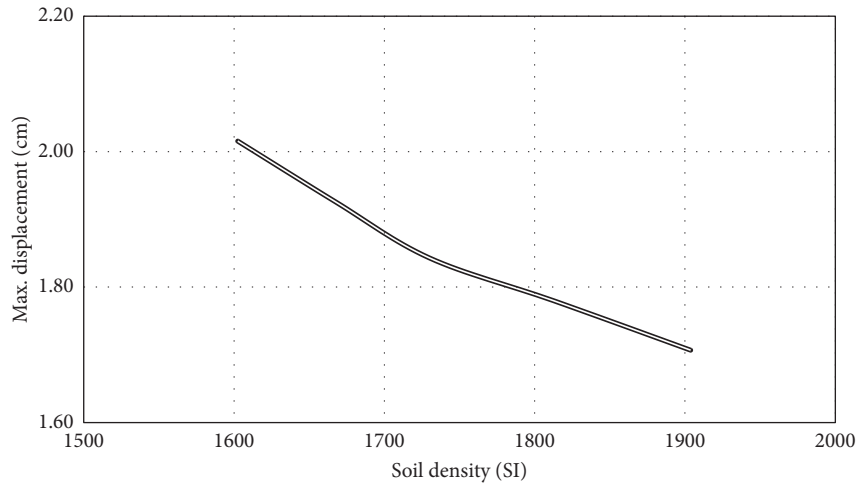
Figure 10: Maximum changes of the displacement above the tanl in terms of the soil density.
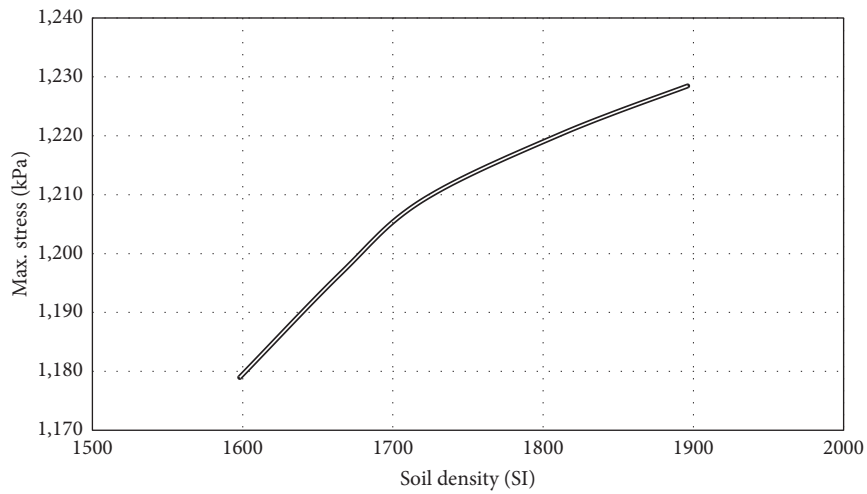
Figure 11: Maximum changes of the pressure on the foot of the tank in terms of the soil density.
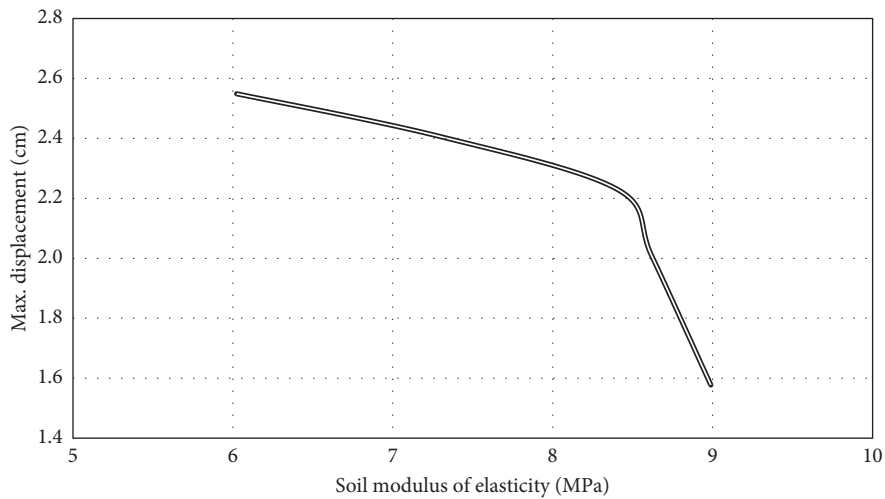
Figure 12: Maximum changes of the displacement above the tank in terms of the soil modulus of elasticity.
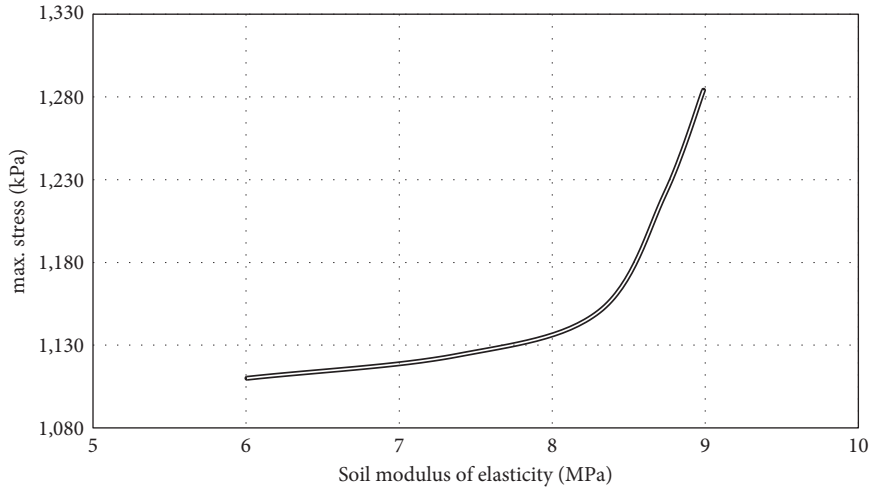
FIGURE 13: Maximum changes of the stress on the foot of the tank in terms of the soil modulus of elasticity.
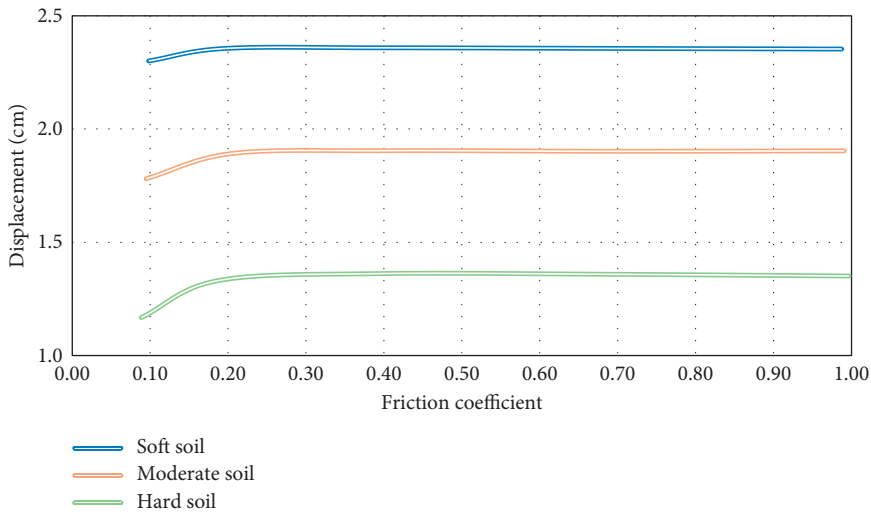
FIGURE 14: Diagram of the maximum displacement changes above the tank in terms of the friction coefficient.
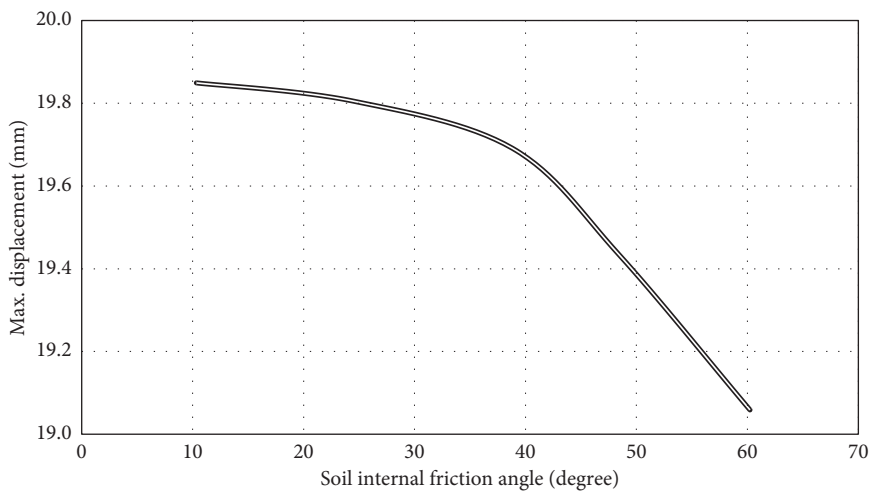
FIGURE 15: Maximum changes of the displacement above the tank in terms of the internal friction angle of the soil.
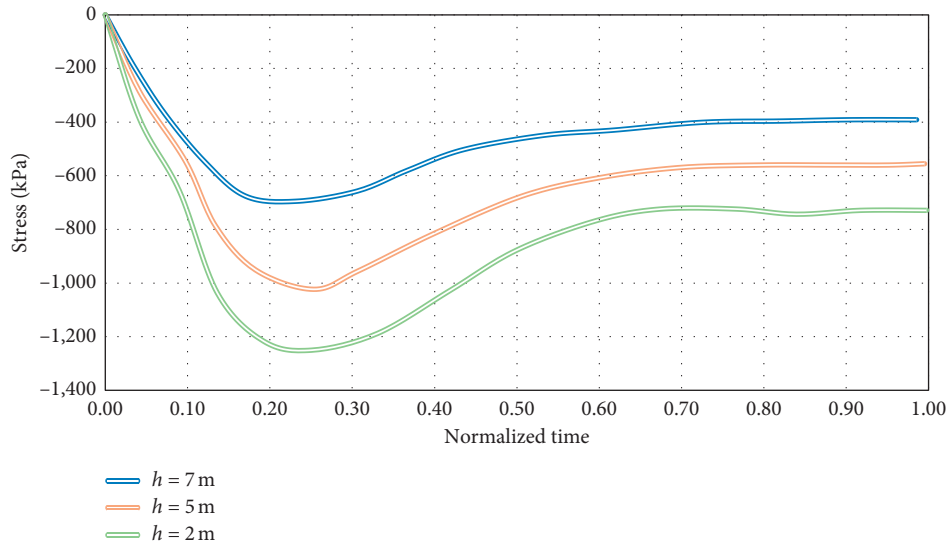
Figure 16: diagram of the time history of the shear stress at the foot of the tank in three states of the water height inside the tank.
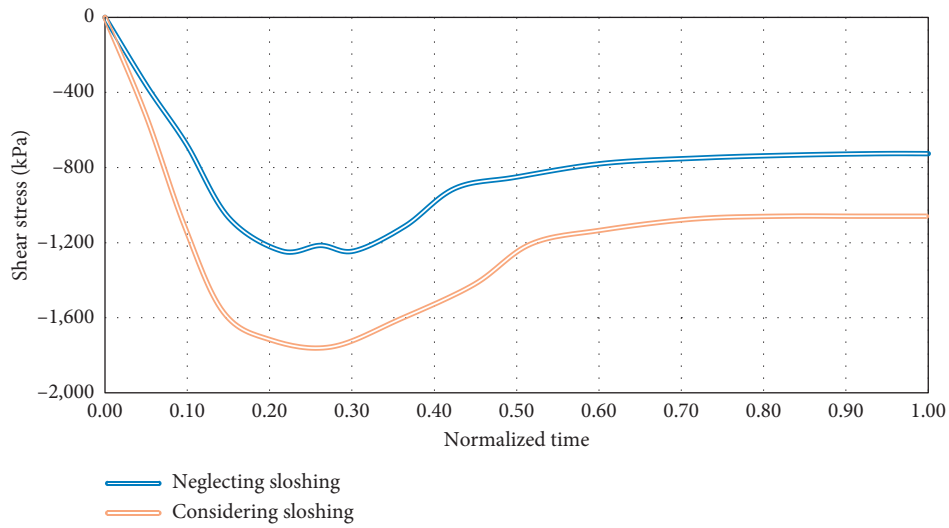
Figure 17: Diagram of the time history of the shear stress at the foot of the tank to study turbulence effect.
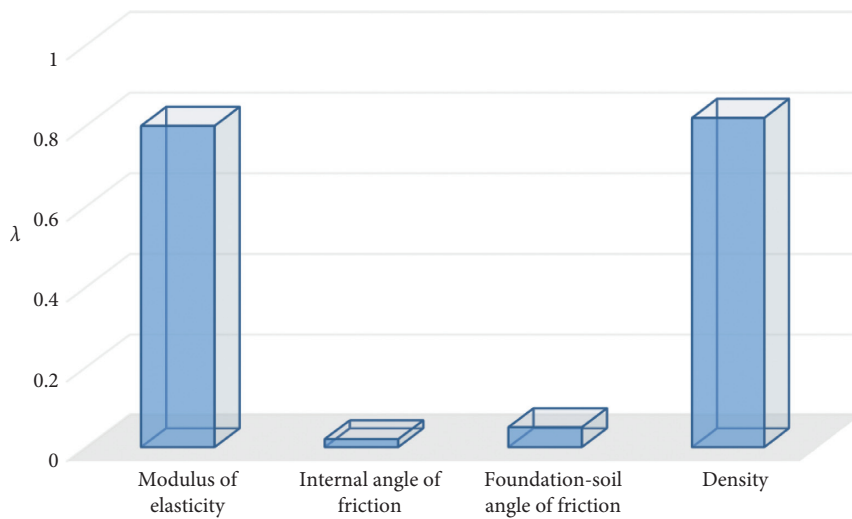
Figure 18: Sensitivity of the tank response to the given parameters.

and foundation surfaces and internal friction angle do not have tangible effect on response.

5. Conclusion

By decreasing soil density, maximum displacement increases above the tank. With 15% decrease in density, the soil becomes softer and soil-structure interactional effect increases and therefore the structure becomes softer and maximum displacement increases by nearly 17%. With 30% decrease in the soil modulus of elasticity, maximum displacement above the tank increases nearly 50%. With decreasing modulus of elasticity to 30%, the soil becomes softer and soil-structure interaction increases and therefore the structure becomes softer and maximum displacement increases by 16%. To study the interactional effect on the seismic response of the surface tank, friction coefficients between the foundation and soil surfaces are considered as 0.1, 0.2, 0.4, and 0.7, and shear stress at the foot of the tank by taking turbulence of the water into account will be nearly 30% higher than base stress. With increasing friction coefficient between the soil and foundation surfaces by 15%, maximum displacement above the tank increases 15% too. With increasing internal angle friction of the soil, maximum displacement above the tank decreases. The obtained results shows that the internal friction angle has negligible effect on the tank displacement because its 6 time increase caused only 1% increase in the maximum displacement of it. The most important results obtained from this study are the amount of sensitivity of the effective parameters on the response of the tank in such a way that response of the structure is more sensitive to the changes of the density and the soil modulus of elasticity and changes of the friction coefficient between the surfaces and foundation and internal angle friction do not have tangible effect on the response.

Data Availability

Requests for access to these data should be made to the corresponding author e-mail address mazharfatahi@ gmail.com.

Conflicts of Interest

The authors declare that there are no conflicts of interest regarding the publication of this paper.

References

[1] R. M. Richard, C. J. Allen, and J. E. Partridge, "Proprietary slotted beam connection designs," *Modern Steel Construction*, pp. 28–33, 1997.

[2] S.-K. Lee, J.-H. Park, B.-W. Moon, K.-W. Lee, and J. Kim, "Design of a bracing-friction damper system for seismic retrofitting," *Smart Structures and Systems*, vol. 4, no. 5, pp. 685–696, 2008.

[3] M. Heshmati, S. M. S. Kolbadi, and S. M. S. Kolbadi, "Comparison between strain-based vs. stress-based criteria in seismic performance evaluation of high arch dams," *American Journal of Civil Engineering*, vol. 3, no. 2-1, pp. 1–8, 2015.

[4] D. Bernal, "Amplification factors for inelastic dynamic-Δ effects in earthquake analysis," *Earthquake Engineering & Structural Dynamics*, vol. 15, no. 5, pp. 635–651, 1987.

[5] S. Maleki and M. Tabbakhha, "Numerical study of slotted-web-reduced-flange moment connection," *Journal of Constructional Steel Research*, vol. 69, no. 1, 7 pages, 2012.

[6] M. R. Adlparvar, M. G. Vetr, and F. Ghaffari, "The importance of panel zone shear strength on seismic behavior of improved slotted-web beam connections," *International Journal of Steel Structures*, vol. 17, no. 1, pp. 307–318, 2017.

[7] R. K. Mohammadi, M. Mirjalaly, M. Mirtaheri, and M. Nazeryan, "Comparison between uniform deformation method and genetic algorithm for optimizing mechanical properties of dampers," *Earthquakes and Structures*, vol. 14, no. 1, pp. 001–010, 2018.

[8] L. F. Ibarra and H. Krawinkler, "global collapse of frame structures under seismic excitations," PEER Report No. 2005/ 06, Pacific Earthquake Engineering Research Center, University of California, Berkeley, CA, USA, 2005.

[9] J. Kim and T. Kim, "Assessment of progressive collapse-resisting capacity of steel moment frames," *Journal of Constructional Steel Research*, vol. 65, no. 1, pp. 169–179, 2009.

[10] M. Liu, "Progressive collapse design of seismic steel frames using structural optimization," *Journal of Constructional Steel Research*, vol. 67, no. 3, pp. 322–332, 2011.

[11] R. Villaverde, "Methods to assess the seismic collapse capacity of building structures: state of the art," *Journal of Structural Engineering*, vol. 133, no. 1, pp. 57–66, 2007.

[12] E. B. Williamson, "Evaluation of damage and P -Δ effects for systems under earthquake excitation," *Journal of Structural Engineering*, vol. 129, no. 8, pp. 1036–1046, 2003.

[13] M. A. Hariri-Ardebili, S. M. Seyed-Kolbadi, and M. Noori, "Response surface method for material uncertainty quantification of infrastructures," *Shock and Vibration*, vol. 2018, Article ID 1784203, 14 pages, 2018.

[14] M. Barkhori, S. Maleki, M. Mirtaheri, M. Nazeryan, and S. M. S. Kolbadi, "Investigation of shear lag effect on tension members fillet-welded connections consisting of single and double channel sections," *Structural Engineering and Mechanics*, vol. 74, no. 3, pp. 445–455, 2020.

[15] D. Vamvatsikos and C. A. Cornell, "Incremental dynamic analysis," *Earthquake Engineering & Structural Dynamics*, vol. 31, no. 3, pp. 491–514, 2002.

[16] S. M. S. Kolbadi, H. Davoodian, and S. M. S. Kolbadi, "Evaluation of nonlinear behaviour of reinforced concrete frames by explosive dynamic loading using finite element method," *Civil Engineering Journal*, vol. 3, no. 12, 20 pages, 2017.

[17] M. Lou, H. Wang, X. Chen, and Y. Zhai, "Structure-soil-structure interaction: literature review," *Soil Dynamics and Earthquake Engineering*, vol. 31, no. 12, pp. 1724–1731, 2011.

[18] M. Bybordiani and Y. Arici, "Structure-soil-structure interaction of adjacent buildings subjected to seismic loading," *Earthquake Engineering & Structural Dynamics*, vol. 48, no. 7, pp. 731–748, 2019.

[19] E. Mock and L. Cheng, "Performance of retaining walls with and without sound wall under seismic loads," *Earthquakes and Structures*, vol. 7, no. 6, pp. 909–935, 2014.

[20] F. E. M. A. P695, *Quantifi Cation of Building Seismic Performance Factors*, Federal Emergency Management Agency, Washington, DC, USA, 2009.

[21] F. Zareian and H. Krawinkler, "Simplifi ed performance-based earthquake engineering," report No. TB 169 stanford (CA), Stanford University, Stanford, CA, USA, 2009.

[22] F. Zareian, H. Krawinkler, L. Ibarra, and D. Lignos, "Basic concepts and performance measures in prediction of collapse of buildings under earthquake ground motions," *The Structural Design of Tall and Special Buildings*, vol. 19, pp. 167–181, 2010.

[23] B. Tang, X. Lu, L. Ye, and W. Shi, "Evaluation of collapse resistance of RC frame structures for Chinese schools in seismic design categories B and C," *Earthquake Engineering and Engineering Vibration*, vol. 10, no. 3, pp. 369–377, 2011.

[24] C. Adam, L. F. Ibarra, and H. Krawinkler, "Evaluation of P-delta effects in non-deteriorating MDOF structures from equivalent SDOF systems," in *Proceedings of 13th World Conference on Earthquake Engineering,* Vancouver, BC, Canada, p. 3407, August 2004.

[25] A. Kaveh and P. Zakian, "An efficient seismic analysis of regular skeletal structures via graph product rules and canonical forms," *Earthquakes and Structures*, vol. 10, no. 1, pp. 25–51, 2016.

[26] S. W. Han and A. K. Chopra, "Approximate incremental dynamic analysis using the modal pushover analysis procedure," *Earthquake Engineering & Structural Dynamics*, vol. 35, no. 15, pp. 1853–1873, 2006.

[27] S. W. Han, K.-H. Moon, and A. K. Chopra, "Application of MPA to estimate probability of collapse of structures," *Earthquake Engineering & Structural Dynamics*, vol. 39, no. 11, pp. 1259–1278, 2010.

[28] B. Shafei, F. Zareian, and D. G. Lignos, "A simplified method for collapse capacity assessment of moment-resisting frame and shear wall structural systems," *Engineering Structures*, vol. 33, no. 4, pp. 1107–1116, 2011.

[29] Fema, *Seismic Performance Assessment of Buildings*, Applied Technology Council as ATC, Redwood, CA, USA, 2012.

[30] M. G. Vetr, "Effect of vertical flange stiffener on the ductility of slotted web exclusive connection on (*I*)-shape profiles through experimental investigation," *Journal of Engineering Research*, vol. 3, no. 4, 2015.

[31] H. E. Estekanchi, V. Valamanesh, and A. Vafai, "Application of endurance time method in linear seismic analysis," *Engineering Structures*, vol. 29, no. 10, pp. 2551–2562, 2007.

[32] E. Miranda and S. D. Akkar, "Dynamic instability of simple structural systems," *Journal of Structural Engineering*, vol. 129, no. 12, pp. 1722–1726, 2003.

[33] H. Takizawa and P. C. Jennings, "Collapse of a model for ductile reinforced concrete frames under extreme earthquake motions," *Earthquake Engineering & Structural Dynamics*, vol. 8, no. 2, pp. 117–144, 1980.

[34] H. T. Riahi and H. E. Estekanchi, "Seismic assessment of steel frames with the endurance time method," *Journal of Constructional Steel Research*, vol. 66, no. 6, pp. 780–792, 2010.

[35] V. Valamanesh and H. E. Estekanchi, "A study of endurance time method in the analysis of elastic moment frames under three-directional seismic loading," *Asian Journal of Civil Engineering (Building And Housing)*, vol. 11, no. 5, pp. 543–562, 2010a.

[36] M. Alembagheri and H. E. Estekanchi, "Seismic assessment of unanchored steel storage tanks by endurance time method," *Earthquake Engineering and Engineering Vibration*, vol. 10, no. 4, pp. 591–603, 2011.

[37] A. Mirzaee and H. E. Estekanchi, "Performance based seismic retrofitting of steel frames by endurance time method," *Earthquake Spectra*, vol. 31, no. 1, pp. 383–402, 2013.

[38] H. Estekanchi, A. Vafaie, and M. Sadeghazar, "Endurance time method for seismic analysis and design of structures," *Journal of Constructional Steel Research*, vol. 11, no. 4, pp. 361–370, 2007.

Research Article

Investigation of Nonlinear Behaviour of Semiburied Cylindrical Concrete Reservoir without Dynamic Load Effect

Mazhar Fatahi [iD],[1] Mahdi Meftah Halghi,[2] and Mehran Soltani Tehrani[3]

[1]*Department of Civil Engineering, Loghman Hakim Golestan Non-Profit Institute, Agh-Ghala, Iran*
[2]*Department of Civil Engineering, Faculty of Water Engineering,*
 Gorgan University of Natural Resources and Agricultural Sciences, Gorgan, Iran
[3]*Department of Civil Engineering, Najafabad Branch, Islamic Azad University, Najafabad, Iran*

Correspondence should be addressed to Mazhar Fatahi; mazharfatahi@gmail.com

This study aimed to examine the effect of rigid and flexible foundations on the response by a semiburied water storage reservoir. In this study, the reservoir support conditions of both flexible and inflexible states were studied. The seismic behaviour of reinforced and prestressed concrete reservoirs was compared based on their support conditions. The powerful numerical method FEM was used to study about the nonlinear behaviour of cylindrical reservoirs using static and dynamic nonlinear analysis. The values of the results correcting factor in the design codes and standards were evaluated. Moreover, the response correcting behaviour (R) was evaluated based on the findings from a push-over and nonlinear dynamic analysis. This research finding indicated that the reservoir shapes and support types affect the deformability of the reservoirs. Reservoirs with prestressed concrete show less flexibility compared to reinforced concrete reservoir. Finally, it is resulted that displacement, base shear, and wave height obtained from time history analysis are more than those of response spectrum analysis, indicating insufficiency of response spectrum analysis.

1. Introduction

Fluid and gas storage tanks are very important. Today, the efficiency of such structures in many industries is undeniable. The main application of these tanks is in industry and for purposes such as water storage and storage. They are usually made of steel or reinforced concrete, and in terms of shape, they are usually made of cubes or cylinders. Conventional reinforced concrete reservoirs have been widely used for urban and industrial equipment for decades [1]. Different configuration of storage reservoirs is going to be built based on the structure shape, building materials, support conditions, and so on. Buried reservoirs are categorized based on the reservoir shapes, the boundary condition, the support types, and the construction material. Many reservoirs, especially cylindrical ones, are made of steel because of their chemical resistance and mechanical strength. The concrete reservoir may envisage a radical

transformation of the conception of technology in the context of the worldwide request of shaping the fourth industrial revolution [2]. This is because of the improved durability compared with the numerous failures observed in steel reservoirs during the past earthquakes.

The number of water storage tanks and its importance is increasing over time. Therefore, it is necessary to carefully study the behavior of this type of structure. In this regard, phenomena such as earthquakes and explosions should also be applied to these structures [3]. The next important goal of such studies, after a proper understanding of the behaviour of these structures, is to identify optimal methods to increase their resistance to these phenomena to reduce damage [4]. Although some studies have been performed on the nonlinear response of reservoirs underground tremors, still the need to study the nonlinear response and the degree of deformability of semiburied cylindrical concrete reservoir are strongly felt. The response factor is a term usually used in

chromatography and spectroscopy useful for the calculation of quantitative responses in detectors that correlate to amounts of investigated analyses [5]. Also, Adom-Asamoah evaluates the structural characteristics of deep beams made from reinforced palm kernel shell concrete (PKSC) and normal weight concrete (NWC) [6].

2. Materials and Methods

2.1. Existing Regulations and Standards for Liquid Reservoirs. In this section, a brief overview of existing regulations and documents for earthquake-resistant guideline of liquid containers is provided. In the Eulerian and Lagrangian methods, the governing fluid structure system equation is calculated using wave propagation through the fluid by assuming linear compressibility and in-viscosity [5]. This review focuses on regulations and standards recently used worldwide. The International Building Code (IBC 2011) is one of the widely used regulations which provides a diverse and detailed technique for calculating dynamic forces on liquid reservoirs but it is more commonly used in the United States. ASCE Standard 7-10 2010 is used for seismic design of conventional liquid storage reservoirs. In this standard, ground motion is defined as the maximum earthquake response spectrum (MCE), with a 2% probability that a more severe earthquake may occur over each half-century period [7].

There are currently no direct guidelines for the design of environmental structures in Canadian design regulations and standards. The ACI 350.3-06 Standard can be considered as the most referential document in this field. The ACI 350 based on the ultimate strength design method, which is based on the Hassner (1963) technique, is considered, and the resulting seismic forces are calculated. The continuity condition of contained fluid in this theory consisted of boundary conditions of the contact interface between tank body and fluid as well as fluid-free surface. The fluid is assumed to be irrotational, incompressible, and inviscid and also there is no mean flow of the fluid. Furthermore, the linear theory of sloshing is utilized for the convective response of the contained liquid in the tank. The velocity of pressure wave is assumed to be infinite in the small volume of containers.

2.2. Seismic Design of Concrete LCs. According to ACI 350.3 (2001 and 2006), all structural parts of liquid container body must be designed to withstand the effects of horizontal and vertical design acceleration in combination with the effects of applied static loads to provide a set of thorough and comprehensive procedures for the seismic analysis and design of all types of liquid-containing environmental concrete structures. Their committee's decision was influenced by the recognition that liquid-containing structures are unique structures whose seismic design is not adequately covered by the leading national codes and standards (ACI 350.3, 2006) [8].

When liquid containers are subjected to seismic loading caused by earthquake, the reflection can be illustrated by two main vibration modes which vary based on phenomena such as wall flexibility and rigidity at the base and level of fluctuation. The first vibration mode is impulsive that is combined with the lower portion of the liquid and can be considered with added mass method and even more recent technique. It should be noted that the second part is convective and is related to the upper part of the fluid in the tank [9].

3. Results and Discussion

3.1. Finite Element Method. In real conditions, the distribution of seismic forces around a circular reservoir is in accordance with Figure 1 and in the form of a cosine distribution. In this study, the use of axially symmetric elements in finite element analysis of circular reservoirs is investigated. Axial symmetry elements are much easier to use than shell elements. The abovementioned evaluation is the most direct method to study the sensitivity of geotechnical parameters, but it is only suitable to study the single-parameter sensitivity problem. However, in applying these elements, the cosine distribution for hydrodynamic forces cannot be used, so the linear pressure distribution must be considered in all around the circular-cross section of the tank. FEM for the correct investigation of the application of the uniform distribution of all-round pressure considering the maximum pressure is shown in Figure 1 [10].

For this purpose, shell elements have been used to model the fluid storage tank wall. This type of element has the ability to model the desired pressure distribution, interaction definition, and other numerical calculations. In order to check the accuracy of the hypotheses made in this section, modelling and numerical analysis are performed by all the mentioned methods and finally the results are compared with each other.

3.2. Numerical Simulations. In this software, a computer model can be created using graphic and interactive techniques. To simplify the problem, this paper only considers one tank and its foundation. The LC is modelled using 3D shell elements and axial symmetric boundary conditioning. Since the properties of materials in this study are assumed to be linear, after static analysis, it has been used to simulate the behaviour of this structure [11].

In this study, three finite element models are used. Full reservoir model (FT): in this case, the reservoir is completely modelled using 1680 square elements of four nodes, with dimensions of 0.9 by 0.9 meters; the name "full reservoir (FT)" is chosen for Figure 2(a). Half reservoir model (1/2T): in this case, half of the reservoir is modelled using 840 square shell elements with a diameter of 0.9 by 0.9 meters and is called the "1/2T" model (Figure 2(b)).

This model is used only for proper modelling research. Axial symmetric model (AXI): in this case, the whole reservoir is modelled using symmetric axial elements; it is called the model with 3 layers along high.

Finite element analysis is performed using ABAQUS software. Using the interaction and powerful simulation
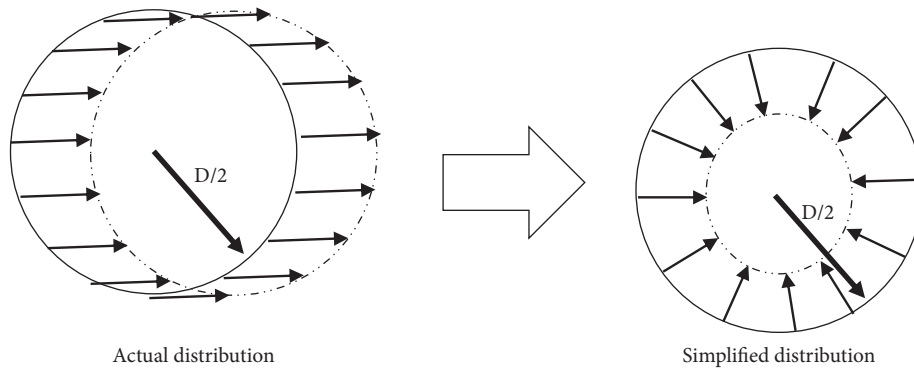
FIGURE 1: Actual and simplified hydrodynamic pressure distribution.
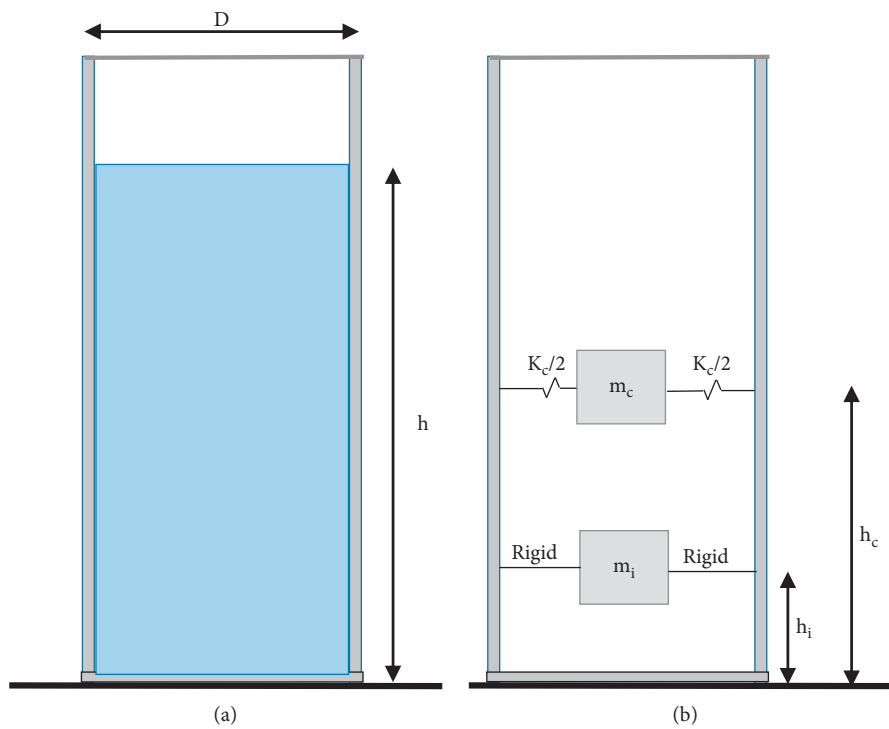
FIGURE 2: Circular reservoir finite element model: (a) full reservoir and (b) added mass and sloshing modelling.

technique of this software, the numerical model of the reservoir is designed. In this study, nonlinear dynamic analysis of time history is used in which the nonlinearity of building materials is considered [12, 13].

3.3. Problem Geometry.

The reservoir is completely designed using quadrilateral shell elements, according to Figure 3. The wall thickness is much less than the height of the wall and the diameter of the reservoir. Therefore, it is justified to consider shell elements in reservoir modelling. The shell elements used in this analysis have three degrees of freedom of movement and rotational in each node. In terms of water height, the reservoir wall is divided into equal elements of one meter, and in this networking, the number of elements along the wall to the water level for reservoir 1, 2, and 3 are considered equal to 3, 6, and 9, respectively. The length of the

highest element for three reservoirs is equal to the free edge of the reservoir, i.e., 0.25, 0.5, and 0.6 meters, respectively. In order to maintain the proportion of the body in the unit value, around each reservoir is divided into 128 equal elements in which the size of each element on the peripheral circle of the reservoir is equal to 1 meter. As a result, the total number of elements for the three reservoirs will be 512, 896, and 1280, respectively.

3.4. Research on the Correctness of the Model.

To investigate the finite element model used in this study, finite element analysis was done for all different models with rigid bases using two finite element numerical programs SAP and ABAQUS. To do this, three different finite element models (out of six models) with fixed base conditions are considered.
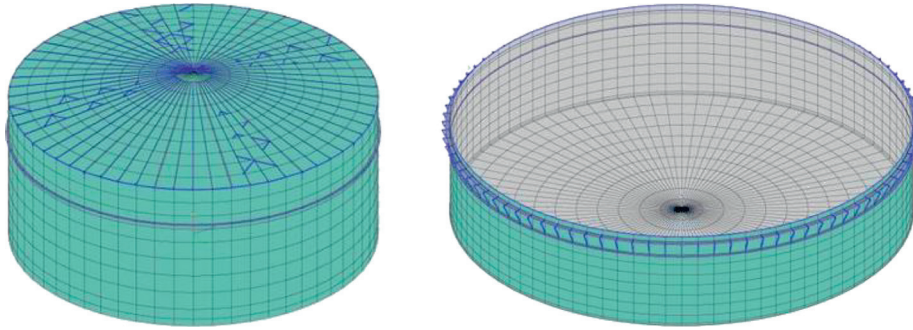
Figure 3: Finite element model for fluid reservoir, ABAQUS/CAE.

Table 1: Reactive force in the radial direction at the base of the reservoir under constant pressure.

Reactive force (kN/m)		Reactive force (kN/m)		Reactive force (kN/m)	
SAP full model	ABAQUS full model	SAP half model	ABAQUS half model	SAP axisymmetric model	ABAQUS axisymmetric model
11.3	11.2	11.3	11.2	11.4	11.3
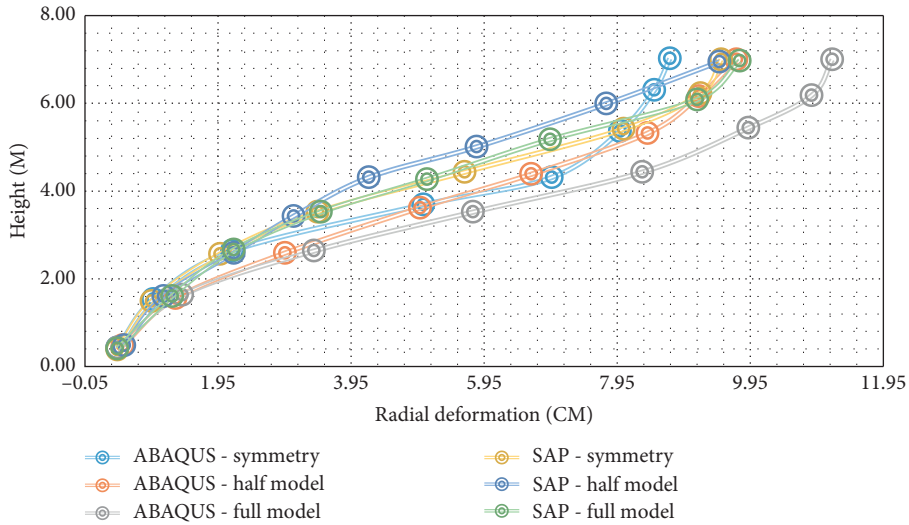
Figure 4: Radial deformation under uniform pressure.
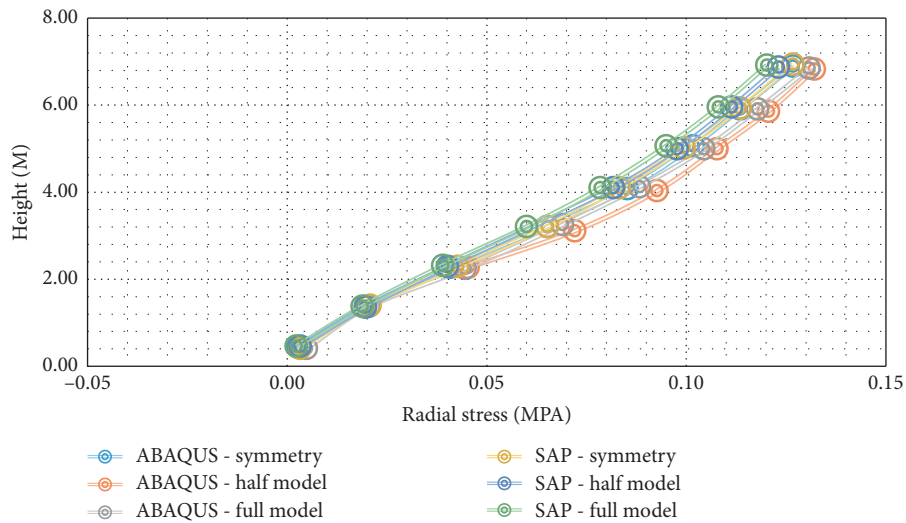
Figure 5: Environmental stress under uniform pressure.
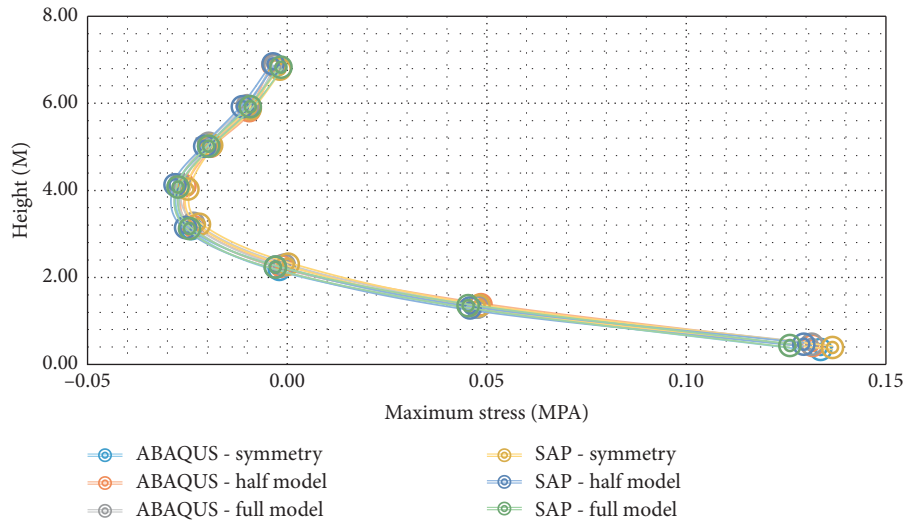
Figure 6: Maximum stresses in the vertical direction under uniform pressure.

Since the purpose of this study is to properly investigate the model selected for the reservoir using the ABAQUS program, a uniform pressure of 1.3 kPa will be applied to the reservoir. As can be seen in Table 1, the reaction force in the radial direction at the base of the reservoir was very close to each other in all models and the maximum difference in results equal to 1.6% between the axisymmetric model and the full model is obtained, which indicates that the reservoir models considered using SAP and ABAQUS are compatible with each other.

As shown in Figure 4, the radial deformation in all FE models of reservoir wall heights is the same for models 1 and 2 in both programs. The maximum difference in radial wall deformation for models 1 and 2 in the two software programs is 7.6% at the top of the wall. This difference is inversely related to height. The average difference between the results for displacement is about 4%, but the results are the same for the axial symmetric model 3 in ABAQUS and SAP.

Figure 5 shows the first principle stresses for all numerical models. The maximum difference between the first principle stresses in models 1 and 2 above the wall is equal to 7.6%; the average difference is equal to 4%. Similarly, the first principle stresses at different levels of height are obtained for models 1 and 2 in both computer programs.

Figure 6 shows that the second principle stresses in the vertical direction obtained almost identically for all FE models indicating the use of models 1, 2, or 3 in each of the two programs can arbitrarily give reliable results in finite element analysis for the considered parameters.

4. Conclusion

The presented problem turned out to be complex in numerical modelling. Moreover, the results did not lead to the real failure mode even though a range of external forces as well as material parameters were used. The complexity of geometry and considerable slenderness of structural elements with very different mechanical properties caused serious complications in stabilizing the algorithm of the applied FE software out of the real range of loads. Hence, the lower bound static estimation focused on the observed failure mode was used. It is suitable to use methods of uniform loads and symmetric axial elements in modelling the reservoir completely and obtaining its maximum response. In the usual method (based on regulations), the response of the reservoir is determined in terms of base shear and base torque more than the amount of analysis. The discrepancy in results is due to the effects of the concentration of impact and convective masses and other simplifying assumptions that are common in regulatory methods. The recommended R_i values for reinforced concrete reservoirs, with clamped and articulated bases, and preconcreted reservoirs with flexible braced bases are 2.5, 2.0, and 1.5, respectively.

Data Availability

Requests for access to these data should be made to the corresponding author via the e-mail address: mazharfatahi@gmail.com.

Conflicts of Interest

The authors declare that there are no conflicts of interest regarding the publication of this paper.

References

[1] S. M. S. Kolbadi, R. A. Alvand, and A. Mirzaei, "Three dimensional dynamic analysis of water storage tanks considering FSI using FEM," *International Journal of Civil and Environmental Engineering*, vol. 12, no. 3, pp. 377–386, 2018.

[2] C. Vargas-Elizondo, "On the role of ethics in shaping technology development," *HighTech and Innovation Journal*, vol. 1, no. 2, 2020.

[3] M. Barkhori, S. Maleki, M. Mirtaheri, M. Nazeryan, and S. M. S. Kolbadi, "Investigation of shear lag effect on tension members fillet-welded connections consisting of

single and double channel sections," *Structural Engineering and Mechanics*, vol. 74, no. 3, pp. 445–455, 2020.

[4] S. M. S. Kolbadi, H. Davoodian, and S. M. S. Kolbadi, "Evaluation of nonlinear behavior of reinforced concrete Frames by explosive dynamic loading using finite element method," *Civil Engineering Journal*, vol. 3, no. 12, 1198 pages, 2017.

[5] A. Hafez, "Seismic response of ground-supported circular concrete tanks," Thesis, Ryerson University, Toronto, Canada, 2012.

[6] M. Adom-Asamoah, J. Banahene Osei, and K. Adinkra-Appiah, "Structural characteristics of reinforced palm kernel shell concrete deep beams," *Civil Engineering Journal*, vol. 4, no. 7, 1477 pages, 2018.

[7] American Society of Civil Engineers (ASCE), "Structural Engineering Institute," *Minimum Design Loads for Buildings and Other Structures*, ASCE, Reston, VA, USA, 2005.

[8] ACI committee 2007, *Report on Thermal and Volume Change Effects on Cracking of Mass Concrete (ACI207.2R-07)*, American Concrete Institute, Farmington Hills, MI. USA, 2007.

[9] P. Mortazavi, S. Bernard, J. Stephenson, B. W0haley, and J. Elliot, "seismic design of liquid retaining structures: a review of design methodologies and retrofit of a case study wwtp," in *Proceedings of the 16th world conference on earthquake, 16WCEE*, Santiago Chile, January 2017.

[10] CSA-A23.3, *Design of Concrete Structures*, Canadian Standards Association, Mississauga, Ontario, Canada, 2010.

[11] M. A. Haroun and G. W. Housner, "Earthquake response of deformable liquid storage tanks," *Journal of Applied Mechanics*, vol. 48, no. 2, pp. 411–418, 1981.

[12] C. A. Kircher, "Seismic regulations for passive structural control systems-overview of United States codes," in *Proceedings of the Second World Conference*, Wiley, Chichester, UK, December 1999.

[13] NZS3106, *Code of Practice for Concrete Structures for the Storage of Liquids*, Standards Association of New Zealand, Wellington, New Zealand, 2010.

Research Article

A Conceptual Model and Evaluating Experiments for Studying the Effect of Soil Deformation on Its Permeability

Masoud Enayat ⓘ**, Gholamreza Shoaei** ⓘ**, and Mohammad Reza Nikudel** ⓘ

Engineering Geology Group, Tarbiat Modares University, Tehran, Iran

Correspondence should be addressed to Gholamreza Shoaei; shoaei@modares.ac.ir

Soil structure and void ratio are the major factors that control the permeability changes during soil deformation. In this research, we proposed and tested a conceptual model considering these two factors based on the concept of permeability anisotropy. This model, which is expressed as $k(e)$ graph, determines the total k values that soil can achieve and shows that as deformation proceeds, soil permeability passes through a specific zone in the $k(e)$ graph. Thus, by deforming a soil sample, measuring its permeability during deformation, and comparing the results using the $k(e)$ graph, it might be possible to predict deformation effects on the permeability. To evaluate this conceptual model, we designed and built a special apparatus to carry out two sets of experiments. The first set was performed to achieve the $k(e)$ graph during static compression based on the conceptual model; and the second set was conducted to investigate the permeability changes relative to $k(e)$ graph during simple shear deformation in constant volume condition. Our results show that the theoretical $k(e)$ graph agrees more with the measured $k(e)$ graph in medium to dense samples that might have no macropore. In addition, particles' preferential orientation and/or anisotropic permeability were not changed during shear deformation due to three possible causes: deformation done in constant volume deformation, relatively low shear strain, and shearing along particle orientation. Void ratio and particle orientation are associated with each other, and soil shearing with constant void ratio might cause the anisotropy of permeability to be relatively constant. Thus, it is needed to design and build a new complex apparatus or use a special method for testing how permeability changes within the $k(e)$ graph zone during soil deformation.

1. Introduction

When a soil body deforms, its permeability might change. Settlement, compression, consolidation, and shearing are the common causes of deformations in soils. However, less extensive deformations such as bending, torsion, and other complicated forms may also occur. Although in some of these deformations, permeability changes are negligible; they would play a key role when fluid infiltration and seepage is a matter of concern. Thus, having a good knowledge of deformation effects could be a great assistance in realistic judgment about permeability variation for designing or foresight events.

In unsaturated conditions, when soil deforms due to changes in void ratio, the degree of saturation varies leading to consequent changes in its permeability [1–3]. Green et al.

[4] reviewed the effects of various types of soil deformation on hydraulic conductivity in order to study the agricultural management practices such as tillage and reconsolidation and wheel-track soil compaction. Yeo et al. [5], Berilgen et al. [6], Fan et al. [7], and Royal et al. [8] conducted some experiments to investigate the permeability changes of slurry materials due to loading or compression occurred in the cut-off walls, cut-off barriers, and storing contaminant soils. Bryant et al. [9] investigated the permeability changes due to the consolidation of fine-grained marine sediments in various depths and introduced empirical relations to estimate the permeability from the void ratio. Morrow et al. [10], Arch and Maltman [11], Zhang and Cox [12], Crawford et al. [13], and Kimura et al. [14, 15] investigated the effect of shearing on the permeability in order to find out permeability behavior of faults and gouge materials.

The review of previous works shows that researchers often have tried to investigate the effect of one specific deformation on the permeability, and generally, there is no comprehensive study on deformation effects. Most researchers had studied the effect of soil compression or consolidation on the permeability through studying void ratio changes on the hydraulic conductivity. This group of researchers often studied one-dimensional compression type of deformation by using the oedometer apparatus or similar devices that have rigid wall cells [5–9, 16–26]. In addition, some researchers studied axial compression with lateral free walls using either a triaxial compression device or compression cell with flexible walls [1, 3, 27–29]. Another type of study focuses on soil permeability changes during exerted shear strain. The main methods employed in this regard are ring shear [14, 18, 30], rotary shear [31], and shear of a thin layer sample [10, 12, 13, 32].

This study is an attempt to investigate the effect of any deformation on the permeability. In this way, we described the anisotropic permeability changes during soil static compression as a conceptual model that could help to understand how any soil deformation affects the permeability. The validity of the conceptual model was investigated through sets of laboratory tests by applying an apparatus designed specifically for this research.

2. Research Theory

2.1. Parameters Controlling the k during Soil Deformation. Soil permeability is controlled by several parameters such as grain size, specific surface area, clay content, porosity, temperature, and pore geometry [33–44]. When a soil deforms, considering laboratory constant conditions, among these effective parameters, the only varying parameters are void ratio and soil structure (including particle arrangement, orientation, and pore geometry). In this view, soil deformations can be divided into two general groups. The first group involves deformations that occur with the changing volume and both void ratio and soil structure vary. Another group comprises deformations developed with fixed volume suggesting that the void ratio is constant and only soil structure varies. Accordingly, by knowing the influence of void ratio variations and soil structure changes on the soil permeability, we can investigate the effect of soil deformation on the permeability.

2.2. Effect of Void Ratio and Soil Structure on the k. Void ratio plays a major role in permeability such that a decrease in this parameter causes a rapid declination in permeability values. Many researchers have studied the effect of void ratio variation on the permeability and some of them proposed empirical relationships to estimate permeability via void ratio [22, 42, 45–49].

In order to understand the effect of soil structure changes on the permeability during deformation, the soil should be studied in constant volume deformation condition so that the effect of void ratio could be negligible. At a certain void ratio, permeability in a specific direction could have different values depending on soil structure. In other words, in a

specific void ratio, the value of k depends on soil particles orientation. In a soil body, if particles have random orientation, the soil would be structurally isotropic and value of permeability in all directions is equal. However, in the same void ratio, when particles are oriented, the soil would be structurally anisotropic, leading to different permeability values in different directions. In this case, permeability in the direction parallel to soil particles orientation is more than that in the direction perpendicular to them. For these conditions, a researcher reported permeability or hydraulic anisotropy in soil, represented by the anisotropy ratio (r_k) [11, 16–18, 20, 21, 31, 32, 50, 51], which is the ratio of horizontal to vertical permeability (k_h/k_v) or ratio of larger to smaller permeability value as follows:

$$r_k = \frac{k_h}{k_v}. \tag{1}$$

2.3. $k_{h(max)}$ and $k_{v(min)}$ Concept. For a given soil with the specific void ratio, if the preferential orientation is at the maximum level, the horizontal permeability (k_h) would be the maximum at this void ratio ($k_h = k_{h(\max)}$) while the vertical permeability (k_v) would be the minimum ($k_v = k_{v(\min)}$). In this situation, the anisotropy ratio is at the maximum state possible ($r_{k(\max)}$) and permeability values in other directions would be between $k_{h(\max)}$ and $k_{v(\min)}$.

2.4. The Conceptual Model. Basak [52], Delage and Lefebvre [53], Al-Tabbaa and Wood [16], Chapuis et al. [54], Brown and Moore [32], and Cetin [55] showed that low compression soils have less anisotropic structures and increasing compression causes the development of the anisotropic structure in the soil. Sloane and Kell [56] and Chapuis and Gill [17] reported that static compression creates a more anisotropic structure in fine-grained and sandy soils than dynamic or other compression methods. As a result, when a saturated soil sample with a high void ratio is one-dimensionally compressed gradually, soil particles can be displaced and rotated perpendicular to the applying load axis. Since particle rotation and structural anisotropy development continues from the beginning of soil compression, the r_k is expected to be maximum at each void ratio. Thus, it is acceptable that the measured k_h and k_v at each void ratio during compression are the $k_{h(\max)}$ and $k_{v(\min)}$. Plotting the obtained $k_{h(\max)}$ and $k_{v(\min)}$ in different void ratios during one-dimensionally static compression in a log-linear scale of $k(e)$ graph would give two $k_{h(\max)}$ and $k_{v(\min)}$ curves, respectively (Figure 1). Although, the soil may be isotropic ($r_k \approx 1$) at the beginning of compression, with a decrease in void ratio and increase in structural anisotropy, differences of these two curves increase, leading to the increase in anisotropic permeability (i.e. $r_k > 1$). A similar behavior can be seen in the results reported by Basak [52], Wilkinson and Shipley [25], and Al-Tabbaa and Wood [16].

The $k(e)$ graph shown in Figure 1 represents a conceptual model according to which the soils composed of particles with unequal dimensions, produce anisotropic permeability
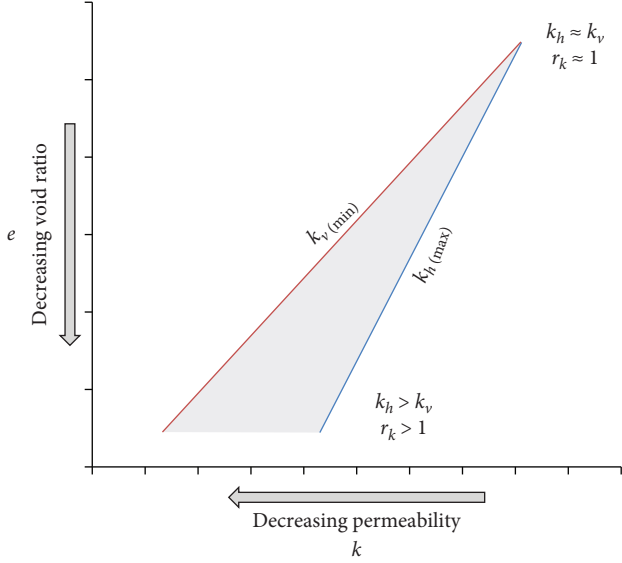
FIGURE 1: The $k(e)$ graph showing a conceptual model of $k_{h(\max)}$ and $k_{v(\min)}$ variations and anisotropic permeability development for a given soil sample having a high void ratio during static one-dimensional compression.

during static compression. This model is valid until there is no fracture or canal in the soil. The $k(e)$ graph is unique for each soil sample because particle shape and geometry in different soils vary and lead to different structural anisotropies. The inferable point from the $k(e)$ graph (Figure 1) is that there is a range of k value for each void ratio, where k varies between $k_{h(\max)}$ and $k_{v(\min)}$ depends on the soil structure as follows:

$$k_{h(\max)} \geq k \geq k_{v(\min)}. \tag{2}$$

In fact, when a soil body with having $k_{h(\max)}$ and $k_{v(\min)}$ (i.e., $r_{k(\max)}$) deformed, it is expected to cause the soil structure changed; consequently, anisotropy structure decreased from the initial state caused k varied between $k_{h(\max)}$ and $k_{v(\min)}$. Therefore, when a soil body deforms with a constant volume, it is expected that k varies only between $k_{h(\max)}$ and $k_{v(\min)}$ values; however, when it deforms with a changing volume, it is needed to estimate the k in relation to its corresponding void ratio. The dashed area between the two curves in Figure 1 presents all possible values of k that soil can achieve under normal conditions. As can be seen, k is not located out of this region except in special conditions, e.g., when soil grading or particle shape changes due to some process like grain crash as a result of excessive loading or water movement along produced fractures.

Thus, any deformation that could occur in the soil, in either a constant or a changing volume, would lead to changes in the permeability within the dashed area in Figure 1. Accordingly, the pattern of k_h and k_v variation during soil deformation with respect to $k_{h(\max)}$ and $k_{v(\min)}$ curves in the $k(e)$ graph can show the effect of soil deformation on its permeability.

Although, the conceptual model maybe theoretically valid for all soil types, in practice, it may not work properly for cohesionless granular soils, because particles in these soils cannot rotate freely under static compression. After a slight compression, they interlock and resist against volumetric compaction [57]. This behavior prevents the development of anisotropic structures in these soil types.

3. Methodology and the Procedure

We tried to study the permeability changes during soil deformation via laboratory tests based on the conceptual model (Figure 1). For this purpose, a procedure with the following steps was defined as follows:

(1) Preparing the $k(e)$ graph ($k_{h(\max)}$ and $k_{v(\min)}$ curves) of soil samples

(2) Determining the k_h and k_v variations of soil samples during progressive simple shear deformation

(3) Comparison of obtained results from steps 1 and 2 in order to determine how the soil permeability changed during deformation within $k(e)$ graph zone

Step 1 includes experiments conducted to obtain $k_{h(\max)}$ and $k_{v(\min)}$ values in different void ratios during one-dimensional static compression in order to prepare the $k(e)$ graph.

In step 2, tests were carried out to measure k_h and k_v variations during simple shear deformation. Through this deformation type, it is possible to deform the soil sample without changing its volume. As a result, we can investigate only the effect of soil structure changes on the permeability without the effect of void ratio variation.

Finally, in step 3, the results of the second step of experiments were plotted on the $k_{h(\max)}$ and $k_{v(\min)}$ curves were obtained from the first step of experiments to display how the permeability changed with respect to its initial state during simple shear deformation. So, it can be determined that whether measured k_h and k_v changed between $k_{h(\max)}$ and $k_{v(\min)}$ curves according to the conceptual model or not.

The mechanism of simple shear deformation is schematically illustrated in Figure 2. In this deformation type, theoretically, material shear and deformation occur without volume change. Here, shear strain (γ) is defined as the ratio of shear displacement (D) to the height of the sample or thickness of shear (H) as follows:

$$\gamma = \frac{D}{H}. \tag{3}$$

3.1. Samples Specifications. To examine the conceptual model, we need a remolded homogeneous sample in order to eliminate the effect of cracks and fractures on the permeability. Thus, two fine-grained soils with no organic matter were selected from loess soil deposits which are widespread in Golestan province, Northern Iran (Table 1). Rezaee et al. [58] showed that the sphericity of the loess particles is between 0.66 and 0.8 with an average of 0.73.
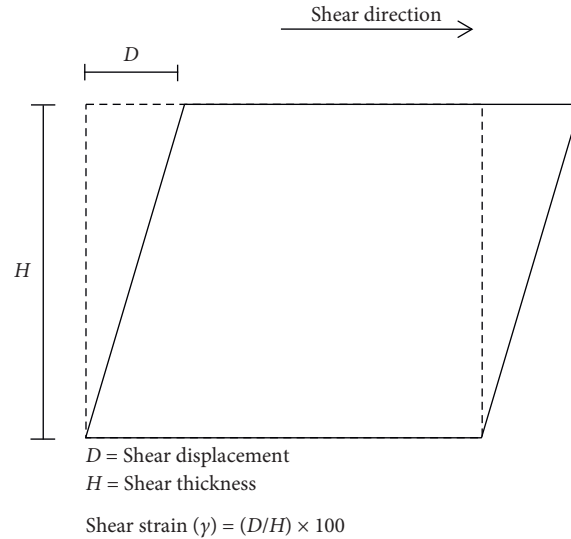
FIGURE 2: The mechanism of simple shear deformation.

TABLE 1: Specifications of the soil specimens.

Sample	Unified classification	Liquid limit (LL) (%)	Plasticity index (PL)	Specific gravity (Gs) (g/cm^3)	Sand 2-0.075 mm (%)	Silt 2-75 μm (%)	Clay <2 μm (%)
I	CL	30	11	2.68	28	51	21
II	CL	34	14	2.72	8	66	26

3.2. Test Apparatus.

In order to implement the two sets of tests (for steps 1 & 2), it was necessary to design and built a special test apparatus. This apparatus must have two main capabilities; first, it should be able to apply an incremental static force to consolidate one-dimensionally the soil sample from a high void ratio to measure $k_{h(\max)}$ and $k_{v(\min)}$ values at the end of each compression step. Second, it should be able to apply simple shear strain to the soil sample and measure the permeability at the end of each simple shear strain. The schematic of the apparatus is illustrated in Figure 3.

This apparatus can measure k_h and k_v values separately through both falling and constant head methods. The cell has a square cross-section with a dimension of 8 cm and a height of 20 cm. Here, k_h can be measured with two components assigned as k_{h1} and k_{h2}.

The shear zone thickness in the sample during shear deformation is 5 cm; so, the dimensions of the sample deformed during the simple shear deformation are 8 cm × 8 cm × 5 cm. The cell is composed of three parts (Figure 3): the upper part is always fixed during compression or shear deformation, the lower part is fixed during the compression test. But, during shear deformation, it can move on a precision rail to the left or right with a fixed strain rate of 0.05 mm.sec^{-1}. The middle part of the cell is a section at which the test sample bears shear deformation during the displacement of the lower part (Figures 3(a) and 3(b)).

Shear deformation in this paper was reported as a strain percentage such that each 1 mm of lateral displacement of the lower part of the cell on the rail is equal to a 2% shear strain.

3.3. Samples Preparation and Test Method.

Samples with a high void ratio can be prepared by two slurry and powder methods. Since performing desired tests on the slurry sample is difficult and involves high mistakes, we decided to prepare the samples using the powder method. For this purpose, soil samples were dried and crushed and then passed through sieve no. 10 (2 mm) such that to obtain a homogeneous soil powder. The prepared powder was put in the cell using a long pipe funnel placed at a constant 2 cm height. Afterward, when the loading piston is located in the cell, the cap would be fitted, closed, and sealed.

Before the beginning of the test, the soil is saturated from the lower to upper openings through the cell valves (Figure 3); as a result, air exits from the upper cell valve. After saturating and deairing the sample, it is ready for the test.

Horizontal permeability in all tests measured with two components: k_{h1} and k_{h2}. In permeability experiments, during shear deformation, k_{h1} is the permeability along the shear direction of the sample; thus, k_{h2} is perpendicular to the shear direction.

For the first set of tests (step 1), after each increment stage of the static load and soil compression, the sample is allowed to reach a new equilibrium condition until displacements are zero. Next, horizontal and vertical permeability values are measured separately.
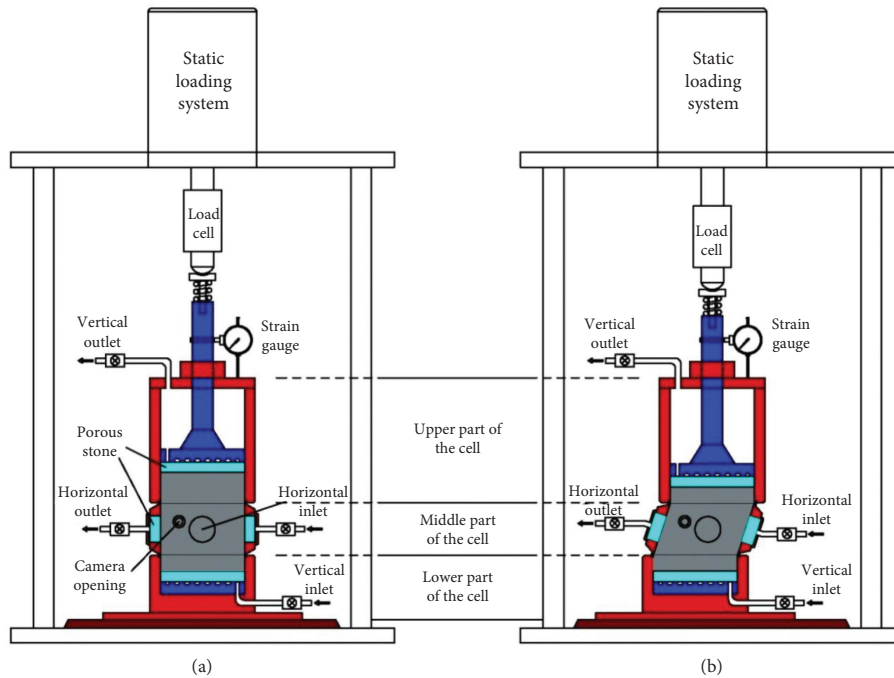
FIGURE 3: The layout of the test apparatus; (a) compression deformation of the soil sample and (b) simple shear deformation of the soil sample.

For the second set of tests (step 2), the sample compressed until reaching the desired void ratio. Then, to prevent the soil volume changes during the shear deformation, especially in dense samples, their vertical load was released and set to about 1 kg/cm^2. However, the applied load was not completely released because removing the load can cause detachment between the sample body and cell wall or produce opening fractures in the sample. After compressing the soil to the desired void ratio, setting the vertical load, and reaching an equilibrium state, the k_h and k_v values were measured. Then, soil sheared by 1 mm shear displacement of the lower part of the cell, which is equivalent to 2% shear strain. After this shearing and reaching an equilibrium state, k_h and k_v values were measured. This process comprises shearing, reaching an equilibrium state, and measuring k_h and k_v was repeated until the cell sealing is not damaged by shear displacement.

It has to be noted that all horizontal and vertical permeability were measured after water flow reached a steady state. Measurements in each step were replicated at least 5 times, and the final value was reported as their average.

4. Results and Discussion

4.1. First Step Results: The k(e) Graph of Samples. Variations of $k_{h(\max)}$ and $k_{v(\min)}$ corresponding to the void ratio in each step of progressive compression for I and II samples (the $k(e)$ graphs) are illustrated in Figures 4 and 5, respectively.

Results show that permeability variations of samples I and II during the static compression were similar, in general. There is a linear relationship between the void ratio and the logarithm of $k_{v(\min)}$, similar to previously published data

[9, 16, 20, 26, 42, 59–62]. However, the decrease in $k_{h(\max)}$ differs from $k_{v(\min)}$ and is not linear. As illustrated in Figure 6, the anisotropic permeability ratio (r_k) of samples has a varying trend during the compression, despite what is expected from the conceptual model. Here, r_k is expressed as $k_{h(av)}/k_v$ which $k_{h(av)}$ denotes the average of k_{h1} and k_{h2}.

As presented *in* Figure 6, the sample's r_k increases rapidly from the beginning of the compression and reaches a maximum level. Then, the increase in compression resulted in a rapid decrease in r_k until reaching near a minimum level. After this drop, at medium void ratios, r_k almost has minimum values with relatively low variations during the compression but it increases again at low void ratios.

Soil structure observations during the compression show that r_k changes were affected by the variation in the geometry of large pores and particle orientation (Figure 7). Macro-structure of the soil was examined using the images captured by a camera installed on the cell wall (Figure 3). Because of the sample preparation method, the samples have a granular structure at the high void ratios and mostly are composed of large units such as ped grains and silt-size grains [63] as well as other fine units such as clays and clay size particles (Figures 7(a) and 7(b)). Additionally, pores with various sizes are seen in the samples; macropores distribute between large units while micropores distribute within these large and fine units [53, 63, 64].

When the soil has a high void ratio, water flows mostly through the macropores. In this regard, permeability is controlled by these pores rather than micropores that are influenced by the capillary force [22, 65, 66]. But at low void ratios, macropores are absent and hydraulic conductivity is controlled by micropores [67].
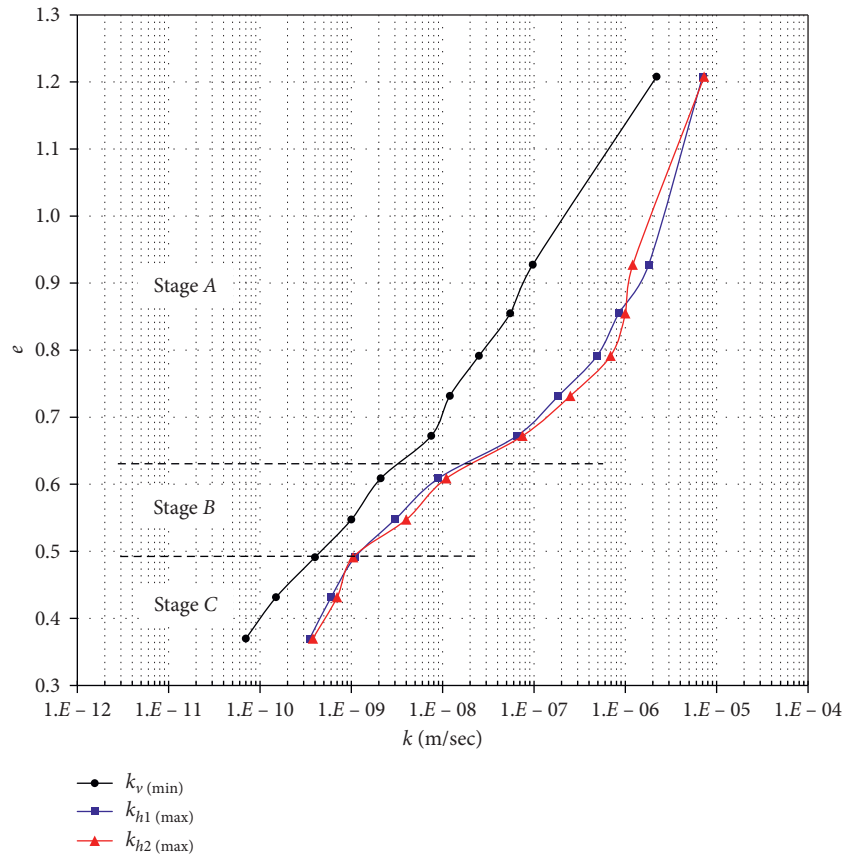
Figure 4: The $k(e)$ graph for sample I.

Macropores are more sensitive to compaction compared to micropores [23, 68]. During soil compaction or consolidation, larger pores close first [53, 69–73]. This evolution of soil structure affects the permeability and r_k variations during soil static compression. Following these variations, generally, three stages can be recognized (Figures 4–6) as follows:

> *Stage A*. A high anisotropic permeability in low compressions due to macropores effects (pseudoanisotropic permeability)
>
> *Stage B*. The lowest amount of anisotropic permeability in medium compressions due to the elimination of macropores affects and undeveloped orientation of the soil particles
>
> *Stage C*. Gradual increase of anisotropic permeability at high compressions due to developing particle orientation

In Stage *A*, the soil has a granular structure and water flow is controlled by macropores (Figure 7(b)). Anisotropic permeability comes from flattening the ped grains and interped macropores perpendicular to the applied load axis. Although fine particles are resorted within larger units (i.e., ped grains), they do not show a clear preferential orientation. Considering the importance of macropores in control of water flow and permeability, there are maximum anisotropy ratios in this stage, and therefore, there is pseudoanisotropy in this stage [63].

At the beginning of compression in this stage, r_k is relatively low but later with a small compression, ped grains, and interped macropores started to deform, and due to the affection of interconnected interped macropores, r_k reached a maximum level. In the following, as compression proceeded, peds started to merge and macropore flow paths were disconnected. This process caused permeability and r_k to decline rapidly.

In *B* stage, ped grains disappeared so there are no large pores in the soil body but few remnant macropores may exist as trapped spaces that started to complete the closure (Figure 7(c)). So decrease in the void ratio during compression in this stage is expected to occur mostly through decreasing the micropores size and particle rotation. There is the least anisotropic permeability in this stage because of the absence of macropores and the lack of evolution in particle orientation. Rotation of particles still is not enough to have a noticeable effect on the increasing r_k.

In Stage *C*, soil completely is compressed and there is no macropore in the soil body (Figure 7(d)). The decreasing void ratio continues by a decrease in micropore size and particle rotation. The r_k increases gently due to the development of particle orientation during the compression.

Soil structure evolution through these three stages indicates that, in stages *A* and *B*, soil particles do not have a preferential orientation and it is only in *C* stage that a preferential orientation is developed. So only in the *C* stage, a
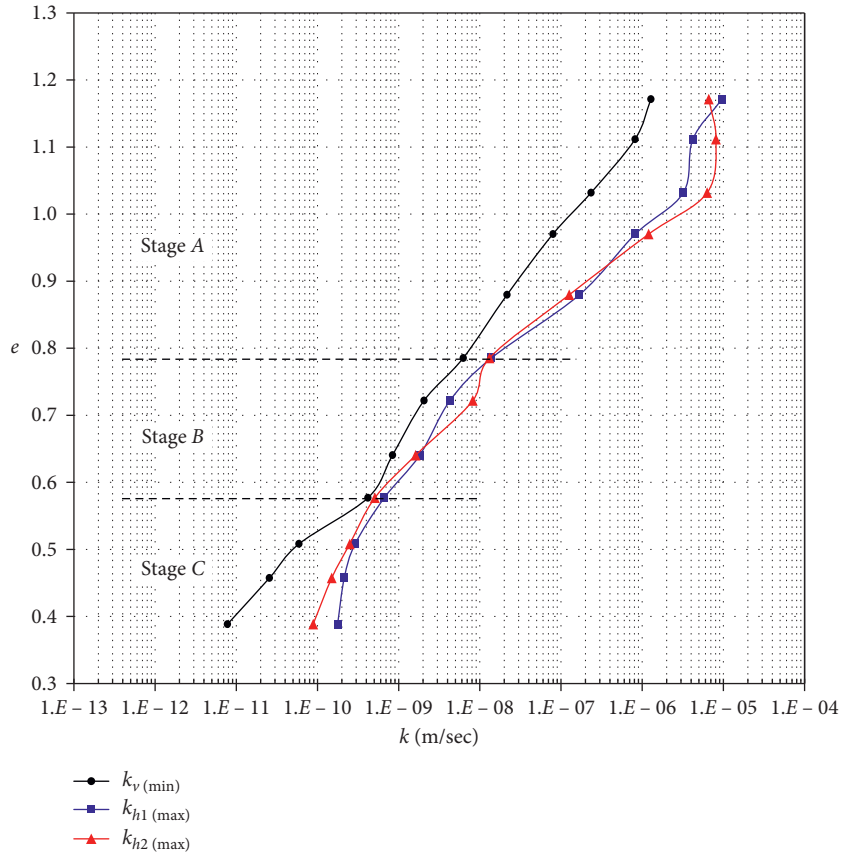
FIGURE 5: The $k(e)$ graph for sample II.

(a)

(b)
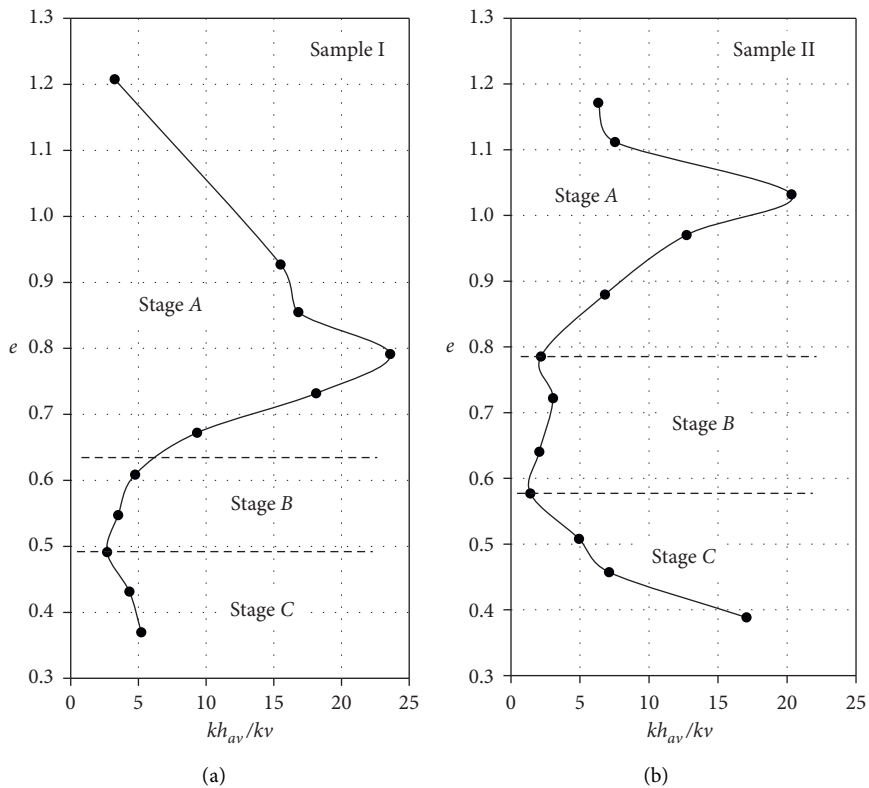
FIGURE 6: Anisotropic permeability variations of samples during the static compression.
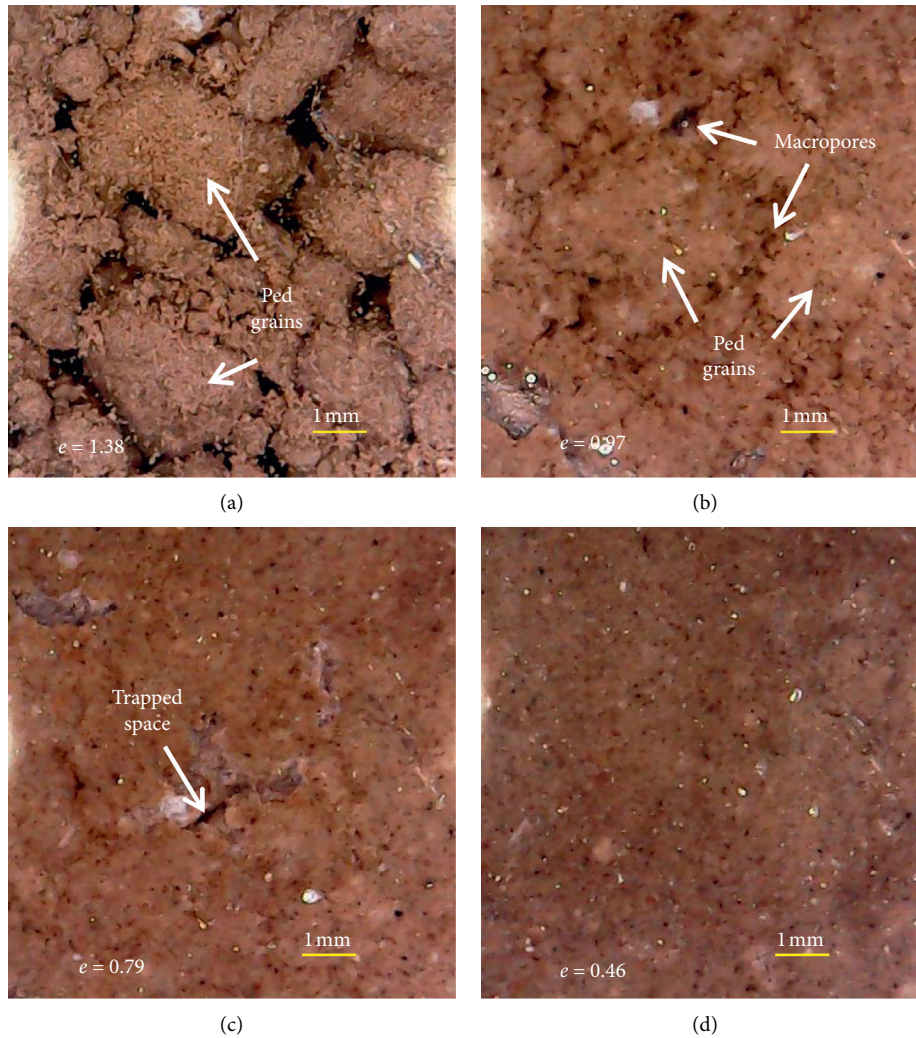
Figure 7: Evolution of soil structure during one-dimensionally compression of sample I.

variation of $k_{h(\max)}$ and $k_{v(\min)}$ during compression coincide with the conceptual model. This result shows that the sample preparation method affects the $k_{h(\max)}$ and $k_{v(\min)}$ curves in the $k(e)$ graph at relatively high void ratios, which are marked by A and B stages. Preparing the sample by the powder method, which was employed in this research, caused the creation of large pores in the soil body and prevented the development of particles preferential orientation until these pores were closed completely. This behavior coincides with the results of Yong and Warkentin [63].

4.2. Second Step Results: Variations of k during Progressive Simple Shear Deformation.
Experiments of the permeability changes during simple shear deformation conducted for all defined three stages A, B, and C, so that to determine variations of k_h and k_v related to $k_{h(\max)}$ and $k_{v(\min)}$ curves in the $k(e)$ graph.

The measured k_v, k_{h1}, and k_{h2}, after each step of 2% incrementing simple shear strain for samples I and II are presented in Figures 8 and 9, respectively. Specifications of samples at the beginning of the tests are presented in Table 2.

In stages A and B, sealing of cell was failed at low shear strain (due to the low compression of the soil sample) thus the experiment was terminated and the strain developed in the sample did not exceed 10%.

4.3. Third Step Results: Comparison of the Results from Steps 1 and 2.
The measured k values in step 2 (Figures 8 and 9) are plotted on the related $k(e)$ graph and shown in Figures 10 and 11. The pattern of points scattering in these figures shows that except in some cases, other plotted data generally are consistent with $k_{h(\max)}$ and $k_{v(\min)}$ curves. Examples of these contradictory behaviors are seen in data such as k_{h2} in II sample in Stage A or k_{h1} and k_{h2} in sample I in Stage A, which are failed data or arisen due to the closure effect of large pores and conduits (summary of the comparison results are presented in Table 2).

This result is unlike the behavior expected from the conceptual model that had expressed structure changes caused permeability changed between $k_{h(\max)}$ and $k_{v(\min)}$ curves. For example, in Stage C of samples in which soil particles orientation is developed, even slight increases in

(a)

(b)

(c)
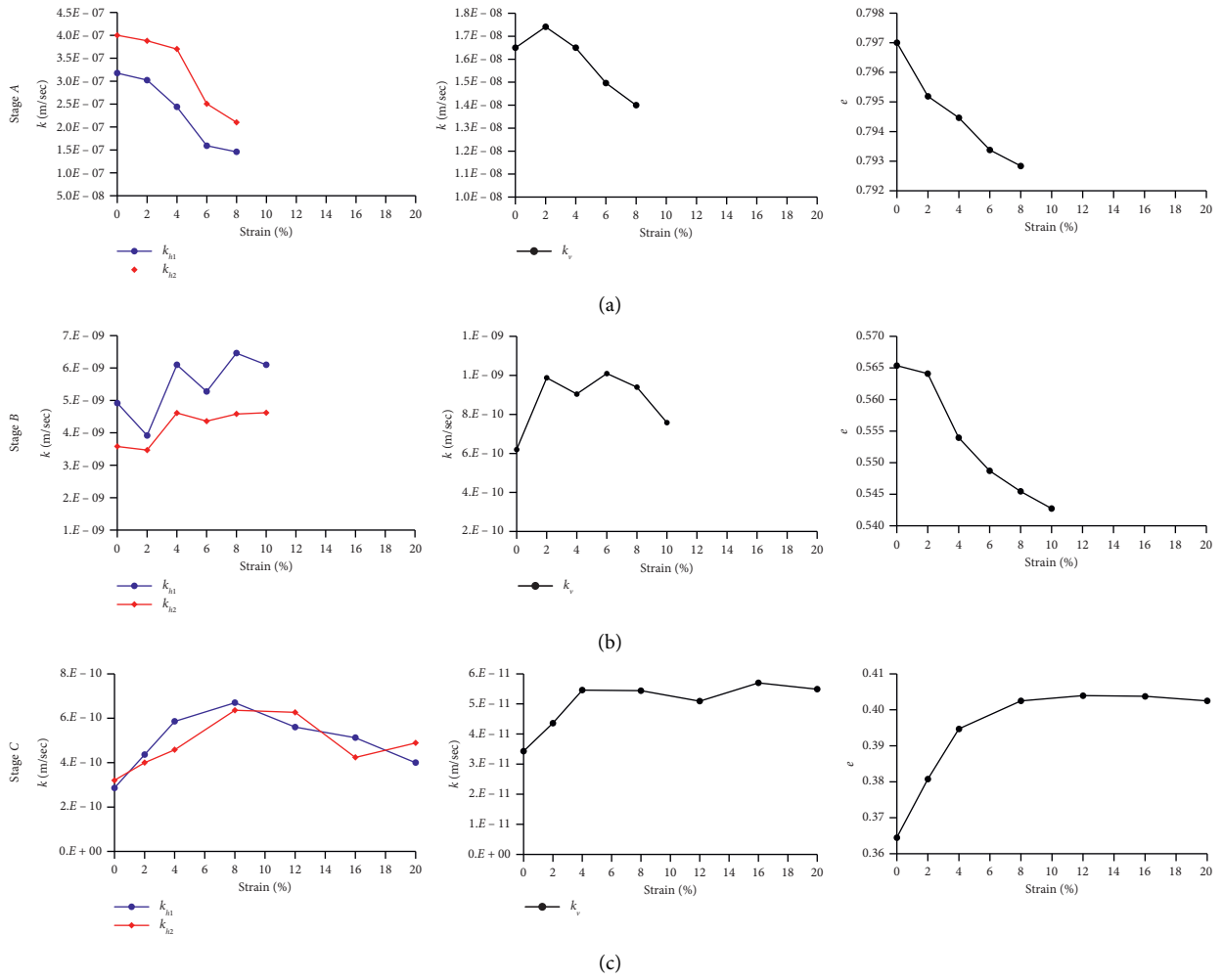
Figure 8: Variation graphs of k_{h1}, k_{h2}, k_v, and e vs. strain for each stage of sample I.

(a)

(b)
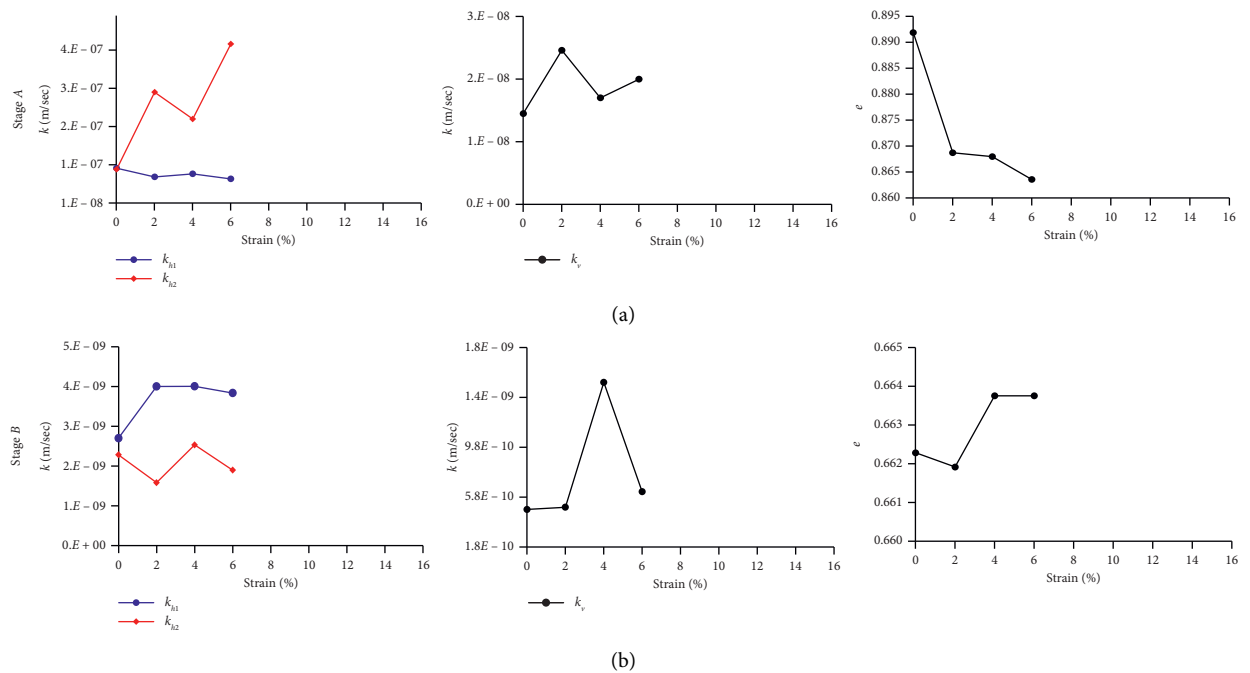
Figure 9: Continued.

(c)
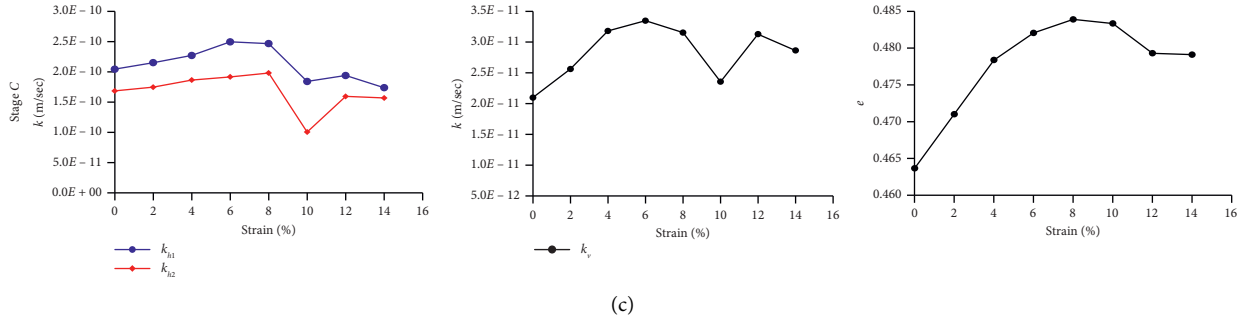
FIGURE 9: Variation graphs of k_{h1}, k_{h2}, k_v, and e vs. strain for each stage of sample II.

TABLE 2: Specifications of samples and their permeability change behaviour during simple shear deformation tests.

k_{h2} variation during s. sh. def.	k_{h1} variation during s. sh. def.	k_v variation during s. sh. def.	Initial vertical loading (kg/cm^2)	Induced shear strain (%)	The maximum variation of (e) during s. sh. def.	Initial void ratio	Stage	Samples
−	−	+	0.5	8	0.004	0.80	A	
+	×	+	1.6	10	0.023	0.57	B	I
+	+	+	1.1	20	−0.039*	0.36	C	
×	+	+	0.8	8	0.028	0.89	A	
+	+	+	1.2	10	−0.002*	0.66	B	II
+	+	+	1.3	14	−0.02*	0.46	C	

+Permeability changes coincide with $k_{h(max)}$ and $k_{v(min)}$ curves and have a similar trend. −Permeability changes are not consistent with $k_{h(max)}$ and $k_{v(min)}$ curves. ×Inaccurate, an outlier or uncertain data. *Negative numbers indicate the swelling and increasing void ratio during simple shear deformation.
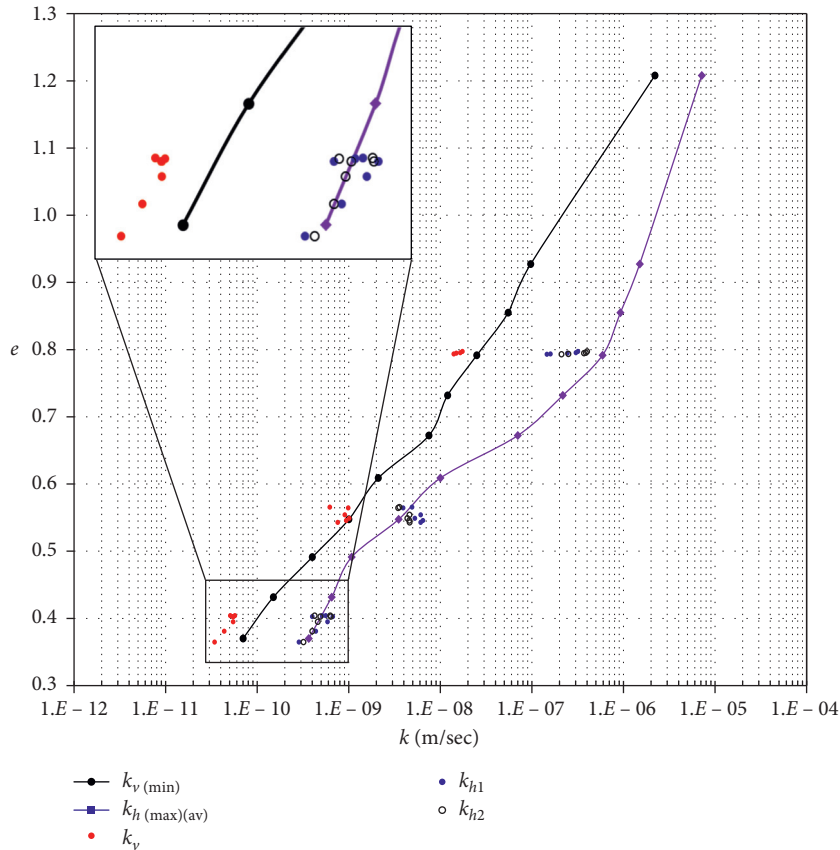
FIGURE 10: The plot of the k_v, k_{h1}, and k_{h2} values measured during simple shear deformation on the $k_{h(max)}$ and $k_{v(min)}$ curves for sample I.
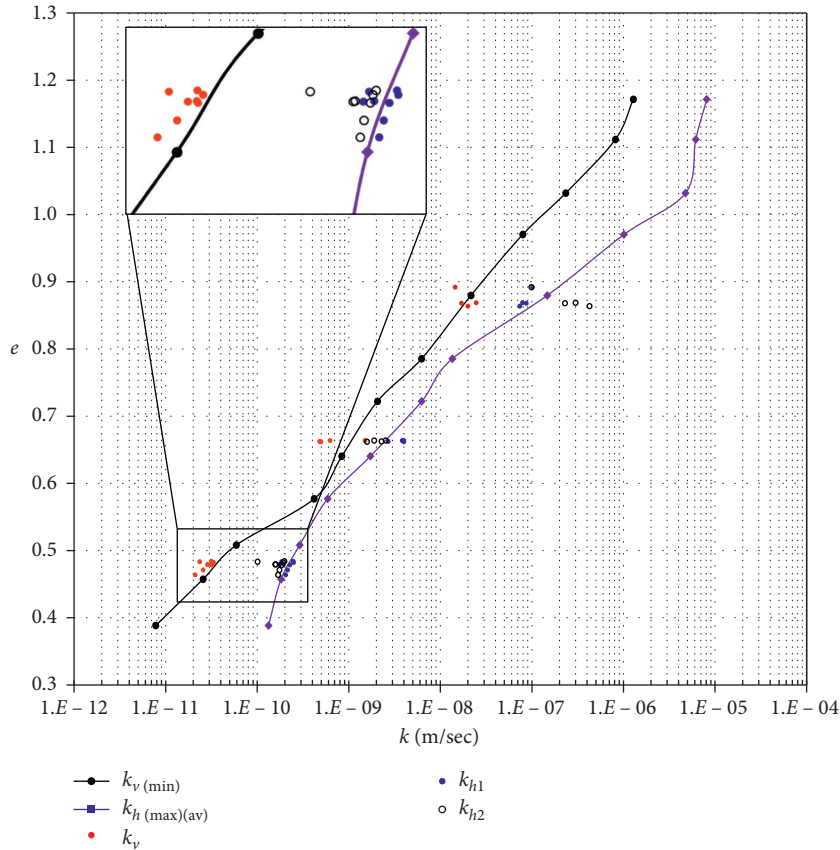
FIGURE 11: The plot of the k_v, k_{h1}, and k_{h2} values measured during simple shear deformation on the $k_{h(\max)}$ and $k_{v(\min)}$ curves for sample II.

void ratios due to swelling caused by shearing led to a scattering data trend similar to $k_{h(\max)}$ and $k_{v(\min)}$ curves (Figures 10 and 11). This result proves that permeability mainly is affected by void ratio changes and structural changes have a negligible effect on it. This result is in line with the findings of other researchers [32, 74].

Lack of consistency between the second set of experiments results and conceptual model predictions arises from the fact that in constant volume condition; the induced simple shear deformation cannot produce significant changes in particle orientation. Soil macrostructure observations during shear deformation confirm this point in all shear deformation tests. Figure 12 illustrates the angularity changes of a small fragment of a gastropod shell in sample I during the static compression. These remnant shell fragments could be found in Golestan province loess deposits. It was noted that fragment angle related to the horizontal plane (perpendicular to applied load or parallel to shear direction) decreased by 23° with a decrease in a void ratio from 0.95 to 0.68.

Also, a simple shear strain was applied to this sample at a void ratio of 0.8 (stage A of sample I in Table 2). The structure observed for this sample revealed that, during the shear deformation up to 8% strain, the angle of the shell did not change. Thus, it is obvious that the effect of simple shear deformation on particle orientation is negligible compared to the effect of compression; so the shear deformation under constant volume conditions cannot change the initial soil particles orientation i.e., soil structural anisotropy. For this
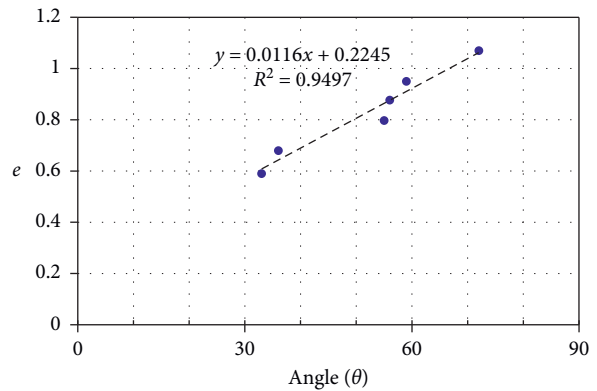
FIGURE 12: The rotation angle of a gastropod skeleton fragment from applied simple shear direction during one-dimensional static compression.

reason, permeability variations during the shear deformation have the most dependency to the void ratio. As a result, plotted data in Figures 10 and 11 are consistent with the $k_{h(\max)}$ and $k_{v(\min)}$ curves and show a similar trend. Another two effective factors might be mentioned that could cause the anisotropic permeability relatively constant during soil shear deformation. First, exerted shear strain was inadequate to develop anisotropic permeability with comparison to severe shearing in other phenomena such as fault zones and shear plane of landslides . Secondly, exerted shear strain took

place tangential to particle orientation. This caused the particles to slide against each other with no change in their orientations or soil volume.

So, it is necessary to change the void ratio during shear deformation to rotate the soil particles and increasing anisotropic permeability. According to Arch and Maltman [11], shear deformation with the decreased void ratio produces the highest amount of orientation compared with compression or shear deformation alone. It is reported in some previous studies that the shear deformation produces much anisotropy rather than compression [11, 13, 18, 25, 32, 75] but according to findings of this research, it reveals that shear deformation and compression occurred simultaneously.

5. Summary and Conclusions

The results of the first set of experiments revealed that when the soil is statically compressed from a high to low void ratio, generally three stages of anisotropic permeability variations could be recognized on the $k(e)$ graph based on the soil structure evolution. Toward the end of stage B at medium to low void ratio, the variations of $k_{h(\max)}$ and $k_{v(\min)}$, as well as r_k, has a good consistency with the conceptual model. This is most likely due to the absence of large pore spaces in the soil body as well as soil particles orientation perpendicular to the applied load. In samples with a high void ratio (both samples in stage A), the macropores play a main role in affecting the permeability, and thus, affect the $k(e)$ graph. So, for these samples, macropore properties, due to the sample preparation method, seem to have the main effect on the $k(e)$ graph. It means that the $k(e)$ graph varied with the sample preparation method for each soil type.

Results of the second set of tests show that measured k values during simple shear deformation coincide with $k_{h(\max)}$ and $k_{v(\min)}$ curves, suggesting that permeability is mainly affected by void ratio and permeability anisotropy not changed significantly; so the measured k_h and k_v are not located within the area between $k_{h(\max)}$ and $k_{v(\min)}$ curves. It seems that the lack of changes in the anisotropic permeability arises from the three points: first, deformation was created under constant volume conditions, second, shear strain is relatively low, and third, shear strain exerted along particle orientations. Deformation in fixed volume conditions may produce few changes in the soil structure but cannot significantly change the orientation of soil particles; because the creation of particles with preferential orientation eliminates spaces and could lead to volume reduction. On the contrary, the reduction in particles' preferential orientation caused the volume increase. Therefore, the key point is that how the soil deformation might change the void ratio and soil particle preferential orientation. The constant void ratio indicates that the soil particles have no preferred orientation changes. In this case, anisotropic permeability has not changed and the values of k_h and k_v follow the $k_{h(\max)}$ and $k_{v(\min)}$ curves. However, if the soil shows any void ratio changes, it should be due to the changes in anisotropic permeability that may cause the values of k_h and k_v not to follow the $k_{h(\max)}$ and $k_{v(\min)}$ curves.

The results show that measured permeability's (k_{h1}, k_{h2} and k_v) have good coincidence with the $k_{h(\max)}$ and $k_{v(\min)}$ curves that validate the conceptual model. The preparation method of samples affects the $k_{h(\max)}$ and $k_{v(\min)}$ curves at very high void ratios (approximately larger than 1), but at lower void ratios, its effects on these curves are negligible. Both conceptual model and validating tests show that, in any soil deformation, the soil particles orientation or structural anisotropy do not change in a fixed void ratio. So the void ratios have a significant role in the permeability for two reasons in soil deformation; the void ratio changes have a larger effect on the permeability relative to the soil structural anisotropy changes. Also, the soil particles' orientation and anisotropy do not change while the void ratio is relatively constant.

Data Availability

The data used to support the findings of this study are available from the corresponding author upon request.

Conflicts of Interest

The authors declare that there are no conflicts of interest regarding the publication of this paper.

Acknowledgments

References

[1] S. S. Agus, E. C. Leong, and H. Rahardjo, "A flexible wall permeability for measurements of water and air coefficient of permeability of residual soil," *Canadian Geotechnical Journal*, vol. 40, no. 3, pp. 559–574, 2011.

[2] G. Cai, A. Zhou, and D. Sheng, "Permeability function for unsaturated soils with different initial densities," *Canadian Geotechnical Journal*, vol. 51, no. 12, pp. 1456–1467, 2014.

[3] S. Huang, D. G. Fredlund, and S. L. Barbour, "Measurement of the coefficient of permeability for a deformable unsaturated soil using a triaxial permeameter," *Canadian Geotechnical Journal*, vol. 35, no. 3, pp. 426–432, 1998.

[4] T. R. Green, L. R. Ahuja, and J. G. Benjamin, "Advances and challenges in predicting agricultural management effects on soil hydraulic properties," *Geoderma*, vol. 116, no. 1-2, pp. 3–27, 2003.

[5] S.-S. Yeo, C. D. Shackelford, and J. C. Evans, "Consolidation and hydraulic conductivity of nine model soil-bentonite backfills," *Journal of Geotechnical and Geoenvironmental Engineering*, vol. 131, no. 10, pp. 1189–1198, 2005.

[6] S. A. Berilgen, M. M. Berilgen, and I. K. Ozaydin, "Compression and permeability relationships in high water content clays," *Applied Clay Science*, vol. 31, no. 3-4, pp. 249–261, 2006.

[7] R.-D. Fan, Y. J. Du, K. R. Reddy, S. Y. Liu, and Y. L. Yang, "Compressibility and hydraulic conductivity of clayey soil mixed with calcium bentonite for slurry wall backfill: initial assessment," *Applied Clay Science*, vol. 101, pp. 119–127, 2014.

[8] A. Royal, A. W. Opukumo, C. S. Qadr, L. M. Perkins, and M. A. Walenna, "Deformation and compression behavior of a cement-bentonite slurry for groundwater control applications," *Geotechnica and Geologica Engineering*, vol. 36, no. 2, pp. 835–853, 2018.

[9] W. R. Bryant, W. Hottman, and P. Trabant, "Permeability of unconsolidated and consolidated marine sediments, Gulf of Mexico," *Marine Geotechnology*, vol. 1, no. 1, pp. 1–14, 1975.

[10] C. A. Morrow, L. Q. Shi, and J. D. Byerlee, "Permeability of fault gouge under confining pressure and shear stress," *Journal of Geophysical Research: Solid Earth*, vol. 89, no. B5, pp. 3193–3200, 1984.

[11] J. Arch and A. Maltman, "Anisotropic permeability and tortuosity in deformed wet sediments," *Journal of Geophysical Research*, vol. 95, no. B6, pp. 9035–9045, 1990.

[12] S. Zhang and S. F. Cox, "Enhancement of fluid permeability during shear deformation of a synthetic mud," *Journal of Structural Geology*, vol. 22, no. 10, pp. 1385–1393, 2000.

[13] B. R. Crawford, D. R. Faulkner, and E. H. Rutter, "Strength, porosity, and permeability development during hydrostatic and shear loading of synthetic quartz-clay fault gouge," *Journal of Geophysical Research*, vol. 113, no. B3, 2008.

[14] S. Kimura, H. Kaneko, T. Ito, and H. Minagawa, "Investigation of fault permeability in sands with different mineral compositions (evaluation of gas hydrate reservoir)," *Energies*, vol. 8, no. 7, pp. 7202–7223, 2015.

[15] S. Kimura, H. Kaneko, S. Noda, T. Ito, and H. Minagawa, "Shear-induced permeability reduction and shear-zone development of sand under high vertical stress," *Engineering Geology*, vol. 238, pp. 86–98, 2018.

[16] A. Al-Tabbaa and D. M. Wood, "Some measurements of the permeability of kaolin," *Géotechnique*, vol. 37, no. 4, pp. 499–514, 1987.

[17] R. P. Chapuis and D. E. Gill, "Hydraulic anisotropy of homogeneous soils and rocks: influence of the densification process," *Bulletin of the International Association of Engineering Geology*, vol. 39, no. 1, pp. 75–86, 1989.

[18] D. N. Dewhurst, K. M. Brown, M. B. Clennell, and G. K. Westbrook, "A comparison of the fabric and permeability anisotropy of consolidated and sheared silty clay," *Engineering Geology*, vol. 42, no. 4, pp. 253–267, 1996.

[19] A. Dhowian and T. Edil, "Consolidation behavior of peats," *Geotechnical Testing Journal*, vol. 3, no. 3, pp. 105–114, 1980.

[20] S. Leroueil, G. Bouclin, F. Tavenas, L. Bergeron, and P. La Rochelle, "Permeability anisotropy of natural clays as a function of strain," *Canadian Geotechnical Journal*, vol. 27, no. 5, pp. 568–579, 2011.

[21] E. E. Malinowska and A. Szymański, "Vertical and horizontal permeability measurements in organic soils," *Annals of Warsaw University of Life Sciences, Land Reclamation*, vol. 47, no. 2, pp. 153–161, 2015.

[22] G. Mesri and R. E. Olson, "Mechanisms controlling the permeability of clays," *Clays and Clay Minerals*, vol. 19, pp. 151–158, 1971.

[23] H. W. Olsen, "Hydraulic flow through saturated clays," *Clays and Clay Minerals*, vol. 9, pp. 131–161, 1960.

[24] P. W. Rowe and L. Barden, "A new consolidation cell," *Géotechnique*, vol. 16, no. 2, pp. 162–170, 1966.

[25] W. B. Wilkinson and E. L. Shipley, "Vertical and horizontal laboratory permeability measurements in clay soils," *Developments in Soil Science*, vol. 2, pp. 285–298, 1972.

[26] G. Cheng, H.-H. Zhu, Y.-N. Wen, B. Shi, and L. Gao, "Experimental investigation of consolidation properties of nano-bentonite mixed clayey soil," *Sustainability*, vol. 12, no. 2, p. 459, 2020.

[27] R. A. Reid, *Triaxial Permeability Device*, M. S. Thesis, Georgia Institute of Technology, Atlanta, Georgia, 1988.

[28] W. R. Whalley, G. P. Matthews, and S. Ferraris, "The effect of compaction and shear deformation of saturated soil on hydraulic conductivity," *Soil and Tillage Research*, vol. 125, pp. 23–29, 2012.

[29] H. Lei, Y. Wu, Y. Yu, and B. Zhang, "Influence of shear on permeability of clayey soil," *International Journal of Geomechanics*, vol. 16, no. 5, 2016.

[30] G. Wang, W. Wang, and X. Wei, "A ring-shear radial-seepage apparatus for evaluating the permeability of shear bands in compacted clay," *Geotechnical Testing Journal*, vol. 44, 2020.

[31] S. Zhang, T. E. Tullis, and V. J. Scruggs, "Permeability anisotropy and pressure dependency of permeability in experimentally sheared gouge materials," *Journal of Structural Geology*, vol. 21, no. 7, pp. 795–806, 1999.

[32] K. M. Brown and J. C. Moore, "Comment on "Anisotropic permeability and tortuosity in deformed wet sediments" by J. Arch and A. Maltman," *Journal of Geophysical Research: Solid Earth*, vol. 98, no. B10, pp. 17859–17864, 1993.

[33] R. P. Chapuis, "Predicting the saturated hydraulic conductivity of soils: a review," *Bulletin of Engineering Geology and the Environment*, vol. 71, no. 3, pp. 401–434, 2012.

[34] B. Dolinar, "Predicting the hydraulic conductivity of saturated clays using plasticity-value correlations," *Applied Clay Science*, vol. 45, no. 1-2, pp. 90–94, 2009.

[35] A. Ilek and J. Kucza, "A laboratory method to determine the hydraulic conductivity of mountain forest soils using undisturbed soil samples," *Journal of Hydrology*, vol. 519, pp. 1649–1659, 2014.

[36] J. Kucza and A. Ilek, "The effect of the shape parameters of a sample on the hydraulic conductivity," *Journal of Hydrology*, vol. 534, pp. 230–236, 2016.

[37] M. A. Malusis, C. D. Shackelford, and H. W. Olsen, "Flow and transport through clay membrane barriers," *Engineering Geology*, vol. 70, no. 3-4, pp. 235–248, 2003.

[38] M. Mejías, P. Renard, and D. Glenz, "Hydraulic testing of low-permeability formations," *Engineering Geology*, vol. 107, no. 3-4, pp. 88–97, 2009.

[39] X. Ren, Y. Zhao, Q. Deng, J. Kang, D. Li, and D. Wang, "A relation of hydraulic conductivity - void ratio for soils based on Kozeny-Carman equation," *Engineering Geology*, vol. 213, pp. 89–97, 2016.

[40] A. J. Roque and G. Didier, "Calculating hydraulic conductivity of fine-grained soils to leachates using linear expressions," *Engineering Geology*, vol. 85, no. 1-2, pp. 147–157, 2006.

[41] M. D. Sante, E. Fratalocchi, F. Mazzieri, and V. Brianzoni, "Influence of delayed compaction on the compressibility and hydraulic conductivity of soil-lime mixtures," *Engineering Geology*, vol. 185, pp. 131–138, 2015.

[42] D. W. Taylor, *Fundamentals of Soil Mechanics*, John Wiley & Sons, NY, USA, 1948.

[43] Q. Wang, Y.-J. Cui, A. M. Tang, J.-D. Barnichon, S. Saba, and W.-M. Ye, "Hydraulic conductivity and microstructure changes of compacted bentonite/sand mixture during hydration," *Engineering Geology*, vol. 164, pp. 67–76, 2013.

[44] S. Zhang, H. Grip, and L. Lövdahl, "Effect of soil compaction on hydraulic properties of two loess soils in China," *Soil and Tillage Research*, vol. 90, no. 1-2, pp. 117–125, 2006.

[45] P. C. Carman, *Flow of Gases through Porous Media*, Butterworths Scientific Publications, London, England, 1956.

[46] R. P. Chapuis, "Predicting the saturated hydraulic conductivity of sand and gravel using effective diameter and void ratio," *Canadian Geotechnical Journal*, vol. 41, no. 5, pp. 787–795, 2011.

[47] P. Raju, N. S. Pandian, and T. S. Nagaraj, "Analysis and estimation of coefficient of consolidation," *Geotechnical Testing Journal*, vol. 18, no. 2, pp. 252–258, 1995.

[48] A. M. Samarasinghe, Y. H. Huang, and V. P. Drnevich, "Permeability and consolidation of normally consolidated soils," *Geotechnical Engineering Division, ASCE*, vol. 108, no. 6, pp. 835–850, 1982.

[49] Q. Liu, Y. Wu, Q. Li, and Y. Yu, "Modified model for hydraulic conductivity of clayey soil under shear," *International Journal of Geomechanics*, vol. 19, no. 11, 2019.

[50] B. C. O'Kelly, "Compression and consolidation anisotropy of some soft soils," *Geotechnical and Geological Engineering*, vol. 24, no. 6, pp. 1715–1728, 2006.

[51] O. N. Scholes, S. A. Clayton, A. F. A. Hoadley, and C. Tiu, "Permeability anisotropy due to consolidation of compressible porous media," *Transport in Porous Media*, vol. 68, no. 3, pp. 365–387, 2007.

[52] P. Basak, "Soil structure and its effects on hydraulic conductivity," *Soil Science*, vol. 114, no. 6, pp. 417–422, 1972.

[53] P. Delage and G. Lefebvre, "Study of the structure of a sensitive Champlain clay and of its evolution during consolidation," *Canadian Geotechnical Journal*, vol. 21, no. 1, pp. 21–35, 1984.

[54] R. P. Chapuis, D. E. Gill, and K. Baass, "Laboratory permeability tests on sand: influence of the compaction method on anisotropy," *Canadian Geotechnical Journal*, vol. 26, no. 4, pp. 614–622, 1989.

[55] H. Cetin, "Soil-particle and pore orientations during consolidation of cohesive soils," *Engineering Geology*, vol. 73, no. 1-2, pp. 1–11, 2004.

[56] R. L. Sloane and T. R. Kell, "The fabric of mechanically compacted kaolin," *Clay and Clay Minerals*, vol. 14, pp. 289–296, 1966.

[57] G. Mesri and B. Vardhanabhuti, "Compression of granular materials," *Canadian Geotechnical Journal*, vol. 46, no. 4, pp. 369–392, 2009.

[58] H. Rezaee, G. Lashkaripour, M. Ghafoori, and N. H. Moghaddas, "Measuring the properties of the microstructure loess in Golestan province," *Australian Journal of Basic and Applied Sciences*, vol. 6, no. 8, pp. 83–92, 2012.

[59] T. W. Lambe and R. V. Whitman, *Soil Mechanics*, pp. 281–294, John Wiley & Sons, NY, USA, 1969.

[60] G. Mesri and A. Rokhsar, "Theory of consolidation for clays," *Geotechnical Engineering Division, ASCE*, vol. 100, no. 8, pp. 889–904, 1974.

[61] Y. Nishida and S. Nakagawa, "Water permeability and plastic index of soils,," in *Proceedings of IASH-UNESCO Symposium Tokyo*, no. 89, pp. 573–578, Tokyo, Japan, 1970.

[62] F. Tavenas, P. Jean, P. Leblond, and S. Leroueil, "The permeability of natural soft clays. Part II: permeability characteristics," *Canadian Geotechnical Journal*, vol. 20, no. 4, pp. 645–660, 2011.

[63] R. N. Yong and B. P. Warkentin, *Soil Properties and Behaviour*, p. 449, Elsevier Scientific Publishing Company, Amsterdam, Netherlands, 1975.

[64] A. Alaoui, J. Lipiec, and H. H. Gerke, "A review of the changes in the soil pore system due to soil deformation: a hydrodynamic perspective," *Soil and Tillage Research*, vol. 115-116, pp. 1–15, 2011.

[65] K. Beven and P. Germann, "Macropores and water flow in soils," *Water Resources Research*, vol. 18, no. 5, pp. 1311–1325, 1982.

[66] J. Jang, G. A. Narsilio, and J. C. Santamarina, "Hydraulic conductivity in spatially varying media-a pore-scale investigation," *Geophysical Journal International*, vol. 184, no. 3, pp. 1167–1179, 2011.

[67] A. R. Dexter, E. A. Czyż, and O. P. Gaţe, "Soil structure and the saturated hydraulic conductivity of subsoils," *Soil and Tillage Research*, vol. 79, no. 2, pp. 185–189, 2004.

[68] L. Alakukku, "Persistence of soil compaction due to high axle load traffic. I. Short-term effects on the properties of clay and organic soils," *Soil and Tillage Research*, vol. 37, no. 4, pp. 211–222, 1996.

[69] S. Assouline, D. Tessier, and J. Tavares-Filho, "Effect of compaction on soil physical and hydraulic properties: experimental results and modeling," *Soil Science Society of America Journal*, vol. 61, no. 2, pp. 390–398, 1997.

[70] V. Dijck and V. Asch, "Compaction of loamy soils due to tractor traffic in vineyards and orchards and its effect on infiltration in southern France," *Soil and Tillage Research*, vol. 63, no. 3-4, pp. 141–153, 2002.

[71] F. J. Griffiths and R. C. Joshi, "Change in pore size distribution owing to secondary consolidation of clays," *Canadian Geotechnical Journal*, vol. 28, no. 1, pp. 20–24, 2011.

[72] J. Lipiec, M. Hajnos, and R. Świeboda, "Estimating effects of compaction on pore size distribution of soil aggregates by mercury porosimeter," *Geoderma*, vol. 179-180, pp. 20–27, 2012.

[73] Y.-N. Wei, W. Fan, N. Yu, L.-S. Deng, and T. Wei, "Permeability of loess from the South Jingyang Plateau under different consolidation pressures in terms of the three-dimensional microstructure," *Bulletin of Engineering Geology and the Environment*, vol. 79, no. 1-2, pp. 4841–4857, 2020.

[74] X. W. Ren and J. C. Santamarina, "The hydraulic conductivity of sediments: a pore size perspective," *Engineering Geology*, vol. 233, pp. 48–54, 2018.

[75] S. H. Haines, B. A. Van Der Pluijm, M. J. Ikari, D. M. Saffer, and C. Marone, "Clay fabric intensity in natural and artificial fault gouges: implications for brittle fault zone processes and sedimentary basin clay fabric evolution," *Journal of Geophysical Research*, vol. 114, no. B5, 2009.

Research Article

Numerical Evaluation on Improvement Performance of Waved Connection to Reduce Damage on Buried Gas Pipeline

Seyed Mohammad Seyed Kolbadi ⓘ**, Nemat Hassani, and Mohammad Safi** ⓘ

Department of Structure and Earthquake Engineering, College of Civil and Environment Engineering,
Shahid Beheshti University, Tehran, Iran

Correspondence should be addressed to Mohammad Safi; m_safi@sbu.ac.ir

One of the major challenges for the oil and gas industry is to keep buried metal pipes safe from faulting. This paper discusses about a solution to keep buried pipes safe. In this study, after examining the different dimensions of the effect of wave connection on improving the performance of buried metal pipes, by changing the geometric shape of the wave connection such as doubling it, the behavior of the pipe is greatly improved. Waved connections, by their local deformation, create a rotational joint in a limited area so that other parts of the pipe remain intact. In this paper, the behavior of buried pipes due to slip direction fault displacement by modelling with Abacus software version 2017 and selection of 4-node shell element and 8-node shell element have been used for pipe and soil modelling, respectively. In this paper, by comparing to a single waved connection with a double waved connection, the performance of the pipe due to the faulting phenomenon was evaluated. The results show the improvement of the excellent performance of the double joint by reducing the plastic strain values. In addition to increasing the ductility of the pipe, the double connection has been able to reduce the strain values by about 50% compared to the single connection. In general, this paper shows that the use of wave connections can significantly increase the level of safety of buried gas pipelines without increasing the cost.

1. Introduction

Many studies have been conducted on the behavior of pipes at fault intersections. Newmark and Hall [1] (pipe intersection with active fault) are the first to analytically calculate the pipe wall stress by considering the cable model and the plate fault under small displacements. Kennedy et al. [2, 3], with the expansion of the previous work, developed analytical models, also taking into account soil and pipe interactions. Wang and Yeh [4] were able to improve this methodology for bending stiffness of pipes. Vegiokas et al. [5] should also publish their research using the theory of beams on the elastic bed and also the effect of both horizontal and vertical fault displacements. Urock and McCaffrey [6] and Dismad et al. [7] studied the distribution of strain on interrupted pipes by faults based on gas and water pipes' performance in the San Fernando earthquake. Wang [8] developed the theory of beam on an elastic bed. Takada et al. [9] also proposed a more simplified method for

a more accurate evaluation of critical strain of steel pipes interrupted by faults using the relationships between the pipe's axial deformation and the transverse deformation. Recently, Karamitros et al. [10] improved the previous analytical achievements by combining the beam model on the elastic bed and the elastic beam theory to estimate the maximum strain due to strike-slip and normal faulting. Trifono and Cherini [11, 12] presented a quasianalytical methodology for pipe stress-strain analysis considering the ratio of transverse to axial displacements.

In general, the behavior of buried pipelines depends on many parameters like underground water surface. Recently, Bouatia et al. [13] investigated about the structural behavior of pipelines buried in expansive soils under rainfall infiltration. In that paper, numerical analyses were performed to investigate the transverse structural behavior of buried pipelines in expansive soils considering the unsaturated behavior of soil under the effect of 4 mm/day rainfall precipitation lasting for 30 days as an external hydraulic

loading. Considering the water supply 800 mm pipeline coming from the Beni-Haroun Dam [14] and buried at 2 m depth in Aine-Tine (Mila, Algeria) [15] high expansive soil, four simulations were performed to demonstrate the effect of the initial suction profiles which may represent different degrees of aridity that characterize regions with arid and semiarid climate. The study highlighted that the unsaturated behavior of expansive soils because of their volume instability is very sensitive to climatic conditions and can exert adverse effects on pipelines buried within such soils. As a result, consistent pipeline design should seriously consider the study of the effect of the climatic conditions on the overall stability of the pipeline structure. Also, various numerical simulations have been performed on the behavior of the pipe on the soil bed. Abbas Haghollahi et al. [16] studied about behavior of connection between steel I-beam and H-column when affected by cyclic loading. They found that reinforcement with a vertical triangular rib plate attached to the top and bottom flange plates can improve cyclic behavior of WFP connections.

According to the results of previous research, in general, the mechanism of pipe failure can be classified into three modes: tensile damage, shear damage and, most importantly, compressive damage (buckling damage). In this regard, we seek to provide a solution in conventional metal pipes that can minimize the mentioned damage and increase the pipes' service life.

Joshi et al. [13] used pipe modelling as a beam to investigate pipelines' behavior facing the faults. Okan et al. [14] also presented a simplified beam-based model as a useful and efficient tool for calculating the critical length of a pipe and the methodology for forming a pipe failure curve. This model has also been implemented and used in common international standards as an effective and reliable computational modelling approach, including Euro Code 8 [15], ALA [16], and ASCE. Vozuras et al. [17] also presented the exact finite element model for the pipeline in the face of the fault phenomenon. In this model, soil properties and pipe passage angle from the fault and mechanical properties of the pipeline are used to express the critical buckling strain. This model was also used by Zhang et al. [18] and Trifonov [12] to study the effects of trench dimensions, soil intrinsic properties, and fault motion simulation.

The behavior of steel pipes under pressure and buckling is very complicated. Hence, a case study on pipe wall failure is quite essential to understand transmission lines' actual behavior in the face of displacement caused by faults. Many researchers have considered the behavior of steel pipe in the face of compressive loading. Reed [19], and more recently, Tutunsa [20] as well as Brady [21] and Kirikidis and Joe [22] evaluated the buckling failure of steel pipes in the face of axial net pressure and flexural behavior. Caramanus and Tassoulas [23] also recently studied the behavior of large diameter pipes that are welded in a spiral. Besides, the effect of peripheral soil on the buckling strength of buried pipes has been investigated by Jon and Kirikides [24].

So far, many studies have been conducted on the behavior of buried pipes due to faults, but few studies have been conducted to provide a practical solution to keep buried pipes safe. Challenges of buried pipes against faulting phenomena include high deformation, high axial strain rate, crimping of pipe cross-section, and local buckling. Using a wave connection can be a good solution to solve these problems. A recent wave connection solution by Packer Wham et al. [25] has been proposed, but this approach only refers to the study of large axial displacements. In the present paper, after examining different dimensions of the effect of wave connection on improving the performance of buried pipes cross-slip fault, for the first time, the geometric characteristics including doubling the wave connection have been improved [26]. This solution can be a safe, practical, inexpensive, and attractive solution for oil and gas industry employers. Due to the fact that the cross-section of the pipe in the fault zone remains unchanged after the fault is displaced, so after the fault is displaced, the pipe can continue to serve [27].

2. Materials and Methods

2.1. Buckling Model including Force-Displacement Characteristics of Soil. The strongest argument for the claim that the nonlinear force-deformation details of the soil significantly affect the starting buckling of the buried pipe was studied by Turgard and Needelman [28]. In simple conditions, the soil is modelled elastically and applies lateral force to the pipe. This force per unit length is equivalent to a spring with a constant stiffness k. In this case, the following equation is valid.

$$EI y''' + P y'' + W = 0, \qquad (1)$$

where E is the modulus of elasticity, I is the inertia moment, y is the beam response, and w is the equation constant. The P parameters also can be driven by equation (2). It is simple to show (for example, reference [29]) that the critical buckling load is obtained from the following equation.

$$P = 2\sqrt{\mathrm{kEI}}. \qquad (2)$$

2.2. Critical Buckling Stress Caused by Bending Moment. The buckling of pipes occurs when the stress exceeds the yielding stress of the material. Due to the strike-slip fault, the bending moment due to the fault's displacement causes the buried pipe to bend. Many approximate relationships explain the amount of buckling stress and moment created in the pipe under bending, without considering the internal pressure. One of the pioneers of these efforts in the nonlinear structural analysis was performed by Brazier [30]. He found that pipes break down when the deformed inner radius of the pipe reaches the pipe's diameter. The M_{cr1} bending moment is calculated based on this type of deformation based on the following.

$$M_{cr1} = \frac{\sqrt{2}}{9} \frac{E\pi D t^2}{\sqrt{1 - v^2}}. \qquad (3)$$

D is the pipe's diameter, t is the thickness of the pipe, E is the modulus of elasticity, and v is the Poisson's ratio. The

maximum flexural stress of the pipe under the M_{cr} buckling moment can be expressed as follows.

$$\sigma_{cr1} = \frac{4M_{cr}}{\pi D^2 t}. \tag{4}$$

If the critical buckling stress of the pipeline under bending is similar to the buckling stress of a pipe under uniform pressure, the buckling stress is expressed as follows:

$$\sigma_{cr1} = \frac{2E}{\sqrt{3(1-\nu^2)}}\left(\frac{t}{D}\right). \tag{5}$$

Then, the buckling moment is extracted as follows:

$$M_{cr2} = \frac{E\pi D t^2}{2\sqrt{3(1-\nu^2)}}. \tag{6}$$

Tymoshenko and Gear [31] stated that the maximum compressive stress in the critical buckling moment is about 30% higher than that obtained from equation (6):

$$M_{cr3} = 0.65\frac{E\pi D t^2}{\sqrt{3(1-\nu^2)}}. \tag{7}$$

These theories are not based on internal pressure. Based on the plastic theory, numerical solutions for stress and strain components are obtained for normal pipe pressures by Hu and Yuan [25]. The internal stress and strain distribution of the pipe can be obtained by formulas. But they did not investigate the buckling problem. Bending deformation of buried pipes is a nonlinear problem. The bending moment is not uniform along the axis of the pipe. Soil-pipe interaction is also an important factor for buckling behavior. Besides, the pipe is a thin shell structure. When large deformations appear on the pipe's cross-section, the superposition principle cannot be used for axial strain and flexural strain interactions. There may also be residual stress and stress concentration for the pipes; therefore, it is difficult to solve the pipe response by the analytical method. The finite element method will be more appropriate.

Because the buckling of pipes due to its geometric characteristics can occur local buckling off the plate on its wall, the study of its behavior will be quite complex analytically. Therefore, for a more detailed study of this issue, the finite element method has been used, and Abacus software has been used for simulation. As shown in Figure 1, the fault's motion depends on the two angles of the fault slope and the pipe's cross-sectional angle, which are presented in the vertical and horizontal planes, respectively [32].

In this paper, to focus more on expanding the application of waved connection on the performance of buried gas pipes under the influence of slip directional fault motion, the same values of β and ϕ are considered equal to 90°. These parameters are equivalent to the angle of the pipe with the fault plane and the direction of the pipe with the fault direction, respectively.

So far, many studies have been conducted on the behavior of buried metal pipes crossing faults. But very few
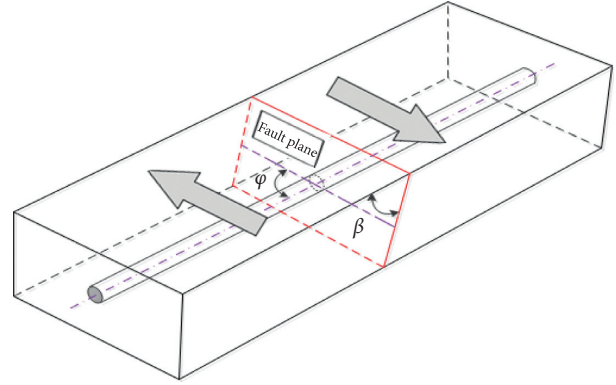
FIGURE 1: Geometric view of pipe crossing fault.

solutions have been proposed to keep buried pipes from fault displacement safe. These solutions must address challenges such as increasing the longitudinal strain rate, pipe cross-sectional crunch, and local buckling. On the other hand, the solution must be a cheap and reliable application to attract the attention of employers in the oil and gas industry. Wave connection can provide a good cover to solve these problems. Although the wave connection solution recently developed by Packer Wham et al. [33] is given, this study merely examines large axial displacements. In the present paper, after evaluating the performance of the wave connection for the first time, by significantly changing the geometric shape of the connection and converting it to a double connection, a significant improvement in the behavior of the buried pipe is evaluated.

2.3. Numerical Analysis

2.3.1. Validation. Packer Wham et al. [34] studied an experimental investigation to evaluate the axial performance of waved connections (Figure 2). In this laboratory study, by applying a large axial displacement by the actuator to a steel pipe with a 20 cm diameter that waved dy 20 mm radius, modulus of elasticity of 217 GPa, and yielding stress of 309 MPa, strain data were recorded by strain gauges and displacement.

In this paper, to verify the numerical model, the experimental and numerical results were compared together. Figure 3 shows 5 steps of compressive force that have been compared with experimental results).

The results show that they are qualitatively consistent with each other. For a quantitative comparison of the laboratory model results and the numerical model results, the values of axial force of the pipe were compared with each other (Figure 4).

As shown in Figure 4, the numerical model results are in good agreement with the laboratory results, so other results of the numerical model can be an acceptable evaluation criterion by comparing the numerical and laboratory results. The numerical model can be obtained to simulate the trend of changes in compressive force against displacement and axial strain against displacement.

FIGURE 2: Experimental test of axial compressure of the pipe with waved connection [34].

2.3.2. Evaluation of Waved Connection Performance on Pipe Performance. So far, the numerical model of the waved connection has been validated based on the experimental model of Packer Loan, and the accuracy of its results can be cited. The depth of the pipe's burial is two times its diameter, which is in accordance with the pipeline engineering method [35] and the len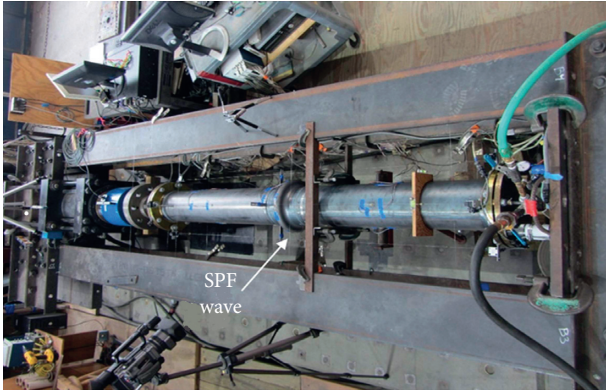gth of the pipe and the surrounding soil. According to the results obtained in this paper, 200 m is equal to 218 times the diameter of the pipe as the optimal length. In the y and z directions, according to the recommendation of Vozoras [17], 6 and 10 times the diameter of the pipe are considered, respectively. The pipe diameter is $D = 0.914$ m, and the thickness is $t = 8$ mm, which is the conventional size of gas transmission pipelines (Figure 5).

Two static analysis steps are applied sequentially. First, the force of gravity is applied to the soil and the pipe's internal pressure, and then, the transverse displacement is applied to one of the fault blocks. The degrees of freedom related to the boundary plates, including the lower plate and the side plates of the first block, are fixed, and the second block is uniformly displaced in the lateral direction. According to the proposal of Vozoras et al. [17], the mechanical properties of the soil are considered as elastic-perfectly plastic with the Mohr–Coulomb model, which includes internal friction angle $\varphi = 0°$, cohesion $C = 50$ kPa, Poisson ratio $\nu = 0.3$, and elastic modulus $E = 25$ MPa. Also, the appropriate coefficient of friction angle, in this case, is considered $\mu = 0.5$.

The results obtained for API 5L [36] are X65 rank of steel pipelines. The stress-strain diagram for the steel materials of gas pipes is traditionally considered equal to X65 steel pipelines. The yielding stress is $\sigma_y = 448.5$ MPa, the modulus of elasticity is Gpa210, Poisson's ratio is 0.3, and the density is $7800 \, (\text{kg/m}^3)$. Additionally, the reliability coefficient of 0.72 and the maximum operating pressure $P_{\max}$ of these pipelines have been obtained according to the relationship [37, 38], where σ_y and $P_{\max}$ are the yielding stress and maximum operating pressure, respectively.

2.3.3. Waved Connection Performance. To better understand this issue, Figure 6 diagrams are used to compare the plastic strain values in the critical areas of two straight and waved pipes.

According to Figure 6, the pipe's plastic strain values with waved connection are two times higher than the straight pipe. But in the critical area, the pressure is much lower. Besides, plastic strain values in the most critical compression area of the straight pipe are about four times higher than the plastic strain values in the same area of the pipe with a waved connection. In other words, by eliminating the local buckling in the compression area, the waved connection was able to reduce the plastic strain values significantly.

The most critical point is a point with the highest strain values per displacement of the fault, and its position is shown in Figure 7. Plastic strain values at these points relative to the fault displacement have been drawn in a coordinate system for each of the straight pipes and the pipes with a waved connection in the compressive area, and the tensile area has been drawn in a coordinate system, and the results are compared with each other.

According to Figure 7(a), the plastic behavior of the straight pipe in the compressive area under the displacement of the 25 cm fault and the tensile area under the displacement of about 40 cm enters the plastic area. It also enters the buckling area at a displacement of 38 cm, in which case, the plastic strain values increase sharply. Thus, the maximum values of plastic strain due to 120 cm fault displacement in the tensile and compressive areas are equal to 0.03 and 0.3, respectively. Local buckling is the reason for the fact that the plastic strain values are ten times higher in the compressive area than in the tensile area. On the other hand, in Figure 7(b), both critical points in tension and compression enter the plastic area in the same displacement of the 20 cm fault and, of course, with increasing fault displacement, have less growth than the straight pipe. With a 120 cm displacement, the plastic strain values of the critical points of tension and compression reach 0.06 and 0.04, respectively. Thus, by comparing the above results, the waved connection has increased the plastic strain values at critical points compared with the straight pipe by 0.03 and decreased by 0.26 in the compressive and tensile areas, respectively.

According to Figure 7, it is clear that the highest values of plastic strain at critical points for straight pipe and waved pipe are in the compressive and tensile areas, respectively. Based on the comparison of plastic strain values in the most critical points of straight pipe and pipe with waved connection, it can be said that the waved connection has been able to reduce the strain values by 87% significantly. Wave connection has been able to reduce the plastic strain values well and limit the stress distribution areas. Then, by considering two waved connections (double connection) next to each other, the pipe's performance is evaluated, as shown in Figure 8.

In critical areas, two consecutive waved connections are installed. The plastic strain values in the tensile and compressive areas are compared with each other and with the single connection mode (Figures 9 and 10).

According to Figure 9, it can be seen that the plastic strain values in the tensile area are distributed in two parts,

Numerical deflection	Experimental deflection	Axial displacement
		Pretest
		13 mm
		51 mm
		94 mm
		127 mm
		163 mm
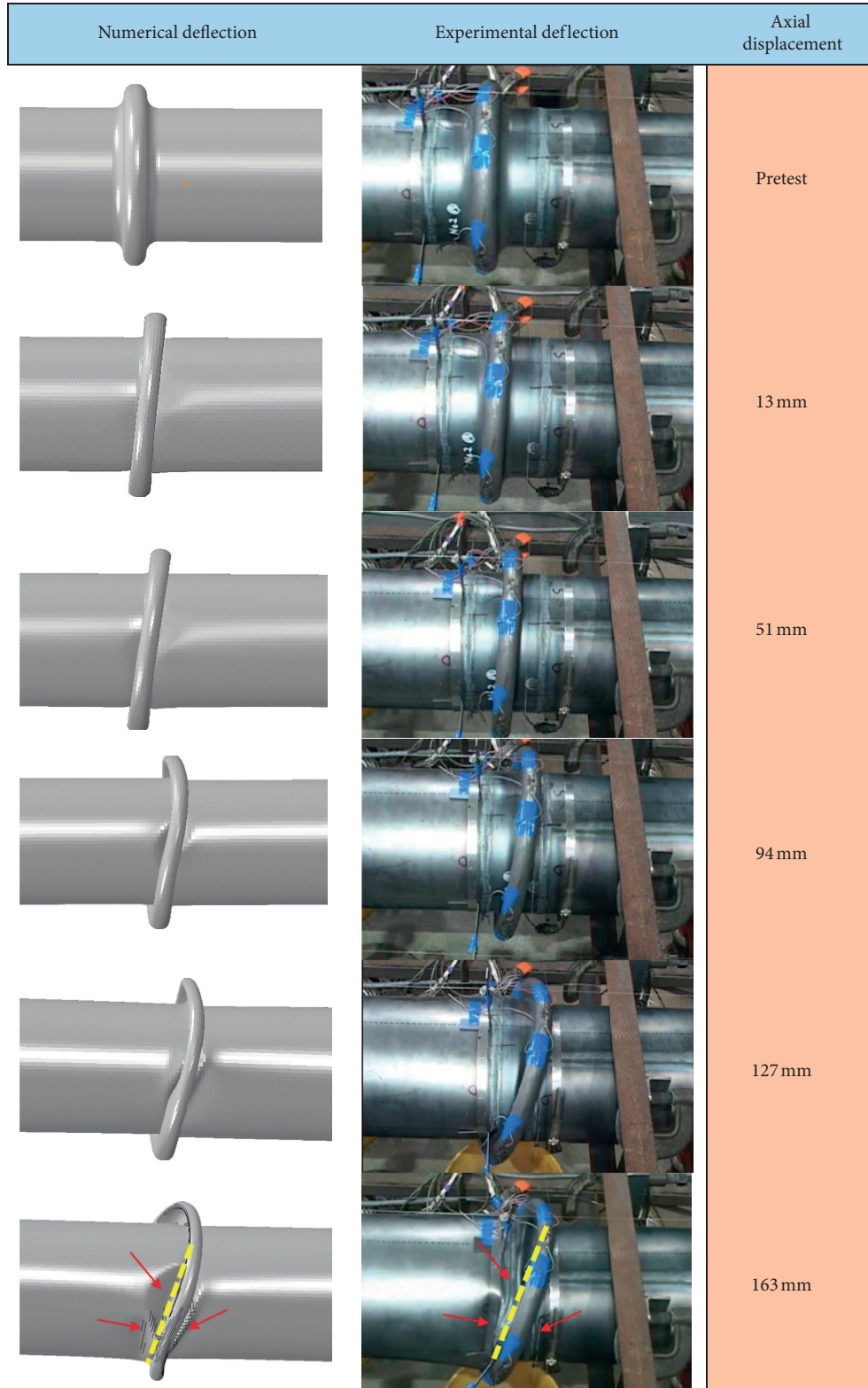
Figure 3: Comparison between deformed pipes of the experimental [34] and numerical models.

but in the compression area, the second connection does not enter the plastic area. The plastic strain values in Figures 9 and 10 are compared to understand better the double connection's performance beside the single connection.

As mentioned, the tensile area of the double connection is divided into two parts. By comparing the first connection with the single connection, the first, second, and third peaks of the diagram have a 10%, 33%, and 9% reduction in plastic
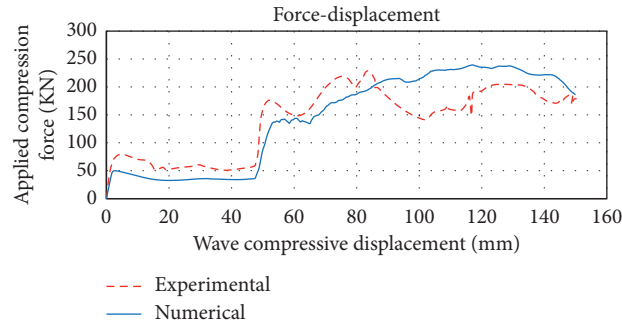
FIGURE 4: Comparison of axial force-displacement results of experimental and numerical models.
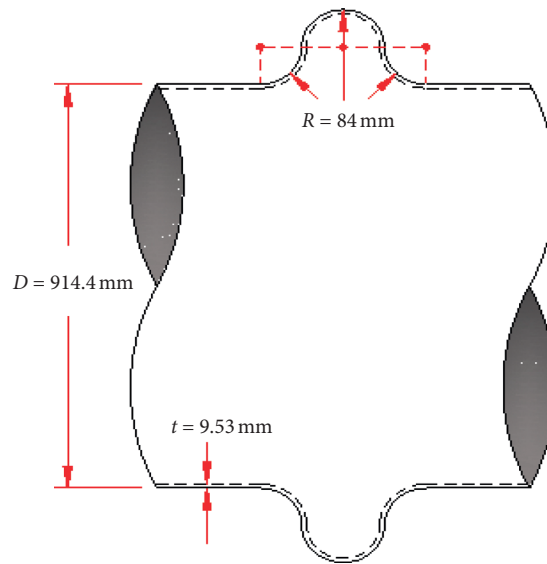
FIGURE 5: Geometric properties of waved connection used in the numerical model.

(a)

(b)
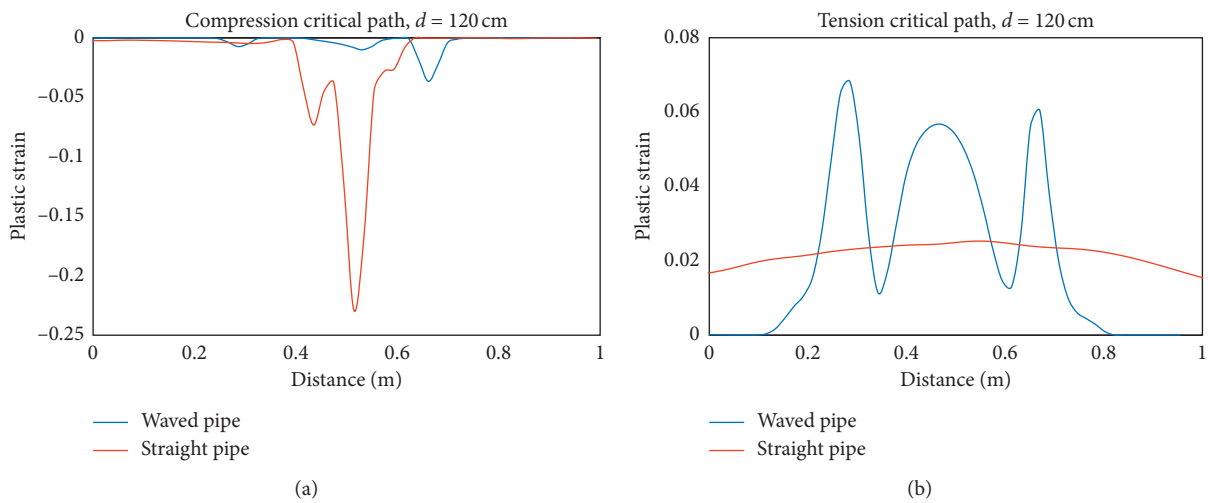
FIGURE 6: Comparison of plastic strain in tension and compression critical areas.
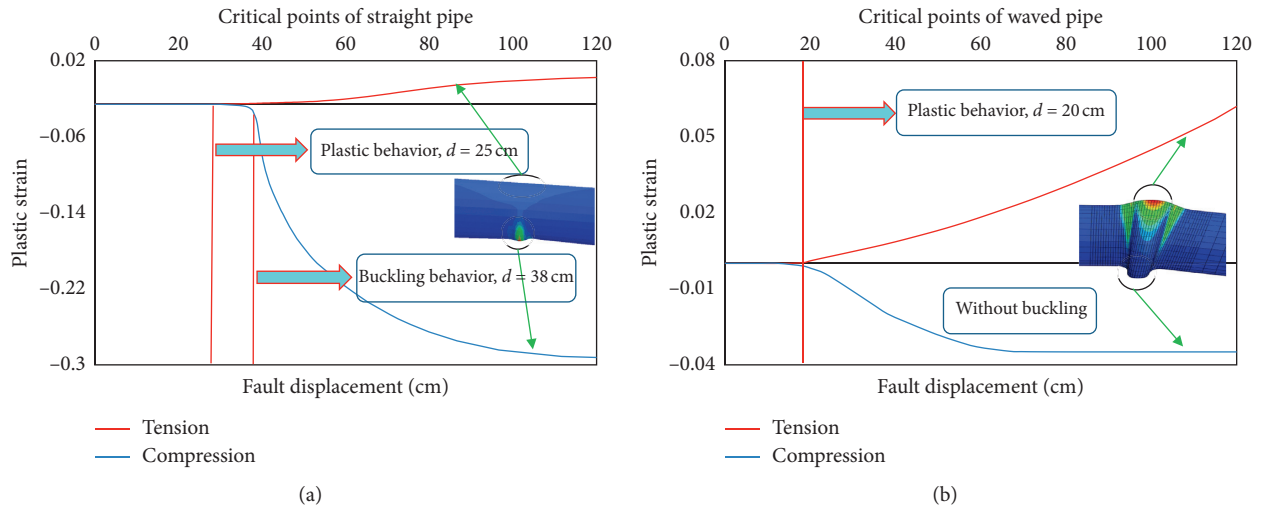
Figure 7: Comparison of plastic strain results in critical point. (a) Straight pipe. (b) Waved pipe.
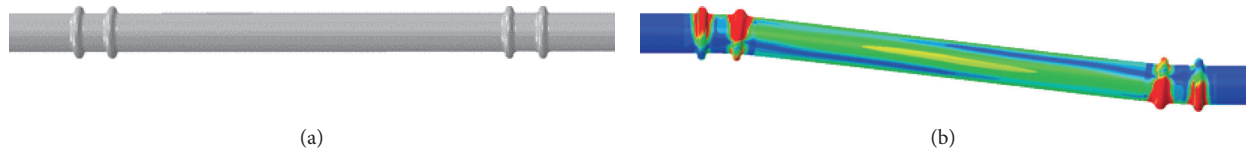
Figure 8: Von Mises contour of pipeline with double connection. (a) Before displacement. (b) After displacement.
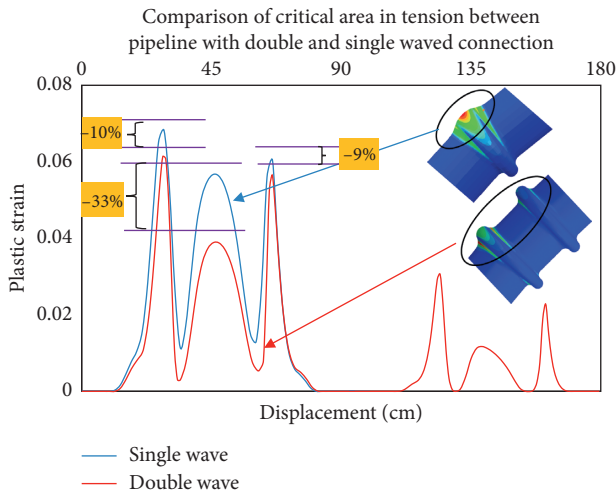
Figure 9: Contour of plastic strain on the critical area in tension.
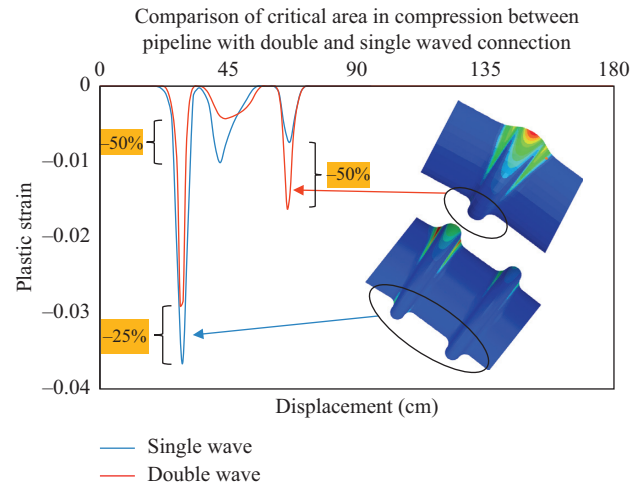
Figure 10: Contour of plastic strain on the critical area in compression.

strain, respectively. This reduction confirms the proper addition of the number of connections in different pipe areas that can improve its performance.

By comparing the plastic strain values in the compression areas of the double connection and the single connection, significant changes can be seen in reducing the plastic strain values. As mentioned, in the double connection, the second connection did not enter the plastic area, but the stress distribution in the two connections was such that the plastic strain values in the two double connections were sharply reduced. This decrease in the first, second, and third peaks was

equal to 25%, 50%, and 50%, respectively. The results show a significant improvement in the double waved connection's performance compared to the single connection.

3. Conclusion

In this paper, one solution to reduce the risks of fault displacement on the pipe's performance is investigated. The solution is to use a waved connection in the pipes. This connection was first proposed in 2017 by Packer Loan, and

its laboratory model is based on large axial deformations. Since steel pipes can withstand many strains after yielding, the plastic strain is considered the main output of the present paper in tensile and compressive critical areas. Its values have been compared in two straight pipes and pipes waved connection.

The double connection's tensile area is divided into two parts by comparing the pipe's performance with a double waved connection and a single waved connection. By comparing its first connection with a single connection, the first, second, and third peaks of the diagram are reduced by 10%, 33%, and 9%, respectively, in their plastic strain, which confirms that a proper increase in the number of connections in different areas of the pipe can improve its performance.

By comparing the plastic strain values in the double connection's compression areas and the single connection, very significant changes can be seen in reducing the plastic strain values. This decrease in the first, second, and third peaks was equal to 25%, 50%, and 50%, respectively. The results show a significant improvement in the double wave connection's performance compared to the single connection. It should be noted that this connection is simple and low cost in construction; besides, it is easily applicable, and according to its optimal performance, it will be an attractive option for employers of oil and gas companies. In addition to being inexpensive and straightforward to build, this connection is easy to implement.

Data Availability

The data used to support the findings of this study are available from the corresponding author upon request.

Conflicts of Interest

The authors declare that there are no conflicts of interest.

References

[1] N. M. Newmark and W. J. Hall, "Pipeline design to resist large fault displacement," in *Proceedings of US national conference on earthquake engineering*, Ann Arbor, Michigan, June 1975.

[2] R. Kennedy, "Fault crossing design for buried gas oil pipelines," *American Society of Mechanical Engineers, PVP*.vol. 77, pp. 1–9, 1983.

[3] R. P. Kennedy, A. Chow, and R. A. Williamson, "Fault movement effects on buried oil pipeline," *Transportation Engineering Journal of the American Society of Civil Engineers*, vol. 103, no. 5, pp. 617–633, 1977.

[4] L. R.-L. Wang and Y.-H. Yeh, "A refined seismic analysis and design of buried pipeline for fault movement," *Earthquake Engineering & Structural Dynamics*, vol. 13, no. 1, pp. 75–96, 1985.

[5] E. Vougioukas, C. Theodossis, and P. Carydis, "Seismic analysis of buried pipelines subjected to vertical fault movement," *Lifeline Earthquake Engineering*, pp. 432–441, 1979.

[6] M. MaCaffrey, "Buried pipeline response to reverse faulting during the 1971 San Fernando Earthquake," *American Society of Mechanical Engineers, PVP*, vol. 77, pp. 151–159, 1983.

[7] T. Desmond, M. Power, C. Taylor, and R. Lau, *Behavior of Large-Diameter Pipelines at Fault Crossings*, American Society of Civil Engineers, New York, NY, USA, 1995.

[8] L. Wang, "Parametric study of buried pipelines due to large fault movement, ASCE," *Technical Coucil on Lifeline Earthquake Engineering*, vol. 6, pp. 152–159, 1995.

[9] S. Takada, N. Hassani, and K. Fukuda, "A new proposal for simplified design of buried steel pipes crossing active faults," *Earthquake Engineering & Structural Dynamics*, vol. 30, no. 8, pp. 1243–1257, 2001.

[10] D. K. Karamitros, G. D. Bouckovalas, and G. P. Kouretzis, "Stress analysis of buried steel pipelines at strike-slip fault crossings," *Soil Dynamics and Earthquake Engineering*, vol. 27, no. 3, pp. 200–211, 2007.

[11] O. V. Trifonov, "Numerical stress-strain analysis of buried steel pipelines crossing active strike-slip faults with an emphasis on fault modeling aspects," *Journal of Pipeline Systems Engineering and Practice*, vol. 6, no. 1, Article ID 04014008, 2015.

[12] O. V. Trifonov and V. P. Cherniy, "A semi-analytical approach to a nonlinear stress-strain analysis of buried steel pipelines crossing active faults," *Soil Dynamics and Earthquake Engineering*, vol. 30, no. 11, pp. 1298–1308, 2010.

[13] M. Bouatia, R. Demagh, and Z. Derriche, "Structural behavior of pipelines buried in expansive soils under rainfall infiltration (Part I: transverse behavior)," *Civil Engineering Journal*, vol. 6, no. 9, pp. 1822–1838, 2020.

[14] W. Chettah, *Investigation des propriétés minéralogiques et géomécaniques des terrains en mouvement dans la ville de Mila « Nord-Est d'Algérie »*, Thèse de Magistère, University of Batna 1 Hadj Lakhdhar, Batna, Algérie, 2009.

[15] A. Djamel, A. Benaissa, A. Hammadi, and M. Bouassida, "Clay and marl formation susceptibility in Mila Province, Algeria," *Geotechnical and Geological Engineering*, vol. 28, no. 6, pp. 805–813, 2010.

[16] A. Haghollahi and H. Ahmadi, "Cyclic behavior of steel beam-to-column moment connections using different sizes of flange plates and reinforced by a single rib plate," *Civil Engineering Journal*, vol. 4, no. 1, pp. 138–150, 2018.

[17] L. Xu and M. Lin, "Analysis of buried pipelines subjected to reverse fault motion using the vector form intrinsic finite element method," *Soil Dynamics and Earthquake Engineering*, vol. 93, pp. 61–83, 2017.

[18] E. Uckan, B. Akbas, J. Shen, W. Rou, F. Paolacci, and M. O'Rourke, "A simplified analysis model for determining the seismic response of buried steel pipes at strike-slip fault crossings," *Soil Dynamics and Earthquake Engineering*, vol. 75, pp. 55–65, 2015.

[19] E. C. F. Standardization, *Eurocode 8: Design of Structures for Earthquake Resistance—Part 4: Silos, Tanks and Pipelines*, 2006.

[20] A. L. Alliance, "Guidelines for the design of buried steel pipe," *American Society of Civil Engineers*, 2001.

[21] P. Vazouras, S. A. Karamanos, and P. Dakoulas, "Mechanical behavior of buried steel pipes crossing active strike-slip faults," *Soil Dynamics and Earthquake Engineering*, vol. 41, pp. 164–180, 2012.

[22] J. Zhang, Z. Liang, and C. J. Han, "Buckling behavior analysis of buried gas pipeline under strike-slip fault displacement," *Journal of Natural Gas Science and Engineering*, vol. 21, pp. 921–928, 2014.

[23] S. R. Reid, "Plastic deformation mechanisms in axially compressed metal tubes used as impact energy absorbers,"

International Journal of Mechanical Sciences, vol. 35, no. 12, pp. 1035–1052, 1993.

[24] I. Tutuncu, *Compressive Load and Buckling Response of Steel Pipelines during Earthquakes*, 2002.

[25] B. Wham, C. Pariya-Ekkasut, C. Argyrou et al., "Large axial deformation performance of steel pipeline designed for fault crossings," in *Proceedings of the Pipelines 2017*, Phoenix, Arizona, August 2017, https://www.researchgate.net/deref/http%3A%2F%2Fdx.doi.org%2F10.1061%2F9780784480878.010.

[26] S. Ghods, A. Kheyroddin, M. Nazeryan, S. M. Mirtaheri, and M. Gholhaki, "Nonlinear behavior of connections in RCS frames with bracing and steel plate shear wall," *Steel and Composite Structures*, vol. 22, no. 4, pp. 915–935, 2016.

[27] N. Hassani, S. M. S. Kolbadi, M. R. Shiravand, and J. H. Golafshani, "Impact of geometric pattern corrosion on limit failure pressure of buried gas pipelines," *Structural Engineering and Mechanics*, vol. 59, no. 5, pp. 795–802, 2016.

[28] F. C. Bardi and S. Kyriakides, "Plastic buckling of circular tubes under axial compression-part I: Experiments," *International Journal of Mechanical Sciences*, vol. 48, no. 8, pp. 830–841, 2006.

[29] S. Kyriakides and J. G.T., "Bifurcation and localization instabilities in cylindrical shells under bending-I. Experiments," *International Journal of Solids and Structures*, vol. 29, no. 9, pp. 1117–1142, 1992.

[30] S. A. Karamanos and J. L. Tassoulas, "Tubular members. II: local buckling and experimental verification," *Journal of Engineering Mechanics*, vol. 122, no. 1, pp. 72–78, 1996.

[31] H. Yun and S. Kyriakides, "On the beam and shell modes of buckling of buried pipelines," *Soil Dynamics and Earthquake Engineering*, vol. 9, no. 4, pp. 179–193, 1990.

[32] N. H. SMS Kolbadi, S. M. S. Kolbadi, and M. R. Shiravand, "Effect of ground motions on nonlinear seismic behavior of corroded buried gas pipeline," *American Journal of Civil Engineering*, vol. 3, no. 2, pp. 9–13, 2015.

[33] M. O'Rourke and X. Liu, *Seismic Design of Buried and Offshore pipelines*, Multidisciplinary Center for Earthquake Engineering Research, Buffalo, New York, USA, 2012.

[34] M. Hetenyi, *Beams on Elastic Foundations*, p. 94, The University of Michigan Press, Ann Arbor, MI, USA, 1946.

[35] L. Brazier, "On the flexure of thin cylindrical shells and other "thin" sections," *Proceedings of the Royal Society of London. Series A, Containing Papers of a Mathematical and Physical Character*, vol. 116, no. 773, pp. 104–114, 1927.

[36] S. P. Timoshenko and J. M. Gere, *Theory of Elastic Stability*, Courier Corporation, Chelmsford, MA, USA, 2009.

[37] L. Hu and S. Yuan, "Plastic deformation analysis of thin-walled tube bending under internal pressure," *Journal of Mechanical Engineering*, vol. 48, no. 14, pp. 78–83, 2012.

[38] S. Joshi, A. Prashant, A. Deb, and S. K. Jain, "Analysis of buried pipelines subjected to reverse fault motion," *Soil Dynamics and Earthquake Engineering*, vol. 31, no. 7, pp. 930–940, 2011.

[39] A. Anon, *B31. 8-2012, Gas Transmission and Distribution Piping Systems*, p. 12, American Society of Mechanical Engineers (ASME), New York, NY, USA, 2013.

[40] ASME, *Pipeline Transportation Systems for Liquid Hydrocarbons and Other Liquids*, American Society of Mechanical Engineers (ASME), New York, NY, USA, 2002.

Research Article

A Novel Approach to Supply the Water Reservoir Demand Based on a Hybrid Whale Optimization Algorithm

Alireza Donyaii [ID]**, Amirpouya Sarraf** [ID]**, and Hassan Ahmadi** [ID]

Department of Civil Engineering, Roudehen Branch, Islamic Azad University, Roudehen, Iran

Correspondence should be addressed to Amirpouya Sarraf; st.ar_donyaii@riau.ac.ir

Managing water resources requires the optimum operation of dam reservoirs. To satisfy the downstream water demand in the operational optimization of Boostan dam reservoir, the improved whale optimization algorithm (IWOA) performance was compared in the present study with that of its constituents (i.e., the whale optimization and differential evolution) based on GAMS nonlinear programming results. The model evaluative indicators and an objective function were used to select the optimal algorithm. The findings suggested that IWOA resulted in the lowest computational duration and fastest convergence rate compared to the other algorithms. Additionally, the average water demand and discharge volume of IWOA were $3.21 \times 10^6 \, m^3$ and $3.03 \times 10^6 \, m^3$, respectively. In contrast, the other algorithms yielded lower water release volumes. IWOA enhanced the WOA performance by 21.7% through reducing the variation coefficient by 78% in optimizing the objective function. The water demand was therefore more effectively satisfied by the IWOA compared to the other algorithms. Furthermore, the IWOA resulted in a lower amount of errors. The hybrid algorithm performance increased in terms of all the evaluative indicators. Developing multicriteria decision-making models using TOPSIS and the Shannon entropy also suggested the IWOA excels the other algorithms in optimizing the reservoir operational problem.

1. Introduction

Managing water resources constitutes an essential domain in hydrological sciences for the sustainable utilization and allocation of valuable resources such as water [1]. Managers of water resources have identified water shortage as a globally major problem in various areas. This practical problem can be solved using state-of-the-art technology, innovative ideas, and strategic decisions made on water utilization [2, 3]. Water scarcity can also be solved through the operational optimization of reservoirs. Water resource policymakers therefore require appropriate optimization algorithms for lowering the difference between the demand for water and water discharge and generating optimal operation rules for water usage [4]. A reservoir operation is controlled mainly to reduce water shortage by developing the rules for the controlled discharge of water for downstream users [5]. The minimum permissible volume of the water stored in reservoirs in critical conditions and dry seasons must also be ensured [6]. Appropriate optimization algorithms should be therefore selected to take the necessary measures for the controlled discharge of water, provide various water users, including agricultural and industrial sectors, with a sustainable water supply, and therefore solve the operational problems of reservoirs [7, 8].

Metaheuristic and evolutionary optimization algorithms have been developed during the past 2 decades to solve complicated engineering problems. The main advantages of these methods include their simplicity of adjusting system constraints and objective functions within their mathematical domain. Obtaining a globally optimal solution can be, however, time-intensive, which is unacceptable in real-time operation. The computational time required by metaheuristic and evolutionary techniques for solving complicated problems has been demonstrated to be the least, making them an optimal choice for main decision-makers who need real-time solutions for their problems [4].

2. Review of the Literature

Genetic programming was applied by FallahMehdipour et al. [9] to a reservoir operation to decrease shortages of irrigation by considering the downstream discharge of water, the decision variable, and testing various mathematical and arithmetic operators for genetic programming. They found the demand for irrigation to be satisfied with the maximum reliability indicator compared to the reliability indicators of genetic algorithm and particle swarm optimization.

A case study was conducted in Iran by Ostadrahimi et al. [10] by applying particle swarm optimization to a multireservoir system to obtain various rule curves and decrease shortages of irrigation. The convergence rate of this new version of PSO was increased by making it function on the basis of a modified inertia weight. The data obtained were compared with those of nonlinear programming and genetic algorithm. The released water met the irrigation demand using particle swarm optimization, whose convergence was found to be faster than that of GA.

The reservoir operation was optimized and the benefits of power generation were improved by Afsahr [5] taking advantage of a modified particle swarm optimization adapted to hydraulic and hydrological boundary conditions of the problem in a way that the algorithm modeled the reservoir operation through a drought. The solution obtained using this version of particle swarm optimization was on average close to the globally optimal solution, and the power generated per year was higher than the power obtained using harmony search and genetic algorithm. Employing ant colony optimization to operationally optimize multireservoir systems helped satisfy the demand for irrigation with the minimum risk and minimize the average irrigation deficit [11]. Afshar and Moeini (2013) increased the diversity of the initial population by developing ant colony optimization on the basis of a mutation operator.

Genetic algorithm and novel dynamic programming proposed by [12] was applied to multireservoir operation to increase the power generated in China. Genetic algorithm outperformed dynamic programming despite the limited power generated in dry years, which required a rationing process. The position of drops was considered the initial population and a decision variable in the water cycle algorithm to reduce deficit in power based on the drop movements in the environment [13]. The running time of the water cycle algorithm was lower than that of genetic algorithm and particle swarm optimization, and this algorithm minimized the average deficit. A case study in Iran by Bozorg-Hadad et al. [14] was aimed at reducing power deficits using the bat algorithm based on surrounding frequencies received by bats. As a decision variable, the position of a bat was updated according to frequency and velocity. The rate of convergence of this algorithm based on random walk and local search was found to be higher than that of particle swarm optimization and genetic algorithm. Moreover, its power generation received a higher index of reliability.

Deficits in supplying demand for irrigation were minimized in a reservoir operation, and the released water

obtained from a third-order nonlinear rule curve on the basis of genetic algorithm was found to satisfy irrigation requirements given the high reliability index obtained [15]. Biogeography-based optimization used in a case study in Iran to reduce deficits in power [16] on the basis of migration processes and habitats in the environment resulted in solutions that approached the globally optimal solution through fewer iterations. The simple algorithm process used an initial species population in the environment. Applying the weed optimization algorithm to increase power generation in a multireservoir operation by Asghari et al. [17] showed the superiority of this algorithm by convergence rate and generated benefits compared to the water cycle algorithm and genetic algorithm as well as particle swarm optimization.

Employing fixed length genetic programming to decrease the demand for irrigation in multireservoir operation [18] found this method to contribute to meeting the demand with a larger convergence rate than that of other algorithms and a higher reliability index than that of genetic programming. Utilizing the gravitational search algorithm to decrease power generation in a multireservoir system [19] suggested the need of this algorithm for accurate analyses of sensitivity to its random parameters. In comparison with particle swarm optimization and genetic algorithm, this algorithm resulted in a higher power generated annually and a larger convergence rate. Applying the shark optimization algorithm to reservoir operation demonstrated the effectiveness of this algorithm in satisfying the demand for irrigation with a larger convergence rate and index of reliability than those obtained from particle swarm optimization or genetic algorithm [20]. Applying monarch butterfly optimization by [5] Ehteram et al. [8] to multireservoir operation in China based on a migration operator for the butterflies showed increases of 14% and 12% in the average annual power generation than that of particle swarm optimization and genetic algorithm, respectively.

A case study by Mousavi et al. [21] using the crow algorithm for extracting rule curves to manage irrigation on the basis of the potential of crows for finding and hiding foods showed significant decreases in the vulnerability index. The average annual deficit in irrigation obtained by applying the krill algorithm to irrigation management and reservoir operation by Karami et al. [22] using the initial krill's position as the decision variable, respectively, decreased by of 20% and 23% compared to the deficit of the particle swarm and genetic algorithms. Applying the kidney algorithm based on the kidney function in the body to a reservoir operation to decrease power generation [23] showed that the kidney algorithm provided the best performance against the other evolutionary algorithms. It was stated that the KA achieved the first rank for the optimization problem and, thus, it showed a high potential to be applied for different problems in the field of water resources management.

The authors of [24] developed the Multiobjective Grey Wolf Optimization (MOGWO) algorithm to obtain the optimum rules on the operation of the Golestan Dam in Golestan province, Iran, under the climate change

conditions. Their results showed that the river flow would decline by 0.17 percent of the baseline period under climate change conditions in addition to increasing the temperature by 20% as well as decreasing the rainfall by 21.1%. In another research in the same year, they studied the Multiobjective Farmland Fertility Optimization (MOFFA) algorithm to derive optimum rules on the operation of the Golestan Dam under climate change conditions. The study results indicated an increase in release rates for climate change conditions in comparison with the baseline ones and stronger dam efficiency in climate change conditions [25].

2.1. Study Objectives, Novelty, and Problem Statement. Great potential for solving water resources management problems has been reported for evolutionary algorithms. Recently developed hybrid models based on 2 rather than a single metaheuristic have been applied to reservoir and dam water systems [24]. The hybrid particle swarm optimization and artificial fish optimization was used for a single-objective single-reservoir system problem. Establishing proper communication between the algorithms constitutes a major challenge in developing the hybrid models [24]. An easily implemented hybrid bat-particle swarm algorithm developed using a certain communication process was inefficient in terms of convergence rate [24]. Moreover, the shortcomings of evolutionary algorithms include being trapped in local optimal points, early convergence, producing immature solutions, and a low convergence rate [26]. Inspired from the social behaviors of humpback whales, Lewis and Mirjalili developed the whale optimization in 2016 as a swarm intelligence algorithm [27]. Inefficiency in examining the entire search space constitutes a major disadvantage of this algorithm. Given the acceptable potential of the differential evolution for exploration [28], the present study developed and implemented the improved whale optimization algorithm as a hybrid whale optimization-differential evolution algorithm in MATLAB and analyzed its application to managing water resources.

3. Materials and Methods

3.1. Differential Evolution. Despite basic similarities between the differential evolution introduced by [29] and the structure of evolutionary algorithms, their difference lies in the way mutation and crossover are applied in the former to update solutions based on a standard evolutionary algorithm. In fact, the solution vectors randomly selected from the population undergo component swapping, addition, and subtraction before updating the generation. The differential evolution performs mutation as a constant and a weighting factor for differential vectors before crossover and mutation. Differential vectors are calculated as the average of several differential vectors obtained from different randomly selected pairs or the difference between 2 of randomly selected solution vectors from the population. An updated solution vector known as the noisy vector is obtained by adding the weighted difference vector to a solution vector that is selected randomly. The trial vector then obtained through a

crossover between the target vector in the population and the noisy vector is ultimately compared to the target vector to pass the better one to the next generation. This process continues to fill up the next generation by the number of newly generated candidate solutions.

The stages of the differential evolution are shown in Figure 1. The randomly selected vectors need to be discriminated from one another. In contrast to genetic algorithm, no selection mechanisms are used in the differential evolution and minimum-cost vectors in minimization problems associated with trial vectors or parent target vectors are advanced to the next generation. The differential evolution is based on $P(G)$ as the population of generation G including n_{pop} individuals as candidate solutions. Position matrix $P(G)$ is expressed as follows:

$$P^{(G)} = X_i^G \begin{bmatrix} X_{1,1}^G, & X_{2,1}^G, & X_{3,1}^G, & \cdots \cdots \cdots & X_{n\,pop,1}^G \\ X_{1,2}^G, & X_{2,2}^G, & X_{3,2}^G, & \cdots \cdots \cdots & X_{n\,pop,2}^G \\ X_{1,3}^G, & X_{2,3}^G, & X_{3,3}^G, & \cdots \cdots \cdots & X_{n\,pop,3}^G \\ & & \vdots & & \\ X_{1,nvar}^G, & X_{2,nvar}^G, & X_{3,nvar}^G, & \cdots \cdots \cdots & X_{n\,pop,nvar}^G \end{bmatrix},$$

(1)

where G_{max} represents the maximum number of generations defined by users, n var the number of variables or diameters to be selected, $X_{i,j}^G$ the jth component, i.e., that is, the jth link diameter, of the ith candidate solution, and X_i^G the ith candidate solution or individual in the Gth generation.

An arbitrarily generated initial population represented as $P(0)$ in the differential evolution is as follows:

$$P^{(0)} = X_{i,j}^{(0)} = X_j^{(L)} + \text{rand}_{i,j}\left(X_j^{(U)} - X_j^{(L)}\right)i = 1 \text{ to } n_{pop}, j$$
$$= 1 \text{ to } n_{var},$$

(2)

in which $X_j^{(L)}$ and $X_j^{(U)}$, respectively, represent the lower and upper bounds of variable jand randij a random variable uniformly distributed on [0, 1].

Subsequent generations $P^{(G+1)}$ or new vectors are generated successively through mutation as a combination of vectors that are selected randomly from the current population. Afterwards, a predetermined target vector is combined with the noisy vector. Moreover, $P^{(G+1)}$ as the trial vectors population is generated through mutation and recombination as follows:

$$X_{i,j}^{(G+1)} = \begin{cases} X_{C,j}^{(G)} + F \times \left(X_{A,j}^{(G)} - X_{B,j}^{(G)}\right), & \text{if rand}_{i,j} \leq C_r; \quad \forall j = D_i, \\ X_{i,j}^{(G)}, & \text{otherwise}, \end{cases}$$

(3)

in which $D = 1, \cdots \cdots \cdots n_{param}$, $A \in [1, \ldots \ldots n_{param}]$, $B \in [1, \ldots \ldots n_{pop}]$, $C \in [1, \ldots \ldots n_{pop}]$, $A \neq B \neq C \neq i$, $C_r \in [0 \text{ to } 1] F \in [0 \text{ to } 1] \text{ rand} \in [0 \text{ to } 1]$. F represents a mutation constant or weighting factor defined by users on [0, 1] and C_r the minimization problem defined by users.
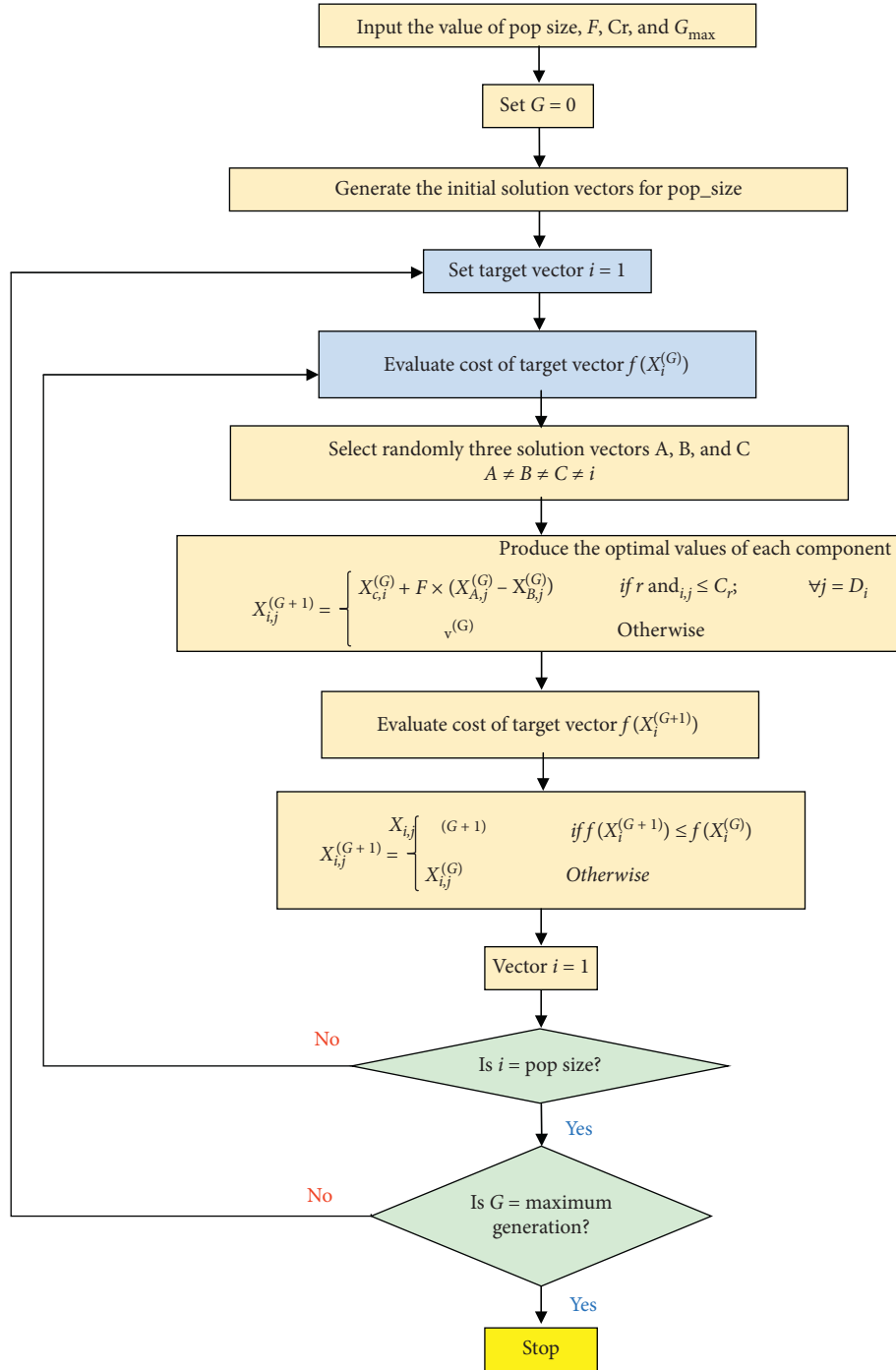
FIGURE 1: Flowchart of the differential evolution.

Otherwise, the target vector is selected for the following generation, whose population $P^{(G+1)}$ is selected using the following equation:

$$X_{i,j}^{(G+1)} = \begin{cases} X_{i,j}^{(G+1)}, & \text{if } f\left(X_i^{(G+1)}\right) \leq f\left(X_i^{(G)}\right), \\ X_{i,j}^{(G)}, & \text{otherwise,} \end{cases} \quad (4)$$

in which $f\left(X_i^{(G)}\right)$ denotes the cost of the ith individual of the Gth generation [30].

The computational modules applied to optimally designing a water distribution network using the differential evolution are shown in Figure 2. Given the proper explorative potential of mutation in the differential evolution, this algorithm can effectively identify the zone of a global optimum despite its inappropriate exploitation [28].

3.2. Whale Optimization Algorithm. In 2016, inspiring from a bubble-net hunting strategy, A. Lewis and Seyed Ali

Select target | Randomly select two vectors | Third R. Vev.

Current population

	Individual 1	Individual 2	Individual 3	Individual 4	Individual 5	Individual 6
Cost	454000	495000	448000	487000	427000	439000
Pipe 1	457.2	457.2	508	454.2	457.2	508
Pipe 2	203.2	355.6	355.6	355.6	355.6	355.6
Pipe 3	457.2	457.2	406.4	457.2	355.6	355.6
Pipe 4	355.6	203.2	76.2	50.8	25.4	50.8
Pipe 5	355.6	304.8	355.6	304.8	355.6	304.8
Pipe 6	101.6	25.4	254	25.4	50.8	25.4
Pipe 7	76.2	304.8	203.2	355.6	355.6	355.6
Pipe 8	254	304.8	50.8	304.8	304.8	254

Diff. vector	WDV
50.8	40.64
0.0	0.0
101.6	81.28
0.0	0.0
50.8	40.64
228.6	182.88
-152.4	−121.92
-254.0	−203.2

X F

Mutation weighted difference vector added to third randomly selected vector randomly

Trial vector	Crossover With probability Cr, select parameter value from noisy vector, otherwise select value from target vector	Noisy vector
566000		548.64
558.8		355.6
203.2		436.88
457.2		50.8
50.8		354.44
355.6		208.28
101.6		233.68
254.0		50.8
50.8		

Selection Trial or target vector selecting, the one with the lower cost survive

Following generation population

	Individual 1	Individual 2	Individual 3	Individual 4	Individual 5	Individual 6
Cost	454000					
Pipe 1	457.2					
Pipe 2	203.2					
Pipe 3	457.2					
Pipe 4	355.6					
Pipe 5	355.6					
Pipe 6	101.6					

FIGURE 2: Computational modules applied to optimally design a water distribution network using the differential evolution.

Mirjalil proposed the whale optimization as metaheuristic describing unique hunting behaviors of humpback whales. According to this algorithm, whales follow typical bubbles and create a circular or 9-shaped route while encircling prey during their hunting. The bubble-net feeding/hunting behavior can be explained by the fact that humpback whale go down in water by approximately 10–15 meters followed by producing spiral bubbles encircling the prey while following the bubbles and moving toward the surface. The following expression is

used to mathematically present the whale optimization algorithm.

3.3. Equation for Encircling a Prey.

After encircling small fish as the prey by humpback whales, they update their position towards the optimal solution as the number of iterations is maximized:

$$\overrightarrow{D} = \left| C \cdot \overrightarrow{X}^*(t) - X(t) \right|,$$
$$\overrightarrow{X}(t+1) = \overrightarrow{X}^*(t) - \overrightarrow{A} \cdot \overrightarrow{D}, \tag{5}$$

in which $X(t)$ represents the vector of position, $\overrightarrow{X}^*(t)$ the vector of position of the most recent optimal solution, t the current iteration, and $\overrightarrow{A}$ and D coefficient vectors which can be calculated as follows:

$$\overrightarrow{A} = 2r\overrightarrow{a} - \overrightarrow{a},$$
$$\overrightarrow{C} = 2r, \tag{6}$$

where r represents a random value on [0, 1] and $\overrightarrow{a}$ a linearly decreasing variable from 2 to 0 throughout the iterations.

3.4. Bubble-Net Attacks.

Two methods proposed as the mathematical representation of the bubble-net behavior of humpback whales, as illustrated in Figure 3, are as follows.

3.4.1. Shrinking Encirclement.

This method is based on a linear decrease from two to zero in $\overrightarrow{a}$. The vector random value lies on [−1, 1].

3.4.2. Spiral Position Updates.

The spiral position between humpback whales and the prey following a helix shape can be mathematically expressed as follows:

$$\overrightarrow{X}(t+1)\overrightarrow{D}.e^{bl}.\cos(2\pi l) + \overrightarrow{X}^*(t), \tag{7}$$

in which b is a constant defining the logarithmic shape, l a random value over [−1, 1], and $\overrightarrow{D} = |X^*(t) - X(t)|$ the distance between the prey and the ith whale used to update the solution. The probability of the whale following a logarithmic path or perform shrinking encircling during optimization is assumed to be 50%. The related mathematic equation is expressed in the following:

$$\overrightarrow{X}(t+1) = \begin{cases} \overrightarrow{X}^*(t) - \overrightarrow{A}.\overrightarrow{D}, & p < 0.5, \\ e^{bt}\cos(2\pi l)\overrightarrow{D} + \overrightarrow{X}^*(t), & p \geq 0.5, \end{cases} \tag{8}$$

with p being a random value over [0, 1].

3.4.3. Searching for the Prey.

$\overrightarrow{A}$ is used to find the prey on the basis of the following 2 conditions while taking values above 1 or below −1:
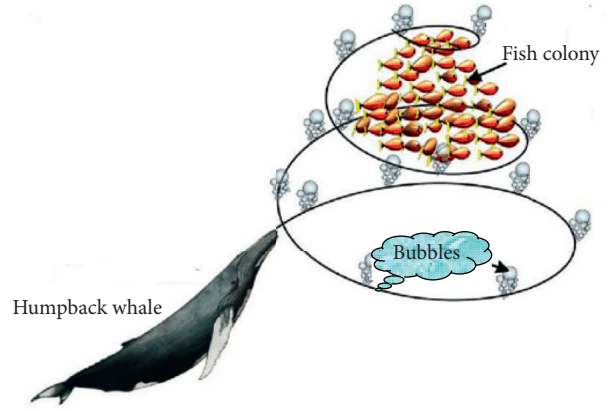

FIGURE 3: Bubble-net behavior based on whale optimization algorithm.

$$\overrightarrow{D} = \left| C.\overrightarrow{X_{\text{rand}}} - \overrightarrow{X}(t) \right|, \tag{9}$$

$$\overrightarrow{X}(t+1) = \overrightarrow{X}_{\text{rand}} - \overrightarrow{A}.\overrightarrow{D}. \tag{10}$$

The following conditions are ultimately met:

(i) $|\overrightarrow{A}| > 1$ ensures that traps in local optimal solutions are avoided throughout the search by the whale optimization algorithm.

(ii) $|\overrightarrow{A}| < 1$ is selected to update the current search agent/best solution in terms of position [27]. The whale optimization algorithm flowchart is illustrated in Figure 4.

3.5. Improved Whale Optimization.

This section presents improvement in the whale optimization algorithm. The present study integrated the mutation of the differential evolution with the whale optimization algorithm to improve and balance the exploration and exploitation phases and increase its convergence rate. The algorithm proposed is explained as follows.

The trade-off existing between the exploration and exploitation of the whale optimization algorithm was solved in the improved whale optimization algorithm using a hybrid model comprising the operators of this algorithm and the mutation operator of the differential evolution. The main hybrid operator of the improved algorithm (see lines 10–28 of proposed algorithm) is a combination of mutation in the differential evolution and the components of the whale optimization algorithm, namely, encircling prey, search for prey, and spiral updating position. The improved whale optimization algorithm consists of two main parts, that is, exploration (see lines 11–18 of proposed Algorithm) and exploitation (see lines 19–27 of proposed Algorithm). If rand < k, the exploration part changes the individuals. Equation (8) was used to adjust k.

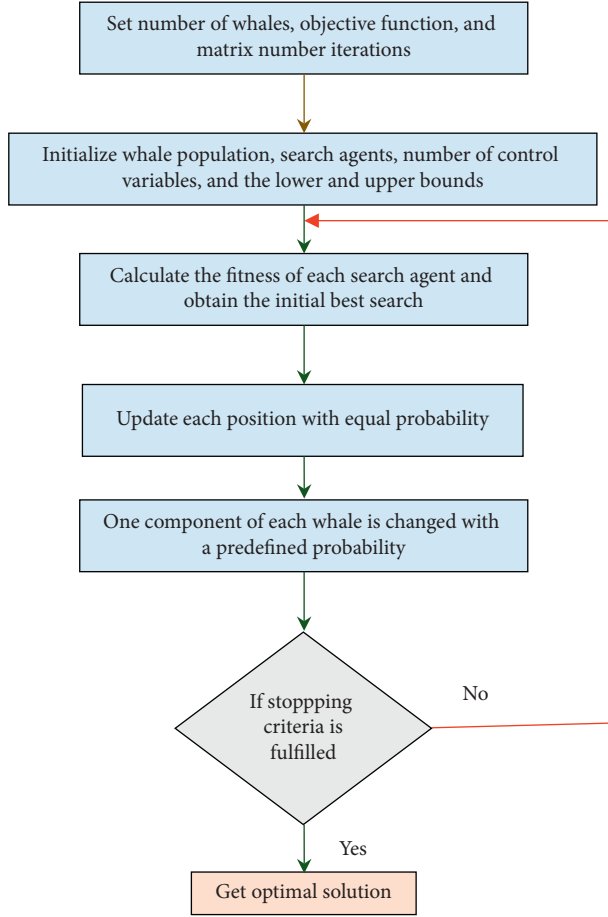$$\lambda = 1 - \frac{t}{t_{\text{max}}}, \tag{11}$$

FIGURE 4: Flowchart of whale optimization algorithm.

in which $t_{\max}$ and t, respectively, show the maximum number of generations and the current generation and k is utilized to control the exploration and exploitation of the improved whale optimization algorithm. According to (8), decreasing k over time from 1 to 0 allows the individuals to explore the initial generation, while doing exploitation as time passes. The exploration part contains the mutation of the differential evolution and search for the prey of the whale optimization algorithm. The improved algorithm is integrated with mutation to enhance exploration throughout the search space [28]. The exploitation component of the improved whale optimization algorithm resembles that of the whale optimization, although the improved algorithm is an elitist method. In fact, the updated position of the ith individual in the next generation is selected as the fitter one of offspring U_i and parent X_i. The solution is obtained by considering the boundary conditions, which should not be violated; otherwise, the repairing rule is applied according to (9).

$$X_i(j) = \begin{cases} \delta_j + \text{rndreal}(0, 1) \times (\mu_j - \delta_j) X_i(j) < \delta_j, \\ \mu_j - \text{rndreal}(0, 1) \times (\mu_j - \delta_j) X_i(j) < \mu_j, \end{cases} \quad (12)$$

with rndreal $(0, 1)$ being a random value between 0 and 1, $X_i(j)$ the jth dimension of the ith solution, while δ_j and μ_j,

respectively, show the lower and upper limits of the jth dimension.

Improved whale optimization algorithm is as follows.

(1) Generating an initial population X_i, $i = 1, 2, \ldots, N_P$
(2) Measuring the individuals fitness in X_i
(3) Calculating X^* as the best individual
(4) While the stopping criterion is not satisfied
(5) Mapping the fitness to the number of species for every individual
(6) For $i = 1$ to N_P
(7) Selecting a uniformly-distributed random value $r1–r2–r3–i$
(8) Updating $a = 2 - t(2/t_{\max})$, $A = 2ara$, $C = 2r$, $l = \text{rndreal}(-1, 1)$, $p = \text{rndreal}(0, 1)$ and $k = 1 - (t/t_{\max})$
(9) $j_{\text{rand}} = \text{rndint}(1, n)$
(10) For $j = 1 : n$
(11) If p_k then
(12) If rndreal$j$ $(0, 1)\_CR$ or $j == j_{\text{rand}}$ then
(13) $U_i(j) = X^*(j) + F\_[Xr2 \cdot (j)\_Xr3(j)]$
(14) Else
(15) Selecting the random individual X_{rand}
(16) $D = |C \cdot X_{\text{rand}} - X_i|$
(17) $U_i(j) = X_{\text{rand}}(j) - A.D$
(18) End if
(19) Else if $p > k$ then
(20) If rndreal$j(0, 1) - 0.5$ then
(21) $D = |C \cdot X^* - X_i|$
(22) $U_i(j) = X^*(j) - A \cdot D$
(23) Else
(24) $D = |X^* - X_i|$
(25) $U_i(j) = D \cdot \text{expbl} \cdot \cos(2 \cdot pi \cdot l) + X^*$
(26) End if
(27) End if
(28) End for
(29) Evaluating the offspring U_i
(30) If U_i is better than X_i then
(31) Updating individual i, $X_i = U_i$
(32) If U_i is better than X^* then
(33) Updating the best individual $X^* = U_i$
(34) End if
(35) End if
(36) End for
(37) $t = t + 1$
(38) End while

The structure of the proposed improved whale optimization algorithm is simple. The only difference between the improved algorithm and the whale optimization lies in integrating the mutation of the differential evolution with

the latter algorithm. The selection function of the improved algorithm resembles that of the differential evolution. The improved algorithm therefore computationally resembles the whale optimization based on $O(\text{MaxGen} \times Np \times O(\text{fitness}))$. The maximum number of generations is denoted as maxgen and $O(\text{fitness})$ is calculated by the application [31]. Figure 5 shows the different stages of the improved whale optimization algorithm.

3.6. Case Study. Boostan is a clay-core Earth dam in northeastern Gonbad-eKavus, Golestan Province, Iran, for satisfying an irrigation demand of 4200 ha of land and environmental and industrial water demand. The dam's length is 665 meters, its top width 10 meters, the minimum storage volume of its reservoir $0.1 \times 10^6 \, \text{m}^3$, and the maximum storage volume $43.7 \times 10^6 \, \text{m}^3$. According to Figure 6 showing the monthly inputs, the present study was conducted during 151 months from October 2005 to April 2018.

Boostan Reservoir Dam lies in the Gorganrood-Gharasoo Basin as part of the $13061 \, \text{km}^2$ Caspian Basin in the southeast of the Caspian Sea. Climate change affects the average annual precipitation in the watershed from the east to west and from the north to south. The average annual temperature in this basin ranges from approximately $17°\text{C}$ at low altitudes to $7.5°\text{C}$ in the southern highland area. The geographical situation of the present research area is illustrated in Figure 7.

Findings obtained from the present case study are recommended to be used by policymakers to satisfy the irrigation demand in agricultural regions. The released water was considered a decision variable, and the water volume should be adequate for supplying the demand of the downstream farmers. The shortage of water was minimized using the following objective function:

$$\text{minimize } F_{\text{Release}} = \sum_{t=1}^{T} \left(\frac{\text{De}_t - \text{Re}_t}{\text{De}_{\text{max}}} \right)^2, \quad (13)$$

in which De_{max} represents the maximum demand for water during the operation, Re_t is the discharged water, De_t is the required volume, and F_{Release} is the objective function. The following continuity equation was also considered:

$$S_{t+1} = Q_t + S_{(t)} - \text{Ev}_{(t)} - \text{Sp}_{(t)} = \text{Re}_{(t)}, \quad (14)$$

in which $\text{Sp}_{(t)}$ represents overflow at time t, $\text{Re}_{(t)}$ the discharged water, $\text{Ev}_{(t)}$ evaporation from the reservoir surface, $S_{(t)}$ the reservoir storage volume at time t as well as an input to the reservoir, and S_{t+1} the reservoir storage volume at time $(t+1)$.

The following constraints were applied to overflow from the reservoir:

$$S_{P_t} = \begin{cases} S_t + Q_t - \text{Re}_t - \text{Ev} - S_{\text{max}}, & \text{if } S_t + Q_t + \text{Re}_t - \text{Ev} > S_{\text{max}}, \\ 0, & \text{if } S_t + Q_t + \text{Re}_t - \text{Ev} \geq S_{\text{max}}. \end{cases} \quad (15)$$

The other constraints were as follows:

$$S_{\text{min}} \leq S_t \leq S_{\text{max}}, \\ \text{Re}_{\text{min}} \leq \text{Re}_t \leq \text{Re}_{\text{max}}, \quad (16)$$

in which Re_{min} represents the minimum discharge volume of the reservoir, Re_{max} the maximum discharge volume, S_{min} the minimum volume of the reservoir, and S_{max} its maximum volume. The following penalty functions were included in the objective function to take account of potentially unsatisfied constraints [32].

$$\text{Penalty 1} = \begin{cases} \sum_{t=1}^{T} \left(\frac{S_t - S_{\text{min}}}{S_{\text{min}}} \right)^2, & \text{if } S_t < S_{\text{min}}, \\ \sum_{t=1}^{T} \left(\frac{S_t - S_{\text{max}}}{S_{\text{max}}} \right)^2, & \text{if } S_t < S_{\text{max}}, \\ 0, & \text{if } S_{\text{min}} \leq S_t \leq S_{\text{max}}, \end{cases}$$

$$\text{Penalty 2} = \begin{cases} \sum_{t=1}^{T} \left(\frac{\text{Re}_t - D_{\text{min}.t}}{D_{\text{min}.t}} \right)^2, & \text{if } \text{Re}_t < \text{De}_{\text{min}.t}, \\ \sum_{t=1}^{T} \left(\frac{\text{Re}_t - D_{\text{max}}}{D_{\text{max}.t}} \right)^2, & \text{if } \text{Re}_t < \text{De}_{\text{max}.t} \\ 0, & \text{if } \text{De}_{\text{min}.t} \leq S_t \leq \text{De}_{\text{max}.t}. \end{cases} \quad (17)$$

The indicators used to measure the performance of various algorithms in solving water resource management problems were as follows. The volumetric reliability indicator is defined as the volume of water discharged in the whole period divided by the overall demand for water as follows [33]:

$$\alpha_V = \frac{\sum_{t=1}^{T} \text{Re}_t}{\sum_{t=1}^{T} \text{De}_t} \times 100. \quad (18)$$

(1) The time-based reliability indicator showing the percentage of time the demand is completely satisfied by the system is expressed as follows [32].

$$\alpha_T = \left(1 - \frac{N \, \text{Def}}{T} \right) \times 100, \quad (19)$$

in which NDef represents the total number of failures that occurs. Higher values of this index suggest a higher system performance.

(2) The vulnerability index refers to the highest failure rate throughout a reservoir operation, with lower values suggesting a higher performance [34]:

$$\lambda = \text{Max}_{t=1}^{T} \left(\frac{D_t - R_t}{D_t} \right) \times 100. \quad (20)$$

(3) The resiliency indicator reflects the recovery rate of a system after failures; for instance, the occurrence of failures in 4 months of a 12-month operation
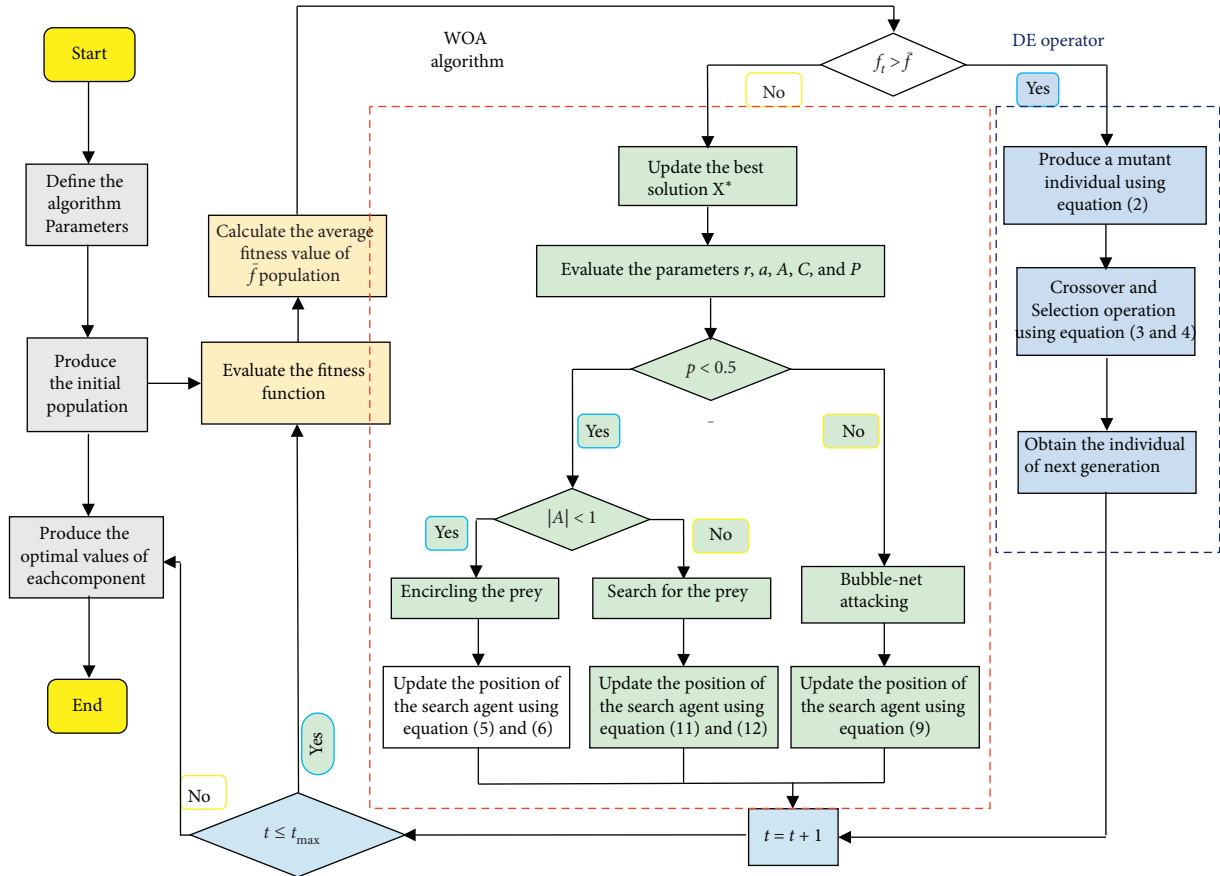
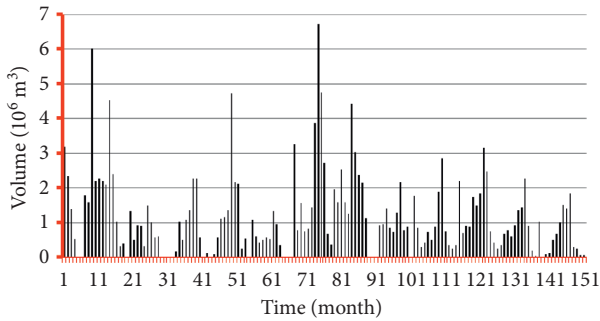FIGURE 5: Flowchart of improved whale optimization (IWOA).

FIGURE 6: The inflow to Boostan Dam reservoir per month.

suggests the significant effect of the sequence of failure periods on the system. Moreover, larger values of this indicator are more desirable.

$$\gamma_i = \frac{f_{si}}{F_i} \times 100. \tag{21}$$

in which F_i represents the total frequency of failure periods and f_{si} the frequency of occurrence of failure series [26].

(4) The sustainability index defined by performance criteria as follows is defined as the sum of system performance measures in one general index to facilitate comparison and decision-making between different management alternatives and water resources plans [35, 36]:

$$SI = \{\alpha \times \gamma_i \times (1 - \lambda)\}. \tag{22}$$

3.7. Calculating the Weights of the Criteria. Subjective weights were mainly calculated using expert comments according to experiences and subjective judgments such as Delphi and AHP, whereas objective weights were obtained reservoir from actual alternative information associated with techniques, including the entropy weight, which decreases the subjective effect of decision makers and improves objectivity.

As a concept of a thermodynamic origin, entropy was used to calculate system disorders and degree of confusion. Entropy was also used by Shannon to solve information theory problems and resolve uncertainty [37]. The entropy theory suggests lower values of the entropy result in more available data. A higher weight can be therefore assigned to the criterion [38]. Numerous studies have used entropy weight in different fields. The Shannon entropy weight can be calculated through the following steps [39] by assuming a decision matrix with n criteria and m alternatives.

The first stage is normalizing the decision matrix:

$$n_j = \frac{a_{ij}}{\sqrt{\sum_{i=1}^{m} a_{ij}}}, \quad i = 1, 2, \ldots, m. \tag{23}$$
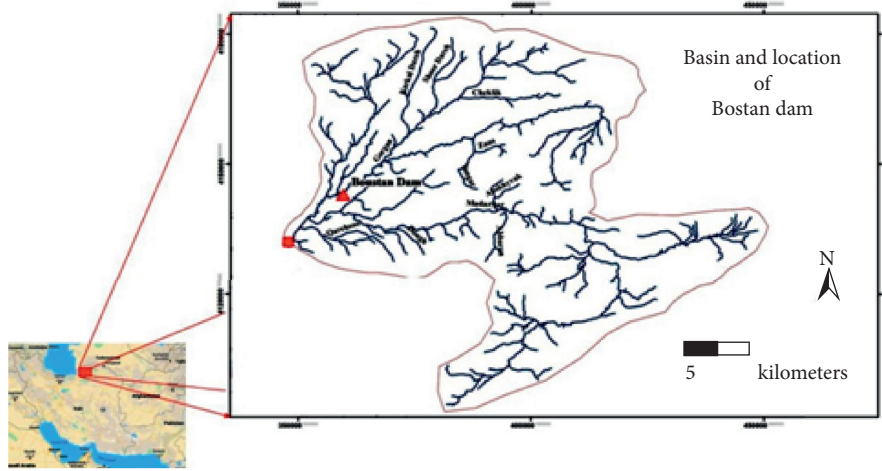
FIGURE 7: The geographical situation of the present study region.

The second stage is calculating entropy:

$$E_j = -K \sum_{i=1}^{m} \left(r_{ij} * \mathrm{Lnr}_{ij} \right), \quad i = 1, 2, \ldots, n, \qquad (24)$$

in which $K = 1/\mathrm{In}\, m$.

The third stage is calculating the weight of individual criteria:

$$w_j = \frac{1 - E_j}{\sqrt{\sum_{i=1}^{n} \left(1 - E_j \right)}}, \quad i = 1, 2, \ldots, n. \qquad (25)$$

3.8. TOPSIS. Yoon and Hwang proposed TOPSIS as a multicriteria decision-making approach [40] for selecting an optimal alternative. According to the main rule of TOPSIS, the best alternative is, respectively, nearest and farthest from positive ideal and negative ideal solutions [41]. Multicriteria decision-making problems have been commonly solved in numerous fields using this technique. According to Yoon and Huang, the following algorithm is presented for TOPSIS [42].

The first stage is building R as the normalized decision matrix:

$$r_{ij} = \frac{a_{ij}}{\sqrt{\sum_{i=1}^{m} a_{ij}^2}}. \qquad (26)$$

The second stage is building the weighted normalized decision matrix:

$$v_{ij} = w_j r_{ij},$$
$$\sum_{j=1}^{n} w_j = 1, \qquad (27)$$

in which w_j represents the jth criterion weight.

The third stage is obtaining the positive ideal and negative ideal solutions, respectively, shown as A^+ and A^- as follows:

$$A^+ = \left\{ \left(\min v_{ij} | j \in J' \right) \mathrm{or} \left(\max v_{ij} | j \in J, \right) \right\}, \quad i = 1, 2, \ldots, m = \{ v_1^+, +, \ldots, v_n^+ \},$$
$$A^- = \left\{ \left(\min v_{ij} | j \in J' \right) \mathrm{or} \left(\max v_{ij} | j \in J \right) \right\}, \quad i = 1, 2, \ldots, m = \{ v_1^-, +, \ldots, v_n^- \}, \qquad (28)$$

in which J and J', respectively, represents the sets of benefit and cost criteria.

The fourth stage is calculating the distance between individual alternatives and positive ideal and negative ideal solutions:

$$d_i^+ = \sqrt{\sum_{j=1}^{n} \left(V_{ij} - A_j^+ \right)^2}, \quad i = 1, 2, \ldots, m, $$

$$d_i^- = \sqrt{\sum_{j=1}^{n} \left(V_{ij} - A_j^- \right)^2}, \quad i = 1, 2, \ldots, m. \qquad (29)$$

The fifth stage is calculating the closeness coefficient and prioritizing the alternatives:

$$cl_i^* = \frac{d_i^-}{d_i^+ + d_i^-}, \quad 0 < cl_i^* < 1, \qquad (30)$$

in which $cl_i^* \in [0, 1]$, $i = 1, 2, \ldots, m$. An optimal alternative is selected based on the priority of cl_i^* whose higher values denote a better alternative. The closer the cl_i^* to unity, the closer the alternative A_i to the positive ideal solution.

4. Discussion

Tables 1–3 present the results of a sensitivity analysis on the random variables of various algorithms. The optimal population size was obtained as 60 for the improved whale optimization algorithm with an objective function value of 25.74 being the lowest compared to the other population sizes. The optimal mutation factor f was obtained as 0.4 and the optimal cross over rate c as 0.3 for the differential evolution and its objective function value of 25.84 was found for these two values.

According to Table 4, after randomly running the individual algorithms for ten times, their performance, convergence rate, and statistical parameters were compared with one another and with the absolute optimal values obtained of GAMS as a nonlinear optimization technique. Ten times of running the improved whale algorithm, the differential evolution and the whale optimization algorithm, respectively, resulted in average responses of 25.74, 25.84, and 32.91. The objective function based on the improved whale optimization algorithm therefore minimized water supply shortages. The calculation duration was obtained as 521 seconds for the improved whale algorithm, 527 seconds for the whale optimization algorithm, and 1040 seconds for the differential evolution, suggesting that the improved algorithm yields the minimum computational duration compared to those of the other two algorithms. The lower variation coefficient obtained after running the improved whale algorithm for 10 times compared to that of the other algorithms suggested the adequately reliable results of even one execution of the improved whale algorithm. Although the globally optimal solution obtained with GAMS was 12.553, the hybrid whale optimization outperformed the whale optimization algorithm given that the former improved the performance of the latter by up to 21.7% in deriving the optimal values of the water supply function through decreasing the variation coefficient by up to 78% and the standard deviation by up to 82%.

Comparing the three algorithms in terms of convergence rate in Figure 8 showed that the improved whale algorithm convergence is the fastest and therefore outperforms in terms of computation duration and response quality. Replacing a poor solution obtained from an algorithm with a good solution obtained from another algorithm improved the rate of convergence of the improved whale algorithm. In fact, despite the poor individual performance of the differential evolution and the whale optimization algorithm, their hybrid performance was higher.

Given the integration of the mutation operator of the differential evolution with the whale optimization, Figure 8 confirmed the performance of the improved whale algorithm by demonstrating the lower minimum values obtained using this algorithm compared to those obtained from the whale optimization algorithm.

The three algorithms were compared in Table 5 in terms of satisfying the demand for water in the 151-month study

TABLE 1: Sensitivity analyses conducted on the whale optimization and differential evolution and improved whale optimization algorithms.

Hybrid whale optimization algorithm		
Population size	Objective function value	Time (s)
20	26.92	176
40	26.03	353
60	25.74	521
80	25.96	699

TABLE 2: Differential evolution.

Population size	Mutation factor (f)	Crossover rate (c)	Objective function value	Time (s)
20	0.2	0.1	28.42	527
40	0.4	0.3	25.84	1040
60	0.6	0.5	27.08	1574
80	0.8	0.7	31.62	2101

TABLE 3: Whale optimization algorithm.

Population size	Objective function value	Time (0)
20	35.13	177
40	33.63	351
60	32.91	527
80	32.98	703

TABLE 4: Results obtained through ten times of randomly running the three algorithms.

Run	Differential evolution	Whale optimization	Improved whale optimization
1	26.79	34.22	25.92
2	26.51	32.21	25.81
3	26.41	33.75	25.78
4	24.35	33.74	25.91
5	25.55	31.63	25.8
6	25.63	33.56	25.68
7	26.75	32.95	25.73
8	24.79	31.78	25.74
9	25.05	32.68	25.65
10	26.6	32.52	25.36
Average	25.84	32.9	25.74
Worst response	26.79	34.22	25.92
Best response	24.35	31.63	25.36
Standard deviation	0.89	0.89	0.16
Variation coefficient	0.034	0.027	0.006
Nonlinear programming minimum value		12.553	

period. The correlation coefficient between the required and actual water discharge obtained as 0.94 for the improved whale algorithm was higher than that of the other algorithms. The root-mean-square errors obtained as $0.72 \times 10^6\,\text{m}^3$ for the improved algorithm, $2.64 \times 10^6\,\text{m}^3$ for
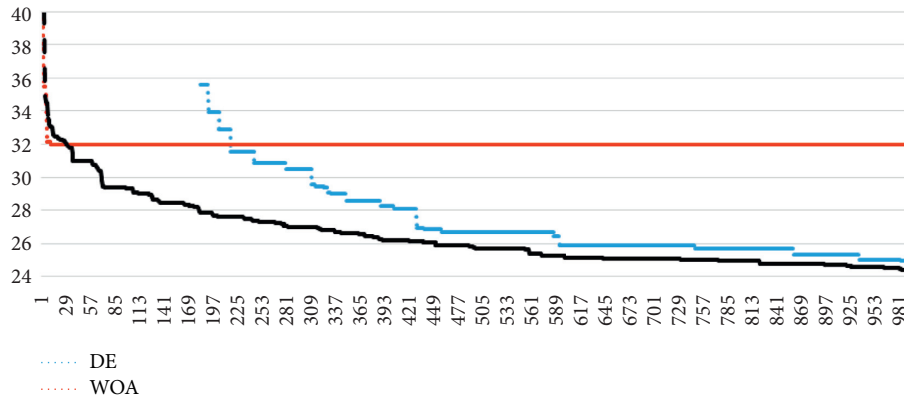
FIGURE 8: Comparing the three algorithms in terms of convergence rate.

TABLE 5: Comparing the different models of supplying demand for water on the basis of statistical indicators.

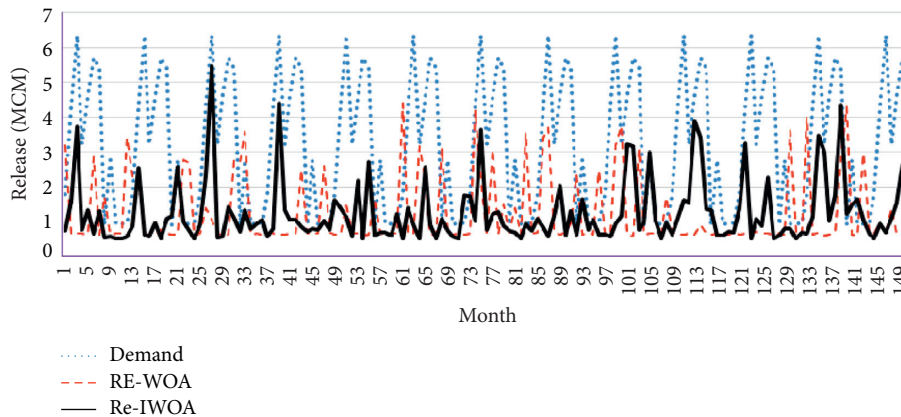| Index	Nonlinear programming	Differential evolution	Whale optimization	Improved whale optimization
Correlation coefficient	0.96	0.53	0.61	0.94
Root-mean-square error (m^3)	1.83×10^6	2.64×10^6	1.99×10^6	0.72×10^6
Mean absolute error	1.718×10^6	2.04×10^6	1.223×10^6	0.186×10^6

FIGURE 9: Volume of water supplied using the different algorithms.

the differential evolution, and $1.99 \times 10^6 \, \text{m}^3$ for the whale optimization algorithm suggested the higher performance of the improved whale optimization algorithm in satisfying demand for water. The lower mean absolute error presented in Table 5 for the improved algorithm compared to that of the other evolutionary algorithms showed that this algorithm outperforms in terms of meeting the downstream demand for water.

With an average demand for water of $3.21 \times 10^6 \, \text{m}^3$, Figure 9 shows the improved whale optimization algorithm resulted in a water discharge volume of $3.03 \times 10^6 \, \text{m}^3$ from Boostan dam for supplying the demand for the reservoir water over the study period, whereas the differential evolution yielded $1.18 \times 10^6 \, \text{m}^3$ and the whale optimization $1.99 \times 10^6 \, \text{m}^3$. The improved algorithm was therefore the best algorithm in terms of meeting the demand for water.

Table 6 compares the performance of the study algorithms by the water resources management indicators,

suggesting that the improved whale optimization algorithm, with a reliability indicator of 94%, outperformed the other evolutionary algorithms in terms of satisfying the downstream demand for water and with the largest resiliency indicator (89%) and the minimum objective function (25.74) has the best status. The optimal decision can therefore be made through considering several indicators and using multicriteria decision-making models. In addition to objective function, the other indicators considered in the present case study to select the best algorithm for supplying the downstream water demand included reliability, vulnerability, and resiliency. Comparing the whale optimization algorithm and the improved whale algorithm confirms performance improvements in terms of all the evaluative indicators. Table 7 presents the positive and negative criteria and the criteria weights obtained using the entropy method. The results showed that two criteria, that is, resiliency and time reliability, have, respectively, the highest weights

TABLE 6: Comparing the evaluative indices obtained using the different optimization algorithms.

	Volumetric reliability	Time reliability	Resiliency	Vulnerability	Sustainability	Objective function
Differential evolution	0.39	0.1	0.09	0.88	0.1	26.8
Whale optimization	0.62	0.53	0.37	0.45	0.11	32.2
Improved whale	0.94	0.94	0.89	0.06	0.79	25.74
			Normalized matrix			
Differential evolution	0.2000	0.0637	0.0667	0.6331	0.1000	0.2000
Whale optimization	0.3175	0.3376	0.2741	0.3237	0.1100	0.3179
Improved whale	0.4821	0.5987	0.6593	0.0432	0.7898	0.4821

TABLE 7: Weighted vector of entropy.

Criterion	Volumetric reliability	Time reliability	Resiliency	Vulnerability	Sustainability	Objective function
Positive or negative criteria	Positive	Positive	Positive	Negative	Positive	Negative
Weight of criteria	0.1735	0.1809	0.1753	0.1544	0.1477	0.1715
Rank	3	1	2	5	6	4

TABLE 8: Priority of the different algorithms based on TOPSIS.

Decision matrix options	Similarity index	Ranking
Improved whale optimization algorithm	0.7585	1
Whale optimization algorithm	0.4730	2
Differential evolution	0.0437	3

followed by the other criteria prioritized as the third to the sixth.

The results obtained from TOPSIS on the basis of the decision matrix are shown in Table 8, suggesting that the improved whale optimization algorithm outperformed the other algorithms with the maximum similarity index, whereas the whale optimization and the differential evolution were, respectively, ranked second to third.

5. Conclusion

The present research proposed the improved whale optimization as a novel hybrid whale optimization differential evolution algorithm to optimize the operation of Boostan dam reservoir through satisfying the downstream demand for water by Boostan dam reservoir in Golestan province and reducing the shortage of water using a single-reservoir system. Exploration was performed in the improved algorithm by combining the mutation operator of the differential evolution and the search for prey of the whale optimization algorithm. The convergence rate, performance, and statistical parameters of the three algorithms were compared with one another and with the globally optimal solution obtained from nonlinear programming in GAMS by running the individual algorithms for ten times.

The obtained results confirmed the performance superiority of the improved whale optimization algorithm over the differential evolution with the objective function value of 25.74, minimum computation duration, and fastest convergence. In addition, the improved whale optimization improved the objective function, standard deviation, and variation coefficient by 21.7%, 82%, and 78% compared to those of the whale optimization, respectively. Lower values of mean absolute error and root-mean-square error obtained

for the improved algorithm also suggest this algorithm can more effectively help supply the demand for water than the other evolutionary algorithms. Given an average demand for water of 3.21×10^6 m^3 over the 151-month study period, the improved whale optimization algorithm outperformed the other evolutionary algorithm with a water discharge volume of 3.03×10^6 m^3, which was higher than that of the other algorithms. In other words, the improvements in performance achieved can be explained by the integration of the mutation operator of the differential evolution with the whale optimization in the hybrid algorithm, which caused the mutation operator to search the exploration space more effectively.

A multicriteria decision-making model was utilized based on TOPSIS and the Shannon entropy to identify the optimal algorithm. Calculating the evaluative indicators for the three algorithms suggested that the improved whale optimization algorithm, with a reliability index of 94%, outperforms the other evolutionary algorithms in terms of meeting the downstream demand for water. This algorithm was also found to be the best in terms of objective function value (25.74) and resiliency index (89%). The multicriteria decision-making model employed in the present research confirmed the functional superiority of the improved algorithm over the other two algorithms in optimizing the operation of Boostan dam reservoir. Moreover, an increase was observed in the volume of Boostan dam reservoir during the exploitation using the improved whale optimization compared to the whale optimization. In line with the results obtained by Kai et al. [4, 32], the present findings showed the superiority of hybrid algorithms over their constituent algorithms. The effect of climate change on this novel hybrid algorithm is recommended to be examined for multi-reservoir operation.

Data Availability

No data were used to support this study.

Conflicts of Interest

The authors declare that they have no conflicts of interest.

References

[1] K. Srinivasan and K. Kumar, "Multi-objective simulation-optimization model for long-term reservoir operation using piecewise linear hedging rule," *Water Resources Management*, vol. 32, pp. 1901–1911, 2018.

[2] M. Ehteram, H. Karami, S. Farzin, and S. Farzin, "Reservoir optimization for energy production using a new evolutionary algorithm based on multi-criteria decision-making models," *Water Resources Management*, vol. 32, no. 7, pp. 2539–2560, 2018.

[3] I. Ahmadianfar, A. Adib, and M. Salarijazi, "Optimizing multi-reservoir operation: hybrid of bat algorithm and differential evolution," *Journal of Water Resources Planning and Management*, vol. 142, no. 2, 2015.

[4] C.-T. Cheng, W.-C. Wang, D.-M. Xu, and K. W. Chau, "Optimizing hydropower reservoir operation using hybrid genetic algorithm and chaos," *Water Resources Management*, vol. 22, no. 7, pp. 895–909, 2008.

[5] M. H. Afshar, "Large scale reservoir operation by constrained particle swarm optimization algorithms," *Journal of Hydro-Environment Research*, vol. 6, pp. 75–87, 2012.

[6] K. W. Chau, "A split-step particle swarm optimization algorithm in river stage forecasting," *Journal of Hydrology*, vol. 346, no. 3-4, pp. 131–135, 2007.

[7] M. H. Afshar, "Extension of the constrained particle swarm optimization algorithm to optimal operation of multi-reservoirs system," *International Journal of Electrical Power and Energy Systems*, vol. 51, pp. 71–81, 2013.

[8] M. Ehteram, H. Karami, S. F. Mousavi, A. El-Shafie, and Z. Amini, "Optimizing dam and reservoirs operation based model utilizing shark algorithm approach," *Knowledge-Based Systems*, vol. 122, pp. 26–38, 2017.

[9] E. Fallah-Mehdipour, O. Bozorg Haddad, and M. A. Mariño, "Real-time operation of reservoir system by genetic programming," *Water Resources Management*, vol. 26, pp. 4091–4103, 2012.

[10] L. Ostadrahimi, M. A. Mariño, and A. Afshar, "Multi-reservoir operation rules: multi-swarm PSO-based optimization approach," *Water Resources Management*, vol. 26, pp. 407–427, 2012.

[11] R. Moeini and M. H. Afshar, "Extension of the constrained ant colony optimization algorithms for the optimal operation of multi-reservoir systems," *Journal of Hydroinformatics*, vol. 15, no. 1, pp. 155–173, 2013.

[12] Z. Zhang, S. Zhang, Y. Wang, Y. Jiang, and H. Wang, "Use of parallel deterministic dynamic programming and hierarchical adaptive genetic algorithm for reservoir operation optimization," *Computers & Industrial Engineering*, vol. 65, no. 2, pp. 310–321, 2013.

[13] O. Bozorg Haddad, M. Moravej, and H. A. Loáiciga, "Application of the water cycle algorithm to the optimal operation of reservoir systems," *Journal of Irrigation and Drainage Engineering*, vol. 141, no. 5, 2014.

[14] O. Bozorg-Haddad, I. Karimirad, S. Seifollahi-Aghmiuni, and H. A. Loáiciga, "Development and application of the bat algorithm for optimizing the operation of reservoir systems," *Journal of Water Resources Planning and Management*, vol. 141, no. 8, 2014.

[15] Y. Bolouri-Yazdeli, O. Bozorg Haddad, E. Fallah-Mehdipour, M. A. Mariño, and M. A. Mariño, "Evaluation of real-time operation rules in reservoir systems operation," *Water Resources Management*, vol. 28, no. 3, pp. 715–729, 2014.

[16] O. Bozorg Haddad, S. M. Hosseini-Moghari, and H. A. Loáiciga, "Biogeography-based optimization algorithm for optimal operation of reservoir systems," *Journal of Water Resources Planning and Management*, vol. 142, 2015.

[17] H. R. Asgari, O. Bozorg Haddad, M. Pazoki, and H. A. Loáiciga, "Weed optimization algorithm for optimal reservoir operation," *Journal of Irrigation and Drainage Engineering*, vol. 142, 2015.

[18] H. Akbari-Alashti, O. Bozorg Haddad, and M. A. Mariño, "Application of fixed length gene genetic programming (FLGGP) in hydropower reservoir operation," *Water Resources Management*, vol. 29, pp. 3357–3370, 2015.

[19] O. Bozorg-Haddad, M. Janbaz, H. A. Loáiciga, and H. A. Loáiciga, "Application of the gravity search algorithm to multi-reservoir operation optimization," *Advances in Water Resources*, vol. 98, pp. 173–185, 2016.

[20] M. Ehteram, M. F. Allawi, H. Karami et al., "Optimization of chain-reservoirs' operation with a new approach in artificial intelligence," *Water Resources Management*, vol. 31, pp. 2085–2104, 2017.

[21] S. F. Mousavi, H. R. Vaziri, H. Karami, and O. Hadiani, "Optimizing reservoirs exploitation with a new crow search algorithm based on a multi-criteria decision-making model," *JWSS*, vol. 22, pp. 279–290, 2018.

[22] H. Karami, S. F. Mousavi, S. Farzin, M. Ehteram, V. P. Singh, and O. Kisi, "Improved krill algorithm for reservoir operation," *Water Resources Management*, vol. 32, pp. 3353–3372, 2018.

[23] M. Ehteram, S. F. Mousavi, H. Karami et al., "Reservoir operation based on evolutionary algorithms and multi-criteria decision-making under climate change and uncertainty," *Journal of Hydroinformatics*, vol. 20, pp. 332–355, 2018.

[24] Z. M. Yaseen, H. Karami, M. Ehteram et al., "Optimization of reservoir operation using new hybrid algorithm," *KSCE Journal of Civil Engineering*, vol. 22, pp. 4668–4680, 2018.

[25] A. Donyaii, A. Sarraf, and H. Ahmadi, "Water reservoir multiobjective optimal operation using Grey Wolf optimizer," *Shock and Vibration*, vol. 2020, Article ID 8870464, 10 pages, 2020.

[26] M. Valikhan-Anaraki, S.-F. Mousavi, S. Farzin et al., "Development of a novel hybrid optimization algorithm for minimizing irrigation deficiencies," *Sustainability*, vol. 11, no. 8, p. 2337, 2019.

[27] S. Mirjalili and A. Lewis, "The whale optimization algorithm," *Advances in Engineering Software*, vol. 95, pp. 51–67, 2016.

[28] W. Gong, Z. Cai, and C. X. Ling, "DE/BBO: a hybrid differential evolution with biogeography-based optimization for global numerical optimization," *Soft Computing*, vol. 15, no. 4, pp. 645–665, 2011.

[29] R. Storn and K. Price, "Differential evolution—a simple and efficient adaptive scheme for global optimization over continuous spaces," Technical Report, International Computer Science Institute, Berkeley, CA, USA, 1995.

[30] C. R. Suribabu, "Differential evolution algorithm for optimal design of water distribution networks," *Journal of Hydroinformatics*, vol. 12, no. 1, pp. 66–82, 2010.

[31] S. M. Bozorgi and S. Yazdani, "IWOA: an improved whale optimization algorithm for optimization problems," *Journal of Computational Design and Engineering*, vol. 6, pp. 243–259, 2019.

[32] M. Mohammadi, S. Mousavi, S. Farzin, and H. Karami, "Optimal Operation of Salman Farsi dam reservoir using Wall algorithm and its hybrid with genetic algorithm based on multi criteria Decision," *Eco Hydrology Journal*, vol. 6, no. 2, pp. 281–293, 2019.

[33] M. Ehteram, H. Karami, S.-F. Mousavi, S. Farzin, and O. Kisi, "Evaluation of contemporary evolutionary algorithms for optimization in reservoir operation and water supply," *Journal of Water Supply: Research and Technology-Aqua*, vol. 67, no. 1, pp. 54–67, 2017.

[34] M. Ehteram, H. Karami, S.-F. Mousavi, S. Farzin, and O. Kisi, "Optimization of energy management and conversion in the multi-reservoir systems based on evolutionary algorithms," *Journal of Cleaner Production*, vol. 168, pp. 1132–1142, 2017.

[35] B. A. Lane, S. Sandoval-Solis, and E. C. Porse, "Environmental flows in a human-dominated system: integrated water management strategies for the Rio Grande/Bravo basin," *River Research and Applications*, vol. 31, no. 9, pp. 1053–1065, 2014.

[36] S. Sandoval-Solis, D. C. McKinney, D. P. Loucks, and D. P. Loucks, "Sustainability index for water resources planning and management," *Journal of Water Resources Planning and Management*, vol. 137, no. 5, pp. 381–390, 2011.

[37] Z. H. Zou, Y. Yun, and J. N. Sun, "Entropy method for determination of weight of evaluating indicators in fuzzy synthetic evaluation for water quality assessment," *Journal of Environmental Sciences*, vol. 18, no. 5, pp. 1020–1023, 2006.

[38] J. Ye, "Fuzzy decision-making method based on the weighted correlation coefficient under instuitionistic fuzzy environment," *European Journal of Operational Research*, vol. 205, no. 1, pp. 202–204, 2010.

[39] F. H. Lotfi and R. Fallahnejad, "Imprecise Shannon's entropy and multi attribute decision making," *Entropy*, vol. 12, no. 1, pp. 53–62, 2010.

[40] C. L. Hwang and K. Yoon, "Methods for multiple attribute decision making," in *Multiple Attribute Decision Making. Lecture Notes in Economics and Mathematical Systems*Vol. 186, Springer, Berlin, Germany, 1981.

[41] N. Chitsaz and M. E. Banihabib, "Comparison of different multi criteria decision-making models in prioritizing flood management alternatives," *Water Resources Management*, vol. 29, no. 8, pp. 2503–2525, 2015.

[42] M. Uneyama, J. K. Chambers, K. Nakashima, K. Uchida, and H. Nakayama, "Histological classification and immunohistochemical study of feline colorectal epithelial tumors," *Veterinary Pathology 2011 Multiple Attribute Decision Making: Methods and Applications*, Chapman and Hall/CRC, Boca Raton, FL, USA, 2020.

Research Article

Water Reservoir Multiobjective Optimal Operation Using Grey Wolf Optimizer

Alireza Donyaii [ID], Amirpouya Sarraf [ID], and Hassan Ahmadi [ID]

Department of Civil Engineering, Roudehen Branch, Islamic Azad University, Roudehen, Iran

Correspondence should be addressed to Amirpouya Sarraf; st.ar_donyaii@riau.ac.ir

This study develops the Multiobjective Grey Wolf Optimization (MOGWO) algorithm to obtain the optimum rules on the operation of the Golestan Dam in Golestan Province, Iran, under the climate change conditions. The tow objective functions defined in the optimization process include minimizing the vulnerability and maximizing the reliability indices of the model under baseline and climate change conditions periods. Results showed that the river flow would decline by 0.17 percent of the baseline period under climate change conditions in addition to increasing the temperature by 20%, as well as decreasing the rainfall by 21.1%. Moreover, the extent of vulnerability index variations in baseline and climate change conditions was 16–45% and 10–43%, respectively. The range of reliability index variations in baseline and climate change conditions was 47–90% and 27–93%. On the other hand, the vulnerability index has also been measured at 29% and 27% for baseline and climate change conditions, respectively, with 75 percent of reliability. Comparison of the reservoir release rate and water demands for all of the Pareto points indicates a rise in release rates for climate change conditions relative to the baseline one; as the result, the higher adjustment in the reservoir release rates to its demand volumes will be highlighted as the higher dam efficiency in climate change conditions.

1. Introduction

Water resources systems are very complex, and in terms of water resources management and use, the advantages of water supplies can be maximized. Therefore, in order to promote sustainable growth and optimize profits, it is important to participate in management activities to satisfy customer needs, particularly in areas where the mismatch problem is severe [1, 2].

The operation of dam reservoirs is of great significance because of the inadequate water supplies, owing to the economic value of the reservoirs resulting from the optimum management of water resources, growing water demands, and the scarcity of usable water supply. Furthermore, it is important to use a system that provides optimum management of the operation of dam reservoirs, particularly under the conditions of climate change. Thus, both priorities and multiobjective modeling frameworks must be used to derive decision-making alternatives [3].

Therefore, a group of approximate solution algorithms called metaheuristic algorithms has been produced over the last decades in the optimization of the reservoir system that investigate the computational complexity efficiently and safely and avoid the solution method from being stuck within the boundaries of the search space. For multiobjective optimization of water resource systems, particularly dam reservoirs, several methods have been used in the recent decades. Multiobjective evolutionary algorithms are among the most significant and commonly used, providing a range of optimal solutions in each iteration that can be expressed in the form of the Pareto curve [4].

Sun et al. [5] proposed a model of multiobjective optimization for reservoir operation (MORO) with the objectives of maximizing water diversion and power generation. The multiobjective evolutionary algorithm based on decomposition with adaptive weight vector adjustment (MOEA/D-AWA) was applied to solve the MORO problem. In addition, the performance of the MOEA/D-AWA was

compared with two other algorithms based on the hypervolume index.

Their results showed that (1) the proposed model was effective and reasonable in theory; (2) the optimization results obtained by MOEA/D-AWA demonstrated this algorithm could be applied to the MORO problem, providing a set of evenly distributed nondominated solutions; and (3) water diversion and power generation were indeed contradictory objectives.

Donyaii et al. [6] introduced a combined model of Crow Search (CSA) and Grey Wolf (GWO) Optimization algorithms called Grey Wolf -Crow Search Hybrid algorithm to optimize the operation of the single-reservoir system of the Golestan Dam, considering the objective function (supplying downstream water demand). To compare the convergence and performance of these algorithms, the statistical parameters of each algorithm were calculated and compared with each other, as well as with the analytical solution of a nonlinear programming model (i.e., GAMS Software). Then, in order to analyze the performance of the algorithms, the Combinative Distance-based Assessment (CODAS) Multicriteria Decision-Making Model was used to rank the decision alternatives (i.e., optimization algorithms) based on volumetric and time-based reliability, reversibility, and vulnerability criteria, as well as the optimized objective function. Their results showed that not only the hybrid model approach has a response closer to the absolute optimal value but also the CODAS Multicriteria Decision-Making Model identified that it was better than its constituent algorithms, namely, CSA Optimization and GWO algorithm in optimizing the objective function.

Wu et al. [7] carried out a multiobjective hydropower reservoir activity using NSGA-II and objective functions to optimize water supply and hydropower generation benefits and mitigate water scarcity for environmental demands and demonstrated the efficacy and reliability of the proposed algorithm and model by using it in the Yellow River of China's Lango reservoir.

Ashofteh et al. [8] used the multipurpose genetic programming (GP) to optimize the Aydoghmush dam reservoir in East Azerbaijan Province in Iran under baseline and climate change conditions. The optimization results revealed that the rules of reservoir performance that are involved in climate change lead to an improvement from 29% to 32% in the reservoir performance due to climate change compared to baseline. Ehteram et al. [9] applied the kidney algorithm to generate an optimal operation of the Aydoghmush reservoir in Eastern Azerbaijan Province in Iran to decrease irrigation deficit downstream of the dam. They compared the results of the kidney algorithm with other evolutionary algorithms, including bat (BA), genetic (GA), particle swarm (PSO), shark (SA), and weed algorithms (WA). The results showed that the kidney algorithm provided the best performance against the other evolutionary algorithms.

The efficiency of two models of Extreme Learning Machines (ELM), Artificial Neural Network (ANN), and the combination of two models with wavelet propagation algorithms (W-ELM and W-ANN) was evaluated by Afkhamifar & Sarraf [10]. They discovered the W-ELM-QPSO hybrid model has increased quality than other models and

this model has a high speed in terms of training and testing speed in addition to forecasting power than other models.

In the present study, as an innovative approach in the field of water management, the development and implementation of the multiobjective Grey Wolf optimization algorithm (MOGWO) was proposed, which was not discussed in the previous studies.

Moreover, the optimal operation rules of the Golestan Dam reservoir (in Golestan Province, Iran) in baseline conditions (from April 2006 to October 2018) and climate change conditions (April 2021 to October 2033) using MOGWO algorithm, with two objectives of minimizing vulnerability and maximizing reliability index in demand-supply, were determined and compared in the mentioned periods as a necessity for the future water recourses planning management.

The methods applied in this research are as follows:

(i) Assessing climate change parameters

(ii) Simulation of rainfall-runoff processes for determining Golestan Dam reservoir discharge volume in Iran

(iii) Estimation of baseline water demand volume and climate change conditions and multiobjective operating rules extraction (based on three variables of storage volume, demand volume, and discharge to the reservoir) in climate change and baseline conditions

Ultimately, the procedures for this investigation were to compare optimum allocation policies in baseline and climate change conditions with the performance measures and efficiency indices of the reservoir.

2. Initial Information and Processing

In this study, in order to obtain a more realistic approximation, by averaging three scenarios (i.e., RCP 2.6, RCP 4.5, and RCP 8.5), a new scenario named as the average scenario was proposed after downscaling the CANESM2 Climate model with SDSM 4.2 software. The findings show that, also in the average scenario, the monthly average temperature increases in all three cases, which averages 20% for the prediction duration. Analyzing the average monthly precipitation variations have shown that the drop in the next period of precipitation rate was obvious, and this trend has been diminished by to 21.1 percent regarding to the baseline.

A second-order Neurofuzzy model with a Gaussian membership function was conducted to simulate the rainfall-runoff process focusing on the climate change phenomena at the entrance to the Golestan Dam, including 20 training epochs and 10000 iterations for 95% of training data (in each prediction). ANFIS's best influence radius for calculating the runoff reached 0.04.

Consequently, the volume of runoff during the climate change conditions with respect to the baseline period would be decreased to 0.17 percent. Therefore, this could be a warning for water resources management.

3. Optimization Model Development

The simulation of the reservoir through the continuity equation would be described as follows:

$$S_{(t+1)} = S_{(t)} + Q_{(t)} - \text{Re}_{(t)} - Sp_{(t)} - \text{Loss}_{(t)}, \quad (1)$$

$$\text{Loss}_{(t)} = A_{(t)} \times Ev_{(t)}, \quad (2)$$

$$A_{(t)} = aS_{(t)}^3 + bS_{(t)}^2 + cS_{(t)} + d, \quad (3)$$

where $A_{(t)}$ implies to the reservoir surface in the t-th month, $Ev_{(t)}$ is the net evaporation from the reservoir (the difference among the amount of rainfall and evaporation in the t-th month), and $a, b, c,$ and d imply the constant coefficients of the volume-area equation of the reservoir for the Golestan Dam reservoir. $Q_{(t)}$ is the inflow to the reservoir in the t-th month, $\text{Re}_{(t)}$ is the release from the reservoir in the t-th month, $Sp_{(t)}$ is the reservoir overflow in the t-th month, $\text{Loss}_{(t)}$ s the evaporation losses in the t-th month, and shortage is the difference between the demand and the actual release when it is less than the demand. Overflow of the reservoir imposes some constraints on the calculations as follows:

$$S_{P_t} = \begin{cases} S_t + Q_t - \text{Re}_t - \text{Loss}_{(t)} - S_{\max}, & \text{if } S_t + Q_t - \text{Re}_t - \text{Loss}_{(t)} > S_{\max}, \\ 0, & \text{if } S_t + Q_t - \text{Re}_t \leq S_{\max}. \end{cases} \quad (4)$$

Other constraints are as follows:

$$S_{\min} \leq S_t \leq S_{\max}, \quad (5)$$

$$\text{Re}_{\min} \leq \text{Re}_t \leq \text{Re}_{\max}, \quad (6)$$

where $S_{\max}$ and $S_{\min}$ imply the maximum and minimum volumes of the reservoir and $\text{Re}_{\max}$ and $\text{Re}_{\min}$ are referred to as the maximum and minimum releasable volumes from the reservoir, respectively [11].

Two objective functions have been used in the present study to mitigate vulnerability and optimize the reliability index in baseline and climate change conditions based on the following equations [12]:

$$\text{Minimize } F_1 = \frac{\sum_{t=1}^{T} (D_t - \text{Re}_t | \text{Re}_t < D_t)}{\left[N_{t=1}^T (\text{Re}_t < D_t) \right] \cdot D_{\max}}, \quad \forall_t = 1, 2, \dots, T, \quad (7)$$

$$\text{Maximize } F_2 = \frac{N_{t=1}^T (D_t - \text{Re}_t | \text{Re}_t \geq D_t)}{T}, \quad \forall_t = 1, 2, \dots, T, \quad (8)$$

where F_1 implies the objective function of a vulnerability index, F_2 is the objective function of the reliability index, D_t is referred to as the demand volume throughout the t-th period, $D_{\max}$ implies the maximum water demand in the operating period, $N_{t=1}^T (\text{Re}_t < D_t)$ implies the number of months of water shortage, and $N_{t=1}^T (D_t - \text{Re}_t | \text{Re}_t \geq D_t)$ implies the number of months of water supply equations:

$$S_t \geq S_{\min}, \quad \forall_t = 1, 2, \dots, T, \quad (9)$$

$$\text{Re}_t \leq \text{Re}_{\max}, \quad \forall_t = 1, 2, \dots, T. \quad (10)$$

In the event of violations of constraints 9 and 10, penalty functions will be introduced to the objective functions as follows:

$$F_1 (\text{or } F_2) = F_2 (\text{or } F_1) \pm \left[A' \cdot \left(\frac{S_{\min} - S_t}{S_{\max} - S_{\min}} \right) + B' \right],$$
$$\forall_t = 1, 2, \dots, T, \quad (11)$$

$$F_1 (\text{or } F_2) = F_2 (\text{or } F_1) \pm \left[C' \cdot \left(\frac{\text{Re}_t}{D_{\max}} \right) + D' \right],$$
$$\forall_t = 1, 2, \dots, T, \quad (12)$$

where $[A' \cdot (S_{\min} - S_t / S_{\max} - S_{\min}) + B']$ implies the penalty function achieved from the violation of equation (9) and $[C' \cdot (\text{Re}_t / D_{\max}) + D']$ is referred to as the penalty function resulted from the violation of equation (10). A' to D' coefficients imply the positive constants of penalty functions with $A' = 1$, $B' = 0.5$, $C' = 1$, and $D' = 16$ values [12].

3.1. Operation Rule Curve.
In the existing study, the rule of decision is derived based on equations (13) and (14) for the operation of the Golestan Dam single-reservoir system to minimize the vulnerability resulted from the system shortage and to provide the necessary demand and also to optimize the demand-supply reliability using MOGWO algorithm equations:

$$\text{Re}_{bt} = g_1 (Q_{bt} + S_{bt} + D_{bt}), \quad \forall_t = 1, 2, \dots, T, \quad (13)$$

$$\text{Re}_{ft} = g_2 (Q_{ft} + S_{ft} + D_{ft}), \quad \forall_t = 1, 2, \dots, T, \quad (14)$$

where $g_1 (Q_{bt} + S_{bt} + D_{bt})$ of the first option implies the rule from MOGWO in the baseline operating period for baseline conditions and $g_2 (Q_{ft} + S_{ft} + D_{ft})$ of the second option implies the rule from MOGWO in the climate change operating period for climate change conditions. The b index is for baseline conditions, and the f index is for climate change conditions [12].

3.2. Grey Wolf Optimization.
Mirjalili et al. [13] proposed the Grey Wolf Optimization Algorithm (GWO) to mimic the hunting behavior of Grey Wolves in nature. The key goal of the GWO strategy is to use a network of searching agents to determine the optimal for a specific problem. Usually, these wolves reside in groups of between five and twelve. The basic difference between the algorithm of Grey Wolf Optimization and the other algorithms of optimization is the dominant social structure that decides the convergence rate for each optimization iteration. Furthermore, the Grey Wolf Optimization algorithm mimics the wolves' foraging actions in finding and assaulting prey [13]. Figure 1 shows the
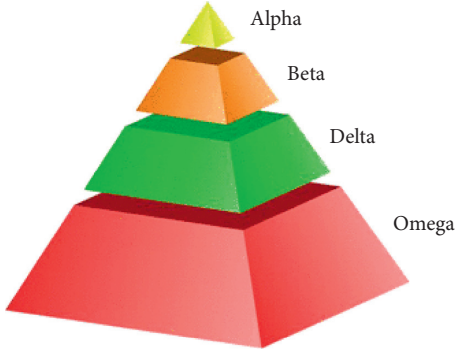
Figure 1: Social hierarchy of the group of Grey Wolves [13].

Figure 2: Graphical representation of Grey wolf hunting procedure in a circle or sphere space around the prey (X_p) based on the direction (D) between the wolf ($X_{(t)}$) and the prey [13].

hierarchical order of the group of wolves. The leader is shown by alpha as the strongest alternate member. In reality, the alpha, accompanied by the other wolves, is the leader wolf. Beta is the second alternative candidate who encourages alpha in decision-making and is a conduit between the leader and the rest of the squad. The third alternate nominee responsible for providing data for two higher stages (alpha and beta) is indicated by delta. In comparison, the remaining alternatives are indicated by the omega, which is responsible for submitting information to the three higher stages. Furthermore, the hunting process consists of three steps: the prey is found, surrounded, and targeted. Therefore, the Grey Wolves Empirical hunting technique used to address a structural optimization topic is demonstrated by GWO. It is, then, presumed that the victims are the ideal solution to the issue.

The motion of the top three stages, provided in the given equations, replicates the covering of the victim by Grey wolves [13].

$$D = \left| \vec{C} \cdot \overrightarrow{X_p}(t) - \vec{X}(t) \right|, \tag{15}$$

where in t represents the current iteration, Xp represents the victim's location vector, X indicates the Grey wolf's position, and C is the coefficient's vector. As stated in Figure 2, the consequence of vector D is, then, used by the following equations to move the individual object to or away from the area where the best solution representing the victim is located [13]:

$$\vec{X}(t + 1) = \overrightarrow{X_p}(t) - \vec{A} \cdot \vec{D}, \tag{16}$$

$$\vec{A} = 2\vec{a} \cdot \vec{r}_1 - \vec{a}, \tag{17}$$

$$\vec{C} = 2 \cdot \vec{r}_2, \tag{18}$$

where $\vec{r}_1$ is selected randomly in [0, 1] and $\vec{a}$ is reduced from 2 to 0 using a fixed quantity of iterations.

In case $|A| < 1|$, this corresponds to the behavior of the exploitation and simulates the behavior of the attack on the prey. Otherwise, if $|A| < 1$, this fits the exploration behavior and simulates the victim's wolf spacing away, as illustrated in Figure 2. The proposed values for A are given in [−2, 2]. Therefore, the following mathematical expressions are used to measure three higher levels alpha, beta, and delta [13].
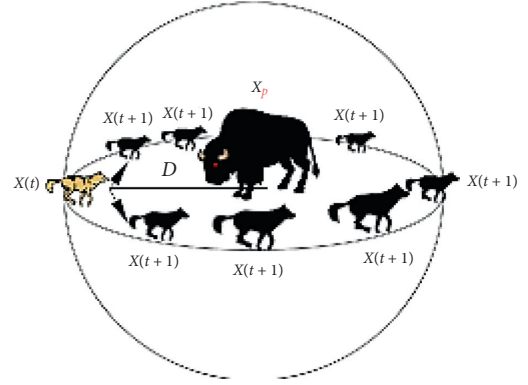
This refers to the exploitation action in the case $|A| < 1$ and approximates the actions of the attack on the victim. Otherwise, if $|A| > 1$, this matches the exploration actions and approximates the positioning of the victim's wolf, as seen in Figure 2. In [−2, 2], the suggested values for A are provided. The following mathematical equations are, then, used to calculate alpha, beta, and delta at three higher stages [13].

$$\overrightarrow{D_\alpha} = \left| \vec{C_1} \cdot \overrightarrow{X_\alpha} - \vec{X} \right| \overrightarrow{X_1} = \overrightarrow{X_\alpha} - \overrightarrow{A_1} \cdot \left(\overrightarrow{D_\alpha} \right),$$

$$\overrightarrow{D_\beta} = \left| \vec{C_2} \cdot \overrightarrow{X_\beta} - \vec{X} \right| \overrightarrow{X_2} = \overrightarrow{X_\beta} - \overrightarrow{A_2} \cdot \left(\overrightarrow{D_\beta} \right), \tag{19}$$

$$\overrightarrow{D_\delta} = \left| \vec{C_3} \cdot \overrightarrow{X_\delta} - \vec{X} \right| \overrightarrow{X_3} = \overrightarrow{X_\delta} - \overrightarrow{A_3} \cdot \left(\overrightarrow{D_\delta} \right).$$

We consider that alpha, beta, and delta have enough knowledge of the potential location of the prey for mathematically mimicking the Grey Wolf hunting process. In reality, as defined in the following equations, the first three best solutions that have been obtained are rescued and enable the other agents to adjust their positions based on the best agents alpha, ß, and d [13]:

$$\vec{X}(t + 1) = \frac{\overrightarrow{X_1} + \overrightarrow{X_2} + \overrightarrow{X_3}}{3}. \tag{20}$$

4. Results and Discussion

Using metaheuristic algorithms in civil engineering optimization issues is inevitable [14, 15]. In this study, the MOGWO metaheuristic algorithm was used to derive the operating rules from the Golestan Dam Single-Reservoir System in Northeastern Iran, Golestan Province (Figure 3), and a 4200-hectare downstream network. The reservoir has a capacity of 43.7 million cubic meters at the normal level, 100 meters above sea level, and 54 million cubic meters at the level of overflow.

The curve of the surface-volume of the reservoir was extracted through the following equation with the $R^2 = 0.997$ correlation coefficient and based on Figure 4:
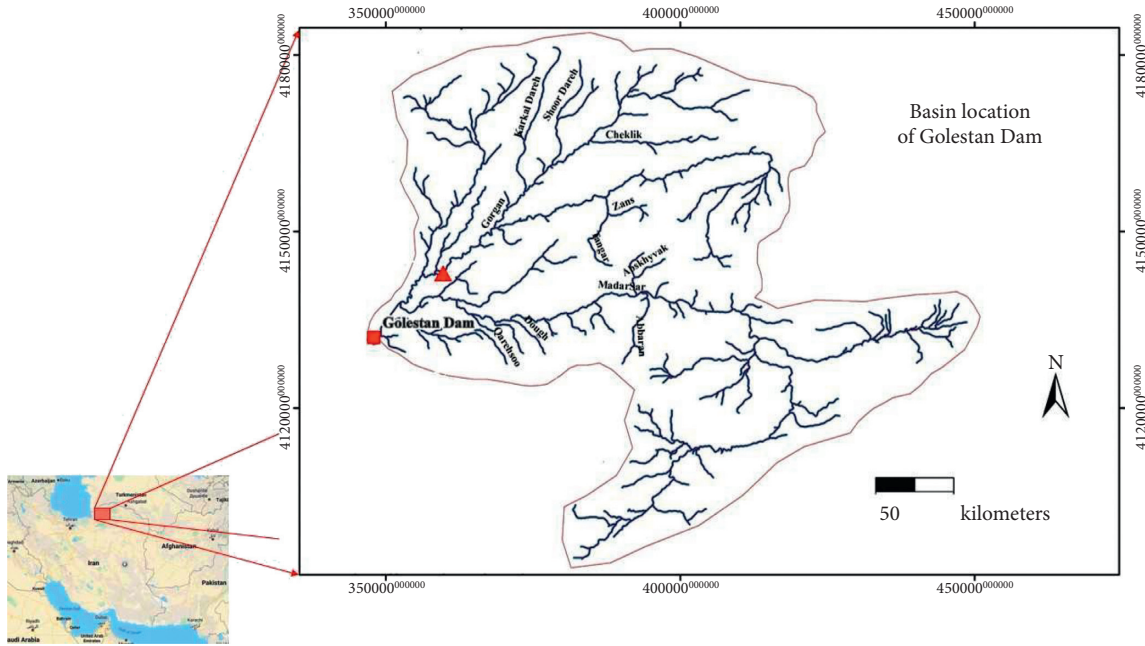
$$Y = -0.003X^2 + 0.184X + 1.435. \tag{21}$$

FIGURE 3: The geographical location of the study region.

$$y = -0.002x^2 + 0.184x + 1.453$$
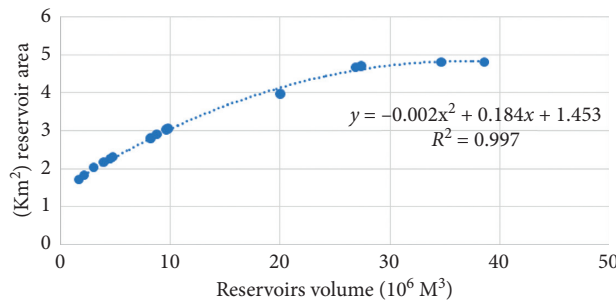$$R^2 = 0.997$$

FIGURE 4: Surface-volume curve of the Golestan Dam reservoir.

The maximum baseline and climate change demands are 37.84 and 41.86 million cubic meters. Figure 5 indicates the average monthly release volume, as well as the monthly average evaporation volume and the monthly average demand volume for water under baseline and climate change conditions.

The results revealed that the ratio of discharge into the reservoir and demand for water under climate change conditions decreased by approximately 17 percent and increased by 10 percent relative to baseline conditions, respectively.

The optimum operating rules of the Golestan Dam reservoir were obtained from a two-targeted problem, using the MOGWO algorithm. The two-target problem involved maximizing demand reliability and reducing system vulnerability.

According to Figure 6, if we assume the model reliability index of 75%, there will be an obvious difference between the vulnerability values under the climate change and baseline conditions. In other words, Figure 6 displays the effects of the two-objective optimization algorithm in the

sense of the Pareto curve for baseline and climate change conditions. There are 16 percent to 45 percent and 10 percent to 43 percent of vulnerability shifts in baseline and climate change conditions as stated in Figure 6. In baseline and climate change conditions, the number of reliability adjustments is 47 percent to 90 percent and 27 percent to 93 percent. In comparison, for baseline conditions and climate change conditions, 29 percent and 27 percent of vulnerabilities are generated for every 75 percent of reliability, respectively. In other words, the degree of vulnerability and reliability of climate change is higher than that of the average. A reservoir activity rule, including its vulnerability and reliability indices, is shown by each point in the Pareto curve (Figure 6). None of the Pareto points has taken precedence over others; based on catchment conditions and policies, they can differ. The next phase was to determine the optimum level of rules on water demand in the sense of baseline and climate change conditions. Therefore, the optimum rules were compared to the optimum rules arising from climate change conditions. On the other hand,
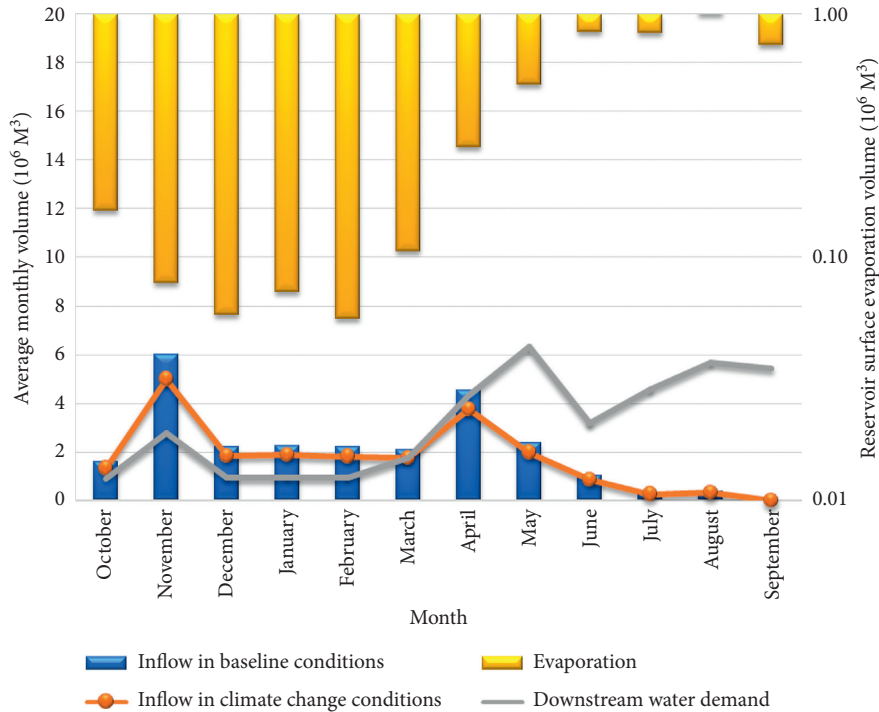
FIGURE 5: The average monthly release volume, as well as the monthly average evaporation volume and the monthly average demand volume, for water under baseline and climate change conditions.
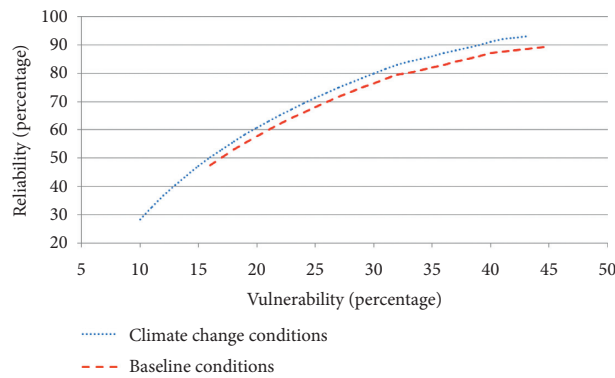

FIGURE 6: The comparison of the Pareto curve and changes in vulnerability and reliability objective functions.

Figure 6 shows that, in all the values of common reliability between baseline and climate change conditions (i.e., 45% to 89%), the vulnerability values of the model have been significantly reduced, which will evaluate the model more stable in climate change conditions.

For the baseline and climate change conditions, the results for the supply of water demands for the 75 percent reliability index are stated in the Figures 7(a) and 8(a).

Compared to the corresponding demand for water, the following two alternatives were determined by the changes for shortages due to the optimal operational rules arising from the proposed optimization algorithm, as shown earlier. A comparison of the baseline and climate change conditions shows that, in the climate change conditions, the volume of

released water from the reservoir is more consistent with irrigation demand. In addition, reservoir storage in the climate change conditions is lower compared with the baseline one, which is due to increases in the release (Figure 8(b)). The results are seen, respectively, in (Figure 7(b)) and (Figure 8(b)). Climate change release rates are higher than under baseline conditions, according to (Figure 7(a)) and (Figure 8(a)), which will be 10 percent due to the increased demand for water under climate change conditions.

On the other hand, Figures 7(b) and 8(b) indicate that, under climate change conditions, the output of the dam has also improved. In the next step, the objective function values of 75 percent reliability per Pareto point were calculated in
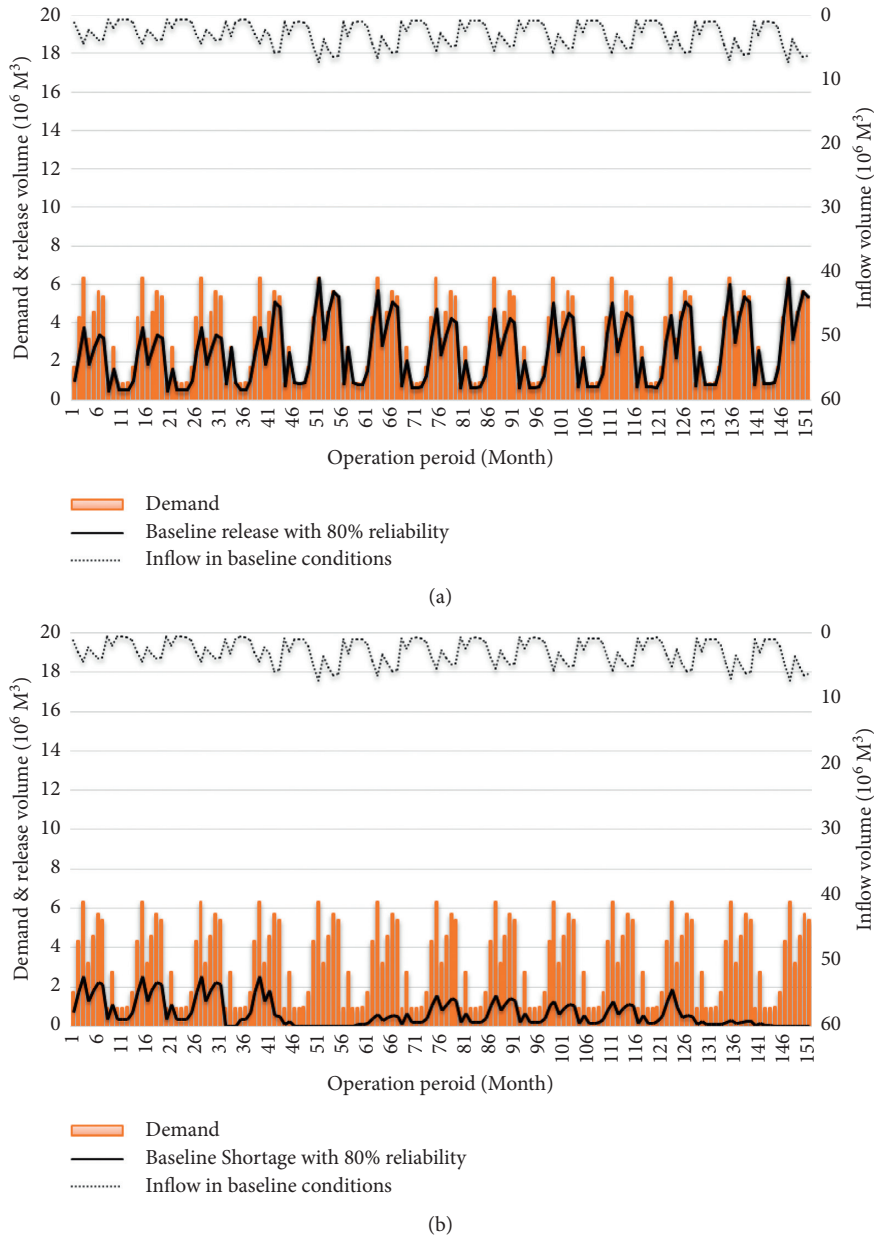
(a)

(b)
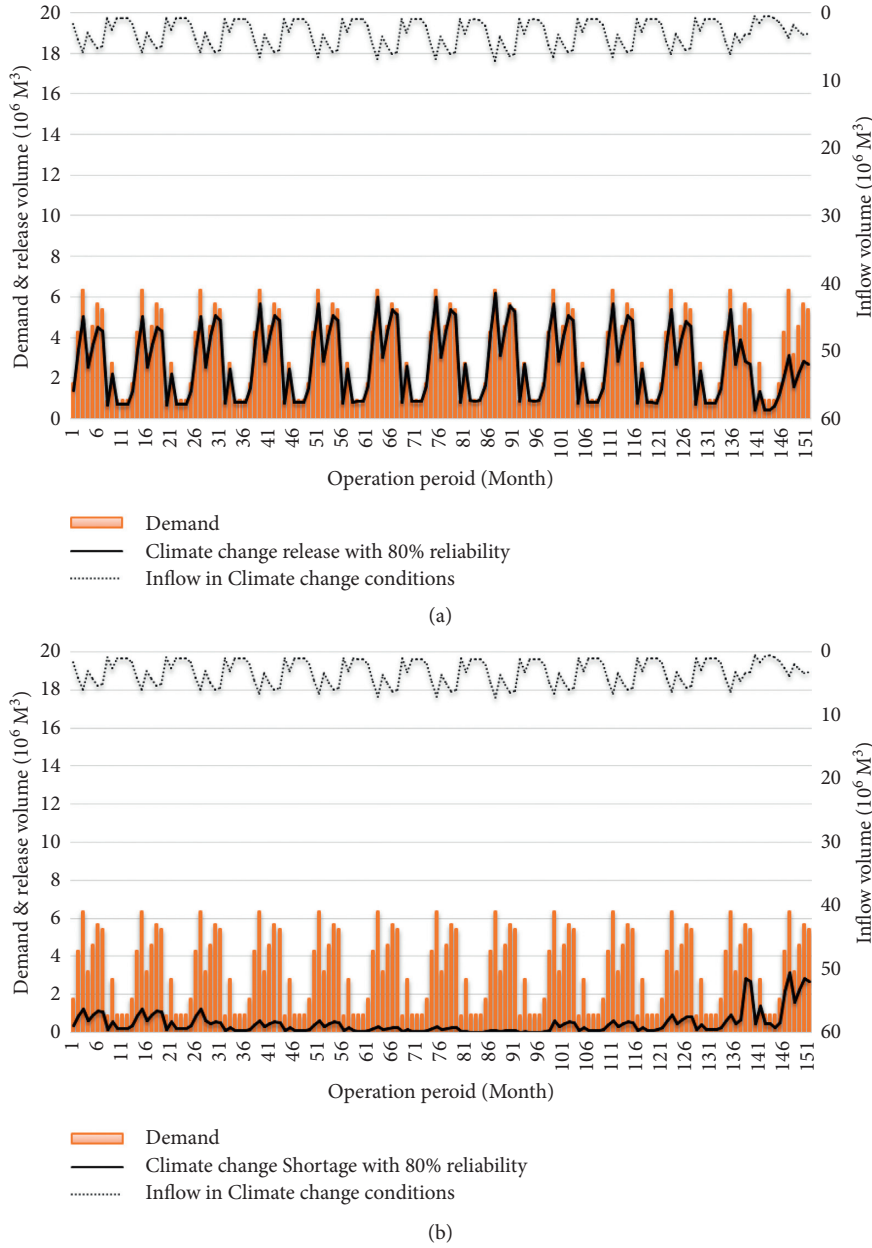
FIGURE 7: The comparison of (a) release volume (b) and shortage volume per each Pareto point resulted from 75% reliability in baseline conditions.

the conditions to evaluate the reservoir output in the supply of downstream water requirements, as described in (Table 1). Reservoir release is more compatible with climate change conditions, according to (Table 1). Therefore, under the effects of climate change, the dam's performance is even better.

It should be mentioned that the results obtained in this study are consistent with the results obtained by other researchers such as Ashofteh et al. [12] and Donyaii et al. [4] who applied genetic programming and Farmland Fertility optimization algorithm, respectively.

(a)

(b)

FIGURE 8: The comparison of (a) release volume and (b) shortage volume per each Pareto point resulted from 75% reliability in climate change conditions.

TABLE 1: The comparison of objective functions in baseline and climate change conditions for each Pareto point (75% reliability).

Conditions	Reliability (%)	Vulnerability (%)
Baseline	75	29
Climate change	75	27

5. Conclusions

One of the main considerations in water resources management is to take into account all priorities within policies governing the development of water resources systems to satisfy water demand. Moreover, in the light of climate change, it is important to include a range of decision-making alternatives (Pareto curve) in such a manner that executive managers and operators can assess the relative value of the objectives in this respect. Therefore, it is unavoidable to derive multiobjective operating rules from reservoirs, as each of the curve points in the Pareto curve

means a reservoir operation rule that can be modified under the conditions and policies regulating the catchment. The objective of this work was to draw up a general guideline for the operation of such Pareto points so that it could determine how to achieve these points such that 75 percent of the downstream Golestan Dam lands in Iran are provided with water needs.

In the current research, after assessing the climate change parameters such as temperature and precipitation values for baseline condition, they were predicted for the future period as the parameters of climate change conditions by downscaling the CANESM2 climate model with SDSM 4.2 software. Analyzing the average monthly precipitation variations have shown that the drop in the precipitation rate in the next period was obvious, and this trend has been diminished by to 21.1 percent regarding to the baseline as a warning for water resources management. Next, a second-order Neurofuzzy model with a Gaussian membership function was conducted to simulate the rainfall-runoff process focusing on the climate change phenomena at the entrance to the Golestan Dam. Results showed that the volume of runoff during the climate change conditions with respect to the baseline period would be decreased to 0.17 percent. Finally, the Grey Wolf Optimization algorithm was used to solve the problem of the reservoir system of the Golestan Dam under baseline and climate change conditions in the province of Golestan. In order to obtain reservoir discharge rules (based on the Pareto curve), objective functions, including maximizing the reliability index and minimizing the vulnerability index, were based on parameters such as the discharge volume to the reservoir, the storage volume, and the water demand volume derived from the MOGWO algorithm. The study showed that the amount of vulnerability changes under the baseline and climate change conditions was 16 percent to 45 percent and 10 percent to 43 percent, respectively. Moreover, the reliability increase under the baseline and climate change conditions ranged from 47 percent to 90 percent and 27 percent to 93 percent, respectively. Meanwhile, for 75% reliability index of the model, the vulnerability ranged between 29% and 27% under the baseline and climate change conditions, respectively. In the next step, in order to evaluate the efficiency of the reservoir in meeting the downstream water requirements, in the abovementioned conditions, the values of the objective function were compared to 75 percent reliability. The results show that the rate of release of the reservoir is far more in line with the demand for climate change, so evidence is given that the Golestan Dam performs better under the conditions of climate change.

Abbreviations

$A_{(t)}$:	Reservoir surface in the t-th month
$Ev_{(t)}$:	Net evaporation from the reservoir
a, b, c, d:	Constant coefficients of the surface-volume equation
$Q_{(t)}$:	The inflow to the reservoir in the t-th month
$Re_{(t)}$:	The release from the reservoir in the t-th month
$Sp_{(t)}$:	The reservoir overflow in the t-th month
$Loss_{(t)}$:	The evaporation losses in the t-th month
S_{max} and S_{min}:	Maximum and minimum volumes of the reservoir
Re_{max} and Re_{min}:	Maximum and minimum releasable volumes from the reservoir
F_1:	Objective function of a vulnerability index
F_2:	Objective function of reliability index
D_t:	Demand volume throughout the t-th period
D_{Max}:	Maximum water demand in the operating period
$N_{t=1}^{T}(Re_t < D_t)$:	Number of months of water shortage
$N_{t=1}^{T}(D_t - Re_t \mid Re_t \geq D_t)$:	Number of months of water supply
$[A' \cdot (S_{min} - S_t / S_{max} - S_{min}) + B']$:	Penalty function achieved from the violation of equation (9)
$[C' \cdot (Re_t / D_{Max}) + D']$:	Penalty function resulted from the violation of equation (10)
A' to D':	Coefficients imply the positive constants of penalty functions with $A' = 1$, $B' = 0.5$, $C' = 1$, and $D' = 16$ values
$g_1 (Q_{bt} + S_{bt} + D_{bt})$:	The rule from MOGWO in the baseline operating period for baseline conditions
$g_2 (Q_{ft} + S_{ft} + D_{ft})$:	The rule from MOGWO in the climate change operating period for climate change conditions
The b index:	For baseline conditions, f index = for climate change conditions
GWO:	Grey Wolf Optimization Algorithm
Xp:	Victim's location vector
X:	Grey wolf's position

C:	Coefficient's vector
D:	Direction between the wolf and the prey
$(X_{(t)})$:	Prey position
$\vec{r}_1$ and $\vec{r}_2$:	Randomly selected value of $[0, 1]$
$\vec{a}$:	Fixed quantity of iterations reduced from 2 to 0
A:	Proposed values given in $[-2, 2]$
R^2:	Correlation coefficient.

Data Availability

The manuscript data can be obtained from the Shock and Vibration Journal.

Conflicts of Interest

The authors declare that they have no conflicts of interest.

References

[1] M. A. Hariri-Ardebili, S. Mahdi Seyed-Kolbadi, V. E. Salamon, J. W. Salamon, and L. K. Nuss, "Anatomy of the vibration characteristics in old arch dams by random field theory," *Engineering Structures*, vol. 179, no. 15, pp. 460–475, 2019.

[2] H. Mirzabozorg, M. A. Hariri-Ardebili, M. Heshmati, and S. M. Seyed-Kolbadi, "Structural safety evaluation of Karun III Dam and calibration of its finite element model using instrumentation and site observation," *Case Studies in Structural Engineering*, vol. 1, pp. 6–12, 2014.

[3] M. A. Hariri-Ardebili, H. Rahmani-Samani, and M. Mirtaheri, "Seismic stability assessment of a high-rise concrete tower utilizing endurance time analysis," *International Journal of Structural Stability and Dynamics*, vol. 14, no. 6, Article ID 1450016, 2014.

[4] A. R. Donyaii, A. P. Sarraf, and H. Ahmadi, "Application of a new approach in optimizing the operation of the multi-objective reservoir," *Journal of Hydraulic Structures*, vol. 6, no. 3, pp. 1–22, 2020.

[5] X. Sun, J. Luo, and J. Xie, "Multi-objective optimization for reservoir operation considering water diversion and power generation objectives," *Water*, vol. 10, no. 11, p. 1540, 2018.

[6] A. R. Donyaii, A. P. Sarraf, and H. Ahmadi, "Presenting a new hybrid evolutionary algorithm in optimizing reservoir operation based on new combinative distance-based assessment techniques (CODAS)," *Journal of Water and Soil Conservation*, in Persian, 2020.

[7] X. Wu, X. Wei, and W. Guo, "Multi-objective ecological operation model of cascade hydropower reservoirs," in *Proceedings of the International Workshop on Information and Electronics Engineering (IWIEE)*, pp. 3996–4001, Harbin, China, March 2012.

[8] P. S. Ashofteh, O. Bozorg Haddad, H. Akbari-Alashti, and M. A. Mariño, "Determination of irrigation allocation policy under climate change by genetic programming," *Journal of Hydrologic Engineering*, vol. 141, no. 4, Article ID 04014059, 2014.

[9] M. Ehteram, H. Karami, S. F. Mousavi, S. Farzin, A. B. Celeste, and A.-E. Shafie, "Reservoir operation by a new evolutionary algorithm: Kidney algorithm," *Water Resources Management*, vol. 32, no. 14, pp. 4681–4706, 2018.

[10] S. Afkhamifar and A. P. Sarraf, "Prediction of groundwater level in Urmia plain aquifer using hybrid model of wavelet transform-extreme learning machine based on quantum particle swarm optimization," *Watershed Engineering and Management*, vol. 12, no. 2, pp. 351–364, 2020, in Persian.

[11] M. Nouri, "Management of multi-objective and multi-reservoir water resources systems using optimization models in climate change conditions," Ph.D. thesis, Faculty of Civil Engineering, Ferdowsi University of Mashhad, Mashhad, Iran, 2015.

[12] P. S. Ashofteh and O. Bozorg Haddad, "Using GP optimization tools developed for the multi-objective operation of reservoirs in climate change," *Iranian Journal of Soil and Water Research*, vol. 46, no. 3, pp. 415–422, 2015.

[13] S. Mirjalili, S. M. Mirjalili, and A. Lewis, "Grey wolf optimizer," *Advances in Engineering Software*, vol. 69, pp. 46–61, 2014.

[14] R. Karami Mohammadi, M. Mirjalaly, M. Mirtaheri, and M. Nazeryan, "Comparison between uniform deformation method and genetic algorithm for optimizing mechanical properties of dampers," *Earthquakes and Structures*, vol. 1, no. 14, pp. 1–10, 2018.

[15] M. Mirtaheri, S. Sehat, and M. Nazeryan, "Improving the behavior of buckling restrained braces through obtaining optimum steel core length," *Structural Engineering and Mechanics*, vol. 65, no. 4, pp. 401–408, 2018.

Research Article

Seismic Analysis of a Large LNG Tank considering the Effect of Liquid Volume

Yi Zhao ⓘ,^{1,2} Hong-Nan Li,^{1,3} Xing Fu,^{1} Shuocheng Zhang,^{2} and Oya Mercan^{2}

^{1}State Laboratory of Coastal and Offshore Engineering, Dalian University of Technology, Dalian 116023, China
^{2}Department of Civil and Mineral Engineering, University of Toronto, Toronto, ON, Canada M5S 1A4
^{3}School of Civil Engineering, Shenyang Jianzhu University, Shenyang 110168, China

Correspondence should be addressed to Yi Zhao; yz@mail.dlut.edu.cn

Large Liquefied Natural Gas (LNG) tanks are prone to damage during strong earthquakes, and accurate seismic analysis must be performed during the design phase to prevent secondary disasters. However, the seismic analysis of large LNG tanks is associated with high computational requirements, which cannot be satisfied by the calculation efficiency of traditional analytical techniques such as the Coupled Eulerian–Lagrangian (CEL) method. Thus, this paper aims to employ a less computationally demanding algorithm, the Smoothed Particle Hydrodynamics-Finite Element Method (SPH-FEM) algorithm, to simulate large LNG tanks. The seismic response of a 160,000 m^3 LNG prestressed storage tank is evaluated with different liquid depths using the SPH-FEM algorithm, and simulation results are obtained with excellent efficiency and accuracy. In addition, large von Mises stress at the base of the tank indicates that strong earthquakes can severely jeopardize the structural integrity of large LNG tanks. Therefore, the SPH-FEM algorithm provides a feasible approach for the analysis of large liquid tanks in seismic engineering applications.

1. Introduction

Natural gas is a reliable source of energy that is used globally to meet growing energy demands. With the increasing consumption of natural gas over the past few years, Liquefied Natural Gas (LNG) tanks have become a major component of urban infrastructure. As a result, the scale of tank construction has also increased, but this change has been associated with various safety risks. LNG storage tanks have high seismic risks compared to traditional buildings because they can lead to secondary disasters, such as explosions and environmental pollution, that result in significant property damage or loss of life. In addition, LNG tanks are more vulnerable to earthquakes owing to their low redundancy, low ductility, and low energy-dissipating capacity compared to conventional structures [1]. For example, the destruction of an LNG tank during the 1964 Japan earthquake caused fires and explosions that resulted in serious societal losses and pollution. Another example was the 1976 Tangshan earthquake in which the bottom ring of a storage tank

buckled and led to liquid leakage [2]. Thus, it is of paramount importance to investigate the seismic performance of LNG tanks to ensure their structural safety.

To analyze the dynamic performance of large LNG tanks, it is essential to understand fluid–structure interaction (FSI) and dynamic performance of the structure. Different from conventional structures, seismic analysis of liquid storage tanks must account for fluid–structure interaction as a result of inertial earthquake loading and hydrodynamic pressure. The seismic design of storage tanks was initially established on the rigid wall model proposed by Housner [3] in 1957, and many subsequent models have improved on this theory. However, many tanks designed according to this model have suffered damage during earthquakes [2]. Consequently, Veletsos and Yang [4, 5] proposed a single-degree-of-freedom model for a flexible tank wall that assumed that the tank vibrated under a given bending mode. In 1981, Haroun and Housner [6] developed a more realistic model that considered the dynamic interaction of liquid and the tank wall. This method is known as the coupled vibration effect model,

and it divides the liquid into three components: a convection component, a flexible impulsive component, and a rigid impulsive component. In addition, Hu et al. [7] presented a method for mass addition using user subroutines to study the seismic response of a large cylindrical thin-walled storage tank based on the theories of Housner and Veletsos. Liquid mass was added to the solid wall without considering liquid sloshing. Hariri-Ardebili et al. [8] compared the endurance time analysis (ETA) method to the time-history analysis (THA) and incremental dynamic analysis (IDA) method to investigate the seismic performance of a high-rise telecommunication tower. Hadj-Djelloul and Djermane [9] used the three-dimensional finite element technique to study the seismic response of perfect and imperfect elevated water tanks. They also investigated the effect of geometric imperfection on the dynamic performance of elevated water tanks.

Based on applicable theories regarding fluid–structure interaction, since the 1950s, there have been several studies on the dynamic analysis of LNG storage tanks. Hwang [10] investigated the dynamic response of an LNG tank using a combination of Boundary Element Method (BEM) and Finite Element Method (FEM) programs. Wu [11] performed time-history analysis of LNG storage tanks with FEM software and found that deformation of the inner tank was effectively prevented by adding a prestressed concrete wall and an insulating layer. Christovasilis and Whittaker [12] investigated the seismic response of a conventional and isolated vertical cylindrical LNG tank by applying finite element analysis to mechanical models. The results obtained from two numerical models were in good agreement and demonstrated that a mechanical model could be used with confidence for the preliminary analysis and design of conventional and isolated LNG tanks. Sun et al. [13] derived and calculated the dynamic response of base-isolated LNG storage tanks considering soil–structure interaction, the effect of which was proven to be insignificant. Chen et al. [14] investigated the dynamic response of a typical 160,000 m^3 LNG prestressed concrete outer tank under impact loading, and types of impact damage were determined based on dynamic response results including stress, displacement, energy, and critical impact velocity. Li et al. [15] conducted numerical dynamic analysis of LNG storage tanks and concluded that filling the space between the outer and inner tank could improve seismic performance with little effect on the sloshing height. Du [16] adopted the Coupled Eulerian–Lagrangian (CEL) analysis technique in ABAQUS to simulate fluid–structure interaction [17] in LNG tanks, but the CEL method exhibited liquid leakage and low simulation efficiency.

The aforementioned numerical simulation methods are very computationally intensive due to the sheer size of large LNG tanks. Given the recent rise in large LNG tank construction, it is essential to employ a fast analysis method that can simulate the seismic response of LNG tanks in practical engineering applications. Thus, an efficient smoothed particle hydrodynamics-finite element method (SPH-FEM) algorithm [18], which has not been previously applied to large land-based LNG tanks, is proposed in this paper.

SPH-FEM methods retain the advantages of FEM in simulating FSI problems while adopting the advantages of SPH in modeling fluid behaviour.

SPH is suitable for modeling fluid behaviour because it is a mesh-free method that discretizes a liquid field into particles [19]. A kernel function is used to approximate differential equations, and the function value at any point is then expressed by neighboring nodes based on a local approximation. The SPH algorithm can overcome the weakness in mesh-based methods regarding fluid simulation by effectively addressing free surfaces and moving interfaces in addition to large deformation of materials. As a result, after its development by Lucy [20] and Gingold [21] in 1977, the SPH method has been successfully adopted for studies in continuous solid mechanics and fluid mechanics to solve problems related to structural failure, large deformation, and liquid sloshing [22]. Huang et al. [23] verified the feasibility of liquid sloshing analysis using the SPH method by obtaining results that corresponded to theoretical analysis. Liu et al. [24] performed a three-dimensional numerical simulation of free surface liquid sloshing in a prismatic tank subjected to a sinusoidal excitation using the SPH algorithm, and the numerical results exhibited good agreement with experimental data. Shao et al. [25] also presented an improved SPH algorithm to model liquid sloshing dynamics, and the numerical results agreed well with the experimental observations. The SPH algorithm has also been widely applied to simulate embankment flow [26], wave breaking [27], and explosions [28]. Therefore, the SPH algorithm is a versatile analysis method that can be applied to a variety of structural problems, including the fluid component of large LNG tanks.

Coupled with a FEM method for the solid component, an SPH-FEM algorithm greatly improves the calculation accuracy and efficiency for fluid–structure impact problems. The coupled SPH-FEM method was first proposed by Attaway et al. [29] using a master–slave algorithm to account for the contact between FE elements and SPH particles. Kalateh and Koosheh [30] used the SPH-FEM method to simulate the interaction between a convergent-divergent nozzle and cavitating flow, and the results showed that the behaviour of liquid and vapor at the interface matched other numerical and experimental methods. Liang and Chen [31] applied the SPH-FEM method to soil–structure interaction problems during the seismic analysis of a rectangular underground structure, and results indicated that the distribution and magnitude of seismic earth pressure were influenced by the magnitude of soil deformation. Fragassa et al. [32] analyzed the effect of air in FSI problems by coupling FEM and SPH. They concluded that air had little effect on stress prediction, but it had a greater effect on the behaviour of the structure after the initial fluid impact. In this study, the SPH-FEM algorithm provides an accurate and efficient method for the analysis of a large LNG tank under dynamic earthquake loading.

Section 2 of this paper presents an overview of the SPH-FEM methodology. Section 3 verifies the SPH-FEM algorithm by comparing it to the traditional Coupled Eulerian–Lagrangian (CEL) method on the analysis of a cubic water tank under

sinusoidal excitation. Subsequently, Section 4 analyzes the dynamic response of a 160,000 m^3 LNG storage tank under three earthquakes with the same site conditions. Section 5 concludes the study and reiterates the advantages of the SPH-FEM algorithm as an innovative, accurate, and efficient method to simulate large LNG tanks.

2. Methodology

2.1. SPH Theory. The formulation of the SPH method is often divided into two parts: the integral representation of the field function and the particle approximation [33]. The integral representation of the function $f(x)$ in the SPH algorithm begins with the following identity [18]:

$$f(x) = \int_\Omega f(x')\delta(x - x')\mathrm{d}x', \tag{1}$$

where $f(x)$ is a function of the three-dimensional position vector x, and the Dirac delta function is given by the following equation:

$$\delta(x - x') = \begin{cases} 1, & (x = x'), \\ 0, & (x \neq x'). \end{cases} \tag{2}$$

If a smoothing function $W(x - x', h)$ replaces the Delta function kernel $\delta(x - x')$, the integral representation of $f(x)$ can be written as follows:

$$f(x) \approx \int_\Omega f(x')W(x - x', h)\mathrm{d}x', \tag{3}$$

where W is the smoothing kernel function and h is the smoothing length that defines the area of influence of the smoothing kernel function W. The smoothing kernel function W should satisfy the following conditions (see equations (4)–(6)):

(1) The normalization condition states that

$$\int_\Omega W(x - x', h)\mathrm{d}x' = 1. \tag{4}$$

(2) The Delta function property is observed when the smoothing length approaches zero

$$\lim_{h \longrightarrow 0} W(x - x', h) = \delta(x - x'). \tag{5}$$

(3) The compact condition implies that

$$W(x - x', h) = 0, \quad \text{when} |x - x'| > \kappa h, \tag{6}$$

where κ, which is a constant related to the smoothing function of the point at x, defines the effective (nonzero) area of the smoothing function.

The basic governing fluid dynamics equations are based on three fundamental laws of conservation: conservation of mass, momentum, and energy. The governing equations for dynamic fluid flows can be written as a set of partial differential equations using the Lagrangian method; this system of partial differential equations is the famous Navier–Stokes

equations, the governing equations of which are given as follows (see equations (7)–(9)):

(1) The continuity equation:

$$\frac{\mathrm{d}\rho}{\mathrm{d}t} = -\rho \frac{\partial v^\beta}{\partial x^\beta}. \tag{7}$$

(2) The momentum equation:

$$\frac{\mathrm{d}v^\alpha}{\mathrm{d}t} = \frac{1}{\rho} \frac{\partial \sigma^{\alpha\beta}}{\partial x^\beta}. \tag{8}$$

(3) The energy equation:

$$\frac{\mathrm{d}e}{\mathrm{d}t} = \frac{\sigma^{\alpha\beta}}{\rho} \frac{\partial v^\alpha}{\partial x^\beta}. \tag{9}$$

A continuous density particle approximation method is employed to approximate the density. This approximation method is obtained by applying the SPH approximation concept to transform the continuity equation. Different forms of density approximation equations can be obtained by applying different conversions and operations to (7). One such approach is to apply the SPH approximation to the velocity divergence; then, the particle density in (7) can be evaluated in the following form of a gradient:

$$\frac{D\rho_i}{Dt} = \rho_i \sum_{j=1}^{N} \frac{m_j}{\rho_j} v_{ij}^\beta \cdot \frac{\partial W_{ij}}{\partial x_i^\beta}. \tag{10}$$

The particle approximation method for the momentum equation is similar to the abovementioned continuous density method, and some transformations are required. The momentum equation approximation can be derived in differential form based on different transformations. Equation (11) can be obtained using the SPH particle approximation method to transform the gradient term of the momentum equation (equation (8)):

$$\frac{Dv_i^\alpha}{Dt} = \sum_{j=1}^{N} m_j \frac{\sigma_i^{\alpha\beta} + \sigma_j^{\alpha\beta}}{\rho_i \rho_j} \frac{\partial W_{ij}}{\partial x_i^\beta}. \tag{11}$$

There are several approximation expressions of the work performed by pressure; thus, the internal energy calculation for the work performed by pressure has many alternative forms. The following form (12) is the most commonly used:

$$\frac{De_i}{Dt} = \frac{1}{2} \sum_{j=1}^{N} m_j \left(\frac{p_i}{\rho_i^2} + \frac{p_j}{\rho_j^2} \right) v_{ij}^\beta \frac{\partial W_{ij}}{\partial x_i^\beta} + \frac{\mu_i}{2\rho_i} \varepsilon_i^{\alpha\beta} \varepsilon_j^{\alpha\beta}. \tag{12}$$

Time stepping in ABAQUS is explicit and is limited by the Courant Condition as shown below (equation (13)):

$$\Delta t = \min_a \left\{ \frac{0.5l}{(c_s + (2\xi\mu_a/l\rho_a))} \right\}, \tag{13}$$

where c_s is the local speed of sound. The time step used in all simulations is 1.0×10^{-6} s, and the convergence of the simulation is guaranteed [34].

2.2. Coupled SPH-FEM. The main concept in SPH-FEM coupling is centered around the relationship between the two algorithms. In each time step, the velocity and displacement of FEM nodes are transferred to particles. Simultaneously, the coordinate and velocity of particles are transferred to FEM nodes. While particles supply boundary conditions for FEM, FEM maintains the continuity of the particles by preventing the boundary effect [35]. In this study regarding fluid–structure interaction, velocity and displacement fields on the solid–fluid interface are exchanged in order to couple the interaction forces between SPH and FEM. A schematic computation flowchart of the SPH-FEM coupling method is displayed in Figure 1.

3. Example Verification

Compared to the SPH-FEM method, the coupled Eulerian–Lagrangian (CEL) method developed by Du [16] is another analysis technique that is suitable for most fluid–structure interaction problems. Qiu et al. [36] applied the CEL method to large deformation problems in geotechnical engineering such as pile sinking and ship grounding to demonstrate its reliability. Meng et al. [37] used the CEL method to simulate the influence of pile-sinking construction on the soil around the pile under undrained conditions. In this section, a simple example is provided to compare the accuracy and efficiency between the SPH-FEM and the CEL method using ABAQUS software [34].

3.1. Description of the Problem. A cubic water tank is taken as a model and is designed according to the following geometric specifications: the side length is 1 m, the wall thickness is 10 mm, and the liquid height is 0.8 m. The tank model is composed of concrete with the following material properties: density $\rho = 2500 \, \text{kg/m}^3$, Young's modulus $E = 3.25 \times 10^9 \, \text{N/m}^2$, and Poisson's ratio $U = 0.3$. The behavior of a material experiencing liquid sloshing is extremely complex, and an equation of state is used to describe the pressure, volume, and energy of the material. The Newtonian fluid constitutive material formulation is used for water in this section, and the Mie–Grüneisen equation of state, which describes the volumetric strength and density of a material, is defined in Table 1. The isotropic pressure in the Mie–Grüneisen equation of state is defined as follows:

$$\begin{cases} p(\rho, e) = \left(1 - \frac{1}{2}\Gamma_0\eta\right)P_H + \Gamma_0\rho_0 E_m, \\ \\ p_H = \frac{\rho_0 c^2 \eta}{(1 - s\eta)^2}, \\ \\ \eta = \frac{\rho}{\rho_0} - 1, \end{cases} \tag{14}$$

where H is the Hugoniot curve, E_m is the internal energy per unit mass, η is the volumetric compressibility, and c is the sonic speed of the material. The coefficients s and c can be
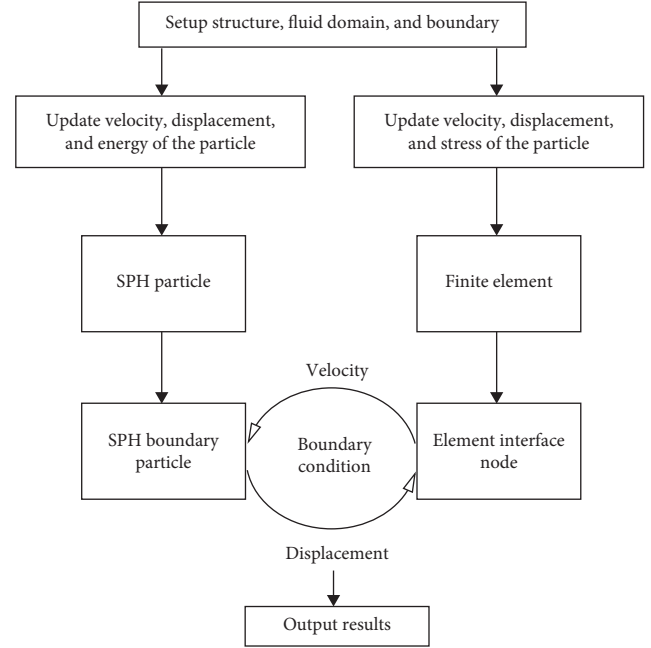
Figure 1: Computation flowchart of the SPH-FEM coupling method.

described by the linear relationship between shock velocity and particle velocity:

$$U_s = c + sU_p, \tag{15}$$

where U_s is shock wave velocity and U_P is particle velocity. This equation of state describes the fluid motion.

The equation of state of $U_s - U_p$ provides a model for the hydrodynamic material, and the properties of water are listed in Table 1.

The water-filled models constructed based on the two algorithms are shown in Figures 2 and 3. The models both use 1600 C3D8R-type concrete elements, and the SPH-FEM algorithm model uses 22000 PC3D-type liquid elements. In the SPH-FEM algorithm, the ratio of liquid element size to the side length of the container is 5:270. The SPH method also uses a cubic spline as the interpolation polynomial. Smoothing length is an important parameter and has significant influence on the accuracy of the prediction [38, 39]. By default, ABAQUS calculates a smoothing length at the start of the analysis so that an element is associated with approximate 30 to 50 particles on average. Since the smoothing length remains constant throughout the analysis, depending on whether the behavior in the model is expansive or compressive, the average number of particles per element can either decrease or increase [34]. In the CEL model, a total of 80,000 EC3D8R-type liquid elements are used, including 20,000 elements in the initial position. The Eulerian elements in the CEL method must be finely meshed over the entire tank trajectory and allow liquid to move freely in the grid, because the quantity and quality of the mesh affects simulation accuracy. Gravity is applied to the entire model ($g = 9.8 \, \text{m/s}^2$), and the tank is subjected to a horizontal excitation given by $v(t) = \sin(wt)$.

TABLE 1: Material properties of water.

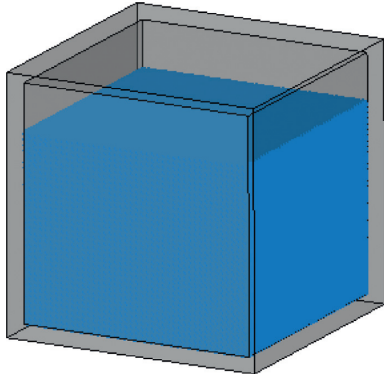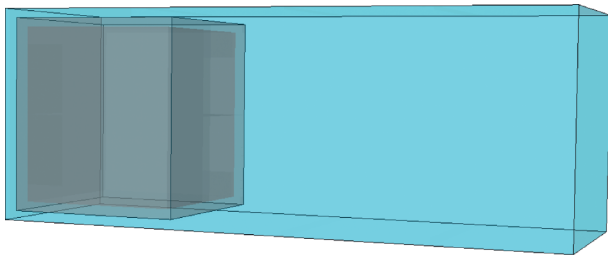| Material	Density (kg/m^3)	Sonic speed (m/s)	Dynamic viscosity (kg/(m·s))	Coefficients of the equation of state	
				s	Γ_0
Water	1000	1480	0.001	0	0

FIGURE 2: Model for the SPH-FEM algorithm.

FIGURE 3: Model for the CEL method.

3.2. Comparison of Results between the SPH-FEM and CEL Method. The results of the two algorithms during one period are compared based on three factors: sloshing wave pattern, stress distribution on container wall, and computational efficiency. Both methods can accurately reflect the sloshing wave pattern (as shown in Figure 4), but the CEL method exhibits liquid leakage, especially at the bottom of the water tank. The CEL method is also not applicable when the liquid volume fraction in the Eulerian element is less than 0.5, because some elements are no longer contained within the container wall [34].

Using the two algorithms, the von Mises stress distribution on the container wall at 0.8 s and 1.6 s in one period is shown in Figure 5. The maximum von Mises stress and the von Mises stress distribution on the walls calculated using the two methods are in good agreement. Thus, the liquid element size in the SPH-FEM method can be scaled up based on an optimal ratio of 5 : 270 and applied to a large LNG tank while maintaining calculation accuracy.

As shown in Table 2, the simulation time for the CEL method is twice that of the SPH-FEM method, indicating that the SPH-FEM algorithm is much more efficient than the CEL method. In summary, both methods can accurately simulate stress on tank walls and the liquid sloshing pattern,

but the CEL method exhibits liquid leakage. Fluid leakage is a common problem in CEL method and has not been solved so far. Therefore, the SPH-FEM method has a significant advantage over CEL in the analysis of large liquid storage tanks.

4. Seismic Analysis of a 160,000 m^3 LNG Tank

4.1. Project Overview. This study employed a 160,000 m^3 LNG prestressed storage tank, which was adapted from an LNG technical manual as shown in Figure 6 [40]. The inner diameter of the outer tank is 82 m, the wall height is 38.55 m, the wall thickness is 0.8 m, and the dome thickness is 0.4 m. The tank also has components to secure the moisture-proof linings and roof-bearing rings.

The inner tank has a total of 10 layers as shown in Figure 6, each of which has a height of 3.55 m. For example, Layer R1/24.9 refers to the first layer from the bottom with a thickness of 24.9 mm. These layers gradually thicken from the top to the bottom as given in Table 3.

The LNG storage tank consists of four parts: LNG, an inner tank, an insulation layer, and an outer tank. The inner tank is composed of 9% Ni steel. The tank exhibits excellent low-temperature resistance [41, 42]. The tank is also characterized by good weldability and low susceptibility to cold cracks. The insulation layer is composed of expanded perlite and resilient felt. The expanded perlite clings to the inner wall of the outer tank, and the outer wall of the inner tank is fitted with resilient felt, which prevents the perlite from settling and provides elastic properties for the perlite. This elasticity is necessary because the tank shrinks due to temperature changes. The prestressed concrete external tanks are constructed to increase the overall safety of the tank in the event of accidental LNG leakage. Adapting to the advice of Huang [43], the material of the outer tank is 60 MPa high-strength concrete. The material characteristics of the tank and LNG are listed in Tables 4 and 5, respectively.

4.2. Finite Element Model. ABAQUS software [44, 45] is used to establish the finite element model (FEM) as shown in Figure 7. The tank model is relatively large, and the associated interactions are extremely complex. Rebar rods are embedded within the tank wall using the "Embedded" option in ABAQUS, which allows the rebar elements to work in conjunction with each other. The outer tank and the insulation layer are composed of C3D8R mesh elements, and the inner tank is composed of S4R shell elements. Shell elements are selected because the thickness of the inner tank is much smaller than its radius of curvature. The LNG is discretized into particles using the aforementioned $U_s - U_p$
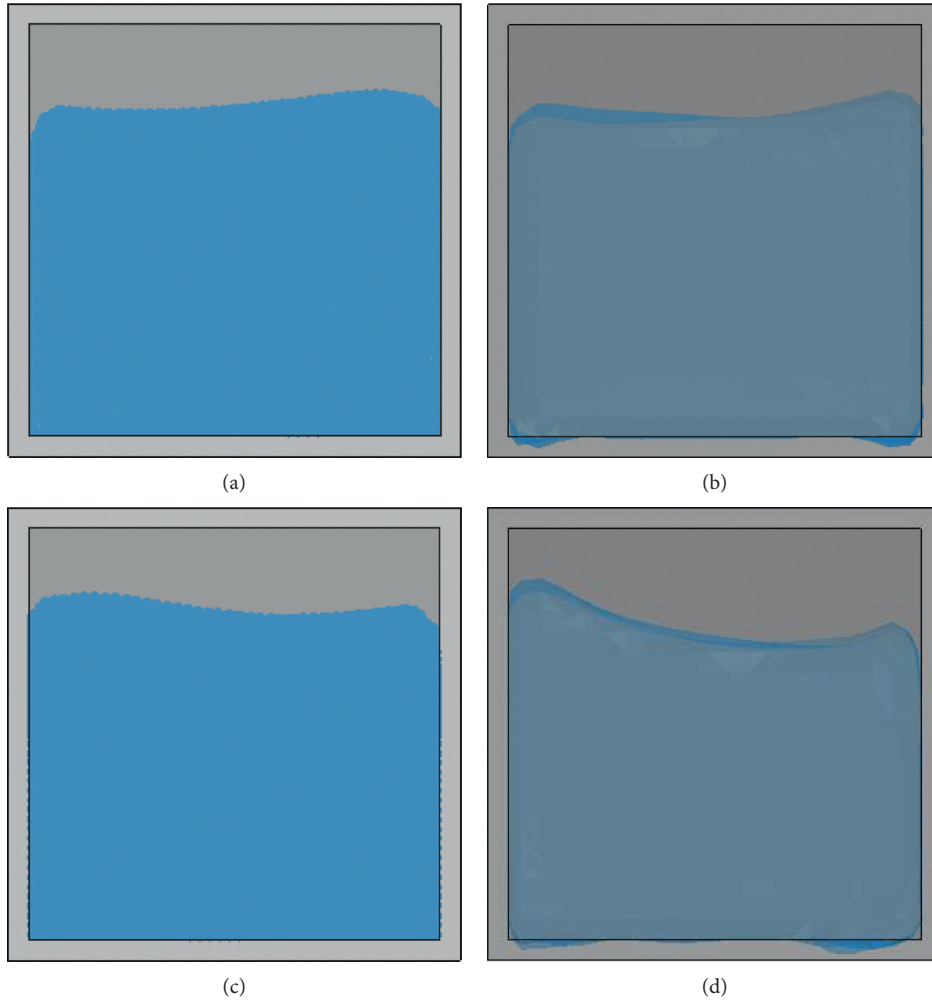
FiGURE 4: Comparison of the sloshing pattern between the two algorithms. (a) At 0.8 s with the SPH-FEM algorithm, (b) at 0.8 s with the CEL method, (c) at 1.6 s with the SPH-FEM algorithm, and (d) at 1.6 s with the CEL method.
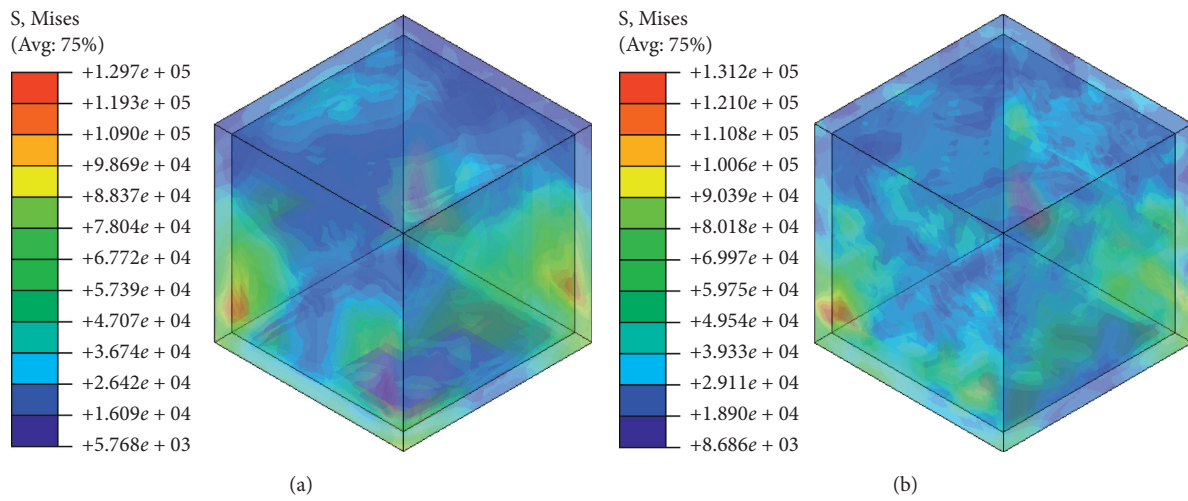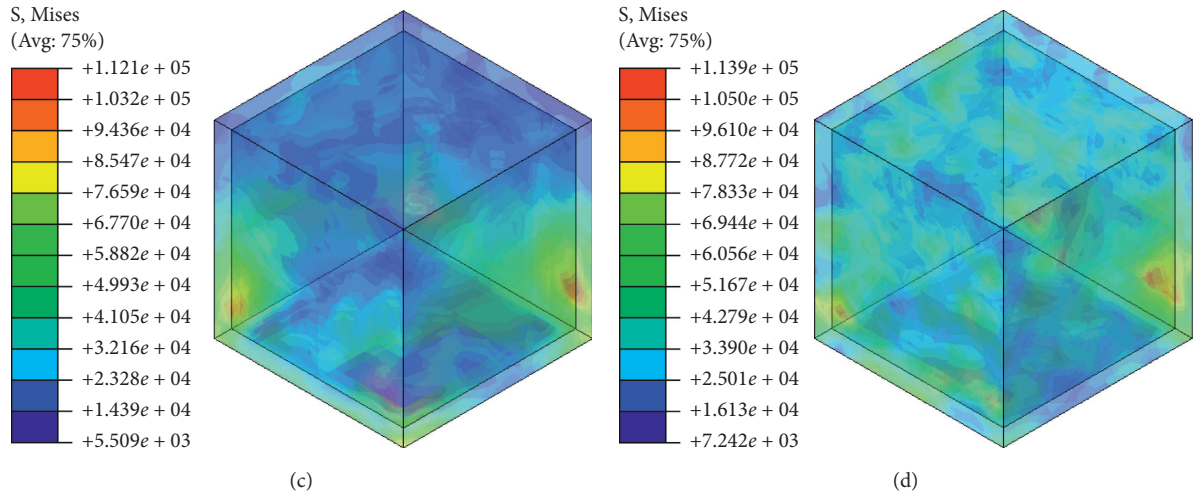

FiGURE 5: Continued.

FIGURE 5: Comparison of the von Mises stress on the walls between the two algorithms. (a) At 0.8 s with the SPH-FEM algorithm, (b) at 0.8 s with the CEL method, (c) at 1.6 s with the SPH-FEM algorithm, and (d) at 1.6 s with the CEL method.

TABLE 2: Comparison of the computational efficiencies of the two algorithms.

Analysis time (s)	Algorithm	Simulation time	Stable time step (s)
10	SPH-FEM	4 h 52 min 13 s	0.0165
	CEL	8 h 58 min 14 s	0.0274
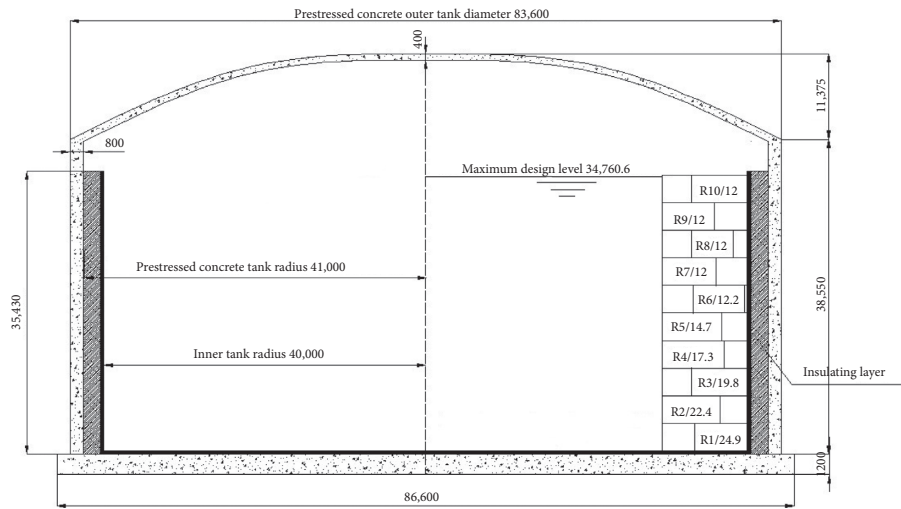
FIGURE 6: LNG storage tank cross section (unit: mm).

TABLE 3: Thickness of each layer in the inner tank.

Layer	1	2	3	4	5	6	7	8	9	10
Thickness (mm)	24.9	22.4	19.8	17.3	14.7	12.2	12	12	12	12

equation in Section 3. The element size is chosen based on the small tank in Section 3 for which the sloshing frequency can be accurately calculated. The ratio of liquid element size to container size in the large LNG tank is identical to the parameters of the small tank in Section 3.

19T15S steel cables with a tensile strength of 1860 MPa are embedded in the protective cover of the tank. A total of 122 steel cables are vertically anchored at the bottom and top of the concrete wall, and 220 circumferential steel cables are anchored in separate half-circles on four vertical supporting columns arranged at 90° [40].

The basic principles of applying prestress in ABAQUS [44] include various approaches, such as the model predictive control (MPC) method, falling temperature method, initial stress method, and single rebar element method. This study adopts the commonly utilized falling temperature

TABLE 4: Material characteristics of the LNG prestressed storage tank.

Parameter/material	Density (kg/m³)	Modulus of elasticity (MPa)	Poisson's ratio	Yield strength (MPa)
Prestressed concrete	2500	3.6×10^{10}	0.2	—
Expanded perlite	56	11.25	0.15	—
Resilient felt	300	800	0.12	—
Rebar HRB400	7800	2×10^{11}	0.3	400
Steel cable	7800	1.95×10^{11}	0.3	1860
9% Ni steel	7850	2.06×10^{11}	0.3	600

TABLE 5: Material properties of LNG.

Material	Density (kg/m³)	Sonic speed (m/s)	Dynamic viscosity (kg/(m·s))	Coefficients of the equation of state	
				s	Γ_0
LNG (liquid)	480	1500	0.00113	0	0

(a)

(b)
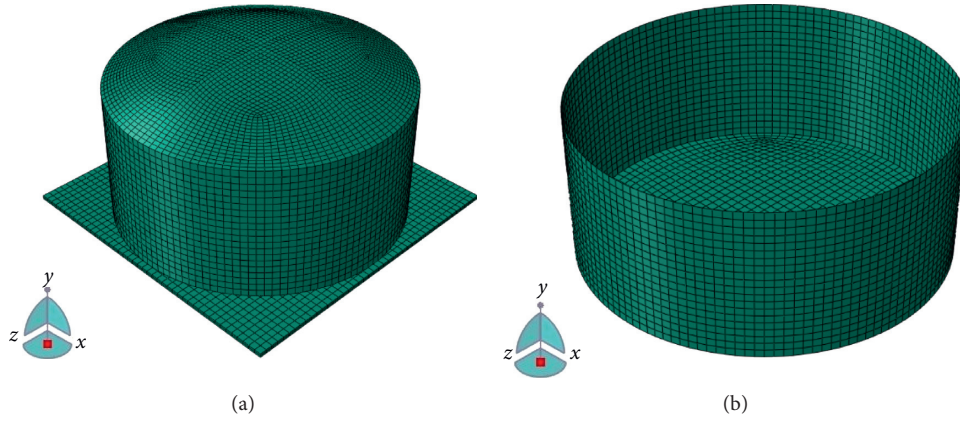
FIGURE 7: FEM of the LNG storage tank. (a) The outer tank. (b) The inner tank.

method that applies prestress by decreasing temperature. The initial temperature is obtained with the following formula:

$$\Delta T = \frac{N}{\lambda \times E \times A}, \quad (16)$$

where N is the tension control force of the prestressed rebar, which should not exceed 75% of the standard value of the strength; λ denotes the thermal expansion coefficient of prestressed rebar; E represents the elastic modulus of prestressed rebar; and A is the cross-sectional area of prestressed rebar.

The bottom boundary of the model is fixed, and the interaction between soil and structure is not considered. The static condition of the LNG tank is primarily calculated based on self-weight to ensure that the LNG liquid reaches steady state. Natural frequencies are important parameters in the design of LNG prestressed storage tanks. There are three primary ways to extract eigenvalues in ABAQUS: the AMS eigensolver, the subspace iteration method, and the block Lanczos algorithm. Here, the first five frequencies of the empty tank are calculated with the Lanczos algorithm as 3.753 Hz, 4.902 Hz, 5.088 Hz, 5.097 Hz, and 5.204 Hz.

4.3. Records Selection. In China, seismic codes for large LNG storage tanks are based on the seismic codes of building structures [46] with specifications for the design of large oil storage tanks. The normative theoretical model is developed from the Housner rigid two-particle theoretical model considering the influence of the elastic tank wall. In addition, Chinese seismic codes classify design objectives into three tiers based on the degree of damage. The design of large LNG tanks belongs to the second tier meaning repairable damage without collapse. Furthermore, the Chinese seismic code divides seismic sites into four classes based on soil stability, shear wave velocity, and thickness of overburden. Soil strength ranges from strongest to weakest from Class I to Class IV with Class I having the strongest soil. In this paper, the large LNG tank is located in a Class II site. Based on guidelines for seismic wave selection [46], three waves are selected and scaled to ensure compatibility with the design spectrum at the chosen site. The details for three ground motions are shown in Table 6, and the acceleration response spectra for ground motions as well as the code acceleration response spectra are shown in Figure 8.

Table 6: Details of the 3 ground motions employed in this study.

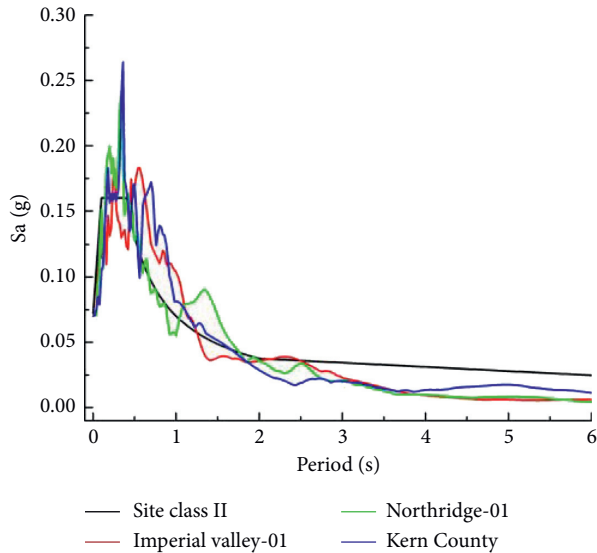| Event	Station	Time
Imperial Valley-01	El Centro Array #9	1940.5.18
Northridge-01	Northridge-Saticoy	1994.1.17
Kern County, California	Taft Lincoln School Tunnel	1994.1.17

Figure 8: Acceleration response spectra of selected ground motions and of code specifications.

4.4. Results. The entire simulation using the SPH-FEM algorithm is conducted using an ordinary personal computer. The processor is an Intel® Core™ i7-8700 CPU @ 4.10 GHz, and the installation memory is 16.00 GB. The von Mises stress distribution of the inner tank alone under hydrostatic conditions at different LNG liquid levels, without the effect of insulation layer and outer tank, is shown in Figure 9.

Among the three seismic waves, Taft produces the greatest von Mises stress on the outer and inner tank at different LNG liquid levels. Therefore, Taft is chosen as the critical wave for this analysis. The stress distribution on the outer tank exhibits a symmetrical trend about the *x*- and *z*-axes. Figure 10 shows the respective maximum stress of the outer tanks with LNG levels of 25%, 50%, 75%, and 100% at the instant corresponding to peak displacement. When the tank is 100% filled with LNG, the maximum stress of the outer tank is 51.35 MPa, which is less than the compressive strength of concrete; thus, the structure is safe. In addition, the maximum stress of the outer tank is located at the dome for liquid levels of 25% and 50%, but it is located at the bottom of the tank for liquid levels of 75% and 100%. This phenomenon occurs because gravity plays a more important role than pressure with LNG liquid levels of 25% and 50%. However, as liquid level increases, pressure at the bottom of the tank increases at a much faster rate relative to the dome. Furthermore, while the maximum stress of the outer tank is nearly identical at 25%, 50%, and 75%, it increases significantly from 75% to 100% liquid level. In general, close attention should be paid to the dome and the bottom of the

tank during the design of large LNG tanks to ensure structural safety.

The respective maximum stress of the inner tank with LNG liquid levels of 25%, 50%, 75%, and 100% is shown in Figure 11. The fact that dynamic conditions generate much greater stress than static conditions deems dynamic analysis critical for LNG tanks. When the tank is 100% full, the maximum stress of the inner tank exceeds 500 MPa and jeopardizes the safety of the structure considering that the yield strength of 9% Ni steel is between 500 MPa and 600 MPa [47]. Due to the severity of consequences after large LNG tank failure, it is imperative to reduce the stress of the inner tank to ensure its safety. At the same time, an early warning system should be implemented to control the maximum liquid level. Different from the outer tank, the stress of the inner tank changes significantly with the liquid level. When the liquid level is at 25% and 50%, maximum stress of the inner tank is below 300 MPa. At a liquid level of 75% and 100%, maximum stress exceeds 300 MPa and 500 MPa, respectively. With an increase in the amount of LNG, the stress at the base of the inner tank gradually increases to notable levels. Therefore, more attention should be paid to the control of liquid level in the dynamic analysis and seismic design of large LNG storage tanks.

According to postprocessing results, three representative paths, as shown in Figure 12, are selected to analyze the variations of the von Mises stress with the height of the tank. Stress distributions on the outer and inner tanks with respect to height at different liquid levels are illustrated in Figures 13 and 14, respectively. It can be observed that the stress distribution on the outer tank changes more gradually compared to that of the inner tank.

In addition, stress values along different paths are different for a given liquid depth, but the overall trends are the same. When the liquid level is less than 50%, the stress on the outer tank first increases and then decreases with an increase in height. When the liquid level exceeds 50%, the stress on the outer tank initially decreases, then increases, and decreases again. Moreover, stress in the lower portion of the tank is much larger than stress in the upper portion when the liquid level is greater than 50%. In addition, a greater LNG liquid volume leads to greater stored energy and greater stress at the base of the tank as shown in Figures 13 and 14. In reality, the bottom of an LNG tank is prone to buckling failure during a strong earthquake, which is consistent with the stress analysis results.

When comparing outer and inner tanks, it is observed that different liquid amounts can produce similar stress levels at a height of approximately 10 m. For the outer tank, the height that correspond to this stress level gradually decreases from Path A to Path C. In contrast, for the inner tank, the height that corresponds to this stress level is nearly identical across all paths.

The displacements of the highest point on the outer wall of the tank filled with 25%, 50%, 75%, and 100% LNG are shown in Figure 15. In a Class II site, the displacements for all three seismic waves are within the same range. For the same seismic wave, variations in displacement with respect to time are nearly identical for each liquid volume. In
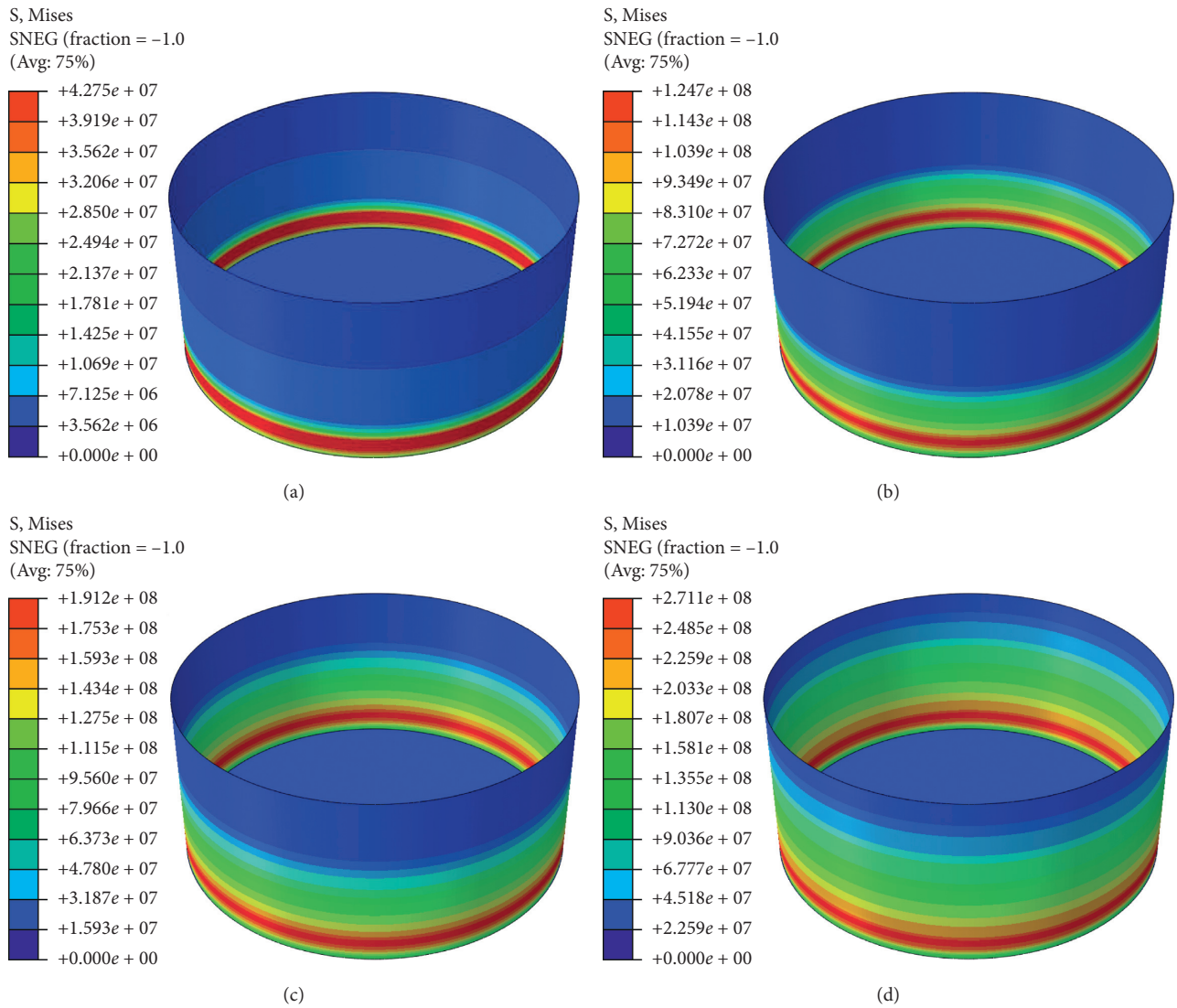
(a)

(b)

(c)

(d)

Figure 9: Distribution of von Mises stress distribution on the inner tank under static conditions at different LNG liquid levels. (a) At 25% full, (b) at 50% full, (c) at 75% full, and (d) at 100% full.
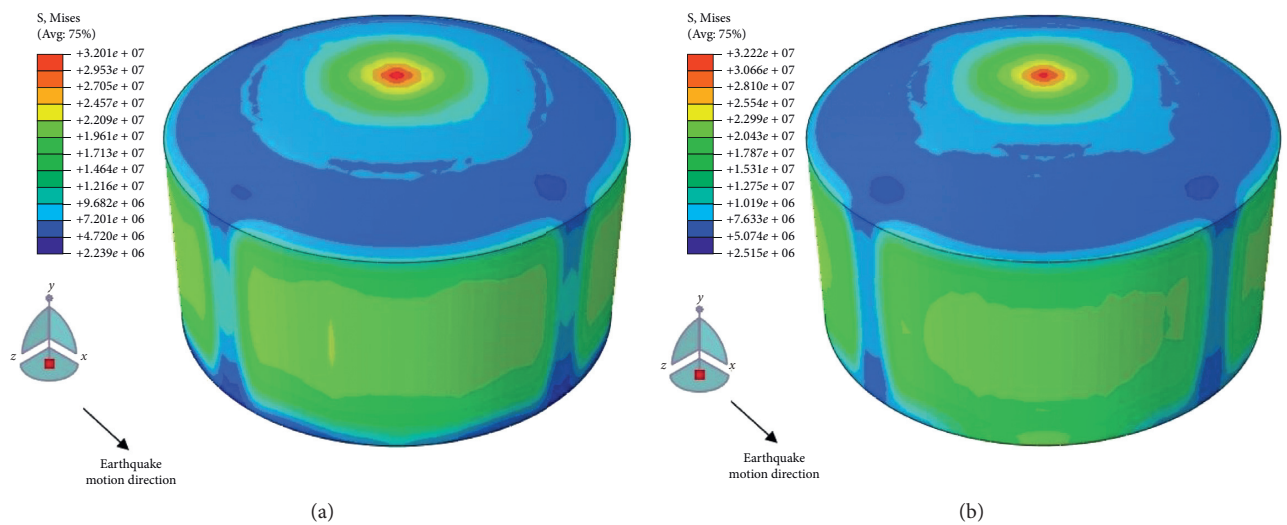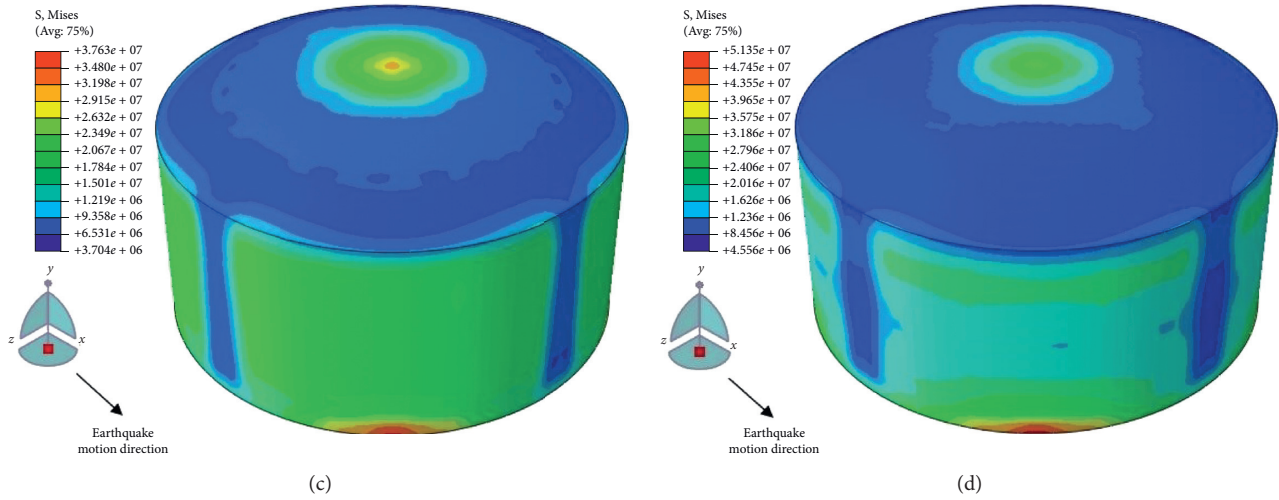

(a)

(b)

Figure 10: Continued.

FIGURE 10: The maximum von Mises stress distribution of the outer tank at different LNG liquid levels. (a) At 25% full, (b) at 50% full, (c) at 75% full, and (d) at 100% full.
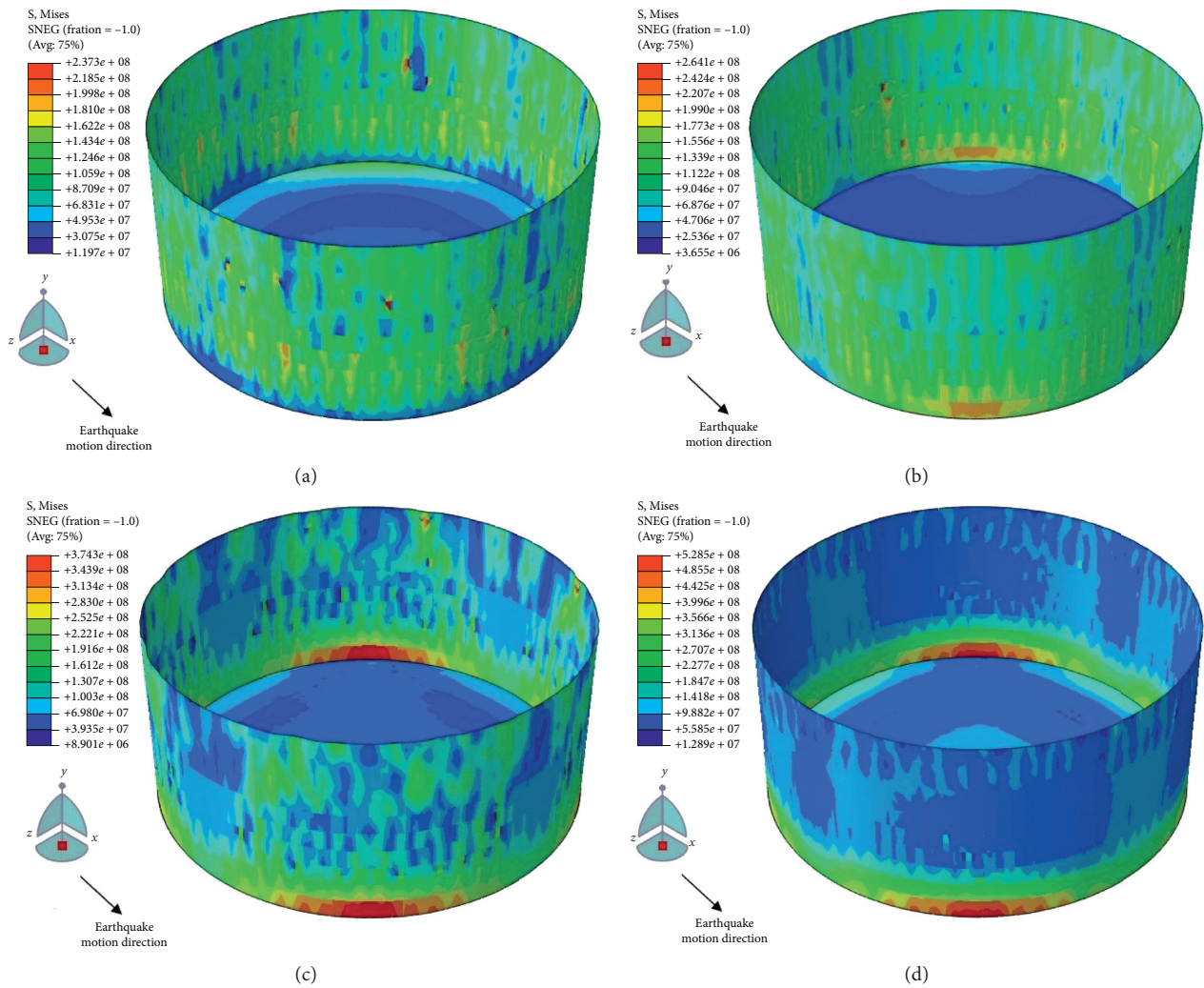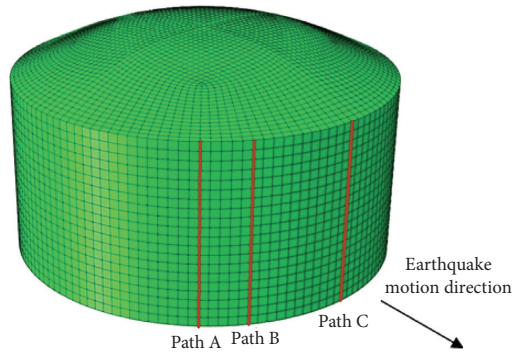

FIGURE 11: The maximum von Mises stress distribution of the inner tank under different LNG liquid levels. (a) At 25% full, (b) at 50% full, (c) at 75% full, and (d) at 100% full.

FIGURE 12: Three representative paths selected to analyze the von Mises stress distribution along the tank wall: A, B, and C.

(a)

(b)

(c)
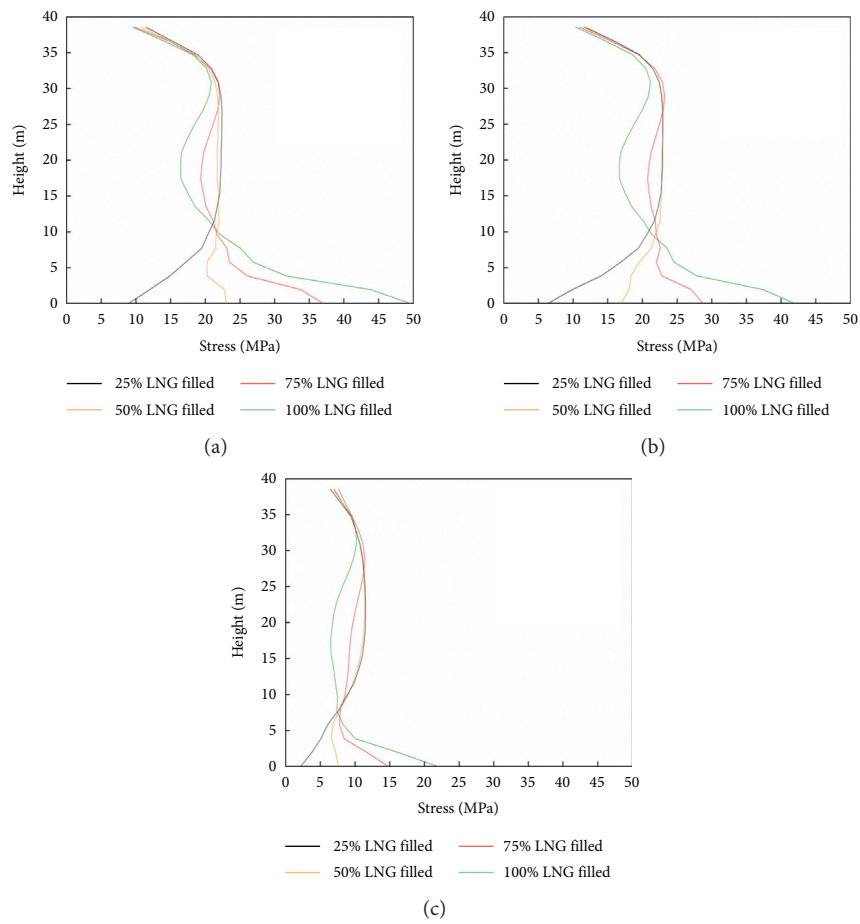
FIGURE 13: Distribution of the von Mises stress on the outer tank with height along different paths. (a) Path A. (b) Path B. (c) Path C.

addition, the location for peak displacement nearly coincides with the peak seismic wave acceleration. The maximum displacement only reaches 4.16 mm when the tank is filled with 100% LNG, and the seismic performance of the LNG tank is satisfactory based on this displacement calculation.

Figure 16 illustrates that the base shear values of the tank are in the same range under different seismic waves for each liquid volume. For the same seismic wave, variations in base shear with respect to time as well as peak base shear forces follow the same general trend for each liquid volume. The maximum base shear reaches 7.99^*10^4 kN when the tank is filled with 100% LNG under the Taft wave; the minimum base shear is 5.28^*10^4 kN when the tank is filled with 25% LNG under the Taft wave. These values demonstrate that the base shear of a LNG storage tank is dependent on the liquid level in the tank.
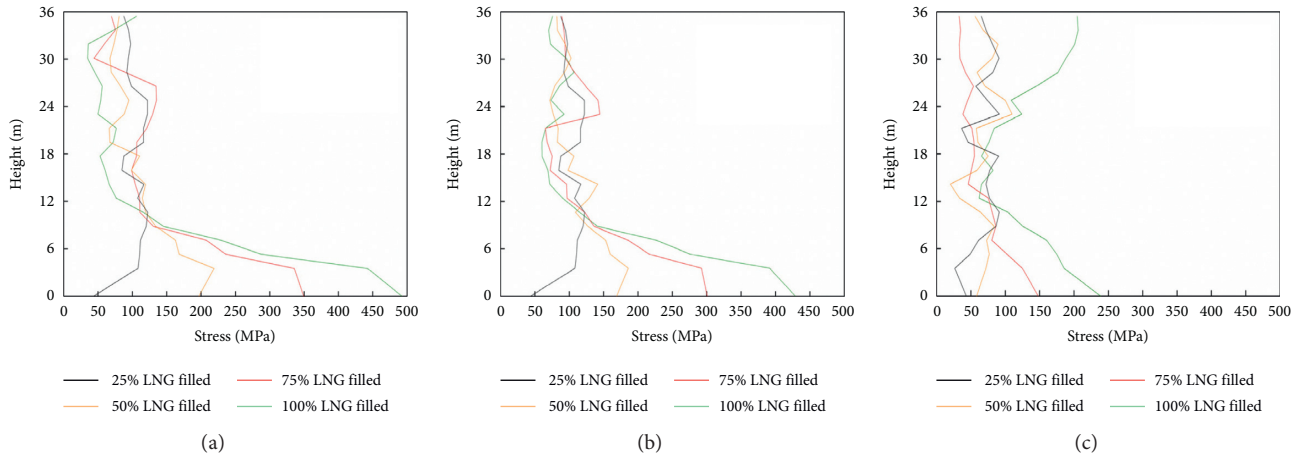
FIGURE 14: Distribution of von Mises stress on inner tank with respect to height along different paths. (a) Path A. (b) Path B. (c) Path C.
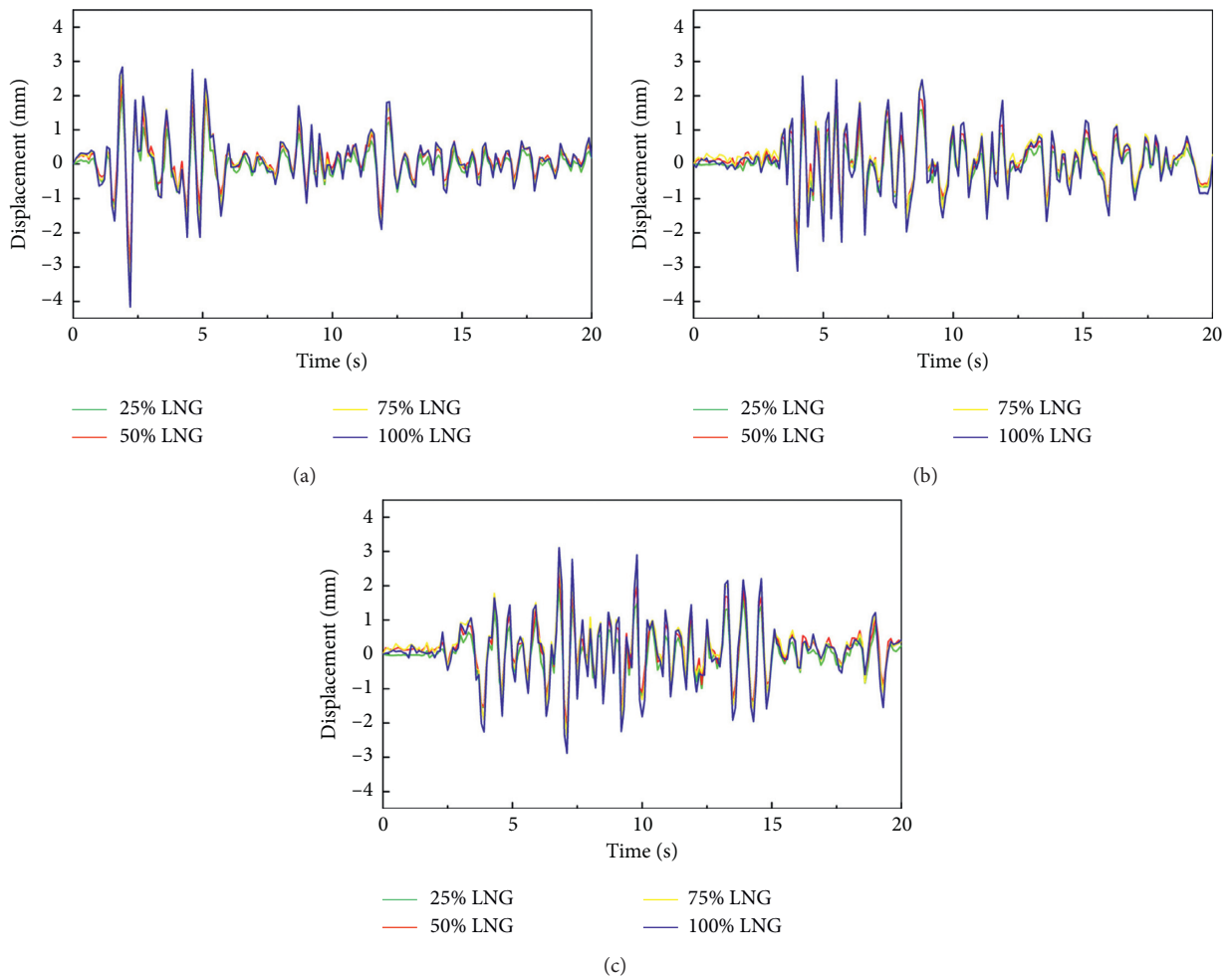
FIGURE 15: Tip displacement of the outer wall under different liquid volume. (a) El Centro, (b) Northridge, and (c) Taft.

4.5. Validation. To verify the SPH-FEM simulation results under earthquake loading, they are compared with CEL simulation results in terms of tip displacements and base shear. The maximum tip displacement and the maximum

base shear using the SPH-FEM and CEL method under El Centro, Taft, and Northridge seismic waves are shown in Figures 17 and 18. The tip displacement of the outer wall and the maximum base shear calculated using the two algorithms

(a)

(b)

(c)
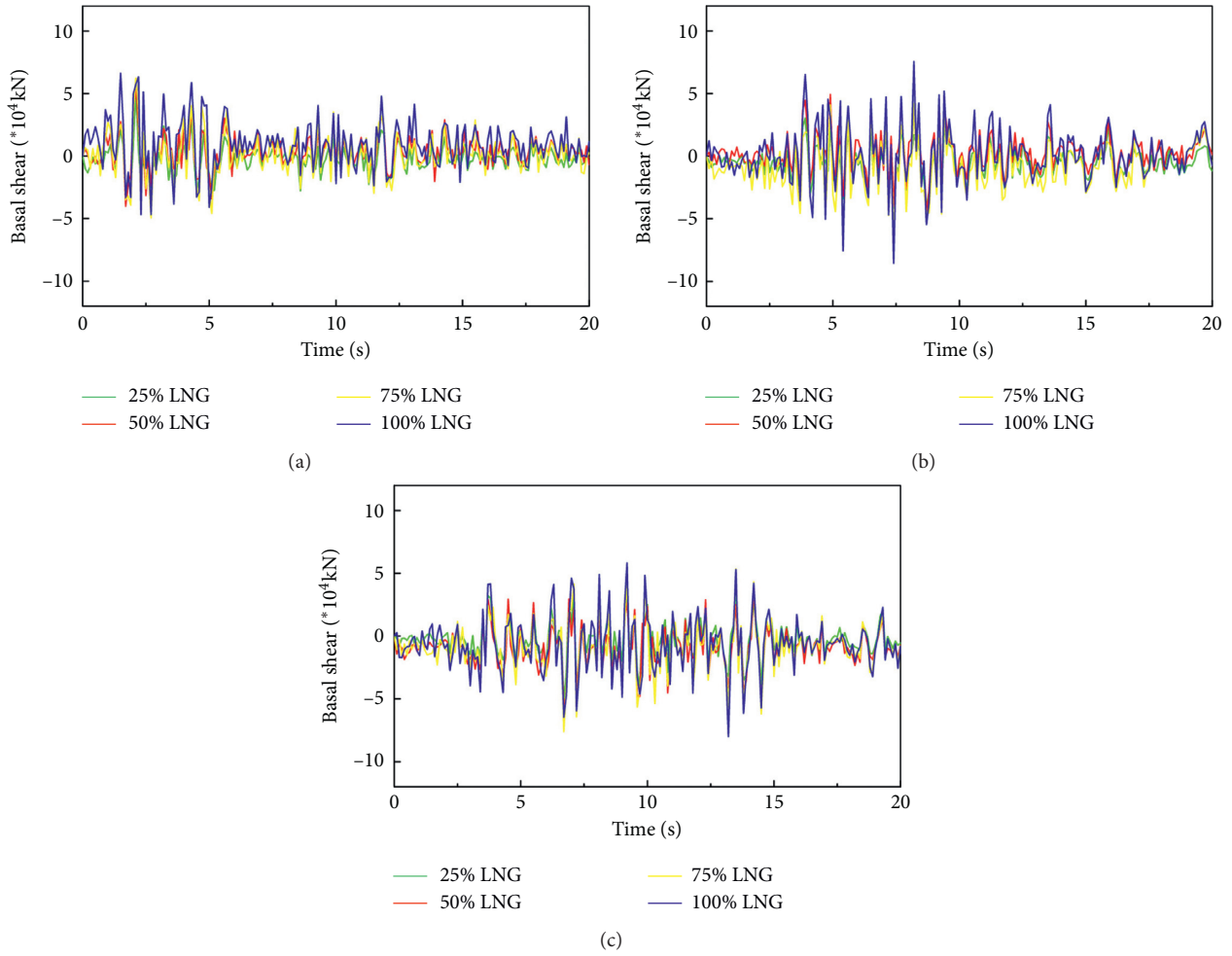
Figure 16: Base shear of the tank under different liquid volume. (a) El Centro, (b) Northridge, and (c) Taft.

(a)

(b)
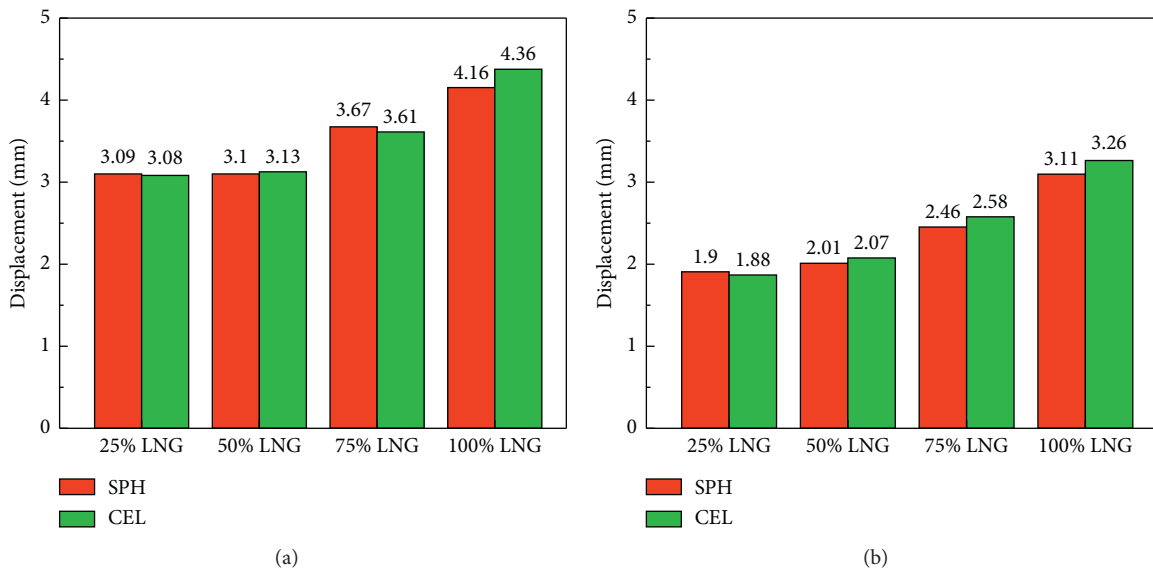
Figure 17: Continued.
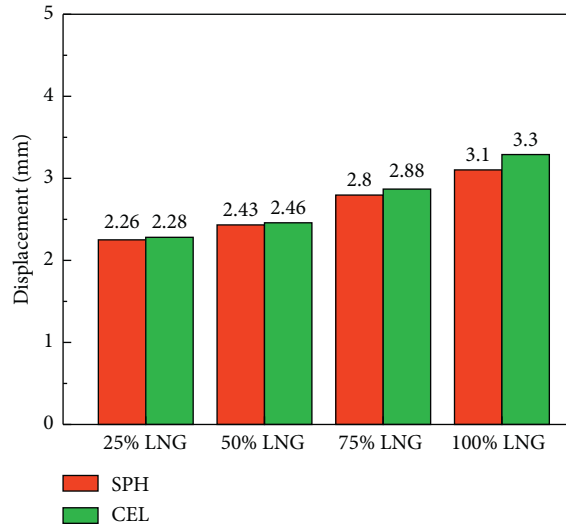
(c)

FIGURE 17: Comparison of the maximum tip displacement of the outer wall under different liquid volume between the two algorithms. (a) El Centro, (b) Northridge, and (c) Taft.
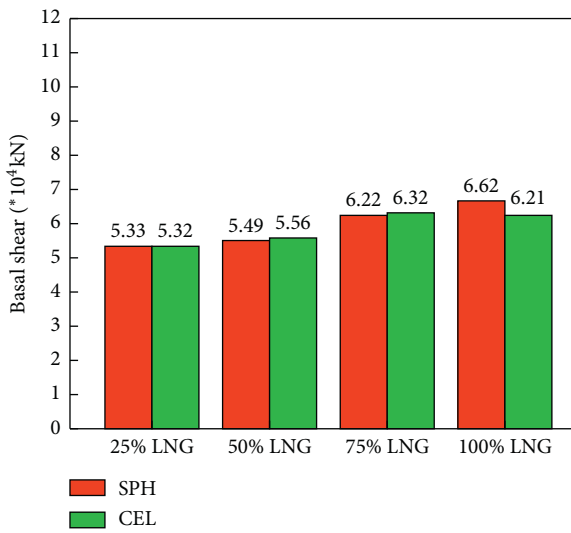
(a)
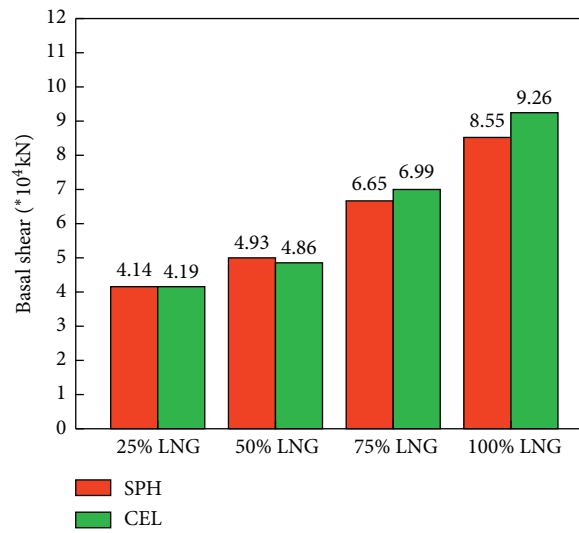
(b)

FIGURE 18: Continued.

(c)
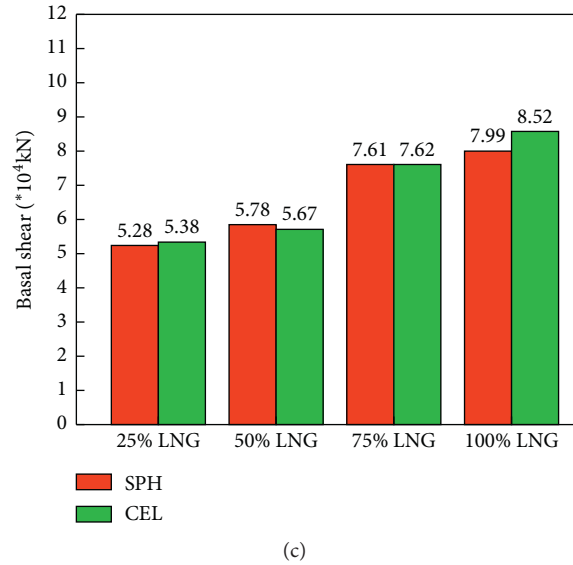
FIGURE 18: Comparison of the maximum base shear under different liquid volume between the two algorithms. (a) El Centro, (b) Northridge, and (c) Taft.

are in good agreement. Therefore, the feasibility of using the SPH-FEM algorithm for the seismic analysis of large LNG tanks is verified.

5. Summary and Conclusions

In this study, the SPH-FEM method is compared with the CEL method to demonstrate the advantage of SPH-FEM in terms of efficiency and accuracy. Then, the SPH-FEM algorithm is used to analyze the dynamic response of a $160{,}000\,\mathrm{m}^3$ LNG prestressed storage tank subjected to three earthquake waves in a Class II site. The main conclusions drawn from the numerical simulations can be summarized as follows:

(1) Under static conditions, the von Mises stress increases at a linear rate with an increasing liquid volume. Under dynamic conditions, the von Mises stress increases at a nonlinear rate.

(2) The stresses produced on the outer and inner tanks under earthquake loading are very similar at a height of approximately 10 m for each liquid volume. The maximum tip displacement of the outer tank is 4.16 mm, and the maximum base shear is 7.99^*10^4 kN.

(3) The maximum stress of the inner tank with 100% LNG liquid level exceeds 500 MPa under the chosen seismic waves and raises concerns for its structural safety. Development of an improved structural system and a warning mechanism is of paramount importance to the design of LNG tanks at high liquid levels.

(4) The SPH-FEM algorithm is accurate and more efficient than the CEL method. Moreover, the SPH-FEM algorithm exhibits excellent capability for simulating large storage tanks under a reasonable time to provide

a reference for the design and construction of large LNG tanks.

The largest LNG prestressed storage tank in China is currently $200{,}000\,\mathrm{m}^3$. The sheer size of the tank requires a significant amount of meshing during seismic simulation, which is almost impossible to accomplish on an ordinary computer using a mesh-based method. The SPH-FEM algorithm provides a feasible method to simulate extremely large LNG tanks on a personal computer, which can help designers obtain its seismic performance in an acceptable time range without significant reliance on hardware capabilities. Ongoing work is being performed to optimize the design of large LNG tanks under different earthquakes using the SPH-FEM algorithm and will be reported at a later time.

Nomenclature

Ω: Domain of integration
$W(x)$:   Kernel function
h: Smoothing length
ρ: Density, kg/ m^3
Δt: Time step size
N: Number of particles
g: Gravitational acceleration
m: Mass of particle
c_s: Local speed of sound
E_m: Internal energy per unit mass
η: Volumetric compressibility
σ: Stress
v: Velocity
α: Direction of coordinates
β: Direction of coordinates
U: Poisson's ratio
ξ: Small positive number
i: The ith component of a vector

j: The jth component of a vector.

Data Availability

Disclosure

Conflicts of Interest

Acknowledgments

References

[1] J. Jia, *Modern Earthquake Engineering: Offshore and Land-Based Structures*, Springer, Berlin, Germany, 2016.

[2] J. G. Sun, *Isolation of Large Vertical Storage Tanks: Theory, Methods and Test*, Science Press, Beijing, China, 2009.

[3] G. W. Housner, "Dynamic pressures on accelerated fluid containers," *Bulletin of the Seismological Society of America*, vol. 47, no. 1, 1957.

[4] A. Veletsos, "Seismic effects in flexible liquid storage tanks," in *Proceedings of the 5th World Conference on Earthquake Engineering*, Rome, Italy, June 1974.

[5] A. Veletsos and J. Yang, "Dynamics of fixed-base liquid storage tanks," in *Proceedings of the US–Japan Seminar for Earthquake Engineering Research with Emphasis on Lifeline Systems*, Tokyo, Japan, 1976.

[6] M. A. Haroun and G. W. Housner, "Dynamic interaction of liquid storage tanks and foundation soil," *Dynamic Response of Structures: Experimentation, Observation, Prediction and Control*, American Society of Civil Engineers, New York, NY, USA, 1981.

[7] Y. H. Hu, Z. Zhuang, and X. C. You, "Added mass approach to a large-scale liquid storage tank under seismic excitations," in *Proceedings of the Beijing Society of Theoretical and Applied Mechanics Annual Meeting*, Beijing China, June 2010.

[8] M. A. Hariri-Ardebili, H. Rahmani-Samani, and M. Mirtaheri, "Seismic stability assessment of a high-rise concrete tower utilizing endurance time analysis," *International Journal of Structural Stability and Dynamics*, vol. 14, no. 6, Article ID 1450016, 2014.

[9] N. D. H. Djelloul and M. Djermane, "Effect of geometric imperfection on the dynamic of elevated water tanks," *Civil Engineering Journal*, vol. 6, no. 1, 2020.

[10] I.-T. Hwang and K. Ting, "Boundary element method for fluid-structure interaction problems in liquid storage tanks," *Journal of Pressure Vessel Technology*, vol. 111, no. 4, pp. 435–440, 1989.

[11] L. Wu, *Comparative Research Analysis of the Effect of Earthquake on LNG Tank*, Harbin Engineering University, Harbin, China, 2013.

[12] I. P. Christovasilis and A. S. Whittaker, "Seismic analysis of conventional and isolated LNG tanks using mechanical analogs," *Earthquake Spectra*, vol. 24, no. 3, pp. 599–616, 2008.

[13] J. Sun, L. Cui, X. Li, Z. Wang, W. Liu, and Y. Lv, "Design theory and method of LNG isolation," *Earthquakes and Structures*, vol. 16, no. 1, pp. 1–9, 2019.

[14] Y. Chen, X. Zhai, and Y. Wang, "Numerical study on the dynamic response of a massive liquefied natural gas outer tank under impact loading," *Journal of Zhejiang University Science*, vol. 20, no. 11, pp. 823–837, 2019.

[15] J. Li, J. Sun, L. Cui, X. Wang, and J. Hao, "Seismic performance numerical simulation analysis of LNG storage tank with filled wall," *Earthquake Engineering and Engineering Dynamics*, vol. 1, no. 3, pp. 157–164, 2014.

[16] X. H. Du and X. P. Shen, "Numerical simulation of fluid-structure interaction of LNG prestressed storage tank under seismic influence," *Computers, Materials and Continua*, vol. 20, no. 3, pp. 225–241, 2010.

[17] R. C. Ju, *Coupled Vibration Theory of Elastic Structure and Liquid*, Geological Publishing Press, Bath, UK, 1983.

[18] G. R. Liu and M. B. Liu, *Smoothed Particle Hydrodynamics: A Meshfree Particle Method*, World Scientific, Singapore, 2004.

[19] M. B. Liu and G. R. Liu, "Smoothed particle hydrodynamics (SPH): an overview and recent developments," *Archives of Computational Methods in Engineering*, vol. 17, no. 1, pp. 25–76, 2010.

[20] L. B. Lucy, "A numerical approach to the testing of the fission hypothesis," *The Astronomical Journal*, vol. 82, no. 82, pp. 1013–1024, 1977.

[21] R. A. Gingold and J. J. Monaghan, "Smoothed particle hydrodynamics: theory and application to non-spherical stars," *Monthly Notices of the Royal Astronomical Society*, vol. 181, no. 3, pp. 375–389, 1977.

[22] L. Wang, Z. Wang, and Y. Li, "A SPH simulation on large-amplitude sloshing for fluids in a two-dimensional tank," *Earthquake Engineering and Engineering Vibration*, vol. 12, no. 1, pp. 135–142, 2013.

[23] Y. T. Huang, D. U. Faxi, H. Liu et al., "Analysis on sloshing characteristics of liquid in elastomer tank based on SPH method," *Computer Aided Engineering*, vol. 24, no. 2, pp. 36–41, 2015.

[24] F. Liu, M. B. Tong, and J. P. Chen, "Numerical simulation of three-dimensional liquid sloshing based on SPH method," *Journal of Nanjing University of Aeronautics and Astronautics*, vol. 42, no. 1, pp. 122–126, 2010.

[25] J. R. Shao, H. Q. Li, G. R. Liu, and M. B. Liu, "An improved SPH method for modeling liquid sloshing dynamics," *Computers & Structures*, vol. 100-101, no. 6, pp. 18–26, 2012.

[26] D. Violeau and R. Issa, "Numerical modelling of complex turbulent free-surface flows with the SPH method: an overview," *International Journal for Numerical Methods in Fluids*, vol. 53, no. 2, pp. 277–304, 2007.

[27] S. Shao, "Simulation of breaking wave by SPH method coupled with k-ϵ model," *Journal of Hydraulic Research*, vol. 44, no. 3, pp. 338–349, 2006.

[28] Z. Zhang, L. Wang, F. Ming, V. V. Silberschmidt, and H. Chen, "Application of smoothed particle hydrodynamics

in analysis of shaped-charge jet penetration caused by underwater explosion," *Ocean Engineering*, vol. 145, pp. 177–187, 2017.

[29] S. W. Attaway, M. W. Heinstein, and J. W. Swegle, "Coupling of smooth particle hydrodynamics with the finite element method," *Nuclear Engineering and Design*, vol. 150, no. 2-3, pp. 199–205, 1994.

[30] F. Kalateh and A. Koosheh, "Simulation of cavitating fluid-Structure interaction using SPH-FE method," *Mathematics and Computers in Simulation*, vol. 173, pp. 51–70, 2020.

[31] S. Liang and Z. Chen, "SPH-FEM coupled simulation of SSI for conducting seismic analysis on a rectangular underground structure," *Bulletin of Earthquake Engineering*, vol. 17, no. 1, pp. 159–180, 2019.

[32] C. Fragassa, M. Topalovic, A. Pavlovic, and S. Vulovic, "Dealing with the effect of air in fluid structure interaction by coupled SPH-FEM methods," *Materials*, vol. 12, no. 7, p. 1162, 2019.

[33] J. K. Chen, J. E. Beraun, and C. J. Jih, "An improvement for tensile instability in smoothed particle hydrodynamics," *Computational Mechanics*, vol. 23, no. 4, pp. 279–287, 1999.

[34] ABAQUS 6.13, Abaqus Analysis User's Manual, Dassault Systémes Simulia Core, Providence, RI, USA, 2013.

[35] Y. Li, Z. Chen, X. Ren, R. Tao, R. Gao, and D. Fang, "Experimental and numerical study on damage mode of RC slabs under combined blast and fragment loading," *International Journal of Impact Engineering*, vol. 142, Article ID 103579, 2020.

[36] G. Qiu, S. Henke, and J. Grabe, "Application of a coupled Eulerian-Lagrangian approach on geomechanical problems involving large deformations," *Computers and Geotechnics*, vol. 38, no. 1, pp. 30–39, 2011.

[37] Z. Meng, J. Chen, and J. Wang, "The coupled Eulerian-Lagrangian analysis of pile jacking process in saturated soft clay by using modified cam-clay model," *Journal of Shanghai Jiaotong University*, vol. 51, no. 3, pp. 263–268, 2017.

[38] F. Salehi and R. Shamsoddini, "SPH simulation of the penetrating object in the wet soil," *Geomechanics and Geo-engineering*, pp. 1–11, 2020.

[39] T. El-Gammal, E. E. Khalil, H. Haridy, and E. Abo-Serie, "Influence of smoothing length and virtual particles on SPH accuracy," *International Journal of Materials, Mechanics and Manufacturing*, vol. 1, no. 2, pp. 166–170, 2013.

[40] A. Z. Gu, Q. G. Jin, Y. L. Ju, and J. Wang, *Technical Manual for Liquefied Natural Gas*, Machine Press, Beijing, China, 2010.

[41] N. N. Lv, J. Xie, and J. J. Yang, "Review on construction technology of large LNG low temperature storage tank," *Unique Construction*, no. 1, pp. 115–118, 2010.

[42] H. Fang, H. Wu, D. G. Wang, and X. G. Chen, "Review of research on seismic safety of liquid storage tanks," *Earthquake Disaster Prevention Technology*, vol. 7, no. 2, pp. 144–151, 2012.

[43] S. N. Huang and Z. Q. Wang, "The first 160,000 m^3 full capacity LNG storage tank in China," *Petroleum Engineering Construction*, vol. 35, no. 4, pp. 15–17, 2009.

[44] Y. Z. Wang and C. G. Fu, *Structural Engineering Analysis of Abaqus and Detailed Explanation of Examples*, China Building Industry Press, Beijing, China, 2010.

[45] Y. P. Shi and Y. R. Zhou, *Example and Analysis of Finite Element Software ABAQUS*, Machine Press, Beijing, China, 2006.

[46] Ministry of Housing and Urban-Rural Development of China, Code for seismic design of buildings GB 50011-2010, Ministry of Housing and Urban-Rural Development of China, Beijing, China, 2010.

[47] Standardization Administration Committee of the People's Republic of China, 9% Nickel Steel Plates for Pressure Vessels with Specified Low Temperature Properties, Standardization Administration Committee of the People's Republic of China, Beijing, China, 2010..

Research Article

Study on Long-Term Dynamic Mechanical Properties and Degradation Law of Sandstone under Freeze-Thaw Cycle

Qingsong Pu,[1,2] **Junhong Huang** ⓘ**,**[1,3,4] **Fuling Zeng,**[1,2] **Yi Luo** ⓘ**,**[1] **Xinping Li,**[1] **Jixue Zhou,**[1,2] **and Shilong Zheng**[1,2]

[1]*Hubei Key Laboratory of Roadway Bridge and Structure, Wuhan University of Technology, Wuhan, China*
[2]*School of Civil Engineering and Architecture, Wuhan University of Technology, Wuhan, China*
[3]*School of Safety Science and Emergency Management, Wuhan University of Technology, Wuhan, China*
[4]*School of Resource, Environmental Science and Engineering, Hubei University of Science and Technology, Xianning, China*

Correspondence should be addressed to Junhong Huang; junhonghuang@whut.edu.cn

This study is based on the tunnel-face slope engineering of Dongfeng tunnel in Shanxi section of China's Shuozhou-Huanghua Railway. The sandstone specimens in the perennial freeze-thaw zone of the slope were collected to carry out freeze-thaw cycle static physical mechanics test and split Hopkinson pressure bar (SHPB) dynamic mechanical test. Thus, the damage process of sandstone under freeze-thaw cycle and impact load is studied. Also, the dynamic compressive strength and dynamic elastic modulus of sandstone are analysed under different loading strain rates and freeze-thaw cycle based on LS-DYNA, a dynamic finite element program. The results showed that the dynamic compressive strength of sandstone subjected to multiple freeze-thaw cycles under 0.04 MPa air pressure has a greater damage ratio than that under 0.055 MPa and 0.07 MPa air pressure, which was more likely to cause damage to slope sandstone than in actual engineering; the dynamic compressive strength and elastic modulus of sandstone decrease greatly within a certain range of freeze-thaw cycles and loading strain rate, leading to significant deterioration. When the freeze-thaw cycle exceeded 200 times and the strain rate was greater than $200 \, s^{-1}$, the physical and mechanical properties of sandstone gradually tended to be stable.

1. Introduction

During the construction of mining, roads, and tunnels, in cold regions, the construction zone is often subjected to blasting vibration, heavy truck transportation vibration, earthquake vibration, and other dynamic loads. The frost heaving effect of the pore water inside the rock with the temperature change promotes the development of pores, and when the pores are subjected to dynamic loading, there is a serious impact on the stability of the rock engineering. It is of great significance for the stability and life cycle prediction of rock engineering in cold regions to analyse the deterioration law of static and dynamic mechanical parameters, strain rate effect, and rock failure mode of fractured rock masses under the coupling of freeze-thaw cycles and dynamic loads [1].

Domestic and international scholars have conducted in-depth research on the static and dynamic mechanical properties of rocks under the action of freeze-thaw cycles [2, 3]. Many scholars have studied the variation law of the longitudinal wave velocity, strength, elastic modulus, and permeability of different rocks under the action of freeze-thaw cycles [4, 5]. In 2013, a serious landslide accident occurred in the Lhasa Jiama mining area in China, causing serious casualties and property losses. The main cause of the accident was the deterioration of the mechanical properties of the rock mass caused by freeze-thaw cycles and dynamic loads [6]. Therefore, it is of great significance to study the dynamic mechanical properties of rocks under the action of freeze-thaw cycles and dynamic disturbance for construction in cold regions.

The freeze-thaw cycle induces the fracture propagation in rock mass and then weakens the mechanical parameters

such as elastic modulus and uniaxial compressive strength of rock mass. Deng et al. [7] made a back analysis of the rock mass mechanical parameters in the underground project through Seepage-Stress Coupled Analysis. Xu et al. [8] and Deng et al. [9] studied the energy distribution and transmission process in dynamic compression tests and dynamic tensile tests for different rock types and analysed the variation law of the dynamic energy parameters, absorption energy, reflection energy, projection energy, and other related energy. Zhang et al. [10], Alam et al. [11], and Yavuz [12] studied the deterioration law of sandstone under freeze-thaw action and quasistatic and dynamic loading conditions and analysed it from the change in the mechanical parameters such as the porosity, P-wave velocity, strength, and elastic modulus. Wang et al. [13] through improved the sandstone rheological constitutive model and optimized the algorithm of parameter inversion and put forward a long-term stability analysis model that can accurately reflect the rheological characteristics of surrounding rocks under the complex geological condition including high stress induced by great depth and high seepage pressure. Mutlutürk et al. [14] and Wang et al. [15] proposed a mathematical model for describing the integrity loss of rocks under freeze-thaw cycles. The reliability of the model was verified by studying ten different types of rocks. Zhang et al. [16] and He and Cui [17] would be simulating the failure process of rock under dynamic loading by a numerical simulation method and analysing the crack propagation path of rock after the reliability of the model was verified by the SHPB tests.

In this paper, the typical sandstone sample of Dongfeng tunnel slope of Shuohuang railway in China is taken as the research object. Through the laboratory freeze-thaw cycle test, SHPB impact compression test, and dynamic finite element numerical simulation test, the degradation law of dynamic mechanical properties of sandstone is studied and the numerical relationship between mechanical parameters such as dynamic strength and the number of freeze-thaw cycles and strain rate is established. It provides theoretical basis for the study of long-term stability and protection engineering of rock mass in the dynamic disturbance environment in cold region. The specific flowchart of research methodology is shown in Figure 1.

2. Dynamic Mechanical Test of Freeze-Thaw Rock Mass in Dongfeng Tunnel-Face Slope

2.1. Engineering Background of Freeze-Thaw Rock Mass in Dongfeng Tunnel-Face Slope.
Dongfeng tunnel is located in the northwest of Shuozhou-Huanghua Railway Shanxi section [18], with a total length of 3,290 meters and an altitude of about 1,200 meters as an area of high latitudes, the highest temperature of 20 degrees Celsius in winter, and the lowest temperature of minus 20 degrees Celsius. It is affected by the freeze and thaw obviously. Besides, Dongfeng tunnel is the hub of the heavy-haul railway such as coal transportation. Due to the heavy tonnage and heavy acting load of transport trains, the rock slope involved in the tunnel has been under unfavorable conditions such as heavy train load
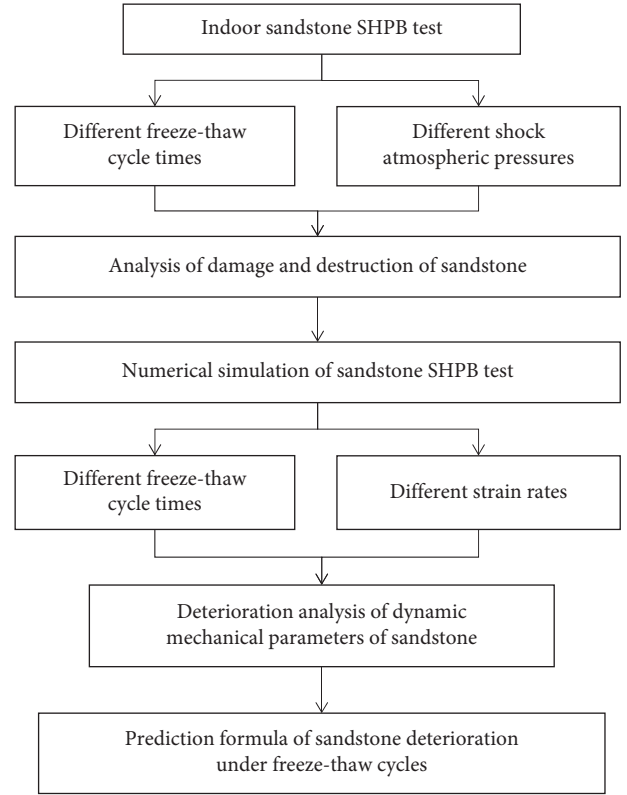

FIGURE 1: Specific flowchart of research methodology.

and freeze-thaw cycle for a long time, so more attention should be paid to its self-stability ability.

2.2. Test Equipment and Principles.
The SHPB device used in the test is shown in Figure 2. The main equipment includes launcher, bullet, buffer rod, bar, adjusting bracket, and control console; the loading system includes air compressor, transmission pipeline, and control valve; the test recording system includes elastic velocity and dynamic strain measuring system, in which the length of the incident rod is 4 m, the transmission rod is 3 m, and the pressure rod diameter is 100 mm. Due to the difference in wave impedance between the rod and the specimen, part of the incident wave is reflected for the incident rod to form a reflected wave, while the other part enters the transmission rod through the specimen to form a transmitted wave (see Figure 3). The voltage data measured by the strain gauge sensor on the incident bar and the transmission bar are converted into the data of stress, strain, and strain rate with calculation principle in the following equations, respectively [1]:

$$\sigma = \frac{A_0 E_0}{2A_1}\left(\varepsilon_I + \varepsilon_R + \varepsilon_T\right), \tag{1}$$

$$\varepsilon = \frac{C_0}{L_1}\int_0^t \left(\varepsilon_I - \varepsilon_R - \varepsilon_T\right)\mathrm{d}t, \tag{2}$$

$$\dot{\varepsilon} = \frac{C_0}{L_1}\left(\varepsilon_I - \varepsilon_R - \varepsilon_T\right), \tag{3}$$
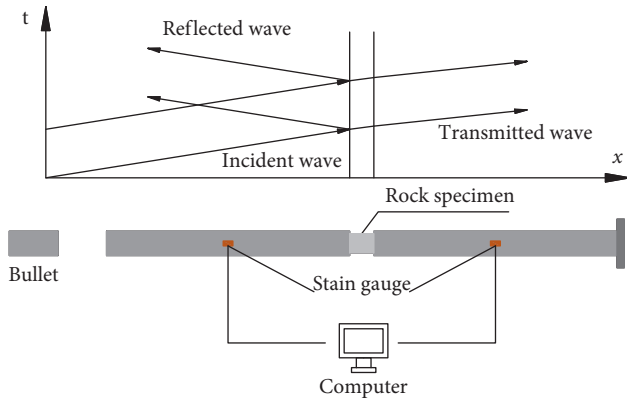
FIGURE 2: Laboratory SHPB test equipment.

FIGURE 3: SHPB impact compression test loading process diagram.

where E_0, A_0, and C_0 refer to the elastic modulus, cross-sectional area, and compressional wave velocity of the pressure bar, respectively, $C_0 = \sqrt{E_0/\rho_0}$; ε_I, ε_R, and ε_T refer to incident strain, reflected strain, and transmitted strain, respectively; ε refers to stain and $\dot{\varepsilon}$ refers to stain rate; A_1, L_1 refer to the cross-sectional area and length of the specimen, respectively.

2.3. SHPB Test Protocol. The sandstone in the test came from the tunnel-face slope of Dongfeng Tunnel of Shuozhou-Huanghua Railway; all sandstone samples in the freezing-thawing cycle tests were in the state of saturated water. According to the International Society for Rock Mechanics rock mechanics test standard, the sandstone specimen is processed into Φ 50 mm × 100 mm cylinders, with flatness, parallelism, and perpendicularity to the test specimens code requirements. The specimens were tested by ultrasonic waves, and the one with similar ultrasonic wave velocity was selected to ensure the uniformity inside.

The rock cutting machine and end face grinding machine and other equipment are used to process freeze-thaw sandstone specimens to produce sandstone specimens with a size of Ø 50 mm × 23 mm. According to the indoor pre-impact test, when the impact pressure is below 0.04 MPa, the bullet will not pop well enough, while when the impact pressure is above 0.07 MPa, the sandstone specimen will be too crushed, which is not conducive to observing the failure

form of the rock under impact load. In this paper, three groups of impact compression tests were designed, with an impact pressure of 0.04 MPa, 0.055 MPa, and 0.07 MPa, respectively. To ensure the accuracy of the tests, each group of tests was carried out three times.

2.4. Analysis of Test Results. In this paper, a comparative analysis is conducted on the sandstone that has undergone 0, 20, 40, 80, and 120 freeze-thaw cycles [19, 20], through which the typical physical and mechanical parameters of the sandstone specimens under the freeze-thaw cycle were obtained (Table 1).

The dynamic stress-strain curves of sandstone specimens with different freeze-thaw cycles under three impact pressures are shown in Figures 4–6. To sum up the dynamic compressive strength in the curve, namely, the stress-strain peak, which is shown in Table 2, it was indicated that when the impact pressure increases from 0.04 MPa to 0.055 MPa and from 0.055 MPa to 0.07 MPa in the same times of freeze-thaw, the dynamic compressive strength of sandstone increased by about two times. However, by comparing the damage values of sandstone specimens under different impact air pressure, it can be found that the dynamic compressive strength of sandstone under 0.04 MPa air pressure suffered from the highest damage rate after being affected by freeze-thaw cycle, and such strength suffered from the lowest damage rate under 0.07 MPa air pressure. This indicated that the smaller was the strain rate of sandstone and the greater was the influence of the mechanical properties produced by the freeze-thaw cycle. Compared with the SHPB impact test in the laboratory, the strain rate was smaller in the heavy-haul train, so it could be inferred that the dynamic mechanical properties of sandstone under the action of the heavy load train were more affected by the freeze-thaw cycle, which should be paid enough attention to.

3. Study on Mechanical Parameter Degradation of Freeze-Thaw Rock Mass in Dongfeng Tunnel-Face Slope

3.1. Study on Degradation of Static Mechanical Parameters of Sandstone with Different Freeze-Thaw Cycles. The design service life of the tunnel is hundred years. Assuming the rock experiences about three freeze-thaw cycles in a year, the dynamic mechanical properties of the rock after about 300 freeze-thaw cycles need to be considered. Through fitting the mechanical parameters of measured sandstone specimens, as shown in Figure 7, uniaxial compressive strength and elastic modulus fitting formulas of sandstone specimens under different freeze-thaw cycles are obtained. Furthermore, the physical and mechanical parameters of sandstone under 150, 200, 250, and 300 freeze-thaw cycles are calculated [21]. A lot of test data show that the density and Poisson's ratio of sandstone specimens are not affected by the freeze-thaw cycle. Therefore, the physical and mechanical parameters of sandstone specimens under the action of high-order freeze-thaw cycles are shown in Table 3.

TABLE 1: Physical and static parameters of sandstone under freeze-thaw cycle.

Number of freeze-thaw cycles	Density (kg/m³)	Elastic modulus (GPa)	Uniaxial compressive strength (MPa)	Poisson's ratio
0	2688	24.11	42.32	0.2537
20	2643	22.78	38.62	0.2635
40	2600	20.21	30.98	0.2672
80	2586	14.36	25.16	0.2715
120	2572	11.02	20.35	0.2756
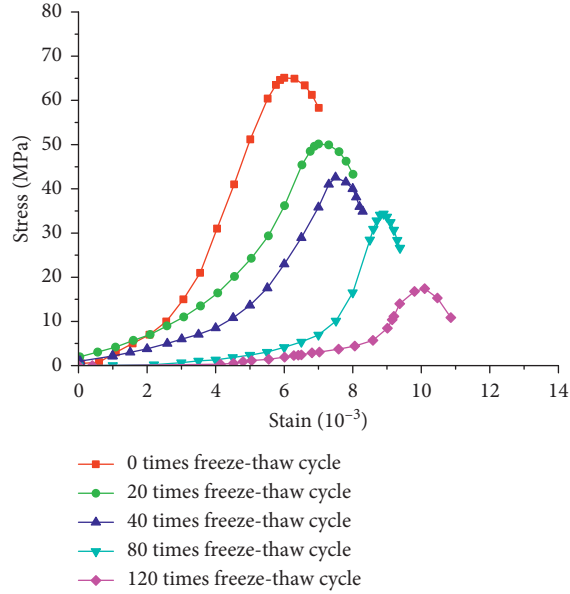
FIGURE 4: Stress-strain curves of sandstone in different freeze-thaw cycles under 0.04 MPa impact pressure.
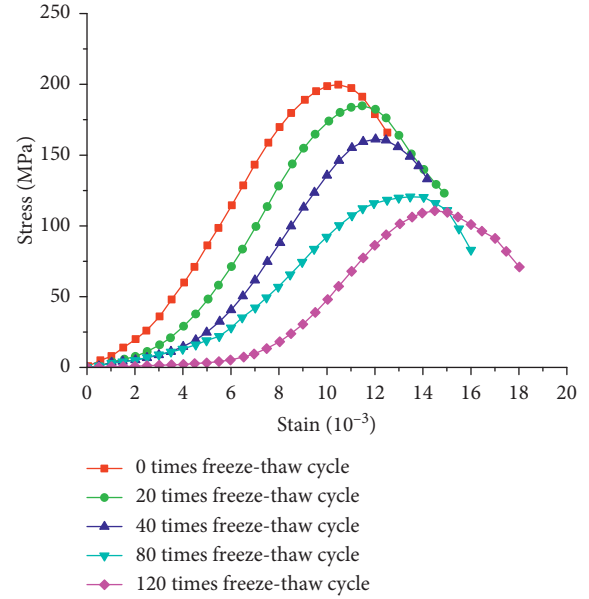
FIGURE 6: Stress-strain curve of sandstone with different freeze-thaw cycles under the impact pressure of 0.07 MPa.

3.2. Establishment of SHPB Numerical Simulation Test Model. In the numerical simulation test, a half sinusoidal stress wave was applied directly at the end of the incident bar to simulate the impulse process of approximate half sinusoidal stress pulse produced by the bullet hitting the incident bar. Different strain rate loading was realized by changing the peak value of the impact loads.

In this paper, the dynamic finite element program LS-DYNA was applied to supplement the interior SHPB experiment analysis, which focused on nonlinear dynamic analysis with static analysis capabilities. Among them, the HJC constitutive model described the damage of rock brittle materials, such as concrete body, using the accumulation of the equivalent plastic strain and the plastic bulk strain, which was capable of dealing with high speed and large deformation. The numerical model used the Solid164 element to simulate the pressure bar and specimen. This is an eight-node hexahedral element, which has the degrees of freedom of translation, velocity, and acceleration in X, Y, and Z directions.

The model length of the bar is 2 m, the thickness of the specimen is 0.023 m, and the radius is 0.05 m. The incident bar and the transmission bar are evenly divided into 200 parts along the axial direction, and the specimen is evenly divided into 50 parts as shown in Figure 8.

FIGURE 5: Stress-strain curves of sandstone in different freeze-thaw cycles under 0.055 MPa impact pressure.

TABLE 2: Stress peaks of sandstone specimens under different impact pressures.

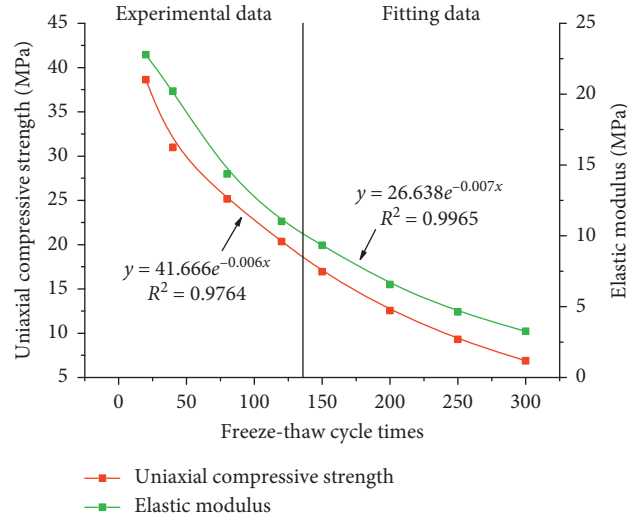| Impact pressure (MPa)	Number of freeze-thaw cycles				
	0	20	40	80	120
0.04	65	50	42	34	17
0.055	112	91	78	57	42
0.07	200	185	161	121	111

FIGURE 7: Fitting formulas for static compressive strength and elastic modulus of sandstone with different freeze-thaw cycles.

TABLE 3: Fitting values of physical and static parameters of sandstone under multiple freeze-thaw cycles.

Number of freeze-thaw cycles	Density (kg/m^3)	Elastic modulus (GPa)	Uniaxial compressive strength (MPa)	Poisson's ratio
150	2572	7.91	14.93	0.2756
200	2572	5.97	11.74	0.2756
250	2572	4.51	9.23	0.2756
300	2572	3.40	7.26	0.2756
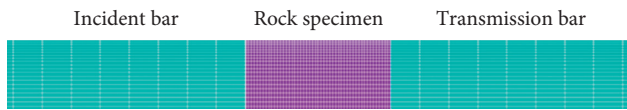
FIGURE 8: Establishment of the numerical simulation SHPB model.

The SHPB is made of steel, and the material parameters used in the numerical simulation are actual physical parameters, namely, density $\rho = 7900 \, \text{kg/m}^3$, elastic modulus $E = 210 \, \text{GPa}$, and Poisson's ratio $\nu = 0.2$. The widely used HJC empirical constitutive model is selected as the material for the sandstone specimen.

3.3. Study on Degradation of Dynamic Mechanical Parameters of Sandstone with Different Freeze-Thaw Cycles

3.3.1. Load Selection in Numerical Simulation of SHPB. In this paper, the indoor SHPB test under the impact pressure of 0.07 MPa is selected as the representative, and LS-DYNA is used to conduct numerical simulation tests. The measured load curve at the strain gauge position on the incident bar is shown in Figure 9, which is approximate to the semisinusoidal wave. In the numerical simulation, the semisinusoidal wave with similar amplitude and frequency is selected as the input load in the LS-DYNA numerical simulation test.

3.3.2. Feasibility Verification of Numerical Simulation Calculation of SHPB. Simulation of impact compression is carried out by LS-DYNA for four model specimens with different freeze-thaw cycles, and the dynamic compressive strength is shown in Figure 10, which is well consistent with the strength measured in the laboratory tests. Meanwhile, the failure morphology of model specimens is similar to that of sandstone in the impact compression test, both of which are split failure modes as shown in Figure 11. Since the numerical simulation results are similar to the laboratory test results in strength characteristics and failure modes, the numerical model could be used to simulate and analyse the impact test results of sandstone under different freeze-thaw cycles.
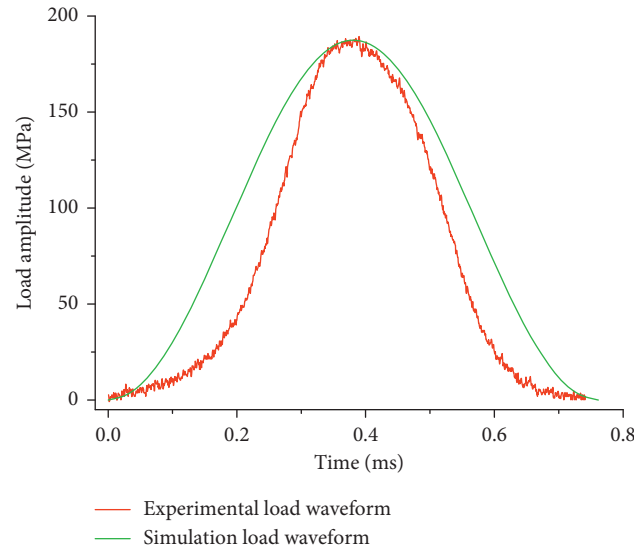
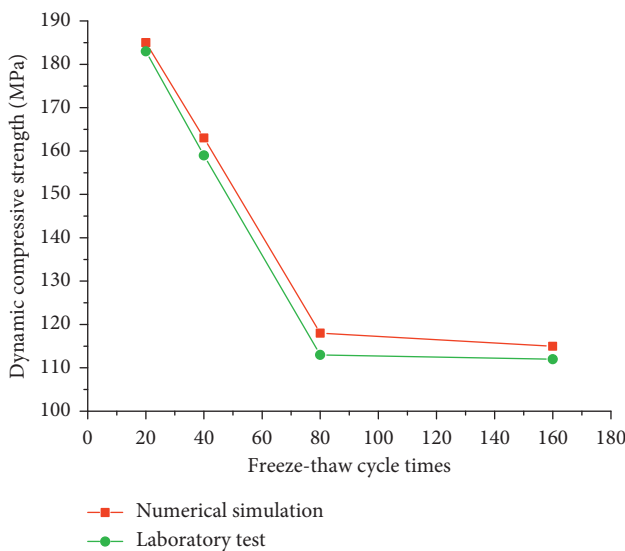FIGURE 9: Test and simulation input load curve.

FIGURE 10: Dynamic compressive strength of sandstone specimens under indoor and numerical SHPB tests.

3.3.3. Analysis of Study Results on Degradation of Dynamic Mechanical Parameters of Sandstone with Different Freeze-Thaw Cycles. The sandstones with 150, 200, 250, and 300 freeze-thaw cycles are simulated under the same impact load, and the stress-strain curve of sandstones is obtained as shown in Figure 12. It is observed that when the number of freeze-thaw cycles increased from 150 to 200 times, the peak stress of the specimen, namely, the maximum compressive strength, decreased greatly. However, when the number of freeze-thaw cycles is greater than 200 times, the amplitude of the peak stress of the stress-strain curve reduced gradually. Combined with the data from the indoor SHPB impact test, it can also be found that as the number of freeze-thaw cycles increases, the compressive strength of the specimen decreases more slowly after reaching a certain number of freeze-thaw cycles. In the laboratory test, there is a long pressure dense section, and the stress-strain curve in the simulation started directly from the elastic section. Therefore, there is a slight difference between the stress-strain curve in the numerical simulation and the test.

Assuming that the ratio of dynamic compressive strength to static compressive strength is dynamic compressive strength growth factor (DIF) [22], the curves of dynamic compressive strength, static compressive strength, and DIF with freeze-thaw cycles of sandstone specimens under the same strain rate are shown in Figure 13. It is observed that the dynamic compressive strength and static compressive strength both decrease with the increase of freeze-thaw cycles, while the value of DIF is always around 4.5, indicating that there is a certain correlation between dynamic compressive strength and static compressive strength, the correlation fluctuates with the number of freeze-thaw cycles, and DIF as a whole shows a slight downward trend.

The ratio between dynamic elastic modulus and static elastic modulus is defined here as a modulus proportional coefficient. Under the same strain rate, the curves of static elastic modulus, dynamic elastic modulus, and modulus proportional coefficient of sandstone specimens changing with the number of freeze-thaw cycles are shown in Figure 14. It is observed that in the numerical simulation experiment, there is a certain correlation between dynamic elastic modulus and static elastic modulus, which increase with the increase of freeze-thaw cycles. This means that with the increase of freeze-thaw cycles, the degradation of dynamic elastic modulus is gradually affected by the static elastic modulus and the number of freeze-thaw cycles.

3.4. Study on Dynamic Mechanical Parameters of Freeze-Thaw Cycle Sandstone under Different Strain Rates. Numerical simulation research of the freeze-thawed sandstone with different loading strain rates is carried out using LS-DYNA,
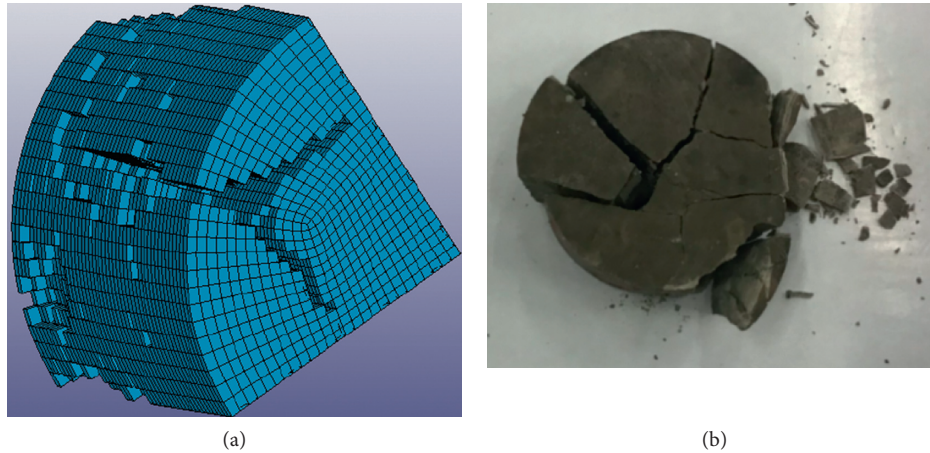
(a)

(b)

FIGURE 11: Failure modes of freeze-thaw cycle sandstone at 0.07 MPa impact pressure. (a) Typical failure patterns of a quarter of the specimen under numerical simulation. (b) Typical failure modes of laboratory test specimens.
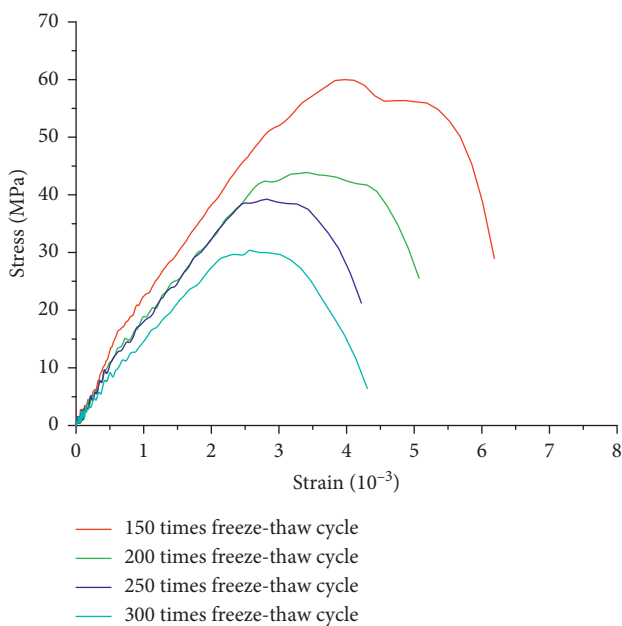

FIGURE 12: Stress-strain curve of different freeze-thaw cycles.

FIGURE 13: Curves of static and dynamic compressive strength and dynamic strength factor of sandstone with the number of freeze-thaw cycles.

a type of numerical simulation software. The software can overcome the weakness in accurate control of strain rates in the laboratory SHPB experiment. It is observed from Figure 15 that with the increase of strain rate, the compressive strength under $200 \, s^{-1}$ significantly increases in comparison with that in static state. However, when the strain rate increases to $380 \, s^{-1}$ of its original value, its dynamic compressive strength only increases by less than 0.1 times; when the strain rate reaches $580 \, s^{-1}$, the dynamic compressive strength increases by an obviously smaller amount; under the strain rate of $750 \, s^{-1}$, the mean increase of its dynamic compressive strength is only 0.03 times of $580 \, s^{-1}$. It shows that the dynamic compressive strength of sandstones will gradually become stable with the strain rate increasing to a certain extent under the same freeze-thaw cycles.
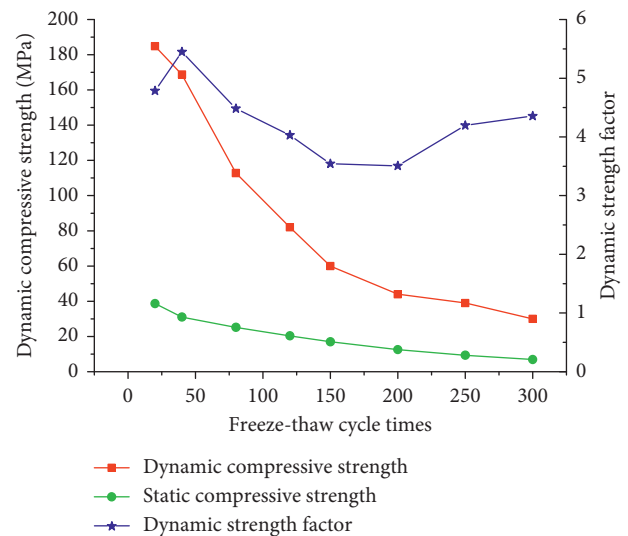
It is observed from Figure 16 that the dynamic elastic modulus of sandstones is affected by both the number of freeze-thaw cycles and the strain rate. Under different strain rates, the law of the dynamic elasticity modulus varying with the number of freeze-thaw cycles is similar. When the strain rate increases to a certain extent, the influence of strain rate on dynamic elasticity modulus is weakened. The law is similar to the dynamic compressive strength.

The least-square method is used to fit the fitting formula of dynamic compressive strength of high-order freeze-thaw cycle rock mass under different strain rates, as shown in Table 4.

Table 4 indicates that the fitting formulas describing the fact that dynamic compressive strength of sandstones varies with freeze-thaw cycles under different strain rates are similar with high correlation coefficient R. Therefore, the
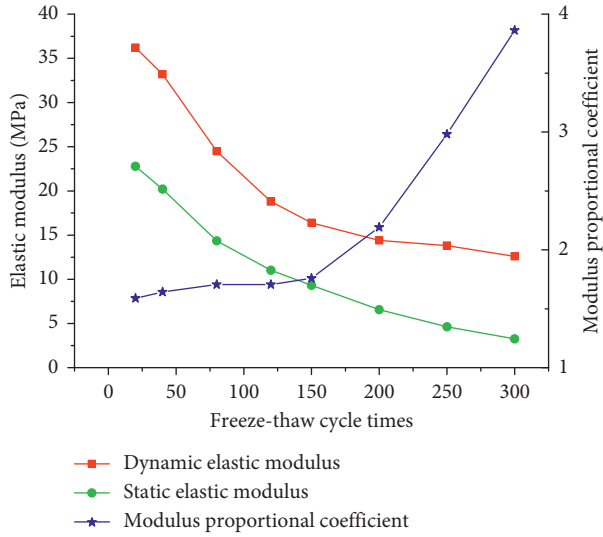
Figure 14: Variation rule of dynamic and static elastic modulus and modulus proportional coefficient with freeze-thaw cycles.
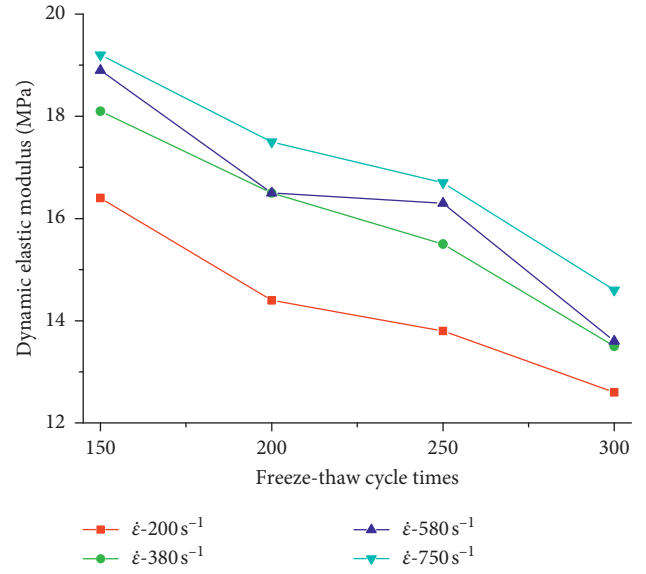

Figure 16: Influence of input load on dynamic elastic modulus of rock mass under different freeze-thaw cycles.
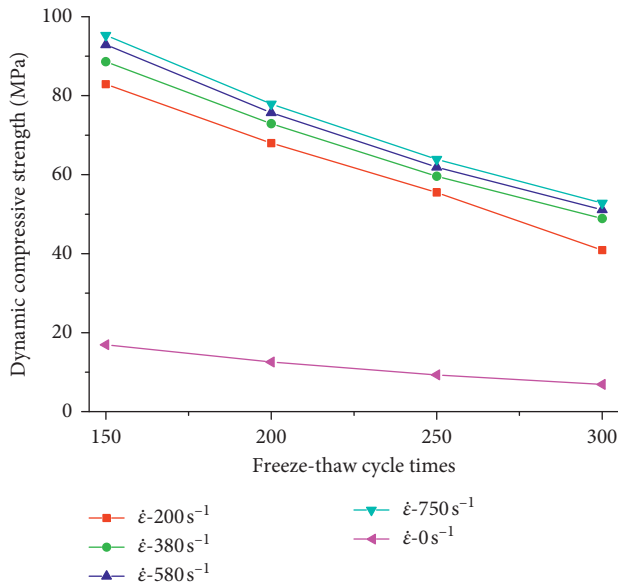

Figure 15: Influence of strain rate on dynamic compressive strength of rock mass under different freeze-thaw cycles.

Table 4: Dynamic compressive strength fitting formula of freeze-thaw cycle sandstone under different strain rates.

Strain rate (s^{-1})	Fitting formula (x is the number of freeze-thaw cycles)	Correlation coefficient R
200	$y = 151.0e^{-0.004x}$	0.978
380	$y = 160.9e^{-0.004x}$	0.999
580	$y = 168.5e^{-0.004x}$	0.998
750	$y = 171.6e^{-0.004x}$	0.997

mass has certain reference value for the safety and stability of practical engineering.

4. Conclusion

In this paper, the indoor SHPB impact compression test was carried out using the sandstone under freeze-thaw cycles as the object. Also, the mechanical parameter degradation law of sandstones under numerous freeze-thaw cycles was studied by LS-DYNA, the dynamic finite element. Results are shown as follows:

(1) With the increase of freeze-thaw cycles in sandstones, the dynamic compressive strength and elastic modulus of rock specimens decreased under the impact pressures of 0.04 MPa, 0.055 MPa, and 0.07 MPa. Under the same freeze-thaw cycle, the dynamic compressive strength of sandstone under 0.04 MPa air pressure suffered from the highest damage rate after being affected by freeze-thaw cycle, and such strength suffered from the lowest damage rate under 0.07 MPa air pressure, which indicates that the smaller was the strain rate of sandstone, the greater was the influence of the strain rate on the mechanical properties under the freeze-thaw cycle.

coefficients of the fitting formula in Table 4 are refitted to obtain the fitting equation (4), the fitting formula of dynamic compressive strength of sandstones with freeze-thaw cycles, which is related to the strain rate:

$$y = Me^{-0.004x}, \quad (4)$$

where $M = 89.5\dot{\varepsilon}^{0.0988}$ correlation coefficient $R = 0.9987$, in which $\dot{\varepsilon}$ referred to strain rate.

This formula can be used to predict the dynamic compressive strength of sandstone under different freeze-thaw cycles based on the number of freeze-thaw cycles and strain rate, and the dynamic compressive strength of rock

(2) When the freeze-thaw cycle of sandstone increases in arithmetic progression, the decrease of stress-strain peak curve of sandstone tapered off under the same impact pressure and the dynamic compressive strength growth factor fluctuated around 4.5 along with the freeze-thaw cycles. Also, the static elastic modulus and the freeze-thaw cycles had a gradually increased influence on the degradation of dynamic elasticity modulus.

(3) With the increase of strain rate, the dynamic compressive strength and dynamic elastic modulus of sandstone with different freeze-thaw cycles decreased with the increase of freeze-thaw cycles and gradually approached a stable value, indicating that the deterioration of sandstone was greater with the strain rate changing below $200\,\mathrm{s}^{-1}$.

In this paper, only the influence of freeze-thaw cycle and impact load on the deterioration of sandstone mechanical parameters was studied. How to improve the soil environment was not considered to increase the bearing capacity of the foundation and therefore to improve the safety and service life of railways [23, 24]. This would be studied in future studies.

Data Availability

The curve data used to support the findings of this study are available from the corresponding author upon request.

Conflicts of Interest

The authors declare that they have no conflicts of interest.

Acknowledgments

References

[1] Y. Luo, D. Qu, G. Wang, X. Li, and G. Zhang, "Degradation model of the dynamic mechanical properties and damage failure law of sandstone under freeze-thaw action," *Soil Dynamics and Earthquake Engineering*, vol. 132, p. 106094, 2020.

[2] J. Eslami, C. Walbert, A.-L. Beaucour, A. Bourges, and A. Noumowe, "Influence of physical and mechanical properties on the durability of limestone subjected to freeze-thaw cycles," *Construction and Building Materials*, vol. 162, pp. 420–429, 2018.

[3] T. Jiang, J. Zhang, and H. Wu, "Experimental and numerical study on hydraulic fracture propagation in coalbed methane reservoir," *Journal of Natural Gas Science and Engineering*, vol. 35, pp. 455–467, 2016.

[4] Q. Liu, S. Huang, Y. Kang, and X. Liu, "A prediction model for uniaxial compressive strength of deteriorated rocks due to freeze-thaw," *Cold Regions Science and Technology*, vol. 120, no. 1, pp. 96–107, 2015.

[5] J. Yu, X. Chen, H. Li, J.-W. Zhou, and Y.-Y. Cai, "Effect of freeze-thaw cycles on mechanical properties and permeability of red sandstone under triaxial compression," *Journal of Mountain Science*, vol. 12, no. 1, pp. 218–231, 2015.

[6] B. Ke, K. Zhou, C. Xu, H. Deng, J. Li, and F. Bin, "Dynamic mechanical property deterioration model of sandstone caused by freeze-thaw weathering," *Rock Mechanics and Rock Engineering*, vol. 51, no. 9, pp. 2791–2804, 2018.

[7] X. Deng, D. Yuan, D. Yang, and C. Zhang, "Back analysis of geomechanical parameters of rock masses based on seepage-stress coupled analysis," *Mathematical Problems in Engineering*, vol. 2017, Article ID 3012794, 13 pages, 2017.

[8] X. Xu, Y. Dong, and C. Fan, "Laboratory investigation on energy dissipation and damage characteristics of frozen loess during deformation process," *Cold Regions Science and Technology*, vol. 109, pp. 1–8, 2015.

[9] Y. Deng, M. Chen, Y. Jin, and D. Zou, "Theoretical analysis and experimental research on the energy dissipation of rock crushing based on fractal theory," *Journal of Natural Gas Science and Engineering*, vol. 33, pp. 231–239, 2016.

[10] J. Zhang, H. Deng, A. Taheri, B. Ke, and C. Liu, "Deterioration and strain energy development of sandstones under quasi-static and dynamic loading after freeze-thaw cycles," *Cold Regions Science and Technology*, vol. 160, pp. 252–264, 2019.

[11] M. S. Alam, T. Chakraborty, V. Matsagar, K. S. Rao, P. Sharma, and M. Singh, "Characterization of kota sandstone under different strain rates in uniaxial loading," *Geotechnical and Geological Engineering*, vol. 33, no. 1, pp. 143–152, 2015.

[12] H. Yavuz, "Effect of freeze-thaw and thermal shock weathering on the physical and mechanical properties of an andesite stone," *Bulletin of Engineering Geology and the Environment*, vol. 70, no. 2, pp. 187–192, 2011.

[13] Z. Wang, X. Chen, X. Xue, L. Zhang, and W. Zhu, "Mechanical parameter inversion in sandstone diversion tunnel and stability analysis during operation period," *Civil Engineering Journal*, vol. 5, no. 9, pp. 1917–1928, 2019.

[14] M. Mutlutürk, R. Altindag, and G. Türk, "A decay function model for the integrity loss of rock when subjected to recurrent cycles of freezing-thawing and heating-cooling," *International Journal of Rock Mechanics and Mining Sciences*, vol. 41, no. 2, pp. 237–244, 2004.

[15] P. Wang, J. Xu, S. Liu, S. Liu, and H. Wang, "A prediction model for the dynamic mechanical degradation of sedimentary rock after a long-term freeze-thaw weathering: considering the strain-rate effect," *Cold Regions Science and Technology*, vol. 131, pp. 16–23, 2016.

[16] X.-L. Zhang, Y.-Y. Jiao, and J.-F. Ma, "Simulation of rock dynamic failure using discontinuous numerical approach," *Computers and Geotechnics*, vol. 96, pp. 160–166, 2018.

[17] P.-P. He and Z.-D. Cui, "Dynamic response of a thawing soil around the tunnel under the vibration load of subway," *Environmental Earth Sciences*, vol. 73, no. 5, pp. 2473–2482, 2015.

[18] C. N. Bai, J. P. Guo, and J. G. Li, "Study on disease analysis and treatment of high slope in Longgong Station of Shuohuang Railway," *Journal of Railway Engineering*, vol. 34, no. 2, pp. 47–52, 2017.

[19] W. Dong, X.-D. Shen, H.-J. Xue, J. He, and Y. Liu, "Research on the freeze-thaw cyclic test and damage model of Aeolian sand lightweight aggregate concrete," *Construction and Building Materials*, vol. 123, pp. 792–799, 2016.

[20] X. Luo, N. Jiang, C. Zuo, Z. Dai, and S. Yan, "Damage characteristics of altered and unaltered diabases subjected to extremely cold freeze-thaw cycles," *Rock Mechanics and Rock Engineering*, vol. 47, no. 6, pp. 1997–2004, 2014.

[21] R. Song, L. Zheng, Y. Wang, and J. Liu, "Effects of pore structure on sandstone mechanical properties based on micro-CT reconstruction model," *Advances in Civil Engineering*, vol. 2020, Article ID 9085045, 21 pages, 2020.

[22] Q. Ma, D. Ma, and Z. Yao, "Influence of freeze-thaw cycles on dynamic compressive strength and energy distribution of soft rock specimen," *Cold Regions Science and Technology*, vol. 153, pp. 10–17, 2018.

[23] M. Yao, Q. Wang, B. Ma, Y. Liu, Q. Yu, and Y. Han, "Effect of freeze-thaw cycle on shear strength of lime-solidified dispersion soils," *Civil Engineering Journal*, vol. 6, no. 1, pp. 114–129, 2020.

[24] A. E. Abu El-Maaty, "Enhancing of CBR strength and freeze-thaw performance of silty subgrade using three reinforcement categories," *Civil Engineering Journal*, vol. 2, no. 3, pp. 73–85, 2016.